# TOWARDS RATIONAL DESIGN OF PRECURSORS FOR FOCUSED ELECTRON BEAM INDUCED DEPOSITION

by

Julie A. Spencer

A dissertation submitted to Johns Hopkins University in conformity with the requirements for the degree of Doctor of Philosophy

Baltimore, MD

October, 2016

ABSTRACT

Focused electron beam induced deposition (FEBID) is an emerging method to fabricate nanostructures without the use of resists or masks. In the FEBID process, a gas phase precursor is introduced into a vacuum chamber and transiently adsorbed onto a substrate. A focused electron beam is used to irradiate the precursor, which decomposes under electron beam irradiation. The non-volatile portions of the precursor molecule remain behind on the surface as a deposit, while the volatile portions are pumped away into the vacuum.

FEBID has a great deal of potential, but it is currently limited by significant amounts of contamination that remain in the nanostructures. Most precursors that are used for FEBID were designed as chemical vapor deposition (CVD) precursors and were optimized for the thermal process of CVD. Under the electron-based process of FEBID, precursors which produce pure metal films in CVD often produce FEBID deposits with significant levels of contamination, due to the different mechanisms of the two processes. This highlights the need to develop precursors specifically for FEBID.

This research used an ultrahigh vacuum surface science approach to investigate the process by which FEBID precursors decompose under electron beam interaction. Specifically, the tools of x-ray photoelectron spectroscopy (XPS) and mass spectrometry (MS) were used to evaluate precursors adsorbed onto cooled substrates under 500 eV electron beam

irradiation; this process allowed investigation of both species that remain on the surface and those released into the gas phase. This surface science approach provides kinetic and mechanistic details of precursor decomposition that are not available in the electron microscopes typically used for FEBID. During this work, several precursors were investigated: $\eta^3$-$C_3H_5$($Ru(CO)_3Br/Cl$, $cis$-$Pt(CO)_2Cl_2$, $Co_2(CO)_8$, and $CpFe(CO)_2Mn(CO)_5$. Purification of $cis$-$Pt(CO)_2Cl_2$ by electrons and atomic hydrogen radicals was also investigated.

Certain ligand types are preferable for FEBID precursors. A small number of carbonyl ligands may desorb under electron beam irradiation. Carbon-rich ligands ($\eta^3$-$C_3H_5$, $\eta^5$-$C_5H_5$) remain behind in deposits as contamination, and halogens are somewhat of a free ligand, as they desorb under a slower, electron stimulated desorption process. Our success in achieving pure Pt films from electron beam irradiation of $cis$-$Pt(CO)_2Cl_2$ prompted further purification studies using atomic hydrogen radicals, which were found to efficiently purify deposits of Cl; however, this resulted in mobility and dispersion of the platinum, creating a porous structure. These results will inform rational design of FEBID precursors as research continues to address contamination in FEBID nanostructures.

Advisor:  Dr. D. Howard Fairbrother

Reader:  Dr. Paul J. Dagdigian

Reader:  Dr. Harris J. Silverstone

## Acknowledgements

The challenge of working towards a Doctor of Philosophy degree in Chemistry has been all-consuming, and I could not have made it to this point without the support of several important people. First, I must thank my fellow members of the Fairbrother Research Group. Their assistance and camaraderie made the hours seem shorter and the task less daunting. Thank you to Dr. Samantha Rosenberg, Dr. Julie Bitter, Dr. David Goodwin, Jr., Miranda Gallagher, Ronald Lankone, Rachel Thorman, David Durkin, Benjamin Frank, and Dr. Ilyas Unlu—I learned a great deal from you. Without your help, the laboratory work would have been much less enjoyable and the overall process would have been much more difficult.

Working with Dr. D. Howard Fairbrother has been a pleasure. I credit him with improving my questioning attitude and my development as a scientist, and teaching me a great deal about ultra-high vacuum systems. I appreciate his sound advice, intellectual curiosity, and willingness to teach.

My family has been consistently supportive and I can't thank them enough for all their assistance. My parents, Jerry and Nila Jean Spencer, provided much assistance and guidance, and many cooked meals when it was too much trouble to cook when doing experiments. I appreciate their unconditional love and support.

Lastly, I appreciate the opportunity that the U.S. Navy and U.S.

## Table of Contents

# List of Tables

# List of Figures

Chapter 1


Introduction and Experimental Methods

Chapter 1.    Introduction and Experimental Methods

1.1. Introduction

As technology continues to improve, products that range from computers, cellular telephones, and digital memory get smaller and smaller. This continued demand for improved and more capable devices drives nanofabrication and the semiconductor industry to continually seek the ability to achieve smaller and smaller integrated circuit feature sizes. This trend can be seen in almost any modern technology. Richard Feynman famously said, "There's plenty of room at the bottom," and indeed, this continues to be borne out by ongoing technology and further development at the nanoscale[1].

The drive for increasingly smaller feature sizes has driven research and motivated huge expenditures for microchip fabrication lines. When the feature size on an integrated circuit is on the order of a micron ($1 \times 10^{-6}$ m) or in the hundreds to tens of nanometers ($1 \times 10^{-9}$ m), even a speck of dust can create havoc; thus, the move towards ever smaller integrated circuit features has led to the need for huge clean room facilities in which < 10 particles (0.1 μm in size)/ft$^3$ are allowed[2]. As the drive to get smaller continues, these fabrication facilities must be upgraded to allow fabrication of smaller features. Moore's law anecdotally states that the number of features that can fit on a chip will double every two years, and this has largely held true, leading to the continued drive towards smaller feature sizes and new technologies to support this effort[3]. Significant research continues into which technology will fuel the next leap to fabrication of smaller integrated circuit sizes. There are a variety of processes that allow fabrication of nanoscale features, including photolithography, electron beam lithography and extreme ultraviolet lithography. This research investigates the emerging technology of focused electron beam

induced deposition (FEBID), a competing or complementary process to those widely used in large-scale nanofabrication. As a preparation to discussion of FEBID, several fabrication techniques will be discussed.

### 1.1.1. Thin Film Deposition Techniques

Thin films may be generated by a variety of methods, which are discussed in more detail below. Thin film deposition techniques are described due to their heavy usage in industry in integrated circuit fabrication and as an integral part of techniques that compete with or complement FEBID.

#### 1.1.1.1. Physical Deposition Processes

Some of the simplest thin film deposition processes are considered physical deposition processes, in which the material to be deposited is physically (rather than chemically) deposited. One method that is heavily used in integrated circuit fabrication in applying resists to silicon wafers is spin coating, but as that primarily applies to liquids/resists, it will not be discussed here. Evaporation was widely used in early manufacturing of semiconductors. The evaporation process involves heating a substance in a vacuum chamber until a vapor is given off, which then spreads throughout the chamber and accumulates on the substrate as a thin film[3]. Industrial fabrication has largely moved from the evaporation process to another physical deposition method, sputtering. Sputtering is the use of a plasma chamber under a vacuum, in which high energy ions (usually Argon) impinge on a target comprised of the material to be deposited. These ions strike the target material which results in some of the target material being sputtered off, which then deposits on the substrate or wafer to be coated[2].

### 1.1.1.2.    Chemical Vapor Deposition

Chemical Vapor Deposition (CVD) is a process in which thin, conformal films may be formed by the interaction of a gas phase precursor (usually metal containing) with a heated substrate[4].  The precursor reacts with the heated substrate, and results in a thin, conformal film of high purity.  CVD has been used extensively in the fabrication of microelectronics/computer chips.  Suitable precursors for CVD are generally volatile and carefully chosen so that the ligand architecture results in relatively pure films after thermal reactions[4,5].  Good CVD precursors have characteristics that also make them good FEBID precursors, and thus, CVD precursors are often used in the FEBID process[6,7].

### 1.1.1.3.    Atomic Layer Deposition

Atomic layer deposition (ALD) is a technique that is heavily used in the semiconductor industry to produce high quality, pinhole-free thin films even on non-uniform surfaces[8].  ALD is a self-limiting process in which a sequence of reactants is used.  In ALD, one reactant is introduced into a vacuum chamber (reactor) and reacts with surface sites on the substrate.  The reaction is self-limited because the technique involves reactions with available surface sites on the substrate; once they are filled, the reaction is complete regardless of the presence of the precursor gas.  Then, the chamber is evacuated of the first reactant, and filled with the second reactant, which again reacts with the substrate surface sites until all are filled.  This technique can be repeated numerous times, each time with the ability to deposit a thin, high quality film of angstrom (Å) or monolayer thickness[8].  ALD is often thermally based, and indeed, many ALD processes were derived from CVD, but ALD often provides higher quality films, especially on high aspect ratio structures[8].  Deposition of some elemental materials is often assisted by other species or methods, such

as plasma or atomic radicals, which can also allow the reaction to take place at lower temperatures.

### 1.1.2. Nanopatterning Methodologies

The thin film deposition techniques are applied as part of a lengthy processing chain to make integrated circuits or microchips, widely used in computers and technological applications. Some of the basic processes will be described below.

#### 1.1.2.1. Photolithography

The most widely used method for large scale production of integrated circuits for use in technology application is photolithography, also known as photomasking or patterning[2,3]. A significant amount of research and development has led to this becoming a robust process capable of producing large volumes of integrated circuits. A detailed analysis of the photolithographic process is beyond the scope of this dissertation; however, an overview of the basic steps is provided. Photolithography[2,3] starts with wafer preparation, in which a base material (generally silicon) is prepared for further processing, and a photoresist is applied (often using a spin-coating process to ensure the wafer is covered to a uniform thickness). The lithographic step takes place when the wafer is aligned to the photomask and the wafer/photoresist system is exposed to radiation, causing a reaction in the exposed area of the photoresist. After exposure, the unreacted photoresist is removed and if the wafer meets quality requirements, a top portion of the wafer is removed by etching, using the hole in the resist layer (from the masking process). Lastly, the photoresist layer is removed, and the wafer is inspected again. This process may be conducted numerous times, in conjunction with various thin film deposition processes and other steps, to produce a modern microchip[2]. It can be noted immediately that although

photolithography is extensively used to produce high quality integrated circuits, the process is quite complex.

### 1.1.2.2. Electron Beam Lithography

Electron beam lithography (EBL) is a robust technology that uses direct electron beam writing to make photomasks for the photolithography process[2]. EBL has similarities to the photomasking process, in that a resist is used, but this resist reacts based on electron induced reactions rather than photon induced reactions as in photolithography. EBL does not require the use of masks, as the pattern to be imaged is determined by computer, and written by computer control. EBL is capable of producing features down to ~ 10 nanometers, but starts to have resolution issues below that size[9]. EBL is currently too slow to be used to pattern wafers on a large scale as done with photolithography, but is used extensively to produce photomasks[2].

### 1.1.2.3. Focused Electron Beam Induced Processing/Deposition

Focused electron beam induced processing (FEBIP) is an emerging technology that has the ability to produce nanostructures on the nanometer scale. Focused electron beam induced processing includes both electron beam deposition and electron beam etching[6,7]. This research is focused on the focused electron beam induced deposition process[6,7,10,11]. To date, focused electron beam induced deposition has been able to produces nanodeposits as small as a dot of 0.7 nm diameter at full width at half maximum[12]. FEBID offers an alternate process to produce nanostructures on the same or smaller size regime than photolithography or electron beam lithography. Focused electron beam induced deposition (FEBID) has a great deal of promise in fabricating structures on the nanoscale; it can even be considered 3-D printing on the nanoscale[13]. However, to realize its potential, the major

issues of nanostructure purity and processing speed must be addressed. This work investigates precursor chemistry involved in the FEBID process.

Focused electron beam induced deposition is generally done in a modified scanning electron microscope and requires a vacuum environment. In FEBID, a gaseous precursor is introduced into the vacuum chamber, where it impinges on a substrate and is transiently absorbed. During this short residence time on the substrate, the precursor is irradiated by a focused electron beam, which causes decomposition of precursor molecules. The non-volatile portion of the molecule remains behind on the surface, while the volatile portions of the molecule are pumped away into the vacuum. FEBID has been referred to as a local electron beam CVD process[13], and indeed, it shares some similarities with CVD in that a gas phase precursor breaks down under a treatment. Unlike CVD, which is a thermally based process, FEBID is an electron-based process. There are many variables involved in producing size and shape specific nanostructures of high purity in FEBID, including the electron beam, identity of electrons that actually cause deposition (from the primary beam, or secondary electrons stimulated from the substrate), beam dwell time, precursor, post treatment processes, identity of the substrate, and deposition conditions[6,7,10,11].

FEBID does not require any resists or masks, so if the issues of purity can be addressed, FEBID could find a wide range of applications. Even with the nanostructure purity issue, FEBID has been successfully used to fabricate ultra-sharp atomic force microscopy (AFM) tips[14], repair photomasks[15,16], and indeed, to make photomasks[17].

1.2. Surface Science and Experimental Techniques

Surface science involves the study of processes at surfaces. The definition of a "surface" is somewhat variable, but generally is considered to be on the order of

nanometers $(5-10)$[18]. Surface science is interesting because all reactions take place at the surface. As technology continues to miniaturize, the surface becomes ever more important because it is a larger proportion of the material as the surface area and surface to volume ratio increase. Many surface science techniques make use of the unique properties of electrons and interactions at surfaces. Since an electron in a material has a limited escape depth (mean free path) before it suffers a collision, techniques such as X-ray photoelectron spectroscopy and Auger electron spectroscopy are of necessity surface sensitive, since electrons from deeper in the bulk suffer collisions prior to escaping the material, thus losing their unique information about the material.

1.2.1. X-ray Photoelectron Spectroscopy

The technique at the heart of this research is X-ray photoelectron spectroscopy (XPS), which is also known as electron spectroscopy for chemical analysis (ESCA)[18,19]. XPS is based on the photoelectric effect, which Einstein elucidated by explaining several experimental observations, that shining light (energy, above a certain threshold frequency) on a material caused electrons to be ejected[18]. This process holds true as the energy of the photon source is increased, and can occur with visible, ultraviolet, and x-ray photons. XPS as currently practiced was developed by Kai Siegbahn, for which he received the Nobel prize in physics in 1981[18]. It has gained increasingly greater use as a powerful tool for surface analysis. The steps involved in XPS are: (1) a surface to be analyzed is irradiated by X-rays of a known photon energy; (2) this causes core level electrons to be ejected from the surface; and (3) the ejected photoelectrons are characterized by an analyzer, providing information about the surface from which they originated. The emitted photoelectrons have characteristic energies based on the element from which they originated, and if the

electrons are sufficiently close to the surface to exit the substrate without suffering a collision, they retain their characteristic information, which can be used to obtain elemental analysis of the sample, and provide information on the bonding present in the sample. To gather XPS information, X-ray energy of a known photon energy is used; this work used Mg Kα X-rays (h$v$ = 1253.6 nm). The photoelectrons are characterized by the analyzer, measuring the kinetic energy (KE) of the ejected photoelectrons; thus, the binding energy (BE), which provides the information used for analysis, may be determined by:

BE = h$v$ - KE – $\phi$ (work function), a function of the instrument.

Electrons from deeper in the sample suffer collisions prior to reaching the detector, and thus, no longer contain characteristic information about the chemical composition, and contribute to the background signal. For this reason, XPS is by nature a surface sensitive technique, but it is quite powerful in determining elemental composition and bonding environments, i.e., the binding energy of a carbon atom bonded to another carbon atom is much different than a carbon atom bonded to a fluorine atom[20]. An image of the XPS used in this research is shown below.
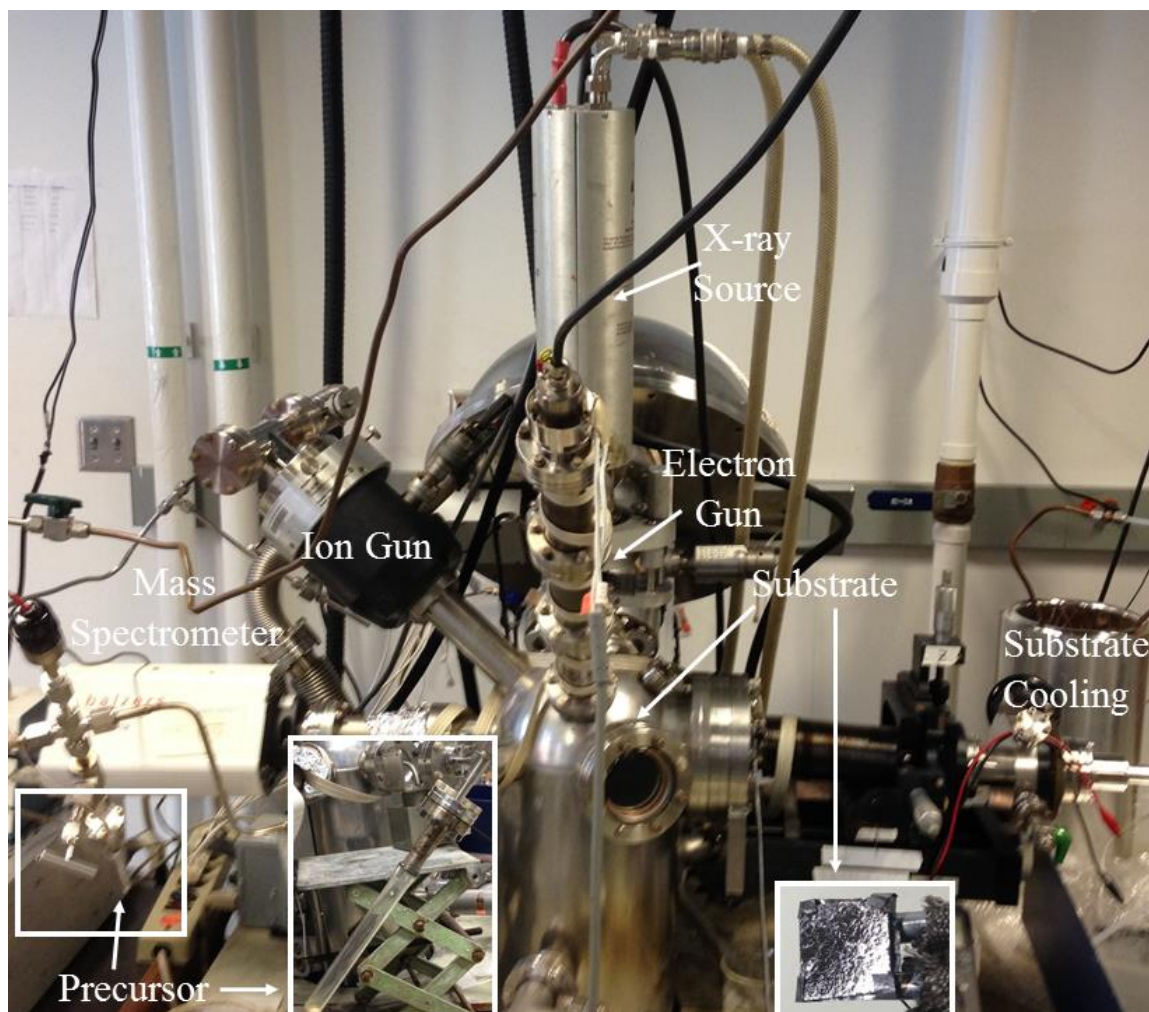
**Figure 1.1**: PHI 5400 X-ray Photoelectron Spectrometer (XPS) used in UHV surface science investigations of FEBID precursors.

### 1.2.2. Auger Electron Spectroscopy

Auger electron spectroscopy (AES) is a surface science technique which uses electrons impinging on a surface to gather compositional information[18,19]. In the Auger process, a high energy electron beam is used to irradiate a substrate. The beam energy must be high enough to allow ionization of a particular transition, and Auger spectrometers often use electron beams of 3, 5 or 10 kV. The initial electron from the primary beam

ejects a core level electron. Next, an electron from one of the higher atomic shells drops down to fill the vacated core hole. The energy difference between the original energy level of the electron that fills the core hole, and the core hole energy level is transferred to a third electron, which is ejected from the atom. If an electron which is ejected from an atom is close enough to the surface of the material so that it does not suffer a collision before exiting the surface, it is detected and contributes to the Auger signal for a particular element. Similar to the transitions observed in XPS, the energy differences of Auger transitions are quantized and thus, Auger spectroscopy can also be used for elemental analysis of a material. As with XPS, the Auger process is inherently a surface sensitive process since the Auger electrons will only travel a short distance in a material before suffering a collision and losing their characteristic information[18]. This research used a PHI 610 Scanning Auger Microprobe to conduct experiments.

### 1.2.3. Mass Spectrometry

Mass spectrometry (MS) is not a surface science technique, and this research used a relatively standard quadrupole mass spectrometer (Balzers Prisma QMS 200). Mass spectrometry allows identification of gas phase species by determining mass to charge ($m/z$) ratio. The MS was used to verify purity of the precursor gas while dosing, as well as to identify species present in the UHV chamber. The MS was particularly valuable in these experiments as it provided the opportunity to identify species which were desorbed into the gas phase during electron beam irradiation. The XPS was used to monitor surface composition of the substrate with adsorbed precursor before and after electron beam irradiation. The powerful combination of the MS data with the XPS data allowed identification of species desorbed during electron beam irradiation, which is not generally

available during FEBID due to the large partial pressure of precursor molecules, and the presences of background gases such as water and hydrocarbons in the SEMs typically used for FEBID[6,7].

### 1.2.4. Scanning Electron Microscopy

Scanning electron microscopy (SEM) provides the ability to image items that are smaller than those which can be imaged in a light microscope, due to the smaller wavelength of electrons and ease of focusing charged particles[19,21]. The SEM is one of the most important surface science tools in use and can provide exceptional images even down to the nanometer scale. For this research, a JEOL 6700 SEM was used to image a variety of deposits formed in an Auger spectrometer.

### 1.2.5. Energy Dispersive Spectroscopy/Wavelength Dispersive Spectroscopy

One of the more powerful tools available in the SEM is elemental analysis, provided by energy dispersive spectroscopy (EDS)[21]. In addition to imaging to a very high resolution, the process of irradiation of a surface with a high energy electron beam results in the emission of characteristic x-rays, as well as a variety of electrons. With the proper detection, these x-rays can provide valuable information about the composition of the sample. The elemental analysis provided by EDS isn't surface specific, although it can be made more so by choice of accelerating voltage used for the SEM electron beam; the higher the voltage (beam energy), the deeper the beam will penetrate into the sample. It provides analysis throughout the bulk of the material, due to the much greater escape depth of x-ray photons compared with electrons (microns compared with nanometers). In the experiments conducted in this research, it was found that an accelerating voltage of 10kV was most useful to gain bulk information about the entire deposit, with minimal (but still visible)

substrate contribution.

Wavelength dispersive spectroscopy (WDS) is a complementary process to EDS. In WDS, the characteristic x-rays generated by the electron beam on a sample are passed through a crystal, and diffracted, using the principle of Bragg's law, and thus much higher resolution of x-ray wavelength is possible than with EDS[21]. WDS does require more complex analysis than EDS, and requires comparison with elemental standards (not usually required with EDS). Although it is less straightforward to use than EDS, WDS can provide significantly better resolution and detection of trace elements. It can be very useful in resolving conflict in EDS signals[21]. In this research, a JEOL JXA-8600 Superprobe SEM, with EDS and WDS capabilities, was used to resolve EDS conflicts.

### 1.2.6. Substrates

The choice of substrate is important in the surface science processes studied in this research. Superior substrates are minimally reactive with the species being studied, and are chosen to minimize or avoid conflicts between substrate signal and the compound of interest signal. Previous research has shown that generally, choice of substrate does not affect the surface reactions studied. However, choice of substrate can be very important to allow adequate evaluation of XPS or AES transitions. In order to observe all transitions, it was often necessary to conduct experiments on more than one substrate. The substrates used in the XPS were amorphous carbon (a:C) in the form of highly ordered pyrolytic graphite (HOPG), polycrystalline Au deposited on a tantalum base to a depth of at least 200 nm (only Au transitions observed due to XPS surface sensitivity), and silicon dioxide ($SiO_2$). Substrates were cleaned *in situ* using Argon ion sputtering (> 1 hour at 4 kV) until the substrate was judged clean by XPS. Sputtering removed the oxide layer from the silicon

dioxide substrate, so it was necessary to regenerate the oxide layer prior to each experiment. We found that the silicon dioxide substrate was easily and reproducibly regenerated by flooding the XPS chamber with $O_2$ at 5 x $10^{-7}$ Torr, and irradiating the substrate with electrons for approximately five hours, generally at 30 μA with a 20V bias applied. This created the effect of FEBID of oxygen, and effectively regenerated the oxide layer.

Substrates used in the AES were HOPG, Au, $SiO_2$, and Ru coated Si/Mo multilayer mirrors (MLMs)[22]. Substrates were chosen for similar reasons as in the XPS. Much of the AES work involving deposits which were to be evaluated in the SEM used the Ru coated Si/Mo multilayer mirrors due to ease of imaging in the SEM. Sputtering with Ar ions was used in some cases to clean the surface and to conduct depth profiles, but due to the process of making a deposit in a discrete spot on a substrate in the Auger spectrometer, it was generally sufficient to move the substrate to a different spot and verify cleanliness by substrate signal. Depth profiling allows evaluation of the entirety of a deposit and was performed in the AES[18]. Several experiments were done in which the surface was evaluated, a small amount of the surface layer was removed by Ar ion sputtering, and then the surface reevaluated. In this way, composition of the deposit through the entire deposit may be verified, as the deposit is removed slowly and a new surface exposed. This is a destructive technique so it is not appropriate in some situations, but it provides valuable information when used.

### 1.2.7. Purification Methods

Nanostructures created by focused electron beam induced deposition often have high levels of contamination that preclude their use in many applications. Many purification or specialized processing methods have been investigated to mitigate this

contamination.  This research focused specifically on electron beam post-processing and cleaning with atomic radicals.  Electron beam post-processing is the continued electron beam irradiation of a structure in the absence of a precursor gas, which is what defines the transition from focused electron beam deposition to electron beam post processing.  Some level of electron beam post-processing takes place even as the nanostructure is being created by deposition; electrons that do not decompose a new molecule technically process a previously deposited molecule on the surface.

Atomic radicals are very reactive species by their nature, and in this research, atomic hydrogen radicals were used to purify nanostructures.  Other research has used atomic oxygen radicals as well as the sequence of application of atomic oxygen radicals, followed by atomic hydrogen radicals.  Research by Plank *et. al.* (unpublished work) indicated that atomic oxygen can clean nanostructures to a certain penetration depth.

Another purification method for FEBID nanostructures is the use of thermal processes, in which the deposit is heated after deposition, or is deposited on a heated substrate.  This research conducted a few thermal processing experiments.

## 1.3.  Conclusion

This research applied the tools of surface science to investigate mechanistic details of electron induced surface reactions of several organometallic molecules to investigate processes occurring during FEBID, and has contributed to the body of knowledge about FEBID precursor chemistry.  This research investigated primarily molecules synthesized "to order" by collaborating organometallic chemists, which was extremely helpful in researching rational FEBID precursor design.  Molecules investigated included $\eta^3$-allyl ruthenium tricarbonyl bromide $[(\eta^3\text{-}C_3H_5)Ru(CO)_3Br]$[23], *cis*-platinum dicarbonyl

dichloride (*cis*-Pt(CO)$_2$Cl$_2$)[24], CpFe(CO)$_2$Mn(CO)$_5$, and for a few experiments, Co$_2$(CO)$_8$, a commercially available compound which is already used to produced FEBID nanostructures of relatively high metal content (>90%)[25]. Chapter 2 of this dissertation reviews the surface science approach to investigation of FEBID precursors, as well as some earlier work on this topic in the Fairbrother research group[26]. Chapter 3 discusses electron induced surface reactions of η$^3$-allyl ruthenium tricarbonyl bromide [(η$^3$-C$_3$H$_5$)Ru(CO)$_3$Br], and for a few experiments, η$^3$-allyl ruthenium tricarbonyl chloride [(η$^3$-C$_3$H$_5$)Ru(CO)$_3$Cl][23]. Chapter 4 details electron induced surface reactions of *cis*-platinum dicarbonyl dichloride (*cis*-Pt(CO)$_2$Cl$_2$)[24]. Chapter 5 extends the research conducted in Chapter 4 with *cis*-platinum dicarbonyl dichloride (*cis*-Pt(CO)$_2$Cl$_2$) to include deposits and purification strategies. Finally, Chapter 6 includes ongoing research into the first bimetallic compound investigated by this group for FEBID, as well as a small amount of research on dicobalt octacarbonyl (Co$_2$(CO)$_8$).

The science is interesting and has increased knowledge of mechanistic details of FEBID precursor decomposition under electron beam irradiation. Specifically, it has demonstrated that the η$^3$-C$_3$H$_5$ ligand behaves similarly to the η$^5$-C$_5$H$_5$ ligand in FEBID; both contribute to carbon contamination in deposits, and thus, polyhapto unsaturated hydrocarbon ligands are poor choices in a FEBID precursor[23]. It has demonstrated that a small number of CO ligands may desorb during the FEBID process, and that halogens operate as somewhat of a "free" ligand, as they can desorb under a slower, electron-stimulated desorption process[23,24]. In addition, this research has shown that while there is no substitute for experimental data, in many cases, the final deposit composition from the FEBID precursor can be predicted with relatively high accuracy. This insight may be as

valuable as the actual data produced in this research, and will be useful in further design of

FEBID precursors.  Focused electron beam induced deposition is an active area of research

and it shows great promise.  The electron beam lithography technique is robust today due

to many years of experiment and refinements[9].  Hopefully, focused electron beam induced

deposition will develop into a mature technology with continued research.

## 1.4. References

(1)       Feynman, R. *Caltech Engineering and Science* **1960**, *23:5*, 22.
(2)       Van Zant, P. *Microchip Fabrication : A Practical Guide to Semiconductor Processing*; 6th ed.; McGraw-Hill Education: New York, New York, 2014.
(3)       Campbell, S. A. *Fabrication Engineering at the Micro and Nanoscale*; 3rd ed.; Oxford University Press: New York : New York, 2008.
(4)       Hampden-Smith, M. J.; Kodas, T. T. *Chemical Vapor Deposition* **1995**, *1*, 8.
(5)       McElwee-White, L. *Dalton Transactions* **2006**, 5327.
(6)       Utke, I.; Hoffmann, P.; Melngailis, J. *Journal of Vacuum Science & Technology B* **2008**, *26*, 1197.
(7)       Van Dorp, W.; Hagen, C. *Journal of Applied Physics* **2008**, *104*, 081301.
(8)       George, S. M. *Chemical reviews* **2009**, *110*, 111.
(9)       Hagen, C. *Applied Physics A* **2014**, *117*, 1599.
(10)      Huth, M.; Porrati, F.; Schwalb, C.; Winhold, M.; Sachser, R.; Dukic, M.; Adams, J.; Fantner, G. *Beilstein journal of nanotechnology* **2012**, *3*, 597.
(11)      Randolph, S.; Fowlkes, J.; Rack, P. *Critical reviews in solid state and materials sciences* **2006**, *31*, 55.
(12)      van Dorp, W. F.; van Someren, B.; Hagen, C. W.; Kruit, P.; Crozier, P. A. *Nano Letters* **2005**, *5*, 1303.
(13)      Luisier, A.; Utke, I.; Bret, T.; Cicoira, F.; Hauert, R.; Rhee, S.-W.; Doppelt, P.; Hoffmann, P. *Journal of The Electrochemical Society* **2004**, *151*, C590.
(14)      Hübner, B.; Koops, H.; Pagnia, H.; Sotnik, N.; Urban, J.; Weber, M. *Ultramicroscopy* **1992**, *42*, 1519.
(15)      Edinger, K.; Becht, H.; Bihr, J.; Boegli, V.; Budach, M.; Hofmann, T.; Koops, H. W.; Kuschnerus, P.; Oster, J.; Spies, P. *Journal of Vacuum Science & Technology B* **2004**, *22*, 2902.
(16)      Liang, T.; Frendberg, E.; Lieberman, B.; Stivers, A. *Journal of Vacuum Science & Technology B* **2005**, *23*, 3101.
(17)      Heerkens, C. T. H.; Kamerbeek, M.; van Dorp, W.; Hagen, C.; Hoekstra, J. *Microelectronic Engineering* **2009**, *86*, 961.
(18)      Vickerman, J. C. *Surface analysis--the principle techniques*; 2nd ed.; John Wiley and Sons: Chichester, England ;, 2009.
(19)      Zhang, S.; Li, L.; Kumar, A. *Materials Characterization Techniques*; CRC Press, Taylor & Francis Group: Boca Raton, FL, 2009.
(20)      Moulder, J. F., Stickle, William F., Sobol, Peter E., Bomben, Kenneth D. *Handbook of X-ray Photoelectron Spectroscopy*; Physical Electronics USA, Inc.: Chanhassen, Minnesota, USA, 1995.
(21)      Goldstein, J. I.; Newbury, D. E., Echlin, Patrick, Joy, David C., Lyman, Charles E., Lifsin, Eric, Sawyer, Linda, and Michael, Joseph *Scanning Electron Microscopy and X-ray Microanalysis*; 3rd ed.; Kluwer Academic/Plenum Publishers: New York :  New York, 2003.

(22)     Bajt, S.; Alameda, J. B.; Barbee, T. W.; Clift, W. M.; Folta, J. A.; Kaufmann, B.; Spiller, E. A. *Optical engineering* **2002**, *41*, 1797.

(23)     Spencer, J. A.; Brannaka, J. A.; Barclay, M.; McElwee-White, L.; Fairbrother, D. H. *The Journal of Physical Chemistry C* **2015**, *119*, 15349.

(24)     Spencer, J. A.; Wu, Y.-C.; McElwee-White, L.; Fairbrother, D. H. *Journal of the American Chemical Society* **2016**.

(25)     Fernández-Pacheco, A.; De Teresa, J.; Córdoba, R.; Ibarra, M. R. *Journal of Physics D: Applied Physics* **2009**, *42*, 055005.

(26)     Spencer, J. A.; Rosenberg, S. G.; Barclay, M.; Wu, Y.-C.; McElwee-White, L.; Fairbrother, D. H. *Applied Physics A* **2014**, *117*, 1631.

Chapter 2


Understanding the Electron-Stimulated Surface Reactions of Organometallic Complexes

to Enable Design of Precursors for Electron Beam-Induced Deposition

Chapter 2.     Understanding the Electron-Stimulated Surface Reactions of Organometallic Complexes to Enable Design of Precursors for Electron Beam-Induced Deposition

This work was co-written with the following authors and is adapted from the following published work:

Spencer, J.A., Rosenberg, S.G., Barclay, M., Wu, Y.-C., McElwee-White, L., Fairbrother, D. H.   Understanding the Electron-stimulated Surface Reactions of Organometallic Complexes to Enable Design of Precursors for Electron Beam-induced Deposition.  *Appl. Phys. A: Mater. Sci. Process.* **2014**, 117, 1631 – 1644.  DOI: 10.1007/s00339-014-8570-5

The final publication is available at http://link.springer.com/article/10.1007/s00339-014-8570-5.

## 2.1.  Introduction

Electron beam induced deposition (EBID) is a resistless, single-step, vacuum based, direct-write lithographic strategy that uses a high energy, focused electron beam to stimulate the deposition of metal-containing nanostructures from organometallic precursors transiently adsorbed on a surface (Figure 1)[1-4].  Primary electrons and/or the secondary electrons, created by the interaction of the primary beam with the substrate, initiate deposition because electron-stimulated decomposition of the precursor produces nonvolatile fragments.
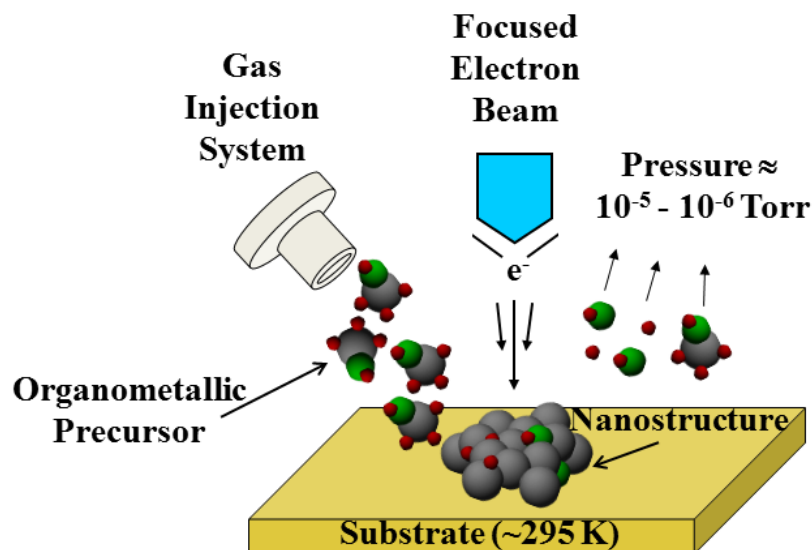
**Figure 2.1**: Schematic representation of a size and shape selected metal-containing nanostructure being deposited by electron beam-induced deposition (EBID).

EBID possesses a unique and attractive combination of capabilities for producing three-dimensional nanostructures since the size, shape, and interparticle distance can all be accurately and independently controlled and varied across a range of length scales. EBID also offers a number of advantages compared to other vacuum-based nanofabrication strategies such as ion beam induced deposition (IBID), electron beam lithography (EBL) and extreme ultraviolet lithography (EUVL) that can also create nanostructures. In particular, EBID can create smaller features than IBID, with less amorphization and without ion implantation[5-7]. While EBID resolution is comparable to EBL and EUVL[8,9], it needs no resist layers or etching step for pattern transfer.

A few examples of EBID structures are shown in Figure 2: an array of platinum containing dots (approximate diameter 3 nm) deposited from MeCpPtMe$_3$ (Figure 2a)[10], a platinum-based probe grown on top of a commercially available atomic force microscopy (AFM) cantilever (Figure 2b)[11], a dense pattern of L-shaped structures deposited from MeCpPtMe$_3$ (Figure 2c)[12], and a high aspect 3D
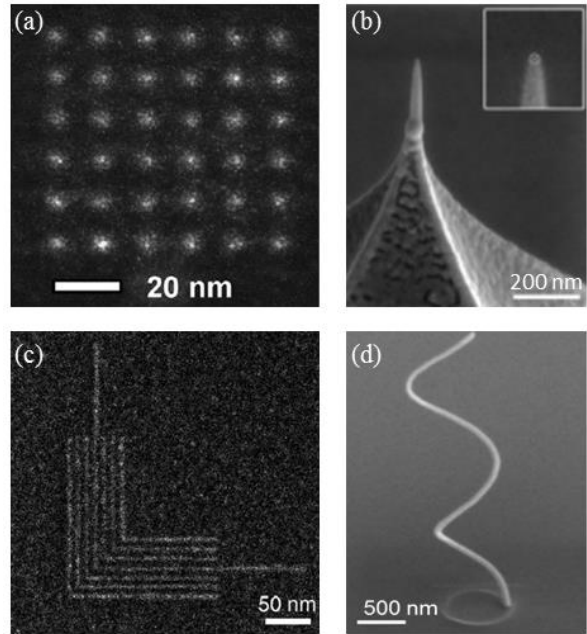


**Figure 2.2**: Structures of different sizes and shapes created by EBID (details in text).

cobalt nanowire (Figure 2d)[13]. EBID nanostructures have the potential to act as components in a variety of technologically important applications, some of which have already garnered broad usage, including a commercial system for repairing EUVL masks[14-17], customized tips for local probe microscopes[18,19], and the fabrication and modification of nanophotonic and nanoplasmonic devices[20-22].

Despite the versatile and attractive capabilities of EBID, and the increasing prominence of electron beam instruments in industry and academia, a number of scientific and technological issues are impeding the further development of EBID as a robust tool for nanofabrication. One of the biggest issues is the low metal content in deposits created from organometallic precursors. For example, structures created from Au(acac)Me$_2$ by EBID exhibit Au contents < 20% [1-3]. Similarly, although pure platinum films can be created by chemical vapor deposition (CVD) from MeCpPtMe$_3$, EBID structures created from the

same precursor have platinum contents <20%[2,23,24]. These EBID deposits/structures typically contain unacceptably high levels of contaminants, particularly carbon and oxygen[25]. These impurities negatively impact the properties of EBID nanostructures because contaminants increase resistivity and adversely affect the electronic structure of the metal atoms in the deposited structures. For example, the resistivity of Pt wires created from $MeCpPtMe_3$ by EBID is typically $>1\Omega$ cm, severely limiting their ability to serve as nanoelectrodes or nanowires[26]. In general, the potential applications for EBID nanostructures as nanowires, catalysts, and biosensors are hindered by the high levels of organic contamination.

The principal reason why EBID structures contain so much residual organic contamination can be traced back to the use of commercially available organometallic precursors, which have been designed to yield pure metallic deposits in thermal deposition processes such as CVD and atomic layer deposition (ALD). Table 1 shows a representative list of CVD precursors that have been used in EBID to deposit metal-containing nanostructures. However, during EBID, precursor ligands that dissociate thermally during CVD are susceptible to electron stimulated decomposition, leading to contamination in the deposited material[27].

The low metal content that characterizes the chemical composition of EBID nanostructures created from existing CVD precursors highlights the need to develop new precursors designed to produce high metal content in EBID nanostructures. Precedent for the value of a targeted synthetic approach can be found in the ability of EBID to deposit pure nanocrystalline gold from $PF_3AuCl$, a precursor synthesized specifically for EBID[28,29]. Unfortunately, $PF_3AuCl$ is sensitive to temperature, air, moisture and

| Metal | Representative EBID Precursors |
|-------|-------------------------------|
| Au | $Au(acac)Me_2$, $Au(hfac)Me_2$ |
| Cu | $Cu(hfac)_2$, $Cu(hfac)(VTMS)$ |
| Co | $Co_2CO_8$, $Co(CO)_3NO$ |
| Fe | $Fe(CO)_5$, $Fe(C_5H_5)_2$, $Fe_3(CO)_{12}$ |
| W | $W(CO)_6$, $WF_6$, $WCl_6$ |
| Pt | $MeCpPtMe_3$, $Pt(PF_3)_4$, $Pt(hfac)_2$ |

**Table 2.1**: Precursors developed for CVD that have been used for EBID

light, with an effective storage lifetime of a few days, rendering it impractical for routine EBID. This example does, however, illustrate the underlying motivation for this methodology: specifically, that the synthesis and evaluation of new precursors could enable EBID to deposit size and shape selected nanoparticles with significantly improved metal content and a corresponding greater range of applications.

### 2.1.1. An Ultra-High Vacuum Surface Science Approach to EBID

In contrast to CVD and ALD, where a substantial body of mechanistic work underlies precursor design[30,31], there is a lack of information on the molecular events that accompany EBID. However, recent ultrahigh vacuum (UHV) surface science studies have begun to provide information useful in formulating design strategies for EBID precursors (see Figure 3)[32-39]. In contrast to studies conducted in electron microscopes, where deposits are created under steady state deposition conditions, the UHV surface science
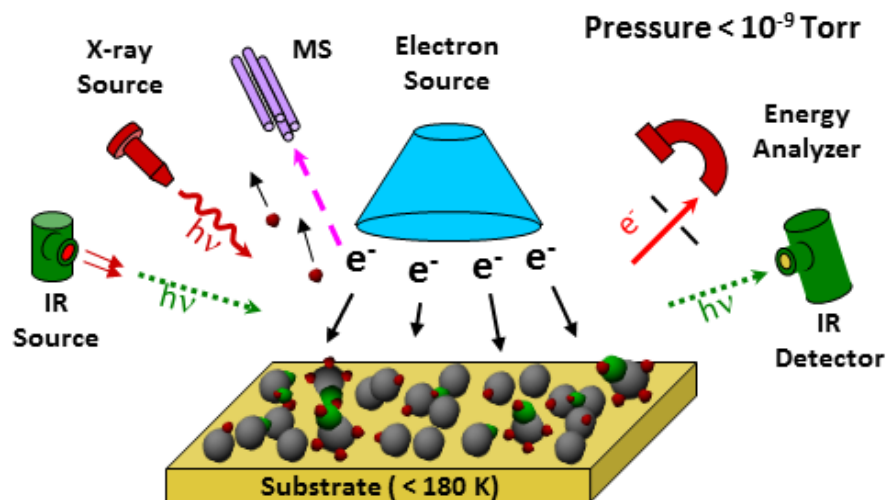
**Figure 2.3**: Schematic representation of the ultra-high vacuum surface science approach to study EBID precursors

approach relies on studying the effect of electron irradiation on nanometer thick films of precursor molecules adsorbed onto chemically inert substrates at low temperatures. Surface analytical tools such as X-ray photoelectron spectroscopy (XPS) and reflection absorption infrared spectroscopy (RAIRS) can follow changes in the surface composition and bonding environment of the various elements within the precursor molecule, complemented by mass spectrometry (MS) which can detect the volatile species ejected from the film as a consequence of electron-stimulated reactions. The UHV environment ($P_{base}$ <5 x $10^{-9}$ Torr) simplifies data interpretation by ensuring that the effects of electron irradiation on adsorbed precursor molecules can be studied without the complicating effects of contaminants (water or hydrocarbons) typically present in electron microscopes ($P_{base} \approx 10^{-5} - 10^{-6}$ Torr regime). Furthermore, the low background pressure allows mass spectrometry (MS) to identify gas phase products produced during EBID. This information cannot be obtained in typical EBID experiments due to the higher base pressure as well as

the presence of a constant partial pressure of precursor molecules during deposition. Compared to the typical EBID experiments (Figure 1) performed in electron microscopes, the UHV surface science approach also allows the effects of electron irradiation on
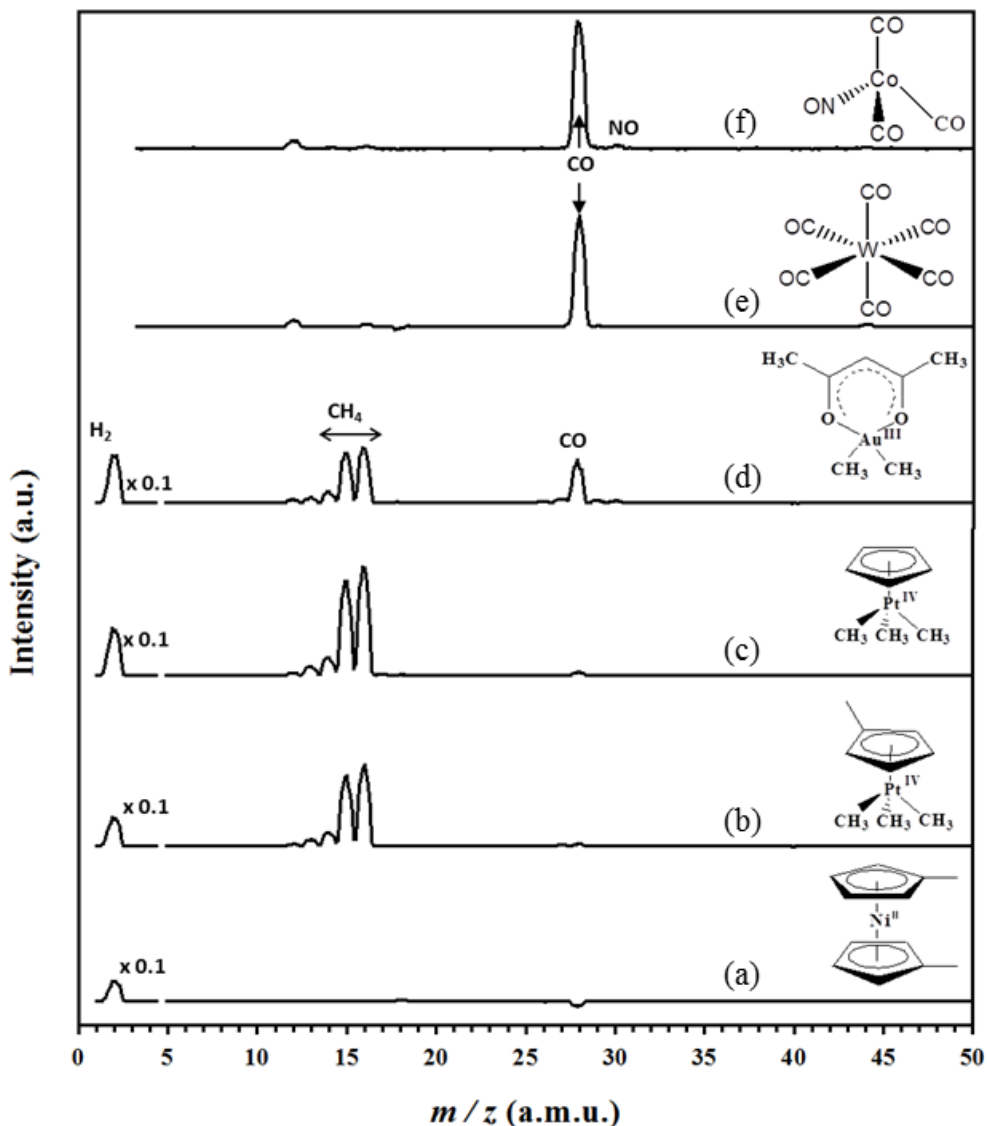


**Figure 2.4**: Mass spectra of the volatile species produced when six different organometallic precursors, adsorbed onto gold substrates, were irradiated by 500 eV electrons. (a) $Ni(MeCp)_2$, (b) $MeCpPtMe_3$, (c) $CpPtMe_3$, (d) $Au(acac)Me_2$, (e) $W(CO)_6$, (f) $Co(CO)_3NO$

adsorbed precursors to be interrogated in situ, and as a function of electron dose. This provides a route to obtain information that can be used to develop a molecular level understanding of EBID.

Evidence for the existence of structure-activity relationships in EBID can be found in MS studies where the volatile carbon-containing species created during electron irradiation of adsorbed organometallic complexes exhibit a systematic dependence on the ligand architecture (Figure 4)[35]. In some instances, this information can be directly related to the chemical composition of EBID depositions. For example, electron irradiation of $Ni(MeCp)_2$ (Figure 4a) produces nonvolatile carbon-containing products, suggesting that $\eta^5$-cyclopentadienyl ligands will be inappropriate for EBID precursors. Consistent with this idea, high carbon contents are observed for EBID structures created from organometallic precursors containing $\eta^5$-cyclopentadienyl ligands[2,23,24,40]. In the case of $Co(CO)_3NO$ (Figure 4f), CO is the dominant gas phase species produced during electron irradiation, with little NO observed. This observation helps to explain why EBID deposits created from $Co(CO)_3NO$ have much higher N/C ratios than the 1:3 ratio present in the precursor[41-46].

Figure 5 describes the elementary steps that we believe underpin the EBID process. In a typical EBID experiment, conducted



**Precursor adsorption**

$$ML_{n(g)} \rightleftharpoons ML_{n(abs)}$$

**Precursor deposition/decomposition**

$$ML_{n(abs)} + e^- \longrightarrow MX_{y(ads)} + Z_{(g)}\uparrow$$

**Post-deposition processing**

Ligand decomposition

$MX_{y(ads)}$ $\xrightarrow{e^-}$

$\xrightarrow{\triangle}$ Ligand desorption

**Figure 2.5**: Elementary reaction steps that underpin the EBID process

in an electron microscope and under a constant partial pressure of precursor molecules, the adsorbed precursor molecules ($ML_{n(ads)}$) are in equilibrium with gas phase species ($ML_{n(g)}$). Results from our UHV surface science studies have shown that the subsequent reactions of the adsorbed precursor during the EBID process can be broken down into a number of sequential steps: an initial electron stimulated deposition event followed by either electron or thermal processing of the adsorbed species created in the initial step[36].

### 2.1.1.1. Initial electron-stimulated (deposition) step

The initial electron interaction converts adsorbed parent precursor molecules ($ML_{n(ads)}$) into a non-volatile species that is now bound to the substrate. From now on this will be referred to as the initial deposition step. Our studies have shown that this initial step is accompanied by desorption of volatile fragments[33,37-39]. In the case of organometallic complexes with monodentate ligands (*e.g.*, $W(CO)_6$, $Pt(PF_3)_4$, $Co(CO)_3NO$, $MeCpPtMe_3$), these gas phase species are typically intact ligands which have dissociated from the parent molecule. This process can be represented by the following general expression:

$$ML_{n(ads)} + e^- \rightarrow MY_{(ads)} + Z_{(g)}\uparrow$$
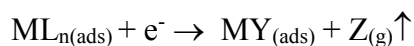
where $MY_{(ads)}$ represents the non-volatile species that is now bound to the substrate after the organometallic precursor $ML_n$ decomposes, and $Z_{(g)}$ represents the volatile fragments released[36-39]. Information on the deposition step can be acquired from data obtained when the adsorbed precursor molecules are initially exposed to electrons, corresponding to comparatively short electron doses (electron dose = (electron flux x time)/surface area, $e^-/cm^2$).

28

The ability of the UHV surface science approach to elucidate the initial bond breaking step for different precursors will be illustrated by considering results obtained on two platinum-containing precursors, MeCpPtMe$_3$[33] and Pt(PF$_3$)$_4$[39].

### 2.1.1.1.1.     Trimethyl(methylcyclopentadienyl) platinum (IV)

Trimethyl(methylcyclopentadienyl) platinum (IV) (MeCpPtMe$_3$) is one of the most common precursors used to create conductive nanostructures/nanowires[23,24,32,47-54].  XPS data from UHV surface science experiments shown in Figure 6 demonstrate that when nanometer thick films of MeCpPtMe$_3$ are exposed to electrons, the C:Pt ratio decreases by $\approx$ 11% of its initial value, creating films that contain 89% carbon and 11% platinum[33].
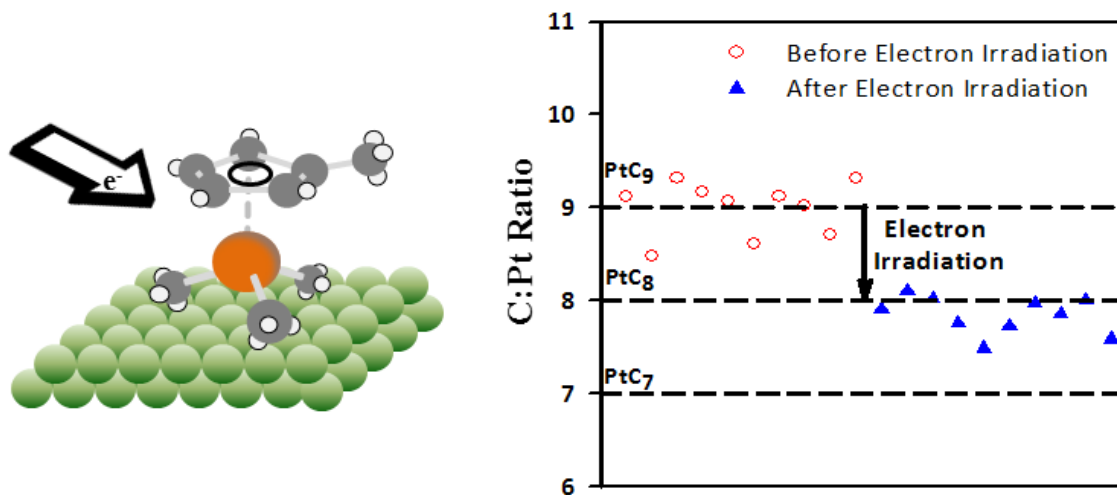


**Figure 2.6**:  Effect of electron irradiation on the C (carbon):Pt (platinum) ratio of a nanometer thick film of MeCpPtMe3 determined by XPS analysis

This change in stoichiometry can be accurately determined by integrating the area of the Pt(4f) and C(1s) peaks observed by XPS before and after electron irradiation. This highlights a notable advantage of the low temperature UHV surface science approach; specifically, the ability to directly measure the film's composition before and after electron

irradiation, facilitating an accurate determination of even relatively small changes in film composition. The significance of this decrease in the ratio of carbon to platinum atoms (C:Pt) is that since the parent molecule contains one central Pt atom and nine C atoms, a decrease of $\approx 11\%$ corresponds to the loss of exactly one carbon atom from the parent molecule as a result of the electron induced deposition step[33]. Complementary MS data (Figure 4) reveal that this carbon atom is released from the adsorbed layer as methane during irradiation, irrespective of whether MeCpPtMe$_3$ or its derivative, CpPtMe$_3$ is used. Collectively, these XPS and MS results point to an initial electron stimulated deposition process that proceeds through the cleavage of one of the Pt-CH$_3$ bonds, with the remaining carbon atoms becoming trapped in the deposit that forms[33].
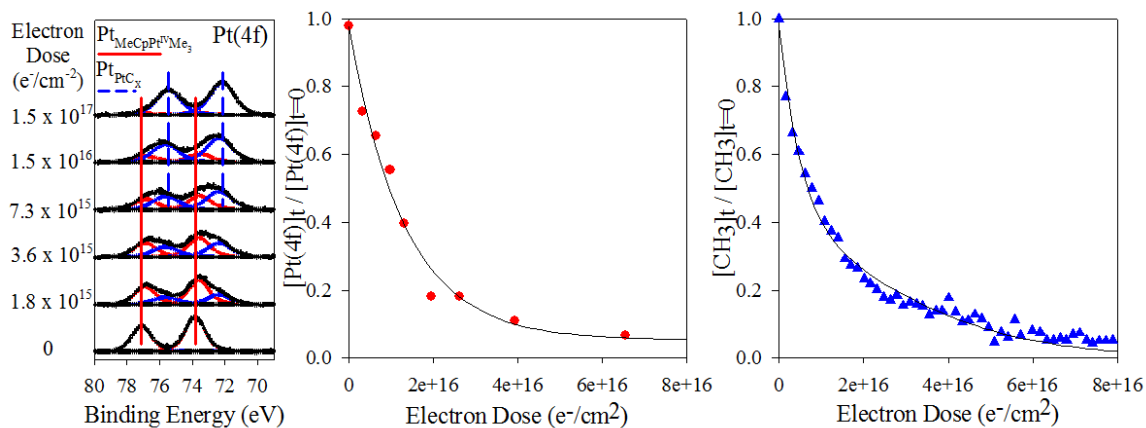


**Figure 2.7**: Effect of electron irradiation on adsorbed MeCpPtMe$_3$ molecules: *Left-hand panel* Evolution of the Pt(4f) region; *Middle panel* Kinetics of Pt(IV) reduction based on Pt(4f) region; *Right-hand panel* Kinetics of CH$_3$/CH$_4$ evolution.

Corresponding XPS data acquired on the Pt(4f) region (Figure 7 (left hand panel)) show that electron irradiation converts the Pt(IV) species in the parent MeCpPtMe$_3$ molecules into a reduced Pt species (Pt$_{red}$). Because of the significant change in formal oxidation state involved in this process, the Pt(4f) binding energy difference between the Pt(IV) and Pt$_{red}$ species is on the order of 2 eV. This facilitates an accurate spectral

deconvolution of the Pt(4f) region and enables the rate of reaction to be determined (Figure 7 (middle panel)). The right hand panel in Figure 7 shows that the rate of methane/methyl radical production (monitored by the $m/z$ = 15 fragment) is, within experimental error, equal to the rate of Pt(IV) reduction (Figure 7 (middle panel)). This demonstrates that the cleavage of one of the Pt-CH$_3$ bonds is involved in the initial deposition step[33]. Comparisons with gas phase studies on the low energy electron interactions with MeCpPtMe$_3$[55] also allow us to conclude that this initial deposition step proceeds via a dissociative electron attachment (DEA) step involving low-energy (<10 eV) electrons generated by the interaction of the high-energy primary beam with the substrate. Consequently, the initial deposition step can be represented by Figure 8 and the following equation:

$$MeCpPtMe_{3(ads)} + e^- \rightarrow [MeCpPtMe_3]^-_{(ads)} \rightarrow [MeCpPtMe_2]^-_{(ads)} + CH_3(g)/CH_4(g)\uparrow$$
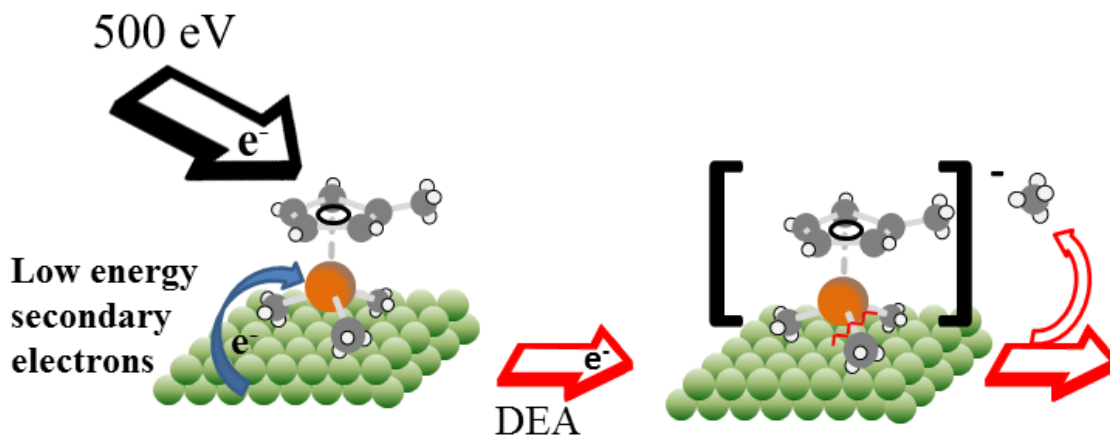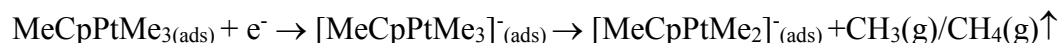


**Figure 2.8**: Electron-stimulated decomposition of MeCpPtMe$_3$. The incident primary beam creates low-energy secondary electrons from the substrate, which subsequently attach to adsorbed MeCpPtMe$_3$ molecules to form a negative ion. These unstable species fall apart via a dissociative electron attachment (DEA) process through the cleavage of one Pt-CH$_3$ bond and the release of CH$_3$/CH$_4$.

Tetrakis(trifluorophosphine)platinum (Pt(PF$_3$)$_4$) is a carbon-free precursor, although EBID structures generated from Pt(PF$_3$)$_4$ are typically dominated by phosphorus contamination[24,56-59]. XPS data (shown in Figure 9) show the effect of comparatively short irradiation times (electron doses <1.5 x 10$^{15}$ e$^-$/cm$^2$) on nanometer thick films of Pt(PF$_3$)$_4$ adsorbed on amorphous carbon substrates[39]. A determination of the dissociation mechanism relies on analyzing how the relative atom concentration and speciation of the elements contained within the ligands change under the influence of electron irradiation. During this initial period of irradiation, Figure 9 shows that phosphorus and fluorine atoms are lost from the adsorbate layer[39]. By integrating the spectral intensity within the P(2p) and F(1s) regions for multiple Pt(PF$_3$)$_4$ films exposed to electron doses <1.5 x 10$^{15}$ e$^-$/cm$^2$, Figure 9 reveals that during this period of irradiation the concentration of adsorbed phosphorus and fluorine atoms both decrease to 75% of their initial values[39]. Moreover, the rate of electron-



**Figure 2.9**: Changes in the fractional coverages of phosphorus (P/P$_{t = 0}$), fluorine (F/F$_{t = 0}$), and the ratio of fluorine/phosphorus (F/P) atoms for Pt(PF$_3$)$_4$ films exposed to comparatively small electron doses (<4 x 10$^{15}$ e$^-$/cm$^2$).

stimulated phosphorus and fluorine atom loss is the same, causing the ratio of phosphorus to fluorine atoms remaining in the film to remain constant (bottom panel in Figure 9). Collectively, these observations indicate that the initial step in the decomposition of adsorbed $Pt(PF_3)_4$ molecules proceeds via cleavage of one of the metal-ligand bonds and loss of one $PF_3$ group[39]. A comparison of gas phase and surface science studies leads to the same conclusion as for $MeCpPtMe_3$; notably, that dissociation of adsorbed $Pt(PF_3)_4$ precursor molecules in EBID occurs via a DEA process, with the low-energy electrons being produced by the interaction of the primary beam with the substrate[39,60]. The overall deposition process can be represented by the following equation,

$$Pt(PF_3)_{4(ads)} + e^- \rightarrow [Pt(PF_3)_4]^-_{(ads)} \rightarrow Pt(PF_3)_{3\ (ads)} + PF_{3(g)} \uparrow$$
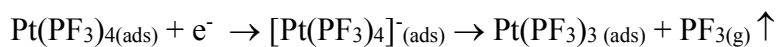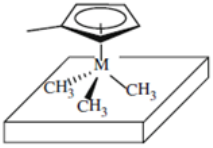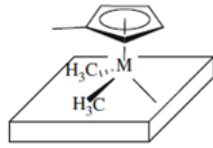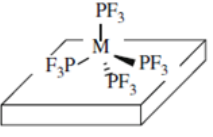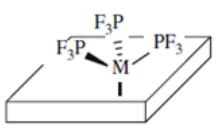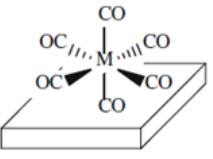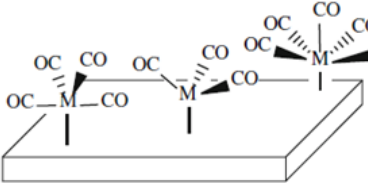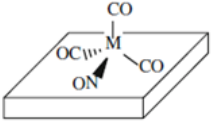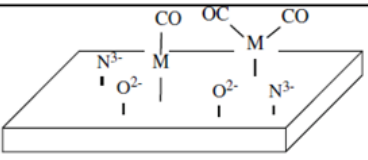
shown schematically in Figure 10.
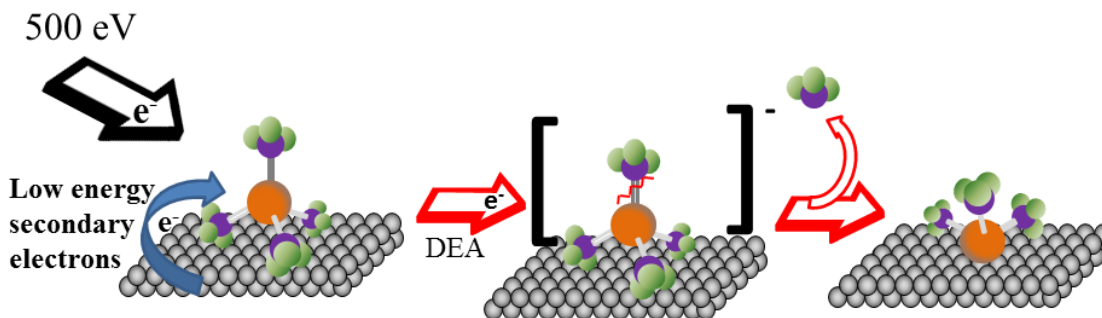


**Figure 2.10**: Summary of the electron-induced deposition step for $Pt(PF_3)_4$. The incident primary beam creates low-energy secondary electrons from the substrate, which subsequently attach to adsorbed $Pt(PF_3)_4$ molecules to form a negative ion which falls apart via a dissociative electron attachment (DEA) process through the cleavage of one $Pt\text{-}PF_3$ bond and the release of a single $PF_3$ ligand.

Similar UHV surface science studies have also been conducted on $W(CO)_6$ and $Co(CO)_3NO$, two other popular EBID precursors. Table 2 summarizes the initial

deposition steps elucidated from our UHV surface science studies on all of the organometallic complexes studied so far.



**Table 2.2**: Summary of the initial electron-induced deposition step for several types of organometallic precursors

### 2.1.1.2.    Post-deposition Processing

Following the initial deposition step, a metal-containing fragment, $MY_{(ads)}$, is left bound on the surface. For some organometallics, the initial ligand ejection step precipitates a reaction within the remaining ligands. For example, CO is ejected from $Co(CO)_3NO$ simultaneously with the decomposition of the surface bound NO ligand[38]. However, the fate of most $MY_{(ads)}$ species left behind on the surface is determined by the effects of subsequent electron or thermal processing[36].

Experimentally, an advantage of the UHV surface science approach over traditional EBID experiments performed in electron microscopes is that the effect of both electron and thermal processing on different $MY_{(ads)}$ species created from various EBID precursors can be studied independently[36]. This can be accomplished in a two-step process. First, the organometallic precursor must be pre-exposed to an electron dose that is just enough to ensure that all of the molecules have undergone the initial deposition step ($ML_{n(ads)} + e^- \rightarrow MY_{(ads)} + Z_{(g)}\uparrow$). Knowledge of the kinetics and nature of the initial deposition step is therefore a necessary prerequisite to studying the effects of post-deposition processing. Once the $MY_{(ads)}$ has been created on the surface using the controlled electron dose the substrate is either: (1) exposed to additional electrons to examine electron processing ($MY_{(ads)} + e^- \rightarrow ?$) or, (2) annealed to increasing temperatures to investigate thermal processing ($MY_{(ads)} + \Delta \rightarrow ?$). In either case, the fate of the $MY_{(ads)}$ species can be determined in situ using surface analytical techniques, principally XPS[36].

### 2.1.1.2.1. Electron processing

In typical EBID experiments conducted in electron microscopes at ambient temperatures, $MY_{(ads)}$ species will invariably be subject to a large degree of electron processing due to the extremely high electron fluxes[1-4]. Under these deposition conditions, experimental evidence suggests that ligand *decomposition* rather than *desorption* dominates[33,37-39]. For example, the XPS data shown in Figure 11 reveal that electron irradiation of the $Pt(PF_3)_3$ intermediate produced in the initial deposition of $Pt(PF_3)_4$ leads to a sustained decrease in the concentration of adsorbed fluorine atoms, while the phosphorus content in the film remains constant at 75% of its initial value[39]. These observations indicate that electron processing of adsorbed $Pt(PF_3)_3$ species does not cause $PF_3$ ligand ejection, but instead decomposes the $PF_3$ ligands by P-F bond cleavage, ejecting fluoride ions into the gas phase, thus:

$$Pt(PF_3)_{3(ads)} + e^- \rightarrow \rightarrow \rightarrow Pt(PF_{3-x})_{3(ads)} + F^-_{(g)}\uparrow$$
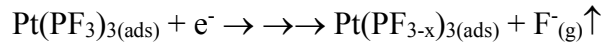
Ultimately, this leads to the retention of residual phosphorus atoms in the deposit. This explains why EBID deposits created from $Pt(PF_3)_4$ are typically dominated by platinum and phosphorus atoms[56-59,61]. Indeed, we have generated an EBID structure in an Auger electron spectrometer, under steady state deposition conditions and an electron flux that closely mimic those used in electron microscopes, that contains only platinum and phosphorus atoms (see Figure 12)[39].
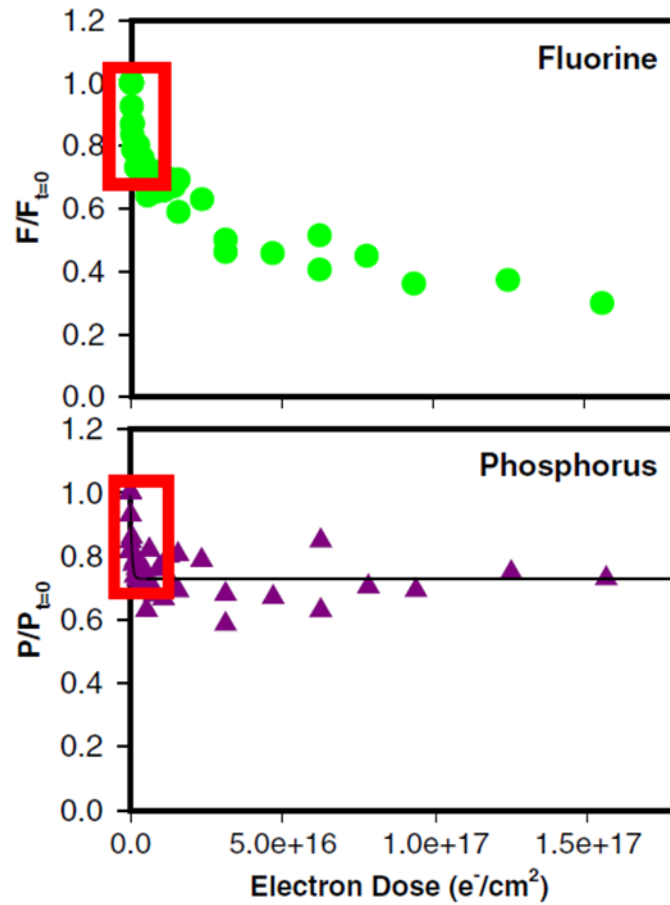
**Figure 2.11**: Changes in the fractional coverages of phosphorus ($P/P_{t=0}$) and fluorine ($F/F_{t=0}$) for $Pt(PF_3)_4$ films exposed to larger electron doses ($> 4 \times 10^{15}$ $e^-$ /$cm^2$). The red box indicates the initial period of electron irradiation described in Figure 2.9.
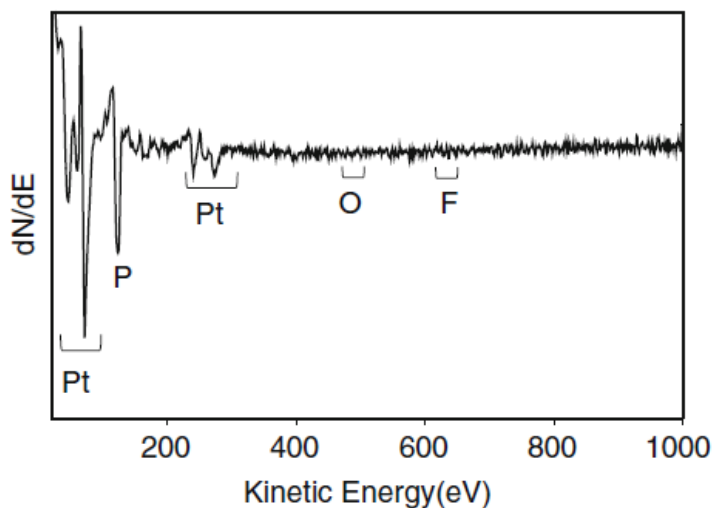
**Figure 2.12**: Auger electron spectra (AES) of an EBID deposit created in a UHV chamber under steady state deposition conditions from $Pt(PF_3)_4$.

In the case of MeCpPtMe₃, experimental evidence suggests that the intermediate produced by the initial Pt-CH₃ bond cleavage event releases hydrogen as a result of electron stimulated C-H bond cleavage, ultimately producing platinum atoms encased in a carbonaceous matrix with an average stoichiometry of $PtC_{8(ads)}$[33]. Thus, except for the single carbon atom lost during the deposition step, the remaining carbon atoms remain trapped in the deposit. This helps to rationalize the experimental observation that EBID nanostructures generated from MeCpPtMe₃ contain only 10-20% atomic concentration of platinum atoms[2,23,24,62].

For metal carbonyls, MS and XPS data indicate that the initial deposition step proceeds via CO desorption, although multiple CO groups can be released[37,38]. However, subsequent electron-stimulated reactions of the remaining partially decarbonylated fragments induce decomposition of the residual CO ligands, producing graphitic carbon and reactive oxygen species that often react with the central metal atom to form a metal oxide[37,38]. The overall process can be represented as

$$M(CO)_{x(ads)} + e^- \rightarrow M(CO)_{x-y(ads)} + yCO\uparrow(g) - \text{deposition step (CO desorption)}$$

$$M(CO)_{x-y(ads)} + e^- \rightarrow MO_{(ads)} + C_{(ads)} - \text{decomposition of residual CO ligands}$$
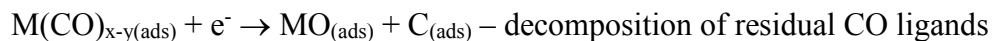
Hence, although electron irradiation initiates ligand desorption from the molecular precursor ($ML_{(ads)}$) in step 1, electron processing of the residual ligands left behind in the $MY_{(ads)}$ species are responsible for ligand decomposition. We believe that this second step is the primary source of organic contamination in EBID structures. One notable exception is metal-halogen bonds which are susceptible to electron-stimulated halide ion desorption of the general form,

$$M\text{-}Z_{(ads)} + e^- \rightarrow M_{(ads)} + Z^-_{(g)} \quad (Z = \text{halogen; F, Br, Cl})$$
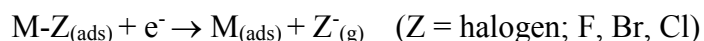
An important consequence of this reaction channel is that halogen atoms directly attached to the central metal atom in organometallic complexes could be scrubbed by electron processing. However, the addition of halogen atoms to organometallic complexes typically decreases their volatility, an important practical requirement for an EBID precursor. Certain halogen-containing complexes can produce highly corrosive species after electron irradiation, which can cause damage to EBID equipment.

### 2.1.1.2.2.    Thermal processing

From some $MY_{(ads)}$ species generated in the initial deposition event, thermal processing represents an alternative to the electron processing described in the previous section. The importance of this reaction pathway is that *thermal reactions are often characterized by ligand desorption as opposed to ligand decomposition*. Consequently, thermal processing of $MY_{(ads)}$ species can significantly decrease the level of organic contamination within the final deposit, with corresponding improvements in metal purity[36,63]. However, there are some important limitations to the value and practical utility of thermal processing in EBID. Not every ligand undergoes thermal desorption, and even if the ligands do desorb, elevated substrate temperatures are typically needed, requiring the

presence of a heated sample stage in the electron microscope.  If a heated stage is used, the substrate temperature during deposition must always be lower than the onset temperature for CVD to prevent conformal deposition.  Moreover, in typical EBID experiments conducted under steady-state deposition conditions in electron microscopes, any potentially positive effects of thermal processing will always have to compete with the generally deleterious effects of electron processing.

One precursor that exemplifies the positive effect of using elevated substrate temperatures during deposition is $Pt(PF_3)_4$.  In this case, thermal desorption of $PF_3$ ligands from the $Pt(PF_3)_3$ intermediate can occur at substrate temperatures only slightly above room temperature.  Experimentally, this information was acquired by exposing thin films of $Pt(PF_3)_4$ to an electron dose ($< 6 \times 10^{15}$ e$^-$/cm$^2$), a value large enough to create $Pt(PF_3)_{3(ads)}$ species, but insufficient to induce any significant P-F bond cleavage[36].  Figure 13 demonstrates the effect of annealing a film, composed predominantly of $Pt(PF_3)_{3(ads)}$ species, and shows that increasing the substrate temperature above room temperature leads to a decrease in the concentration of phosphorus and fluorine atoms, while the Pt signal and the P/F ratio (not shown) remain relatively constant[36].  This is consistent with the thermal desorption of $PF_3$ ligands from the $Pt(PF_3)_{3(ads)}$ intermediate ($Pt(PF_3)_{3(ads)} + \Delta \rightarrow PF_{3(g)}\uparrow$), which is responsible for the increase in the Pt/P ratio shown in Figure 13 at elevated temperatures.  Consistent with this assertion, the degree of phosphorus contamination in EBID deposits created from $Pt(PF_3)_4$ under steady state deposition conditions on a heated substrate has been shown to decrease dramatically when the substrate temperature is raised to only 100 °C during deposition[64].
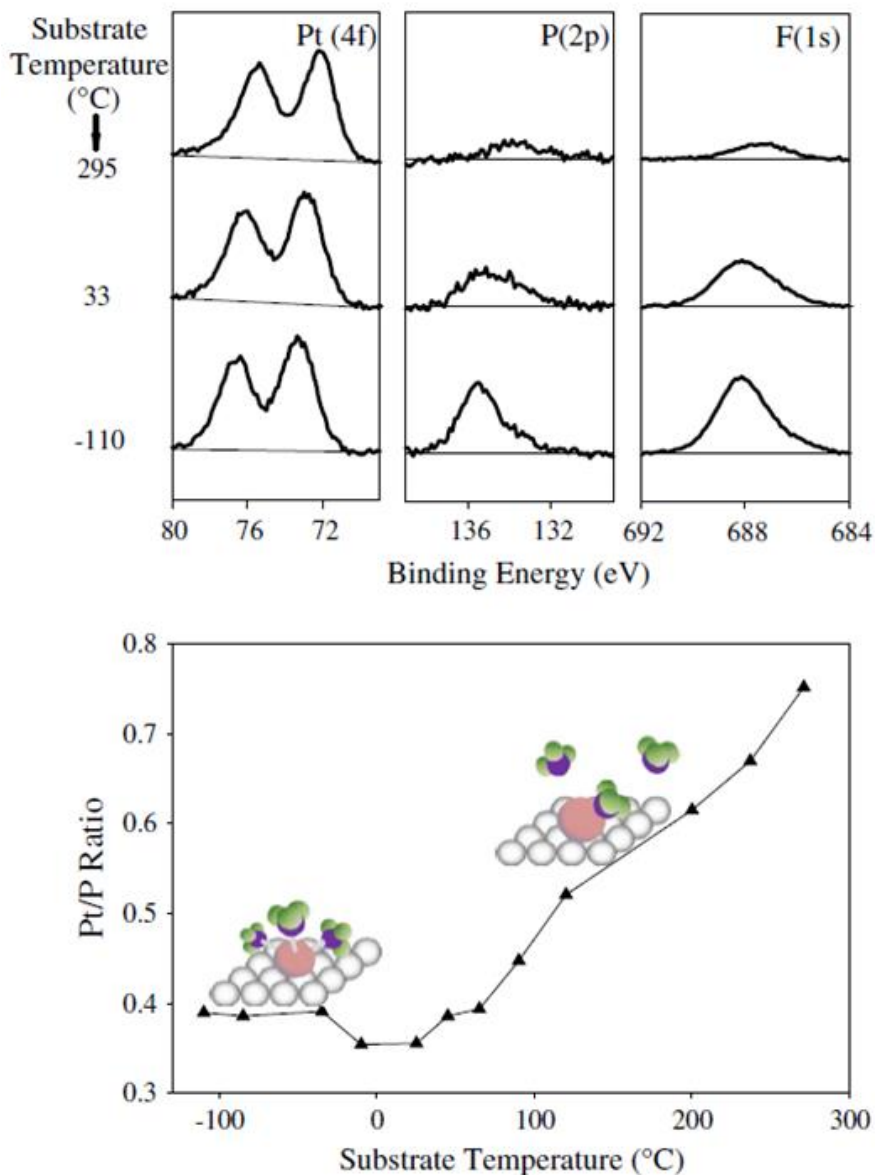
**Figure 2.13**: Influence of substrate temperature on $Pt(PF_3)_{3(ads)}$ species: *(top)* Pt(4f), P(2p) and F(1s) XPS regions and *(bottom)* Pt/P ratio.

The effect of thermal processing is therefore to decrease the level of phosphorus contamination. In contrast, electron processing of the same $Pt(PF_3)_{3(ads)}$ intermediate leads to $PF_3$ decomposition and the formation of nonvolatile phosphorus atoms[36]. Figure 14 shows the overall sequence of elementary reaction steps that can occur during $Pt(PF_3)_4$ EBID.
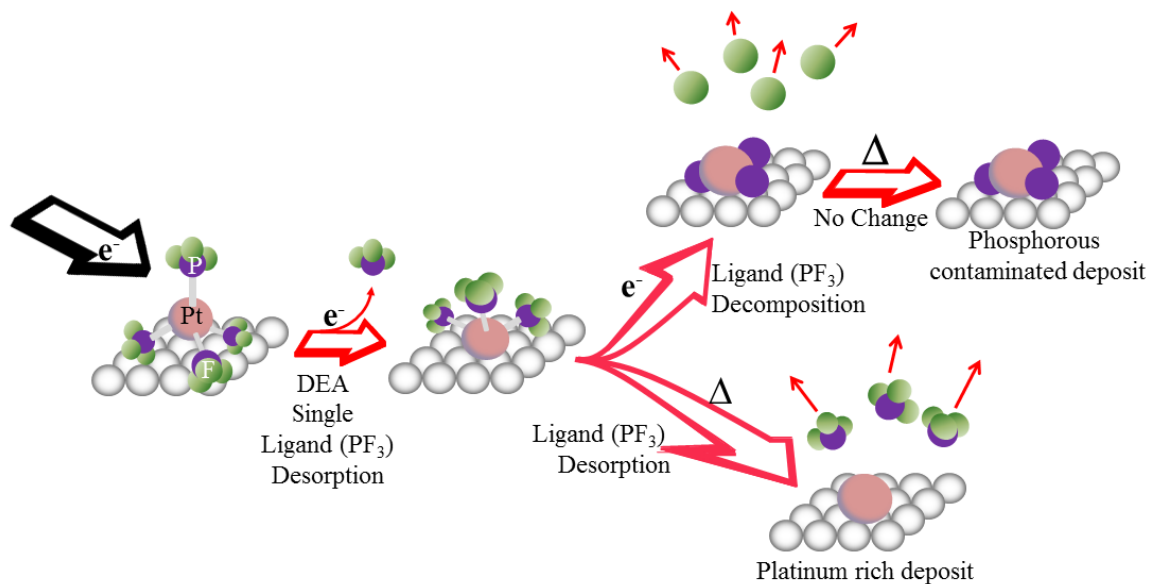
**Figure 2.14**: Summary of the molecular level events that occur during the EBID of Pt(PF$_3$)$_4$
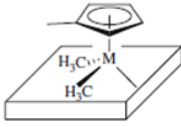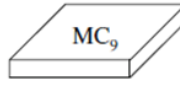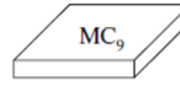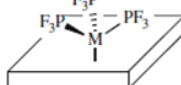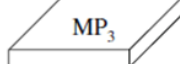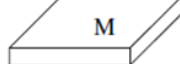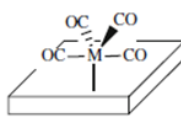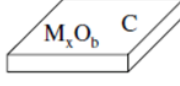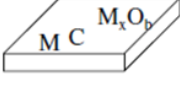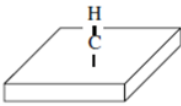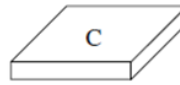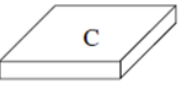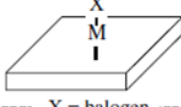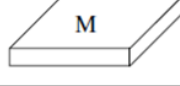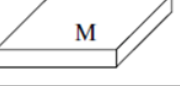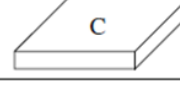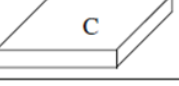
However, not all ligands or ligand architectures benefit from thermal processing. Figure 15 shows the effect of annealing a MePtCpMe$_3$ film that was initially exposed to an electron dose of 3.37 x 10$^{16}$ e$^-$/cm$^2$, an electron dose just sufficient to effect Pt-CH$_3$ bond cleavage in all of the adsorbed MePtCpMe$_3$ molecules[36]. Analysis of Figure 15 reveals that the film's chemical composition is invariant to the substrate temperature in the range -110 to 367 °C, remaining at ≈ 90% carbon and ≈ 10% platinum. This indicates that following the initial Pt-CH$_3$ bond cleavage event that characterizes the deposition step, all of the remaining carbon atoms become incorporated into the deposit[36]. In this instance, results of the UHV surface science studies can be directly compared with data obtained by Mulders *et al.*[65] who also found that the chemical composition of EBID films created from MePtCpMe$_3$ in an SEM was invariant to the substrate temperature between 25 and 360 °C[63]. Thus, there is no advantage to using elevated substrate temperatures for the
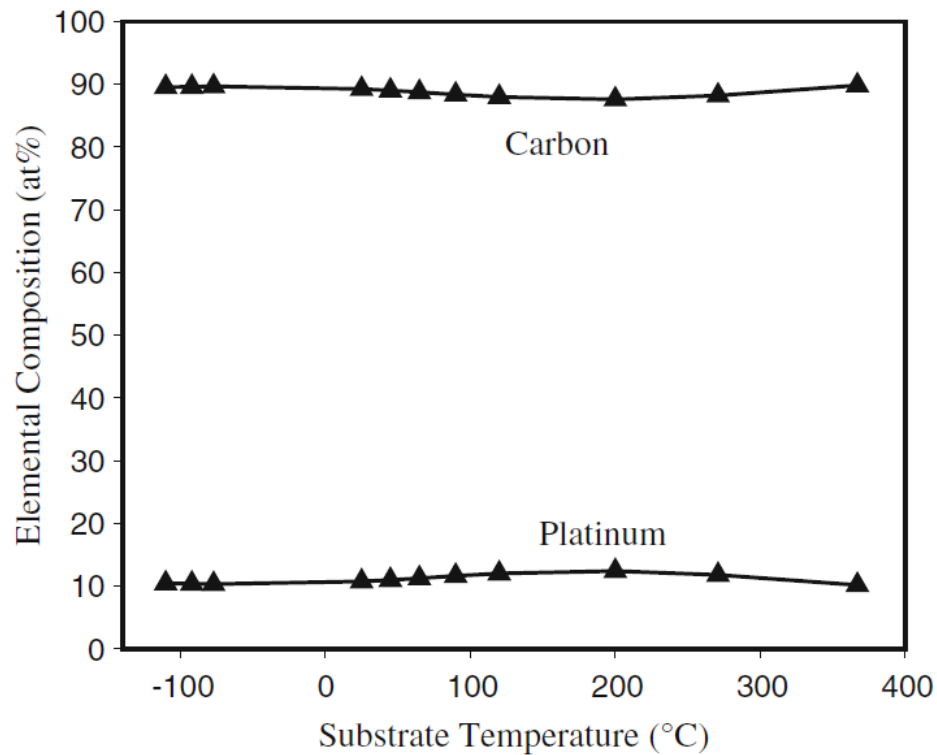
**Figure 2.15**:  Effect of substrate temperature on the chemical composition of EBID films created from MeCpPtMe$_3$.

MeCpPtMe$_3$ precursor. This underlines the need to avoid $\eta^5$-cyclopentadienyl ligands in any precursor designed specifically for EBID.

A summary of the different ways in which MY$_{(ads)}$ species are processed by either electrons or thermal reactions is shown  in Table 3[32-39].

| Intermediate | e⁻ | Δ |
|---|---|---|
| (Cp-M with H₃C, H₃C ligands) | $MC_9$ $+ H_{2(g)} \uparrow$ | $MC_9$ $+ H_{2(g)} \uparrow$ |
| ($F_3P$, $F_3P$—M—$PF_3$, $F_3P$) | $MP_3$ $+ F_{(g)}^- \uparrow$ | $M$ $+ 3PF_{3(g)} \uparrow$ |
| (OC, CO, OC—M—CO) | $M_xO_b$ $C$ | $M_xO_b$ $M\,C$ $+ CO_{(g)} \uparrow$ |
| (H—C—) | $C$ $+ H_{2(g)} \uparrow$ | $C$ $+ H_{2(g)} \uparrow$ |
| (X—M—) X = halogen | $M$ $+ X_{(g)}^- \uparrow$ | $M$ $+ X_{2(g)} \uparrow$ |
| (X—C—) | $C$ $+ X_{(g)}^- \uparrow$ | $C$ $+ X_{2(g)} \uparrow$ |

**Table 2.3**: Summary of the electron (e⁻) and thermal ( Δ) processing routes for $MY_{(ads)}$ intermediates produced by different organometallic precursors in the initial electron-induced deposition step

## 2.2. Precursor Design Strategies for EBID

Based on the insights from UHV surface science studies, the ideal EBID precursor should have a small number of ligands including ones that have been shown capable of desorbing: (1) as neutral molecules (e.g., CO) in the initial deposition step, (2) by thermal processing at elevated substrate temperatures (e.g., $PF_3$) or (3) as a result of electron processing (halogens in metal-halide complexes). In the following section, we describe

how this information could be used in the design of EBID specific precursors, using Au- and Pt-containing organometallic complexes as representative examples.

### 2.2.1. Strategies for Au Precursors

The two Au(I) compounds that have been used successfully in prior studies of gold EBID: $ClAu(PF_3)$[28,29] and $ClAuCO$[66] are both of the type XAuL, featuring one halide ligand X and one strongly π-acidic neutral two electron donor ligand (L = CO, $PF_3$) which is stable as a gas phase species. We hypothesize that XAuL provides an optimal framework to create organometallic precursors capable of depositing pure Au by EBID via the following reaction sequence:

$$XAuL(ads) + e^- \rightarrow L(g)\uparrow + AuX(ads)$$

$$AuX(ads) + e^- \rightarrow Au(ads) + X^-(g)\uparrow$$
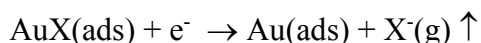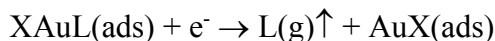
This sequence of proposed reaction steps is based on the observations that both CO and $PF_3$ ligands can be ejected as gas phase species in the initial deposition step, coupled with the susceptibility of metal-halogen bonds towards electron stimulated halide desorption.
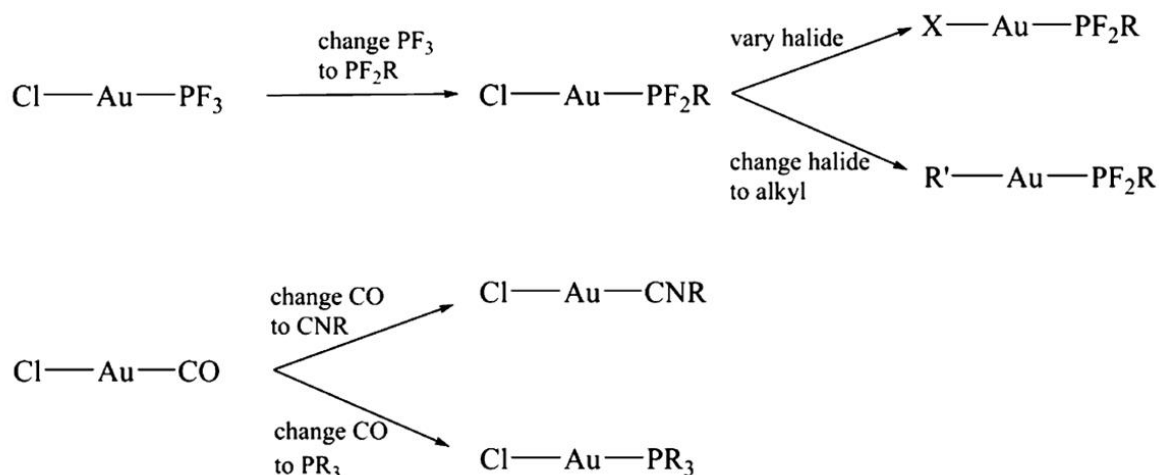


**Figure 2.16**: Conceptual strategy for generating a library of Au(I) precursor candidates

Although ClAu(PF$_3$)[28,29] and ClAuCO[66] have both been used to deposit gold structures of fairly high purity, the sensitivity of these compounds towards temperature, air, moisture and light renders both impractical for storage and scale-up to the quantities needed for any kind of practical applications. In addition to being stable, viable precursors must also be suitably volatile for a vacuum-based deposition process such as EBID. Guided by these basic chemical and physical requirements, a reasonable approach to precursor design would begin with ClAu(PF$_3$) and ClAuCO as lead compounds and vary the coordination sphere using ligands that are isoelectronic to those in ClAu(PF$_3$) and ClAuCO but chosen to impart stability to the compounds without compromising volatility. Some possible strategies for generating a small library of precursor candidates are illustrated in Figure 16. As an example, since ClAuPF$_3$ is well characterized[67,68], one possible approach is to make derivatives of the phosphine ligand that still contain two of the three P-F bonds to maintain the ligand's overall $\pi$-acidic character (Figure 16)[69], but with a new P-R bond that has the potential to improve precursor stability and thus suitability for EBID. This approach is supported by the successful synthesis of ClAuPF$_2$R complexes[70], although no EBID studies with these organometallic precursors have been reported. An example of the dependence of stability on the R group is the amino-substituted complex ClAuPF$_2$N(CH$_3$)$_2$, which has a thermal decomposition temperature of 143 °C, in contrast to the decomposition of ClAuPF$_3$ at only 45 °C. If ClAuPF$_2$R derivatives decompose before sufficient volatilization for EBID, the halide ligand could be varied or replaced with an alkyl group. In complexes of Br or I, the negative effects of higher molecular weight on volatility could potentially be compensated by weaker intermolecular interactions through the halides[71,72].

The lead compounds ClAuPF$_3$ and ClAuCO suggest another series of precursor candidates in which the labile carbonyl ligand in ClAuCO is replaced with another $\pi$-acidic ligand (L, Figure 16), perhaps an isocyanide. An isocyanide is isoelectronic with the CO ligand, although it is a better $\sigma$-donor, which stabilizes the analogous Au(I) complexes. The CO ligand could also be replaced by a $\pi$-basic trialkylphosphine group such as P(CH$_3$)$_3$. Complexes of the type XAuPR$_3$ can be easily prepared using standard Schlenk techniques and handled under ambient light[72], providing significant practical advantages if they are suitable as EBID precursors.

### 2.2.2. Strategies for Pt Precursors

Using the same basic design concept of simple coordination spheres with ligands that have been shown to desorb during the deposition step or are capable of being removed by electron beam processing, four-coordinate square planar Pt(II) complexes would seem to be more attractive for EBID than MeCpPtMe$_3$, the carbon-rich pseudo-octahedral CVD precursor used in prior EBID studies[2,23,24]. As a potential lead compound for Pt, a reasonable candidate is Cl$_2$Pt(CO)$_2$[73], which shares a common ligand set with ClAuCO. Although Cl$_2$Pt(CO)$_2$ has not been used in EBID, it is volatile enough to be purified by sublimation without decomposition[74] and has been used for CVD[75,76]. Based on the existing hypothesis for the EBID reactions of ClAuCO, one potential route for Cl$_2$Pt(CO)$_2$ to create pure Pt deposits via EBID is through the following sequence of steps:

$$Cl_2Pt(CO)_2 \text{ (ads)} + e^- \rightarrow Cl_2Pt \text{ (ads)} + 2CO(g)\uparrow$$

$$Cl_2Pt \text{ (ads)} + e^- \rightarrow \rightarrow Pt \text{ (ads)} + 2Cl^-(g)\uparrow$$
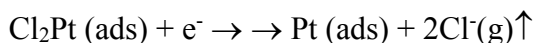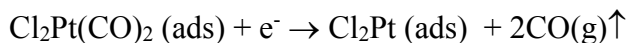
Like ClAu(CO), Cl$_2$Pt(CO)$_2$ is very water-sensitive and prone to carbonyl loss[77], so strategies similar to those described for Au precursors might well be needed to prepare

other, more practically viable EBID precursors. The ligand variation scheme (Figure 17) is analogous to the one for Au(I) complexes incorporating several known compound types, such as $PtX_2(CO)_2$[78], $PtR_2(CO)_2$[79], $PtR_2(PF_3)_2$[79], and $X_2Pt(CNR')_2$[80]. Such studies would be an important step toward developing a set of coherent design rules for EBID precursors.

$$PtCl_2(CO)_2 \xrightarrow{\text{vary halide}} PtX_2(CO)_2 \begin{cases} \xrightarrow{\substack{\text{change halide} \\ \text{to alkyl}}} PtR'_2(CO)_2 \xrightarrow{\substack{\text{change CO} \\ \text{to } PF_3}} PtR'_2(PF_3)_2 \\ \xrightarrow{\substack{\text{change CO} \\ \text{to CNR''}}} PtX_2(CNR'')_2 \end{cases}$$
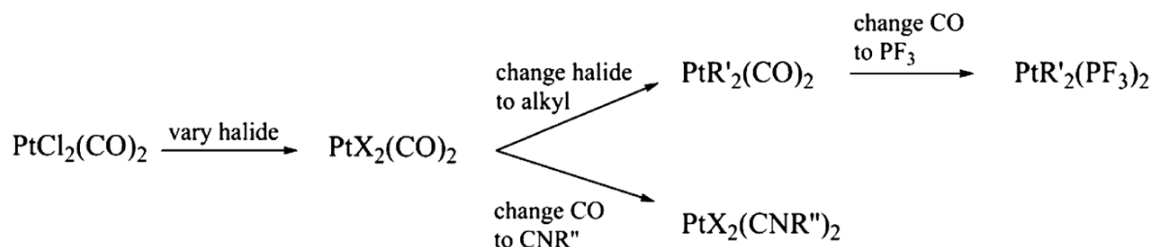
**Figure 2.17**: Conceptual strategy for generating a library of Pt(II) precursor candidates

2.3. The Future

As a result of the increasing engagement of the EBID community with synthetic inorganic chemists, a number of outstanding scientific questions can also now be addressed related to the reactions of organometallic complexes with systemic structural and compositional differences. Specifically, how do organometallic precursors with:

(a) The same metal center but systematic differences in ligand architecture behave under the influence of electron irradiation? A related question is the extent to which the behavior of a particular ligand is sensitive to the surrounding architecture. For example, to what extent is the fate of the CO ligands in an organometallic complex of the general type $M(CO)_3X$ influenced by the nature of ligand X? Information from these studies will be equally useful in testing hypotheses based on studies conducted from existing precursors and also in the development of design strategies for new precursors.

(b) The same ligand architecture but different metal centers behave in EBID? Recent studies on metal(hfac)$_2$ complexes suggest that the nature of the metal center is irrelevant in determining the bond breaking sequence[81]. This assertion is supported by anecdotal evidence from gas phase studies on Ni(PF$_3$)$_4$ and Pt(PF$_3$)$_4$ which have shown that a similar DEA attachment mechanism is operative in both complexes, favoring the loss of only one of the PF$_3$ groups[82]. If this trend is confirmed by more surface science and electron microscopy studies on new precursors, then the behavior of one type of ligand architecture can confidently be extrapolated to other transition metals.

Although a more detailed understanding of EBID will almost certainly benefit from a wider array of customized precursors, one area where progress in the field remains slow is in the development of a more detailed theoretical, molecular level understanding of how and why organometallic precursors fragment in the way they do under the influence of electron irradiation. The difficulty lies in part due to the relative complexity of many of the organometallic complexes used in EBID and also in the need for theory to tackle molecules in electronically excited states where density functional theory (DFT) is unreliable. However, one positive development in this area over the past several years has been the appearance of a number of gas phase studies on electron beam interactions with EBID precursors, which should serve as a less complex starting point for meaningful theoretical efforts.

## 2.4. Summary

The issue of organic contamination in EBID structures is one of the key challenges hampering the development of EBID as a robust technology for fabricating nanostructures

that could otherwise have a wide array of applications in fields as diverse as catalysis, biosensing and plasmonics. Although not complete, insights from UHV surface science studies have started to uncover some of the elementary reaction steps that underpin EBID, including a more detailed understanding of the role of ligand architecture in the deposition process. The state of knowledge has now developed to a point where organometallic chemists can begin the rational design of new precursors specifically for EBID applications. It is hoped that the close interdisciplinary collaboration between surface scientists and synthetic chemists will enable new EBID nanostructures to be created with metal contents than are significantly improved over those possible with existing CVD precursors.

## 2.5. References

(1)     Randolph, S. J.; Fowlkes, J. D.; Rack, P. D. *Crit. Rev. Solid State Mater. Sci.* **2006**, *31*, 55.
(2)     Utke, I.; Hoffman, P.; Melngailis, J. *J. Vac. Sci. Technol., B* **2008**, *26*, 1197.
(3)     van Dorp, W. F.; Hagen, C. W. *J. Appl. Phys.* **2008**, *104*, 081301.
(4)     Huth, M.; Porrati, F.; Schwalb, C.; Winhold, M.; Sachser, R.; Dukic, M.; Adams, J.; Fantner, G. *Beilstein J. Nanotechnol.* **2012**, *3*, 597.
(5)     Frey, L.; Lehrer, C.; Ryssel, H. *Appl Phys A: Mater. Sci. Process.* **2003**, *76*, 1017.
(6)     Igaki, J. Y.; Kanda, K.; Haruyama, Y.; Ishida, M.; Ochiai, Y.; Fujita, J. I.; Kaito, T.; Matsui, S. *Microelectron. Eng.* **2006**, *83*, 1225.
(7)     Fujii, T.; Iwasaki, K.; Muekane, M.; Takeuchi, T.; Hasuda, M.; Asahata, Y.; Kyohara, M.; Kogure, T.; Kijima, Y.; Kaito, T. *J. Micromech. Microeng.* **2005**, *15*, S286.
(8)     Lepore, A. *Handbook of VLSI Microlithography: Principles, Technology and Applications*; 2 ed., 2001.
(9)     Bakshi, V. *EUV Lithography*; SPIE/ Wiley Interscience: New York, 2009.
(10)    van Dorp, W. F.; Lazic, I.; Beyer, A.; Gölzhäuser, A.; Wagner, J. B.; Hansen, T. W.; Hagen, C. W. *Nanotechnology* **2011**, *22*, 115303.
(11)    Brown, J.; Kocher, P.; Ramanujan, C. S.; Sharp, D. N.; Torimitsu, K.; Ryan, J. S. *Ultramicroscopy* **2013**, *133*, 62.
(12)    Van Oven, J. C.; Berwald, F.; Berggen, K. K.; Kruit, P.; Hagen, C. W. *J. Vac. Sci. Technol. B* **2011**, *29*, 06F305.
(13)    Fernandez-Pacheco, A.; Serrano-Ramón, L.; Michalik, J. M.; Ibarra, M. R.; De Teresa, J. M.; O'Brien, L.; Petit, D.; Lee, J.; Coburn, R. P. *Sci. Rep.* **2013**, *3*, 1492.
(14)    Perentes, A.; Hoffmann, P. *Chem. Vap. Depos.* **2007**, *13*, 176.
(15)    Edinger, K.; Becht, H.; Bihr, J.; Boegli, V.; Budach, M.; Hofmann, T.; Koops, H. W. P.; Kuschnerus, P.; Oster, J.; Spies, P.; Weyrauch, B. *J. Vac. Sci. Technol., B: Microelectron. Nanometer Struct.--Process., Meas., Phenom.* **2004**, *22*, 2902.

(16)     Liang, T.; Frendberg, E.; Lieberman, B.; Stivers, A. *J. Vac. Sci. Technol., B: Microelectron. Nanometer Struct.--Process., Meas., Phenom.* **2005**, *23*, 3101.

(17)     Heerkens, C. T. H.; Kamerbeek, M. J.; van Dorp, W. F.; Hagen, C. W.; Hoekstra, J. *Microelectron. Eng.* **2009**, *86*, 961.

(18)     Hubner, B.; Koops, H. W. P.; Pagnia, H.; Sotnik, N.; Urban, J.; Weber, M. *Ultramicroscopy* **1992**, *42-44*, 1519.

(19)     Chen, I.-C.; Chen, L.-H.; Orme, C.; Quist, A.; Lal, R.; Jin, S. *Nanotechnology* **2006**, *17*, 4322.

(20)     Graells, S.; Alcubilla, R.; Badenes, G.; Quidant, R. *Appl. Phys. Lett.* **2007**, *91*, 121112.

(21)     Weber-Bargioni, A.; Schwartzberg, A.; Schmidt, M.; Harteneck, B.; Ogletree, D. F.; Schuck, P. J.; Cabrini, S. *Nanotechnology* **2010**, *21*, 065306.

(22)     Koops, H. W. P.; Hoinkis, O. E.; Honsberg, M. E. W.; Schmidt, R.; Blum, R.; Bottger, G.; Kuligk, A.; Liguda, C.; Eich, M. *Microelectron. Eng.* **2001**, *57-58*, 995.

(23)     Koops, H. W.; Kaya, A.; Weber, M. *J. Vac. Sci. Technol. B* **1995**, *13*, 2400.

(24)     Botman, A.; Hesselberth, M.; Mulders, J. J. L. *Microelectron. Eng.* **2008**, *85*, 1139.

(25)     Klein, K. L.; Randolph, S. J.; Fowlkes, J. D.; Allard, L. F.; Meyer III, H. M.; Simpson, M. L.; Rack, P. D. *Nanotechnology* **2008**, *19*, 345705.

(26)     Botman, A.; Hesselberth, M.; Mulders, J. J. L. *J Vac Sci Technol B* **2008**, *26*, 2464.

(27)     Utke, I.; Hoffmann, P.; Melngailis, J. *Journal of Vacuum Science & Technology B* **2008**, *26*, 1197.

(28)     Tran, P. D.; Doppelt, P. *Journal of the Electrochemical Society* **2007**, *154*, D520.

(29)     Brintlinger, T.; Fuhrer, M. S.; Melngailis, J.; Utke, I.; Bret, T.; Perentes, A.; Hoffmann, P.; Abourida, M.; Doppelt, P. *J. Vac. Sci. Technol., B: Microelectron. Nanometer Struct.--Process., Meas., Phenom.* **2005**, *23*, 3174.

(30)     McElwee-White, L. *Dalton Trans.* **2006**, 5327.

(31)     McElwee-White, L.; Koller, J.; Kim, D.; Anderson, T. J. *ECS Transactions* **2009**, *25*, 161.

(32)     van Dorp, W. F.; Wnuk, J. D.; Gorham, J. M.; Fairbrother, D. H.; Madey, T. E.; Hagen, C. W. *J. Appl. Phys.* **2009**, *106*, 074903.

(33)     Wnuk, J. D.; Gorham, J. M.; Rosenberg, S. G.; van Dorp, W. F.; Madey, T. E.; Hagen, C. W.; Fairbrother, D. H. *J. Phys. Chem. C* **2009**, *113*, 2487.

(34)     Wnuk, J. D.; Gorham, J. M.; Rosenberg, S. G.; van Dorp, W. F.; Madey, T. E.; Hagen, C. W.; Fairbrother, D. H. *J. Appl. Phys.* **2010**, *107*, 054301/1.

(35)     Wnuk, J. D.; Rosenberg, S. G.; Gorham, J. M.; van Dorp, W. F.; Hagen, C. W.; Fairbrother, D. H. *Surf. Sci.* **2011**, *605*, 257.

(36)     Rosenberg, S. G.; Landheer, K.; Hagen, C. W. *J. Vac. Sci. Technol. B* **2012**, *30*, 051805/1.

(37)     Rosenberg, S. G.; Barclay, M.; Fairbrother, D. H. *Phys Chem Chem Phys* **2013**, *15*, 4002.

(38)     Rosenberg, S. G.; Barclay, M.; Fairbrother, D. H. *Journal Physcial Chemistry C* **2013**, *117*, 16053.

(39)     Landheer, K.; Rosenberg, S. G.; Bernau, L.; Swiderek, P.; Utke, I.; Hagen, C. W.; Fairbrother, D. H. *Journal of Physical Chemistry C* **2011**, *115*, 17452.

(40)     Perentes, A.; Sinicco, G.; Boero, G.; Dwir, B.; Hoffmann, P. *J. Vac. Sci. Technol. B* **2007**, *25*, 2228.

(41)     Ervin, M. H.; Nichols, B. M. *J. Vac. Sci. Technol., B* **2009**, *27*, 2982.

(42)     Fernandez-Pacheco, A.; De Teresa, J. M.; Cordoba, R.; Ibarra, M. R. *J. Phys. D: Appl. Phys.* **2009**, *42*, 055005.

(43)     Fernandez-Pacheco, A.; De Teresa, J. M.; Cordoba, R.; Ibarra, M. R.; Petit, D.; Read, D. E.; O'Brien, L.; Lewis, E. R.; Zeng, H. T.; Cowburn, R. P. *Appl. Phys. Lett.* **2009**, *94*, 192509/1.

(44)     Gabureac, M.; Bernau, L.; Utke, I.; Boero, G. *Nanotechnology* **2010**, *21*, 115503/1.

(45)     Gazzadi, G. C.; Mulders, H.; Trompenaars, P.; Ghirri, A.; Affronte, M.; Grillo, V.; Frabboni, S. *Journal of Physical Chemistry C* **2011**, *115*, 19606.

(46)     Gazzadi, G. C.; Mulders, J. J. L.; Trompenaars, P.; Ghirri, A.; Rota, A.; Affronte, M.; Frabboni, S. *Microelectron Eng* **2011**, *88*, 1955.

(47)     Botman, A.; Hesselberth, M.; Mulders, J. J. L. *J. Vac. Sci. Technol., B* **2008**, *26*, 2464.

(48)     Sychugov, I.; Nakayama, Y.; Mitsuishi, K. *J. Phys. Chem. C* **2009**, *113*, 21516.

(49)     van Dorp, W. F.; van Someren, B.; Hagen, C. W.; Kruit, P.; Crozier, P. A. *J. Vac. Sci. Technol., B* **2006**, *24*, 618.

(50)     van Dorp, W. F.; Hagen, C. W.; Crozier, P. A.; Kruit, P. *Nanotechnology* **2008**, *19*, 225305.

(51)     Porrati, F.; Sachser, R.; Schwalb, C. H.; Frangakis, A. S.; Huth, M. *Journal of Applied Physics* **2011**, *109*.

(52)     Frabboni, S.; Gazzadi, G. C.; Felisari, L.; Spessot, A. *Appl. Phys. Lett.* **2006**, *88*, 213116.

(53)     Frabboni, S.; Gazzadi, G. C.; Spessot, A. *Phys. E* **2007**, *37*, 265.

(54)     Rack, P. D.; Randolph, S.; Deng, Y.; Fowlkes, J.; Choi, Y.; Joy, D. C. *Appl. Phys. Lett.* **2003**, *82*, 2326.

(55)     Engmann, S.; Stano, M.; Matejčík, Š.; Ingólfsson, O. *Physical Chemistry Chemical Physics* **2012**, *14*, 14611.

(56)     Barry, J.; Ervin, M. H.; Molstad, J.; Wickenden, A.; Brintlinger, T.; Hoffman, P.; Meingailis, J. *J. Vac. Sci. Technol. B* **2006**, *24*, 3165.

(57)     Botman, A.; Hagen, C. W.; Li, J.; Thiel, B. L.; Dunn, K. A.; Mulders, J. J. L.; Randolph, S. J.; Toth, M. *J. Vac. Sci. Technol. B* **2009**, *27*, 2759.

(58)     Takeguchi, M.; Shimojo, M.; Furuya, K. *Applied Physics a-Materials Science & Processing* **2008**, *93*, 439.

(59)     Wang, S.; Sun, Y.-M.; Wang, Q.; White, J. M. *J. Vac. Sci. Technol. B* **2004**, *22*, 1803.

(60)     May, O.; Kubala, D.; Allan, M. *Phys. Chem. Chem. Phys.* **2012**, *14*, 2979.

(61)     Ervin, M. H.; Chang, D.; Nichols, B.; Wickenden, A.; Barry, J.; Melngailis *J. Vac. Sci. Technol., B* **2007**, *25*, 2250.

(62)     Xue, Z.; Strouse, M. J.; Shuh, D. K.; Knobler, C. B.; Kaesz, H. D.; Hicks, R. F.; Williams, R. S. *Journal of the American Chemical Society* **1989**, *111*, 8779.

(63)     Mulders, J. J. L.; Belova, L. M.; Riazanova, A. *Nanotechnology* **2011**, *22*.

(64)     Wang, S.; Sun, Y.; Wang, Q.; White, J. *Journal of Vacuum Science & Technology B* **2004**, *22*, 1803.

(65)     Mulders, J.; Belova, L.; Riazanova, A. *Nanotechnology* **2010**, *22*, 055302.

(66)     Mulders, J. J. L.; Veerhoek, J. M.; Bosch, E. G. T.; Trompenaars, P. H. F. *J. Phys. D: Appl. Phys.* **2012**, *45*.

(67)     Fuss, W.; Ruehe, M. *Z. Naturforsch., B: Chem. Sci.* **1992**, *47*, 591.

(68)     Schödel, F.; Bolte, M.; Wagner, M.; Lerner, H.-W. *Z. Anorg. Allg. Chem.* **2006**, *632*, 652.

(69)     Woska, D.; Prock, A.; Giering, W. P. *Organometallics* **2000**, *19*, 4629.

(70)     Graefe, A.; Kruck, T. *J. Organomet. Chem.* **1996**, *506*, 31.

(71)     Heathcote, R.; Howell, J. A. S.; Jennings, N.; Cartlidge, D.; Cobden, L.; Coles, S.; Hursthouse, M. *Dalton Trans.* **2007**, 1309.

(72)     Mann, F. G.; Wells, A. F.; Purdie, D. *Journal of the Chemical Society (Resumed)* **1937**, 1828.

(73)     Dell'Amico, D. B.; Labella, L. *J. Organomet. Chem.* **2000**, *593-594*, 427.

(74)     von Ahsen, B.; Wartchow, R.; Willner, H.; Jonas, V.; Aubke, F. *Inorg. Chem.* **2000**, *39*, 4424.

(75)     Vargas Garcia, J. R.; Goto, T. *Mater. Trans.* **2003**, *44*, 1717.

(76)     Guerrero, R. M.; Garcia, J. R. V.; Santes, V.; Gomez, E. *J. Alloys Compd.* **2007**, *434-435*, 701.

(77)     Rand, M. J. *J. Electrochem. Soc.* **1973**, *120*, 686.

(78)     Bagnoli, F.; Belli, D. A. D.; Calderazzo, F.; Englert, U.; Marchetti, F.; Merigo, A.; Ramello, S. *J. Organomet. Chem.* **2001**, *622*, 180.

(79)     Friedemann, R.; Seppelt, K. *Eur. J. Inorg. Chem.* **2013**, *2013*, 1197.

(80)     Browning, J.; Goggin, P. L.; Goodfellow, R. J. *J. Chem. Res. (S)* **1978**, 328.

(81)     Rosenberg, S. G.; Barclay, M.; Fairbrother, D. H. *ACS applied materials & interfaces* **2014**, *6*, 8590.

(82)     Friedman, J. F.; Miller, T. M.; Friedman-Schaffer, J. K.; Viggiano, A.; Rekha, G.; Stevens, A. E. *The Journal of chemical physics* **2008**, *128*, 104303.

Chapter 3


Electron-Induced Surface Reactions of $\eta^3$-Allyl Ruthenium Tricarbonyl Bromide

$[(\eta^3\text{-}C_3H_5)Ru(CO)_3Br]$:  Contrasting the Behavior of Different Ligands

Chapter 3.     Electron-Induced Surface Reactions of $\eta^3$-Allyl Ruthenium Tricarbonyl Bromide [($\eta^3$-C$_3$H$_5$)Ru(CO)$_3$Br]:  Contrasting the Behavior of Different Ligands

### 3.1. Introduction

Electron beam induced deposition (EBID) is a single step, vacuum-based, lithographic strategy typically performed in a modified Scanning Electron Microscope (SEM) that uses a focused electron beam to create metal-containing nanostructures from the deposition of organometallic precursors.[1-4]  Deposition occurs as a result of electron-stimulated decomposition of the molecular precursor to form nonvolatile, metal-containing fragments (the deposit).[3,4]  The inherent flexibility of the electron beam allows EBID to produce an almost unlimited array of three-dimensional nanostructures where the size and shape can be accurately controlled and varied; nanostructures < 1 nm in diameter have been reported.[5,6]  There are numerous potential applications of EBID, particularly in the area of prototyping nanostructures; current commercial uses include the repair of extreme ultraviolet light lithography (EUVL) masks[7-9] and the production of custom tips for scanning tunneling[10] and atomic force microscopies.[11,12]

For the full potential of EBID to be realized, however, one major challenge relating to the high levels of organic contamination found in EBID nanostructures must be overcome.[3,13] These impurities negatively impact properties such as resistivity and conductivity, limiting the current applications of EBID nanostructures.[3,4,14] The organic contamination can be traced back in large part to the structure, chemical composition, and decomposition mechanisms of existing EBID precursors, which have typically been designed for thermal deposition processes, such as chemical vapor deposition (CVD),[3,13] rather than electron-stimulated processes, such as EBID. A better understanding of the fundamental bond-breaking steps involved in EBID would help to elucidate the mechanisms of organic contamination and the fate of different ligands, providing knowledge that could be used in the design of precursors optimized specifically for EBID.[15] Indeed, there is a general need for more fundamental physical and chemical information on the various processes involved in EBID. This has provided the motivation to understand the electron interactions with EBID precursors in the gas phase,[16-20] as well as adsorption energies, surface dynamics[21,22] and reaction cross sections[23] of precursor molecules adsorbed on surfaces.

In typical EBID, it is very difficult to identify the sequence of events that accompany deposition, including bond-breaking and desorption processes, due to the steady state deposition conditions, the extremely large fluxes of electrons used, the presence of additional processes, such as diffusion, and the effects of contaminant gases typically present in electron microscopes.[3,4] To gain more fundamental insights into the EBID process, we have employed an ultrahigh vacuum (UHV) surface science approach to study the reactions of EBID precursors under electron irradiation. In contrast to

traditional EBID studies, the UHV surface science approach examines the effects of electron irradiation on nanometer-thick films of precursor molecules adsorbed onto chemically inert substrates at low temperatures.[24-29]  This experimental approach has also recently been used to examine electron induced reactions of ligands present in EBID precursors.[30]

In our experimental apparatus, X-ray Photoelectron Spectroscopy (XPS) is used in situ to follow changes in bonding environment and surface composition of the various elements contained in the precursor molecule, and Mass Spectrometry (MS) provides complementary information on the volatile species ejected from the film as a result of electron irradiation.  Both XPS and MS can be acquired as a function of electron dose, helping to elucidate the sequence of electron-stimulated processes. Use of a low temperature (<200K) UHV environment ($P_{base}$ <5 x $10^{-9}$ Torr) also simplifies data interpretation because it largely eliminates complicating effects from diffusion and adsorbed contaminants (e.g., water and hydrocarbons).  Additionally, the low background pressure allows identification of gas phase products produced during electron beam irradiation; this information is not available in typical EBID experiments due to both the presence of a constant partial pressure of precursor molecules during deposition and the higher base pressure.[26]

Previous UHV surface science studies[24,25,27,28,31-34] have revealed that the electron beam-induced reactions of organometallic compounds typically occur in two relatively discrete steps.[24,26,27]  In the first step, a transiently adsorbed precursor undergoes an electron-stimulated reaction that results in ligand desorption and leaves behind a partially decomposed surface-bound intermediate.  Continued electron beam irradiation (always

present in EBID due to the large electron fluxes involved) results predominantly in decomposition of the ligands contained in the surface-bound intermediate.[25] It is this second step that we believe is the primary cause of the organic contamination observed in EBID nanostructures. For example, when adsorbed $W(CO)_6$ (an EBID precursor) is irradiated with electrons, some CO ligands are initially desorbed into the gas phase, and a partially decarbonylated surface-bound intermediate, $W_x(CO)_y$, remains behind.[32] Continued electron irradiation of these surface-bound intermediates, however, causes decomposition of the remaining CO ligands, which results in oxidized tungsten atoms encased in a carbonaceous matrix.

The specific goal of the present study is to compare and contrast the behavior of different ligands that are often present in organometallic precursors used in EBID. On the basis of our previous studies,[24,25,27,28,31-34] the fate of ligands in an organometallic precursor undergoing EBID can be expected to fall into two general categories: (1) the ligands are ejected and pumped away into the gas phase as the precursor decomposes; or (2) the ligands are decomposed by electron beam irradiation following precursor decomposition and become incorporated into the deposit, contributing to contamination. As a vehicle to elucidate the behavior of different ligands, we have studied the electron-stimulated reactions of surface-bound $\eta^3$-allyl ruthenium tricarbonyl bromide [$(\eta^3$-$C_3H_5)Ru(CO)_3Br$)] and, to a lesser extent, $\eta^3$-allyl ruthenium tricarbonyl chloride [$\eta^3$-$C_3H_5)Ru(CO)_3Cl$)]. These complexes provide the opportunity to simultaneously evaluate the behavior of three different types of ligands in the same coordination sphere: carbonyl (CO), $\eta^3$-allyl ($\eta^3$-$C_3H_5$), and halides (Br, Cl). Although the bulk of the studies reported in this investigation were UHV surface science studies, to provide a more direct comparison to typical EBID

studies, we also created deposits using $[(\eta^3\text{-}C_3H_5)Ru(CO)_3Br)]$ and $[\eta^3\text{-}C_3H_5)Ru(CO)_3Cl)]$ under steady state deposition conditions in an Auger electron spectrometer, and the chemical composition of the deposits and the effect of post-deposition electron beam processing were studied.

Previous work has indicated that, under electron irradiation, carbonyl groups are susceptible to both ejection as intact molecules and decomposition depending on the number of attached CO groups.[31,32] The $\eta^3$-allyl ($\eta^3\text{-}C_3H_5$) is a polyhapto unsaturated hydrocarbon ligand and is less strongly bound than the $\pi$-facial carbon-bonded cyclopentadienyl ($\eta^5\text{-}C_5H_5$, Cp) ligand, which has been shown to be a poor leaving group under electron irradiation with the carbon atoms being retained in the metal-containing carbonaceous matrix that forms during EBID.[28] Although the $\eta^3$-allyl ligand could reasonably be predicted to behave similarly to the cyclopentadienyl (Cp) ligand, the lower hapticity (and resulting weaker metal-ligand bonding) raised the question of whether it could be removed under EBID conditions. The fate of halides directly bonded to the metal center has not been explicitly explored in EBID.[3,4]

## 3.2. Experimental

An ultrahigh vacuum (UHV) surface science chamber was used to study the effects of electron irradiation on nanometer-thick films of $\eta^3$-allyl ruthenium tricarbonyl bromide $[(\eta^3\text{-}C_3H_5)Ru(CO)_3Br]$ and, for a few comparative experiments, $\eta^3$-allyl ruthenium tricarbonyl chloride $[(\eta^3\text{-}C_3H_5)Ru(CO)_3Cl]$. The UHV chamber is equipped with X-ray Photoelectron Spectroscopy (XPS) and Mass Spectrometry (MS) and, during experiments, operates at a base pressure of $<5 \times 10^{-9}$ Torr. Details of the chamber and its analytical

capabilities, including the manipulator, electron gun and sample cleaning protocols can be found in previous publications.[25,27,28]

### 3.2.1. Precursors

$\eta^3$-Allyl ruthenium tricarbonyl bromide [$(\eta^3$-$C_3H_5)Ru(CO)_3Br$] and $\eta^3$-allyl ruthenium tricarbonyl chloride [$(\eta^3$-$C_3H_5)Ru(CO)_3Cl$] are both stable white solids at standard temperature and pressure. Prior to deposition, the precursor was added to a glass finger, which was coupled to the UHV chamber via a stainless steel tubing manifold and a UHV compatible leak valve. The gas manifold and glass finger were then evacuated by a mechanical pump into the mTorr pressure regime. Both compounds possessed sufficient vapor pressure to be dosed successfully at room temperature, although the chlorine analogue was significantly more volatile and therefore easier to dose. During the course of the experiments, it was also found that by heating the precursor in the glass finger to ~40 °C during film deposition the co-adsorption of a small amount of unwanted hydrocarbons/adventitious carbon could be significantly reduced (see Figure S1, Supporting Information).

#### 3.2.1.1. Synthesis of $\eta^3$-allyl ruthenium tricarbonyl bromide [$(\eta^3$-$C_3H_5)Ru(CO)_3Br$]

[$(\eta^3$-$C_3H_5)Ru(CO)_3Br$] was synthesized using a modified literature procedure.[35] $Ru_3(CO)_{12}$ (1.0073 g, 1.5756 mmol, Sigma-Aldrich) was added to 20 mL of 2,2,4-trimethylpentane (Sigma-Aldrich) under nitrogen. Allyl bromide (5.0 mL, 58 mmol, Sigma-Aldrich) was added and the mixture was immediately refluxed. Upon heating, the $Ru_3(CO)_{12}$ dissolved, turning the solution deep red. After 20 minutes of reflux, the solution

turned yellow, and the solvent was removed in vacuo. The resulting yellow solid was sublimed at 30 °C and 80 mTorr to yield a white solid (1.2907 g, 89%). ^{1}H NMR (CDCl$_3$, 300 MHz): δ 3.14 (dt, 2H, J = 13.1, 1.0 Hz), 4.11 (dt, 2H, J = 7.8, 1.1 Hz), 5.17 (tt, 1H, J = 13.1, 7.8 Hz). The product was identified by comparison to literature data[35] and supported by attenuated total reflectance-infrared spectroscopy (ATR-IR) (see Figure S2, Supporting Information).

### 3.2.1.2. Synthesis of η$^3$-allyl ruthenium tricarbonyl chloride [(η$^3$-C$_3$H$_5$)Ru(CO)$_3$Cl]

[(η$^3$-C$_3$H$_5$)Ru(CO)$_3$Cl] was synthesized using a modified literature procedure.[35] Ru$_3$(CO)$_{12}$ (0.9799 g, 1.533 mmol, Sigma-Aldrich) was added to 20 mL of 2,2,4-trimethylpentane (Sigma-Aldrich) under nitrogen. Allyl chloride (4.6 mL, 56 mmol, Sigma-Aldrich) was added, and the mixture was immediately refluxed. Upon heating, the Ru$_3$(CO)$_{12}$ dissolved, turning the solution deep red. After 50 minutes of reflux, the solution turned yellow, and the solvent was removed in vacuo. The resulting yellow solid was sublimed at 30 °C and 90 mTorr to form a white solid (0.7967 g, 66%). ^{1}H NMR (CDCl$_3$, 300 MHz): δ 2.96 (dd, 2H, J=13.3, 1.5 Hz), 4.19 (dd, 2H, J=7.9, 1.5 Hz), 5.30 (ttd, 1H, J=13.3, 7.9, 1.5 Hz). The product was identified by comparison to literature data[35] and supported by ATR-IR (see Figure S2, Supporting Information).

### 3.2.2. Substrates

The majority of the XPS and MS experiments were performed on an amorphous carbon (a:C) substrate, with a small number conducted on a polycrystalline Au substrate. Consistent with previous studies,[25,31-33] the chemical identity of the substrate did not impact

the low temperature, electron induced reactions of $[(\eta^3\text{-}C_3H_5)Ru(CO)_3Br]$ and $[(\eta^3\text{-}C_3H_5)Ru(CO)_3Cl]$ in terms of the XPS or MS results.

### 3.2.3. Creating films

#### 3.2.3.1. UHV Conditions

Nanometer scale films of $[(\eta^3\text{-}C_3H_5)Ru(CO)_3Br]$ and $[(\eta^3\text{-}C_3H_5)Ru(CO)_3Cl]$ were created by leaking the precursor through a UHV-compatible leak valve onto a cooled substrate. A substrate temperature of -168 °C was necessary to achieve molecular adsorption of the precursors under UHV conditions. Average film thicknesses were determined by measuring the attenuation of the substrate XPS photoelectrons (Au(4f) or C(1s)) upon film deposition.

#### 3.2.3.2. In the Auger Electron Spectrometer (AES)

Films were created by leaking $[(\eta^3\text{-}C_3H_5)Ru(CO)_3Br]$ or $[(\eta^3\text{-}C_3H_5)Ru(CO)_3Cl]$ into the chamber through an UHV-compatible leak valve coupled to a directional doser to create a constant partial pressure of precursor molecules at the Ag substrate surface during deposition. While dosing, the electron beam was rastered across the surface to produce rectangular structures, with lengths on the order of several hundred microns. The films were made with a substrate current of 700 nA, incident beam energy of 3 keV, and a partial pressure of 5 x 10$^{-7}$ Torr with a 90 minute deposition time.

## 3.3.  Results

Figure 1 shows how the C(1s)/Ru(3d), O(1s) and Br(3d) XPS regions of 1 – 2 nm thick films of $[(\eta^3\text{-}C_3H_5)Ru(CO)_3Br]$ adsorbed onto (a:C) substrates evolve as a function of increasing electron dose.  To determine the effect that X-ray irradiation has on the $[(\eta^3\text{-}C_3H_5)Ru(CO)_3Br]$ films, separate control studies were performed on both a:C (Figure S3, Supporting Information) and Au (Figure S4, Supporting Information) substrates. A comparison of the results shown in Figure 1 and Figures S3-S4, Supporting Information, demonstrate that 500 eV incident electrons and XPS irradiation  have similar effects on the C(1s)/Ru(3d), O(1s) and Br(3d) regions.  This is almost certainly a consequence of the transformations being driven by the low energy secondary electrons produced by the interactions of the X-ray beam or the 500 eV incident electron beam with the substrate.  To minimize the effect of X-ray irradiation, we exposed each film to X-ray irradiation only twice: once, to verify the chemical composition and thickness of the as-deposited film, and then after one controlled and quantified electron dose from the electron gun.  Analysis of Figure S4 in the Supporting Information reveals that for $[(\eta^3\text{-}C_3H_5)Ru(CO)_3Br]$ adsorbed on a:C substrates the X-ray irradiation time required for these two XPS to be acquired produces the same effect as an electron dose of $\sim 9.36\text{x}10^{14}$ e$^-$/cm$^2$.  This "additional" electron dose due to XPS acquisition has been factored in to all of the XPS data shown in Figures 1 - 4, 6 and 7.  In practice, however, for all but the shortest electron exposures ($\leq 1.87\text{x}10^{15}$ e$^-$/cm$^2$) the changes observed by XPS are determined almost exclusively by the 500 eV electron beam.
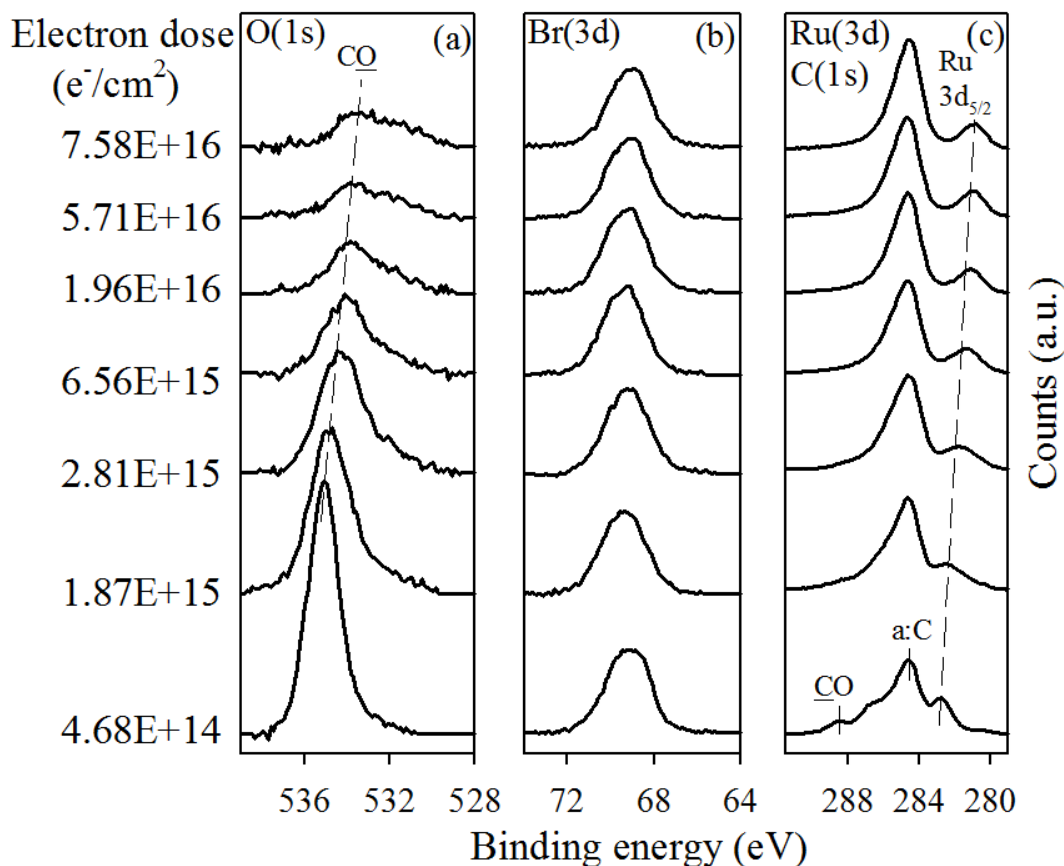
**Figure 3.1**: Evolution of the (a) O(1s), (b) Br(3d), and (c) Ru(3d)/C(1s) XP regions for 1–2 nm thick films of $[(\eta^3\text{-}C_3H_5)Ru(CO)_3Br]$ exposed to electron doses $\leq 7.58 \times 10^{16}$ e$^-$/cm$^2$. Spectra were normalized to account for slight differences in film thickness.

Figure 1a shows that, prior to electron irradiation, the O(1s) region is composed of a single peak centered at 535.1 eV, typical of the binding energy for a CO species.[36] Upon electron irradiation, the O(1s) peak decreases in intensity, broadens and ultimately decreases to a lower binding energy. After an electron dose of $7.58 \times 10^{16}$ e$^-$/cm$^2$ the oxygen peak area is <20% of its initial value, while the binding energy has decreased by 1.5 eV. Prior to electron irradiation, the Br(3d) region (Figure 1b) is composed of a single asymmetric Br(3d$_{5/2,3/2}$) peak, with a maximum at 69.2 eV. Electron doses of $\leq 7.58 \times 10^{16}$ e$^-$/cm$^2$ are seen to have little effect on the Br(3d) peak area or position. Figure 1c shows

63

changes in the Ru(3d) and C(1s) peaks as a consequence of electron irradiation. Both of these transitions lie between 280 and 290 eV, making spectral deconvolution difficult, particularly on an a:C substrate (peak centered at 284.6 eV[36]). However, Figure 1c does show that upon [($\eta^3$-C$_3$H$_5$)Ru(CO)$_3$Br] adsorption a Ru 3d$_{5/2}$ peak appears at 282.8 eV along with a smaller peak at 288.5 eV, the latter corresponding to the C(1s) peak for an adsorbed CO species. After an electron dose of 7.58 x 10$^{16}$ e$^-$/cm$^2$, the CO peak has disappeared, and the Ru 3d$_{5/2}$ binding energy decreased to 280.9 eV.

Figure 2 presents the fractional changes in the O(1s) and Br(3d) peak areas relative to values measured prior to electron beam irradiation, as well as the Ru 3d$_{5/2}$ binding energy, each plotted as a function of electron dose. Of note, the O(1s) and Br(3d) species behave in markedly different fashion. As the precursor film is irradiated, the O(1s) peak area decreases significantly at a rate that closely correlates with the decrease in Ru 3d$_{5/2}$ binding energy. In contrast, electron irradiation has minimal effect on the Br(3d) area.
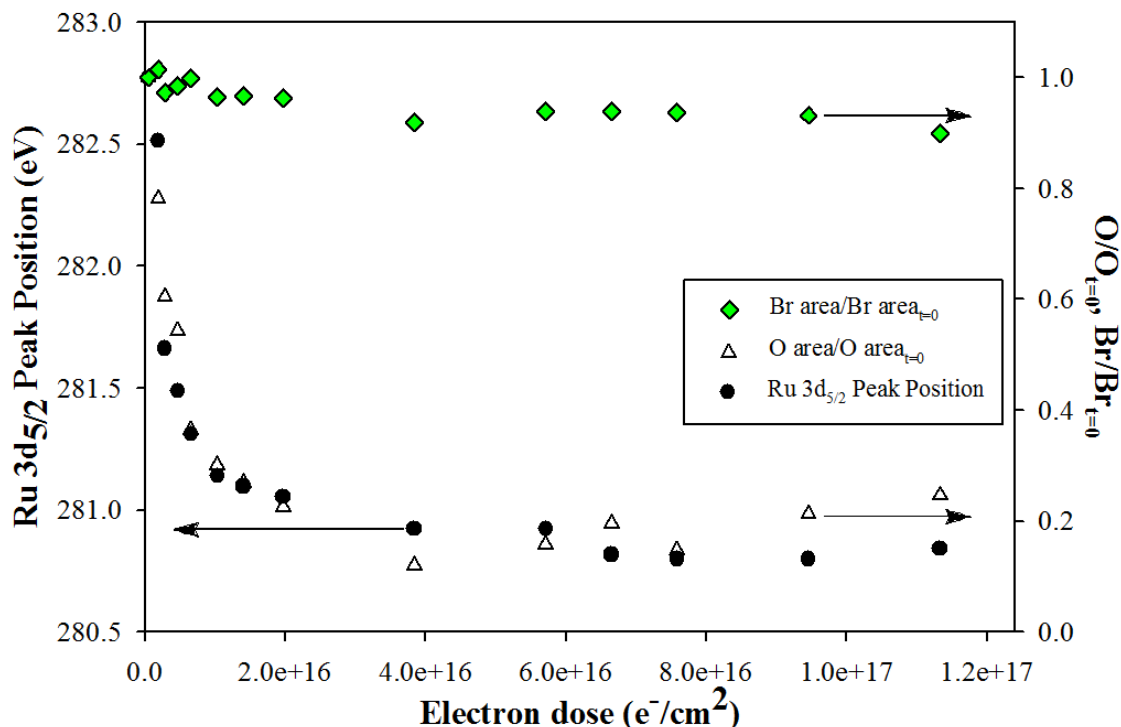
**Figure 3.2**: Changes in the fractional coverage (right-hand axis) of oxygen (open triangles) and bromine (filled diamonds) and (left-hand axis) Ru $3d_{5/2}$ peak position (filled circles) for 1–2 nm $[(\eta^3\text{-}C_3H_5)Ru(CO)_3Br]$ films; each is plotted as a function of electron dose (electron doses $< 1.2 \times 10^{17}$ e$^-$/cm$^2$), all determined by XPS.

Figure 1c shows how the presence of a dominant a:C substrate peak at 284.6 eV prevented a detailed analysis of the effect of electron irradiation on the Ru(3d) and C(1s) binding energies and signal intensities for $[(\eta^3\text{-}C_3H_5)Ru(CO)_3Br]$ molecules. To circumvent this issue, we performed analogous experiments on an Au substrate (Figure 3). These experiments revealed that, along with the precursor, a small amount of unwanted hydrocarbon adsorption was observed. This was overcome by simply heating the precursor to 40 °C to increase the partial pressure of $[(\eta^3\text{-}C_3H_5)Ru(CO)_3Br]$ (Figure S1). Prior to electron irradiation, the Ru(3d)/C(1s) spectral envelope can be fit with four peaks: a peak

65

centered at 288.8 eV, corresponding to the CO species, a peak centered at 285.1 eV, corresponding to an adsorbed allyl ($\eta^3$-C$_3$H$_5$) species, and peaks at 286.8 eV and 282.8 eV, corresponding to the Ru 3d$_{3/2}$ and 3d$_{5/2}$ transitions, respectively.[36] Area analysis reveals that the CO and $\eta^3$-C$_3$H$_5$ peak areas prior to electron irradiation are roughly equal in intensity, consistent with the chemical composition of the precursor. Further evidence for the adsorption of molecularly intact [($\eta^3$-

**Figure 3.3**: Evolution of the Ru(3d)/C(1s) XP region for a 1.4 nm-thick film of [($\eta^3$-C$_3$H$_5$)Ru(CO)$_3$Br] exposed to an electron dose of 1.13 x 10$^{17}$ e$^-$/cm$^2$. The film was adsorbed onto a Au substrate at -168 °C.

C$_3$H$_5$)Ru(CO)$_3$Br] comes from the measured O:Br stoichiometry, which can be determined with reasonable accuracy by XPS (see Figure 1). Thus, analysis of the film shown in Figure 1 prior to electron exposure reveals an O:Br ratio of 3.5:1, which is within experimental error of the 3:1 molecular stoichiometry. The lack of molecular decomposition upon adsorption at -168 °C is consistent with the presence of two C(1s) peaks of approximately equal intensity as well as the single O(1s) peak and well defined Br(3d$_{5/2}$/3d$_{3/2}$) doublet (see Figure 1). After an electron dose of 1.13 x 10$^{17}$ e$^-$/cm$^2$, Figure 3 shows that the CO peak has all but disappeared, while the peak at 285.1 eV persists and possibly increases slightly in intensity. A more quantitative analysis of Figure 3 is not possible or merited,

however, due to the difficulty in obtaining an unambiguous spectral fit in the presence of the overlapping, larger, and asymmetric Ru peaks. Analysis of the Ru $3d_{5/2}$ peak, which is sufficiently well separated from other overlapping Ru and C peaks, indicates that it decreases in binding energy by ~1.7 eV as a result of electron irradiation, which is qualitatively consistent with the observations in Figure 1c.

Figure 4 illustrates that, although comparatively small electron doses ($<1.13 \times 10^{17}$ $e^-/cm^2$; see Figures 1 and 2) caused minimal loss of Br, significantly larger (~2 orders of magnitude) electron doses actually caused the majority of the Br species to desorb. Because of the irradiation time necessary to achieve these larger electron doses (over 50 hours), they were conducted at room temperature after [($\eta^3$-$C_3H_5$)Ru(CO)$_3$Br] films had initially been exposed to an electron dose of $1.13 \times 10^{17}$ $e^-/cm^2$ at -168 °C, a dose sufficient to decompose all of the parent molecules (see Discussion). When the temperature of these electron-irradiated films increased from -168 °C to room temperature, there were no changes in each film's chemical composition or binding energies of the various elements, indicating that the film created by electron irradiation of adsorbed [($\eta^3$-$C_3H_5$)Ru(CO)$_3$Br] molecules remained stable and chemically unaltered. Figure 4a shows evolution of the Br(3d) XPS region of the film. For comparatively small electron doses ($\leq 1.13 \times 10^{17}$ $e^-$/cm$^2$), the Br(3d) region contains an asymmetric peak centered at 69.2 eV which decreases in intensity and broadens slightly as the electron dose increases, although the binding energy remains unchanged. After an electron dose of $1.24 \times 10^{19}$ $e^-/cm^2$, the Br peak area has been reduced to ~20% of its initial value. These larger electron doses also caused a systematic decrease in the Ru $3d_{5/2}$ binding energy correlated to the decrease in the Br(3d) peak area (Figure 4b). The effect of larger electron doses was, however, restricted to the

loss of Br and the shift in Ru binding energy; there were no significant changes in the O(1s), C(1s) or Ru (3d) intensities.
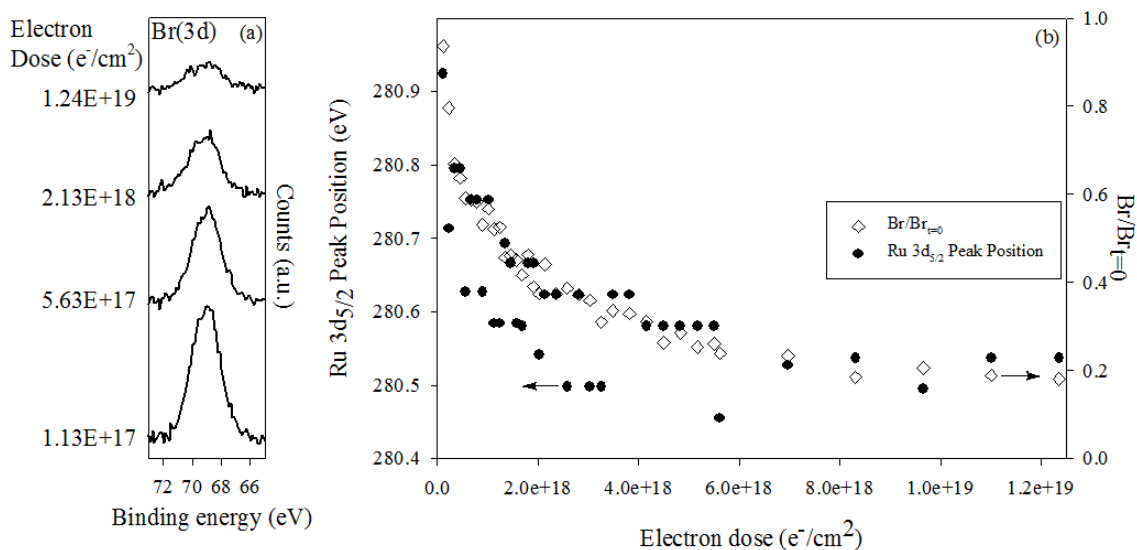


**Figure 3.4**: (a) Br(3d) XP region for a ~2 nm $[(\eta^3\text{-}C_3H_5)Ru(CO)_3Br]$ film exposed to electron doses ranging from $1.13 \times 10^{17}$ to $1.24 \times 10^{19}$ $e^-/cm^2$, and (b) changes in the fractional coverage of adsorbed bromine atoms (open diamonds) and the Ru $3d_{5/2}$ peak position (filled circles) for this film, plotted as function of electron dose.

Figure 5 shows a comparison of mass spectra of the neutral gas phase species produced when (a) *gas phase* $[(\eta^3\text{-}C_3H_5)Ru(CO)_3Br]$ molecules were exposed to 70 eV electrons, and (b) *adsorbed* $[(\eta^3\text{-}C_3H_5)Ru(CO)_3Br]$ molecules were irradiated by 500 eV electrons. In Figure 5a, fragmentation of gas phase $[(\eta^3\text{-}C_3H_5)Ru(CO)_3Br]$ molecules results in significant peaks for CO ($m/z = 28$), O ($m/z = 16$), C ($m/z = 12$), $C_3H_n$ ($n = 0 - 5$, $m/z = 36 - 41$), $C_2H_n$ ($n = 0 - 3$, $m/z = 24 - 27$), and $CH_n$ ($n = 0 - 3$, $m/z = 12 - 15$) with smaller contributions from Br ($m/z = 79, 81$), and $H_2O$ ($m/z = 18$, background species in the UHV chamber). In contrast to Figure 5a, Figure 5b is a much simpler mass spectrum

with the presence of significant peaks for C ($m/z$ = 12), O ($m/z$ = 16), and CO ($m/z$ = 28) with a minor peak corresponding to $CH_2$ ($m/z$ = 14). Notably absent in Figure 5b are significant contributions from the $C_3H_n$ and $C_2H_n$ species observed in Figure 5a, associated with the $\eta^3$-allyl group.
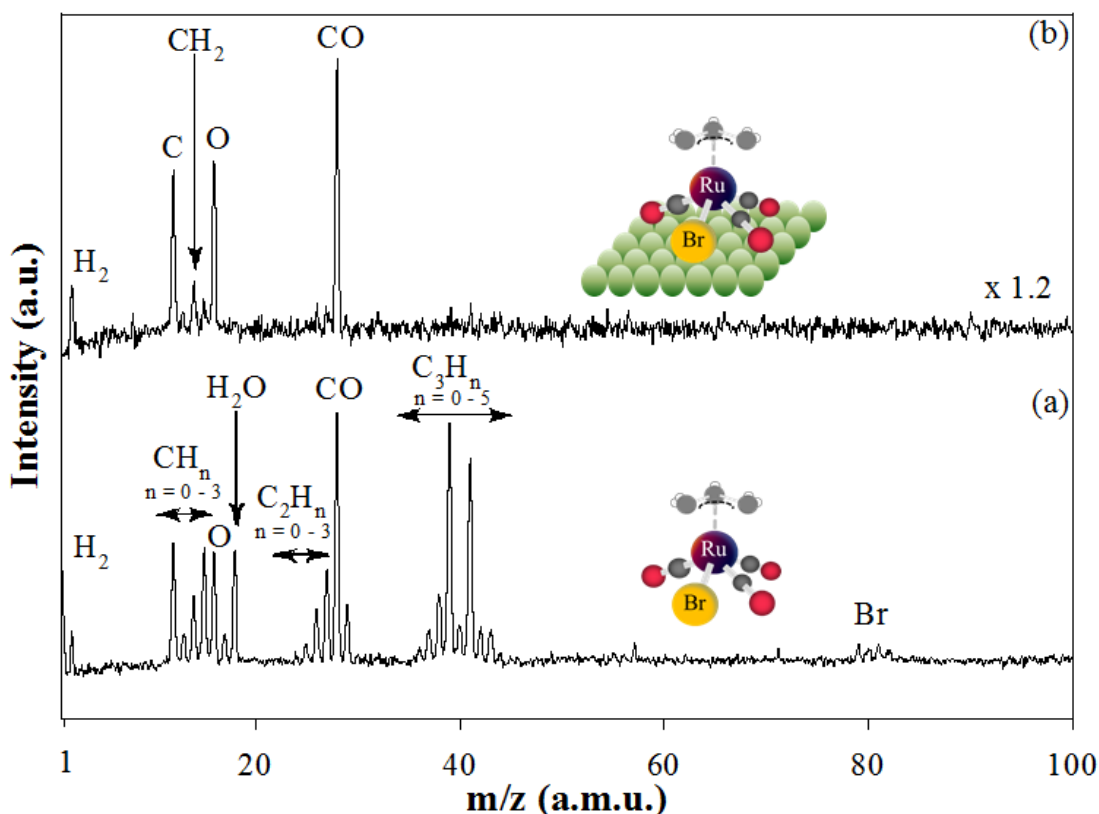


**Figure 3.5**: Mass spectrum (0-100 amu) of (a) gas phase $[(\eta^3\text{-}C_3H_5)Ru(CO)_3Br]$ measured at $P_{[(\eta3\text{-}C_3H_5)Ru(CO)_3Br]}$ ~1.5x10$^{-8}$ Torr, and (b) the volatile neutral species produced when a ~1.3 nm film of $[(\eta^3\text{-}C_3H_5)Ru(CO)_3Br]$, adsorbed onto a gold substrate at -168 °C was irradiated by an electron dose of 1.13 x 10$^{17}$ e$^-$/cm$^2$ (incident energy of 500 eV); the spectrum in (b) represents an average of MS taken every 20 s during the electron exposure. Spectrum (b) was normalized to the CO peak ($m/z$ = 28).

Figure 6 shows how the rate of gas phase CO evolution measured by MS (open circles) and fractional coverage of the surface-bound oxygen species measured by XPS (filled triangles) change as a function of electron dose. The rate of CO evolution and corresponding change in the coverage of adsorbed oxygen atoms both decrease with increasing electron dose and follow a similar kinetic profile, decreasing to ~12% of their initial values after an electron dose of $3.74 \times 10^{16}$ e$^-$/cm$^2$.
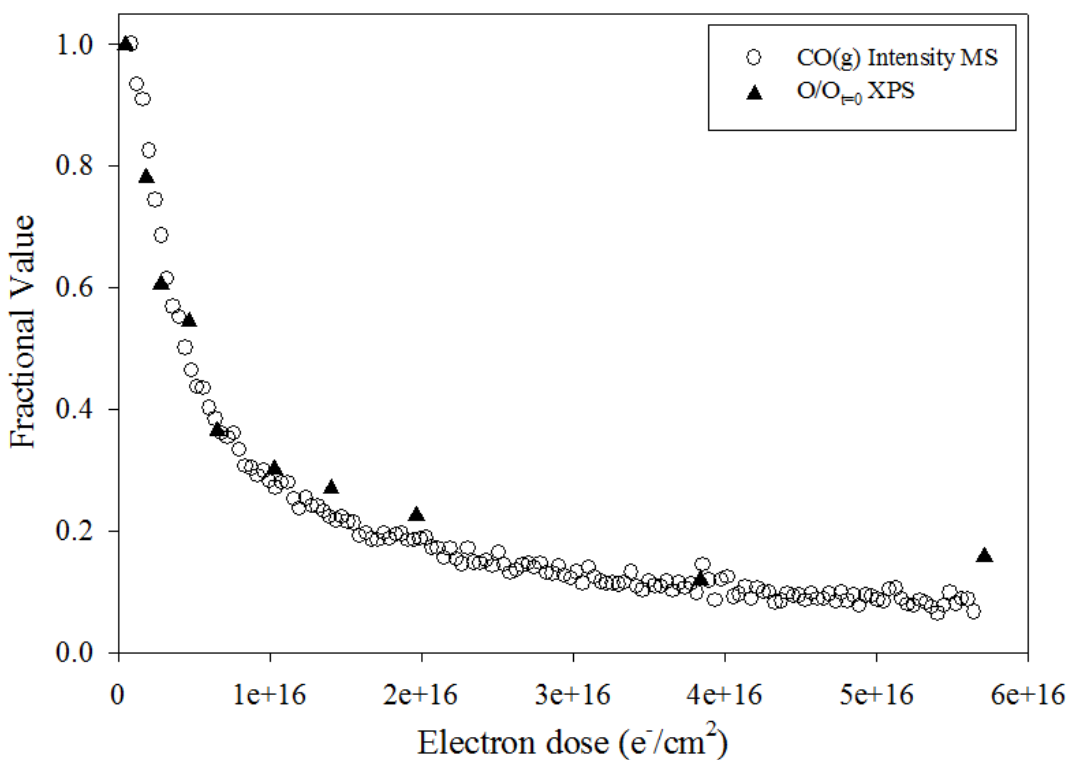


**Figure 3.6**: (Open circles) Kinetics of gas phase CO (*m/z* = 28 amu) evolution from a $[(\eta^3\text{-}C_3H_5)Ru(CO)_3Br]$ film and (filled triangles) change in the fractional coverage of surface bound oxygen species (O/O$_{t=0}$). The fractional oxygen coverage was obtained by dividing the oxygen area by the initial oxygen area obtained by XPS.

Figure 7 provides data from a few selected experiments conducted with the chloride analogue, $\eta^3$-allyl ruthenium tricarbonyl chloride [($\eta^3$-C$_3$H$_5$)Ru(CO)$_3$Cl]. Panels a and b in Figure 7 show the evolution of the O(1s) and Cl(2p) XPS regions, respectively, and Figure 7c displays changes in the O(1s) and Cl(2p) areas and in the Ru 3d$_{5/2}$ binding energy, all plotted as a function of comparatively small electron doses ($\leq$ 7.58 x 10$^{16}$ e$^-$/cm$^2$). Figure 7a shows that the evolution of the O(1s) XPS region is similar to that observed for [($\eta^3$-C$_3$H$_5$)Ru(CO)$_3$Br] with a significant decrease in intensity and downshift in binding energy (compare Figure 7a with Figure 1). Similarly, the lack of change in the Cl(2p) region (<10% decrease after an electron dose of 7.58 x 10$^{16}$ e$^-$/cm$^2$) is similar to the behavior of the Br(3d) region for [($\eta^3$-C$_3$H$_5$)Ru(CO)$_3$Br]. Figure 7c demonstrates that, like Figure 2, the loss of oxygen from the film is also correlated with a decrease in the Ru 3d$_{5/2}$ binding energy (Ru spectral data not shown). Thus, for both adsorbed [($\eta^3$-C$_3$H$_5$)Ru(CO)$_3$Cl] and [($\eta^3$-C$_3$H$_5$)Ru(CO)$_3$Br] films an electron dose on the order of 1.0 x 10$^{17}$ e$^-$/cm$^2$ results in a loss of >80% of the oxygen atoms, and a decrease in the Ru 3d$_{5/2}$ binding energy of ~1.7 eV with little or no change in the concentration of adsorbed halogen atoms.
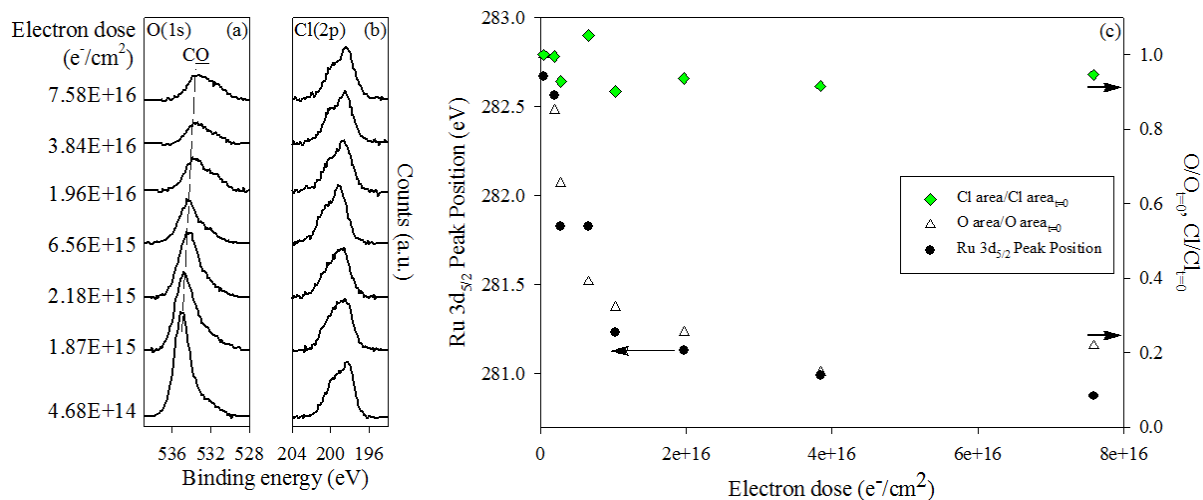
**Figure 3.7**: Evolution of the (a) O(1s) and (b) Cl(2p) XP regions for 1 – 2 nm thick films of $[(\eta^3\text{-}C_3H_5)Ru(CO)_3Cl]$ exposed to similar electron doses as seen for $[(\eta^3\text{-}C_3H_5)Ru(CO)_3Br]$ in Figure 1; (c) Changes in the fractional coverage of adsorbed oxygen and chlorine atoms and changes in Ru $3d_{5/2}$ binding energy for 1 – 2 nm $[(\eta^3\text{-}C_3H_5)Ru(CO)_3Cl]$ films plotted as a function of electron doses similar to those shown for $[(\eta^3\text{-}C_3H_5)Ru(CO)_3Br]$ in Figure 2. Films were adsorbed onto a:C at -168 °C, and spectra were normalized to account for slight differences in film thickness.

Figure 8 shows Auger electron spectra (AES) for EBID deposits created on an Ag substrate under steady state deposition conditions. Figure 8a shows the AES of: (1) a deposit created from $[(\eta^3\text{-}C_3H_5)Ru(CO)_3Br]$ and, (2) the deposit subjected to post-deposition electron irradiation (i.e., post-deposition electron beam processing in the absence of any precursor molecules). Figure 8b shows analogous AES data for a deposition created from the Cl analogue, $[(\eta^3\text{-}C_3H_5)Ru(CO)_3Cl]$. The AES data contained in Figures 8a(1) and b(1) shows that the deposits are characterized by contributions from Ru (273, 231, 200, 184, 176, 150 eV), C (272, 271 eV), and Br (108 eV) or Cl (181 eV), with

72

essentially no contribution from O (503 eV). Thus, a comparison of Figures 1 and 8(a) shows that the chemical composition of the electron deposited films are similar with Ru, Br, and C but little or no evidence of O. A more quantitative analysis of the elemental composition of the deposits created in the AES was precluded, however, by the overlap between the principal Ru and C AES peaks at ~273 eV. Panels a(2) and b(2) in Figure 8 demonstrate that post-deposition electron beam processing produced a decrease in the concentration of adsorbed halogen atoms. This effect is more obvious for the $[(\eta^3-C_3H_5)Ru(CO)_3Cl]$ deposit due to the larger Cl peak present after deposition (Figure 8b(1)).
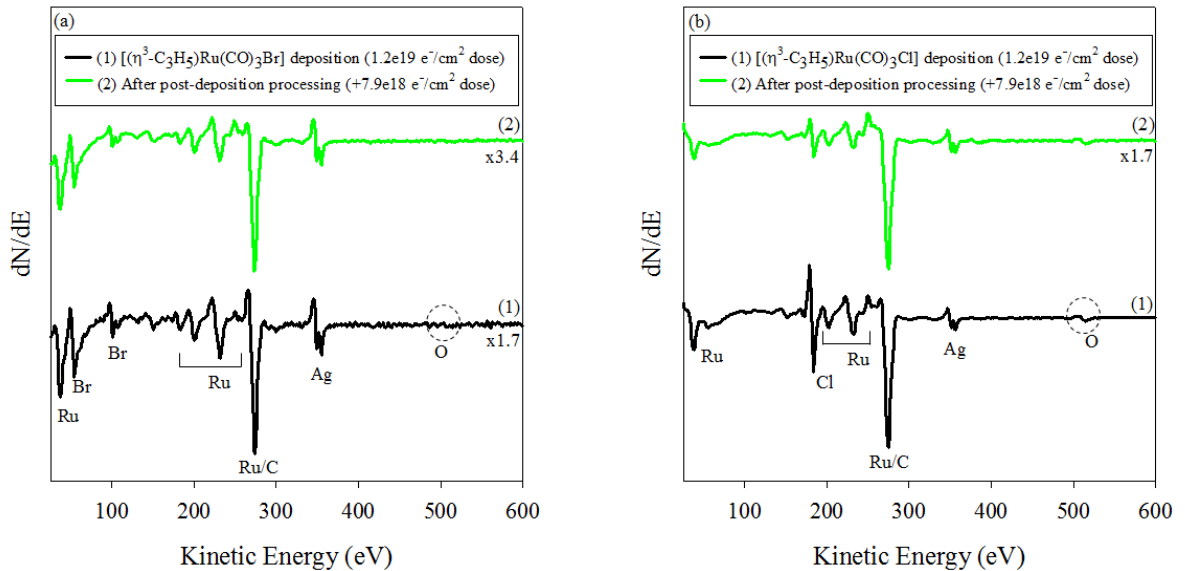


**Figure 3.8**: Auger electron spectra of EBID films created on an Ag substrate from (a) $[\eta^3-C_3H_5Ru(CO)_3Br]$, and (b) $[\eta^3-C_3H_5Ru(CO)_3Cl]$. In each case, the compound was deposited ((1), black line) and then subjected to further electron irradiation ((2), green line). Deposition conditions were $P_{[\eta3-C_3H_5Ru(CO)_3Br/Cl]}$ ~$5\times10^{-7}$ Torr, incident beam energy = 3 keV, substrate current ~ 700 nA for a total electron dose of (a) (1) $1.18 \times 10^{19}$ $e^-/cm^2$, (2) $2.06 \times 10^{19}$ $e^-/cm^2$, and (b) (1) $1.18 \times 10^{19}$ $e^-/cm^2$ and (2) $2.06 \times 10^{19}$ $e^-/cm^2$. All AES were normalized to the Ru/C peak.

3.4. Discussion

XPS and MS data provided complementary information on the effect that electron exposure had on nanometer thick films of $[(\eta^3$-$C_3H_5)Ru(CO)_3Br]$ and $[(\eta^3$-$C_3H_5)Ru(CO)_3Cl]$. This allowed for the correlation of changes in the chemical composition, bonding within the adsorbates, and the nature of the gas phase species. Experiments conducted in the AES instrument enabled data obtained on the chemical composition and effect of post-deposition electron beam processing to be compared between films created under low temperature, UHV conditions, and under steady state deposition conditions.

In summary, our XPS and MS data reveal that the surface reactions of adsorbed $[(\eta^3$-$C_3H_5)Ru(CO)_3Br]$ proceed in two stages. The initial step involves electron-stimulated precursor decomposition accompanied by the evolution of CO into the gas phase. However, under the influence of more prolonged electron beam irradiation, the film that forms as a result of $[(\eta^3$-$C_3H_5)Ru(CO)_3Br]$ decomposition loses Br atoms (step 2). This is the first example of an organometallic precursor we have studied where any ligand desorption has occurred after precursor decomposition. On the basis of previous studies and the similarity in the reactions induced by the 500eV electrons and by X-ray irradiation (compare Figure 1 and Figures S3 and S4 in the Supporting Information) we believe that the reactions we observe are initiated by low energy secondary electrons (energies <100 eV) generated by interactions of the primary beam with the substrate, reacting with the adsorbed species. The overall effect of electron irradiation on $[(\eta^3$-$C_3H_5)Ru(CO)_3Br]$ is shown in Figure 9.
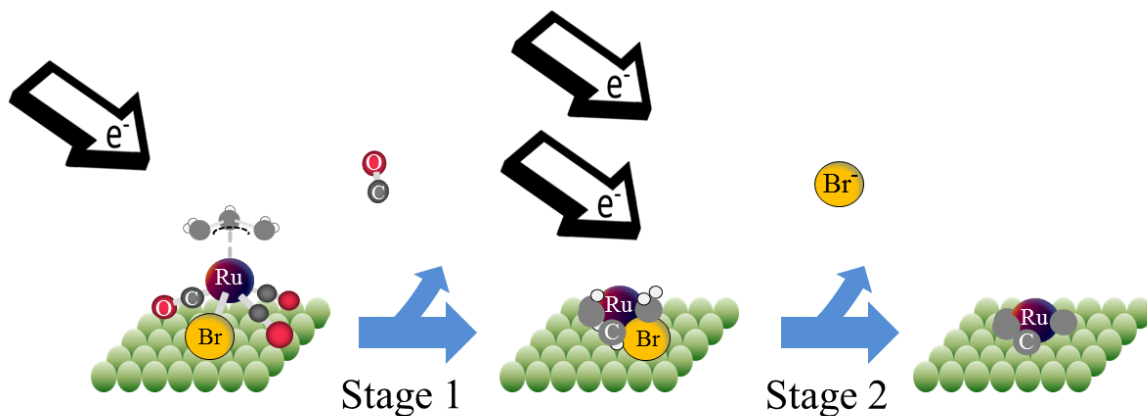
**Figure 3.9**: Reaction Scheme: (Stage 1) Electron Stimulated CO Desorption and ($\eta^3$-C$_3$H$_5$) Decomposition from [($\eta^3$-C$_3$H$_5$)Ru(CO)$_3$Br]; (Stage 2) Electron stimulated desorption of halogens from the residual product from Stage 1.

3.4.1.   Reaction Stage 1

The initial stage of the reaction is complete after an electron dose of ~1.13 x $10^{17}$ e$^-$/cm$^2$ (see Figure 2).  Experimentally, the decomposition of the [($\eta^3$-C$_3$H$_5$)Ru(CO)$_3$Br] precursor is most clearly evidenced by the decrease in binding energy of the Ru 3d$_{5/2}$ peak from 282.8 eV to 280.9 eV as the Ru atoms are reduced from their initial +2 oxidation state.  Analysis of Figures 5 and 6 indicates that it is also during this initial electron dose of ~1.13 x $10^{17}$ e$^-$/cm$^2$ that CO is evolved into the gas phase.  Consistent with these observations the CO peak, initially observed by XPS at ~288.5 eV (Figures 1 and 3) upon [($\eta^3$-C$_3$H$_5$)Ru(CO)$_3$Br] deposition, disappears for electron doses in excess of $\approx$ 1.13 x $10^{17}$ e$^-$/cm$^2$. The ejection of CO into the gas phase is also responsible for the significant (>80%)

decrease in the O(1s) signal intensity (see Figure 1), which is observed to follow the same dependence on electron dose as the rate of CO ejection (Figure 6) and the decrease in Ru $3d_{5/2}$ binding energy (Figure 2). It is possible that some of the oxygen loss occurs as a result of CO ligand decomposition and the ejection of a reactive oxygen species such as O, $O^-$ or $O^+$ ($CO_{(ads)} \rightarrow C_{(ads)} + ROS_{(g)}\uparrow$); this cannot be ruled out due to the inability to perform a quantitative analysis of the change in carbon atom concentration (resulting from the overlap with the Ru 3d peak as shown in Figure 3). However, on the basis of the correlation between the rate of CO evolved into the gas phase and the loss of oxygen from the adsorbate layer (Figure 6), we conclude that on average at least one of the original CO ligands is ejected as the molecular precursor decomposes. The loss of one or more CO ligands as a result of electron-stimulated reactions of surface-bound organometallics has been observed in related studies of other EBID precursors, notably $W(CO)_6$[32] and $Co(CO)_3(NO)$.[31]

In sharp contrast to the loss of CO, there is virtually no change in the Br(3d) signal intensity or binding energy (Figures 1 and 2) nor any evidence of Br desorption (Figure 5) as the precursor decomposes in Stage 1. The lack of any measureable change in the Br binding energy suggests that the Ru-Br bond remains intact. Regarding the $\eta^3$-allyl ($\eta^3$-$C_3H_5$) species, the mass spectrum shows no evidence of $C_3H_n$ fragments being ejected during electron irradiation of surface-bound $[(\eta^3\text{-}C_3H_5)Ru(CO)_3Br]$, although these fragments are prominent in the mass spectrum of gas phase $[(\eta^3\text{-}C_3H_5)Ru(CO)_3Br]$ (Figure 5). Although quantitative analysis of the C(1s) peak associated with the $\eta^3$-allyl ($\eta^3$-$C_3H_5$) species is complicated by overlap with the larger Ru(3d) peaks (Figure 3), by conducting experiments on Au rather than a:C substrates, we can see that a residual C(1s) signal, with

a binding energy consistent with CC/CH species remains after electron irradiation. Moreover, the area of this peak is comparable to that ascribed to the three carbon atoms present in the $\eta^3$-allyl ($\eta^3$-C$_3$H$_5$) ligand observed upon initial deposition (Figure 3). Thus, collectively the MS and XPS data suggest that the carbon atoms in the $\eta^3$-allyl ($\eta^3$-C$_3$H$_5$) ligand do not desorb as the precursor decomposes. This assertion is also consistent with the fate of other polyhapto unsaturated hydrocarbon ligands during electron irradiation of organometallic precursors, specifically $\eta^5$-cyclopentadienyl ligands ($\eta^5$-C$_5$H$_5$), where all of the carbon atoms became trapped in the deposit.[28] Analysis of the Ru(3p) peak area (data not shown) indicates that electron irradiation does not cause any electron stimulated desorption of the parent molecule.

Thus, the initial effect of electron irradiation is to decompose adsorbed [($\eta^3$-C$_3$H$_5$)Ru(CO)$_3$Br] molecules, causing ejection of at least one of the parent CO ligands while the Br atoms and the C atoms in the $\eta^3$-allyl ($\eta^3$-C$_3$H$_5$) ligand are retained, although the $\eta^3$-allyl ($\eta^3$-C$_3$H$_5$) ligand itself most likely decomposes. We believe that the inability of the polyhapto unsaturated hydrocarbon ligands, such as $\eta^3$-C$_3$H$_5$ ($\eta^3$-allyl) and $\eta^5$-C$_5$H$_5$ ligands to desorb during EBID is at least in part a consequence of their multidentate bonding to the central metal atom. Removal of an $\eta^5$-C$_5$H$_5$ ligand under standard solution conditions has been demonstrated to involve conversion first to an $\eta^3$-C$_5$H$_5$ ligand and then to a $\kappa^1$-C$_5$H$_5$ ligand before dissociation from the metal center.[37] As a result, multiple metal-ligand bonds must be broken, and the highly unsaturated and reactive fragments created must desorb from the surface before undergoing any secondary reactions. The chemical transformations described in Stage 1, displayed pictorially in Scheme 1, cause the central metal atom to become reduced. The binding energy of the Ru atoms at the end of stage 1

77

(~280.9 eV) is intermediate between their initial (+2) oxidation state (~282.8 eV) in the

$[(\eta^3\text{-}C_3H_5)Ru(CO)_3Br]$ precursor and metallic Ru (279.9 ± 0.2 eV)[38-40] due to retention of

the Ru-Br bond and encasement of Ru atoms in the carbonaceous matrix that is probably

formed as the $\eta^3$-allyl ligand decomposes.  Assuming that decomposition is initiated by a

one electron process, a kinetic analysis based on the rate of decrease in the O(1s) signal as

a function of electron dose (Figure 2) yields a total reaction cross-section for $[(\eta^3\text{-}$

$C_3H_5)Ru(CO)_3Br]$ decomposition ($\sigma_{[(C_3H_5Ru(CO)_3Br)]} \approx 5$ x $10^{-17}$ cm$^2$) with the 500 eV

incident electrons used in this study, comparable to total reaction cross-sections that have

been calculated for other EBID precursors.[23,24,28]  The similarity in the results observed for

$[(\eta^3\text{-}C_3H_5)Ru(CO)_3Cl]$ (compare Figures 1, 2 and 7) strongly supports the idea that the

elementary reaction steps induced by electron irradiation are independent of the halogen

atom's identity.

### 3.4.2.  Reaction Stage 2

The second stage of the reaction (see Figure 9) is characterized by a loss of Br

atoms from the film (shown in Figure 4), postulated to be a result of an electron-stimulated

desorption (ESD) type process[41-43] that can be written in its most general form as:

$$Ru\text{-}Br_{(ads)} + e^- \rightarrow Ru_{(ads)} + Br^-_{(g)}\uparrow$$
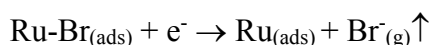
The cleavage of Ru-Br bonds, and the loss of bromine atoms from the film, is responsible

for the closely correlated and systematic decrease in the Ru $3d_{5/2}$ peak position, shown in

Figure 4.  In contrast to the electron-stimulated decomposition  of the parent molecule

(stage 1), which is complete within an electron dose of ~1.13 x $10^{17}$ e$^-$/cm$^2$,  the loss of

measureable (>10%) amounts of Br requires electron doses of >5 x $10^{17}$ e$^-$/cm$^2$, indicating a slower and less efficient process. Indeed, the small (<10%) loss of Br atoms observed in Figure 2 for electron doses <1.13 x $10^{17}$ e$^-$/cm$^2$ represents the beginning of the ESD process, which in reality begins as soon as the precursor has undergone decomposition, although its importance only becomes truly apparent for the much larger electron doses (> 1.13 x $10^{17}$ e$^-$/cm$^2$) shown in Figure 4. Aside from the loss of Br and its effect on the binding energy of the Ru atoms, no other chemical transformations occur during this second stage of the reaction. Figure 6 shows that there is no CO evolution, and there are also no significant changes to the oxygen or carbon concentrations as measured by XPS (data not shown). The overall effect of electron irradiation is shown in Scheme 1.

### 3.4.3. Comparisons to related studies

Previous studies on the electron-stimulated reactions of surface bound organometallics have identified two sequential steps that occur as a function of increasing electron dose: precursor decomposition accompanied by ligand desorption followed by electron-induced decomposition of residual ligands. In the present study, the first step is also characterized by decomposition of the parent [($\eta^3$-C$_3$H$_5$)Ru(CO)$_3$Br] compound accompanied by CO (ligand) desorption. Moreover, a comparison between the reactions of [($\eta^3$-C$_3$H$_5$)Ru(CO)$_3$Br] and Co(CO)$_3$(NO)[31] reveals that, for both molecules, decomposition of the parent leads exclusively to the ejection of CO groups, which appears to be a "preferred leaving group" in these electron stimulated reactions. In the present study, there is also no evidence of significant Br loss during precursor decomposition, consistent with recent gas phase studies on the interactions of low energy (< 100 eV)

electrons with $[(\eta^3\text{-}C_3H_5)Ru(CO)_3Br](g)$.[44] This lack of Ru-Br bond cleavage during the electron stimulated decomposition of $[(\eta^3\text{-}C_3H_5)Ru(CO)_3Br]$ is perhaps somewhat surprising given the high electron affinity of halide ions.

The most notable and significant difference between the electron stimulated reactions of adsorbed $[(\eta^3\text{-}C_3H_5)Ru(CO)_3Br]$ molecules and other organometallic precursors studied to date occurs in the second stage of the reaction (step 2), which has been previously characterized exclusively by ligand decomposition. For example, in the case of $W(CO)_6$,[32] electron-stimulated reactions of the partially decarbonylated species $(W_x(CO)_y)$ left behind after ejection of multiple CO ligands in the initial step, leads to CO decomposition as follows:

$$W_x(CO)_{y\,(ads)} + e^- \rightarrow yC_{ads} + W_xO_{y\,(ads)}$$
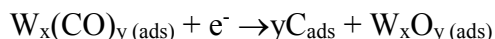
It is this second step which we believe is responsible for most of the unwanted organic contamination prevalent in many EBID deposits created from organometallic precursors. In contrast, the second stage in the electron-stimulated reactions of adsorbed $[(\eta^3\text{-}C_3H_5)Ru(CO)_3Br]$ molecules is characterized not by ligand decomposition but by Br atom desorption; after a total electron dose of $>1.13 \times 10^{19}$ e$^-$/cm$^2$, ~80% of the Br atoms have been removed from the film (Figure 4). Thus, although the halogen atoms are not removed initially as the $[(\eta^3\text{-}C_3H_5)Ru(CO)_3Br]$ molecules undergo electron-stimulated decomposition, they can be removed from the resulting film that forms via a slower electron-stimulated desorption (ESD) process.

3.4.4. Relevance to Electron Beam Induced Deposition Experiments

The UHV surface science studies discussed in Figures 1 – 7 pertain to the electron-stimulated reactions experienced by thin films of precursor molecules adsorbed at low temperatures (<150 K). In contrast, the films created in the Auger electron spectrometer (Figure 8) are generated under steady state deposition conditions, much more representative of those used in typical EBID experiments, where a sample at room temperature is continuously irradiated by an electron beam in the presence of a constant partial pressure of precursor molecules.[1-4] Consequently, the AES data in Figure 8 can be used to gauge the extent to which data from the UHV surface science studies can inform and provide insights on the chemical composition of EBID structures. A comparison of Figures 1 and 8 reveals that the chemical composition of the films created by electron irradiation under UHV conditions (Figure 1) and in the AES (Figure 8) are similar with evidence of Ru, Br and C but little or no evidence of O in the deposits. Moreover, post-deposition electron irradiation of the deposits created in the AES decreases the halogen atom concentration in accordance with the data shown in Figure 4. These similarities support the idea that the same sequence of fundamental bond breaking processes identified in the low temperature UHV studies is also operative during EBID. The electron flux in the AES experiments is greater than the highest electron fluxes used in the UHV surface science studies, so at first glance it appears surprising that there are any residual halogen atoms in the deposits. However, under the steady state deposition conditions that characterize the AES experiments, electron beam processing of the deposits, which would lead to removal of halogen atoms via an ESD process, must compete with electron-stimulated deposition involving reactions of constantly adsorbing precursor molecules. Under conditions where the deposition rate is greater than the rate of electron beam

processing, residual halogen atoms will not desorb but will instead become incorporated into the growing film. However, in the absence of any background partial pressure of precursor molecules, growth ceases and halogen atoms will be more susceptible to removal by post-deposition electron beam processing. This qualitatively explains the observations shown in Figure 8. Indeed, this argument also suggests that the metal concentration in EBID films created from $[(\eta^3\text{-}C_3H_5)Ru(CO)_3Br]$ will be enhanced under so called "precursor-limited" deposition conditions, where the growth rate is limited by the concentration of adsorbed precursor molecules. Under these growth conditions, the products of the initial precursor decomposition step (stage 1) will be subject to extensive post-deposition electron beam processing prior to the next deposition event. As can be seen from the UHV surface science studies, this will promote halogen desorption and thus improve the final metal concentration in the deposit.

The similarity in the electron-stimulated reactions of $[(\eta^3\text{-}C_3H_5)Ru(CO)_3Br]$ and $[(\eta^3\text{-}C_3H_5)Ru(CO)_3Cl]$ also has implications for EBID. On one hand, it is desirable to have precursors that are volatile at room temperature and therefore easier to handle. Organometallic precursors that contain metal-chlorine bonds are typically more volatile than those that contain metal-bromine bonds, due to weaker intermolecular forces and lower molecular weight.[45] This was reflected in the relative volatilities observed for $[(\eta^3\text{-}C_3H_5)Ru(CO)_3Br]$ and $[(\eta^3\text{-}C_3H_5)Ru(CO)_3Cl]$. Consequently, the similar results obtained for these two precursors suggest that the chemical identity of halogen atoms in organometallic complexes can be tuned to optimize volatility and stability during volatilization and transport, without changing the fundamental bond breaking steps involved in EBID. As pointed out recently by Mulders,[13] however, another factor that must

be considered in selecting EBID precursors is the potential for unwanted reactions of by-products formed as a result of ligand decomposition. This includes halogen atoms which can etch Si, often used as the substrate in EBID. In this respect, $[(\eta^3\text{-}C_3H_5)Ru(CO)_3Br]$ would be preferred over $[(\eta^3\text{-}C_3H_5)Ru(CO)_3Cl]$ because Br is far less efficient at etching Si or the native oxide layer typically present on Si surfaces as compared to Cl.[46,47]

Finally, it should be noted that the findings from the present study, notably the preferential ejection of CO ligands in the precursor decomposition step (stage 1), coupled with the ability of post-deposition electron beam processing to remove adsorbed halogen atoms (stage 2), may help to explain why ClAuCO has been used to deposit pure Au nanostructures using EBID via the following reaction sequence.[48]

$$ClAuCO_{(ads)} + e^- \rightarrow CO_{(g)}\uparrow + AuCl_{(ads)}$$

$$AuCl_{(ads)} + e^- \rightarrow Au_{(ads)} + Cl^-_{(g)}\uparrow$$
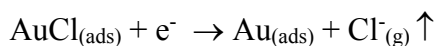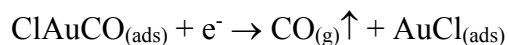
## 3.5. Conclusions

Surface bound $\eta^3$-allyl ruthenium tricarbonyl bromide $[(\eta^3\text{-}C_3H_5)Ru(CO)_3Br]$ molecules are decomposed by electron irradiation in a process that initially reduces the central metal (Ru) atoms and ejects CO ligands into the gas phase, and the carbon atoms contained within the $\eta^3$-allyl ($\eta^3$-C$_3$H$_5$) ligand are incorporated into the metal-containing deposit that forms. In the second step that occurs for significantly larger electron doses, most of the bromine atoms are removed from the deposits via an electron-stimulated desorption process, analogous to a post-deposition electron-beam processing step. The electron-stimulated reactions of the organometallic precursors appear invariant to the nature of the halogen atom. Considered collectively, results from this investigation suggest

that by using organometallic precursors that contain a small number of CO ligands and/or metal-halogen bonds, EBID could create deposits with higher metal percentages under precursor-limited deposition conditions.  This assertion is consistent with previous studies where pure Au nanostructures have been deposited by EBID from ClAuCO.[48]

## 3.6.  Acknowledgments

3.7. Supporting Information
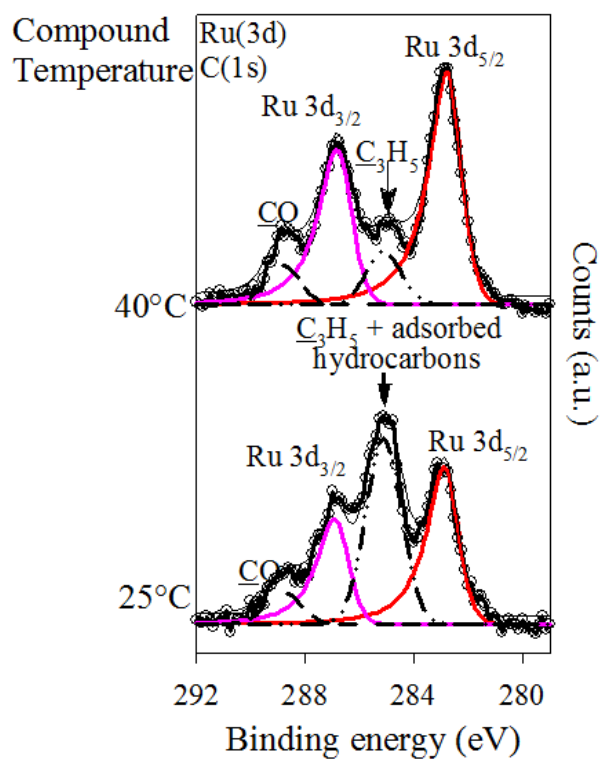


**Supporting Information, Figure 3.1**: Comparison of effect of heating $[(\eta^3-C_3H_5)Ru(CO)_3Br]$ to improve $P_{[(\eta3-C_3H_5)Ru(CO)3Br]}$; temperature to which compound was heated prior to dosing is shown on the left hand side of each spectra.

| [(η³-C₃H₅)Ru(CO)₃Br] Peak Position (cm⁻¹) | [(η³-C₃H₅)Ru(CO)₃Cl] Peak Position (cm⁻¹) | Assignment |
|---|---|---|
| 1016.15 | 1016.15 | C=C symmetric stretch |
| 1467.7 | 1461.1 | C=C antisymmetric stretch |
| 1996.4 | 1997.4 | CO stretch |
| 2011.9 | 2043.7 | CO stretch |
| 2095.8 | 2103.0 | CO stretch |
| 3020.1 | 3042.6 | sp² C-H stretch |
| 3094.2 | 3094.2 | sp² C-H stretch |
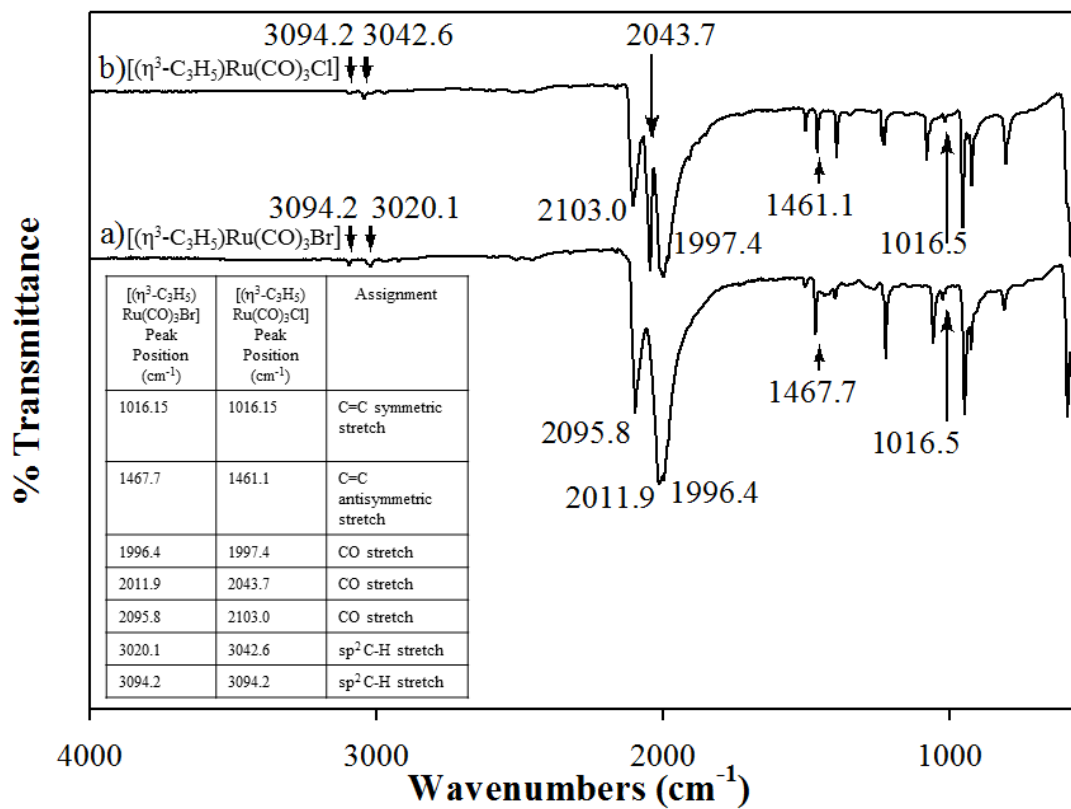
**Supporting Information, Figure 3.2**: Attenuated Total Reflectance (ATR) Infrared spectra for (a) $[(\eta^3\text{-}C_3H_5)Ru(CO)_3Br]$ (b) $[(\eta^3\text{-}C_3H_5)Ru(CO)_3Cl]$.
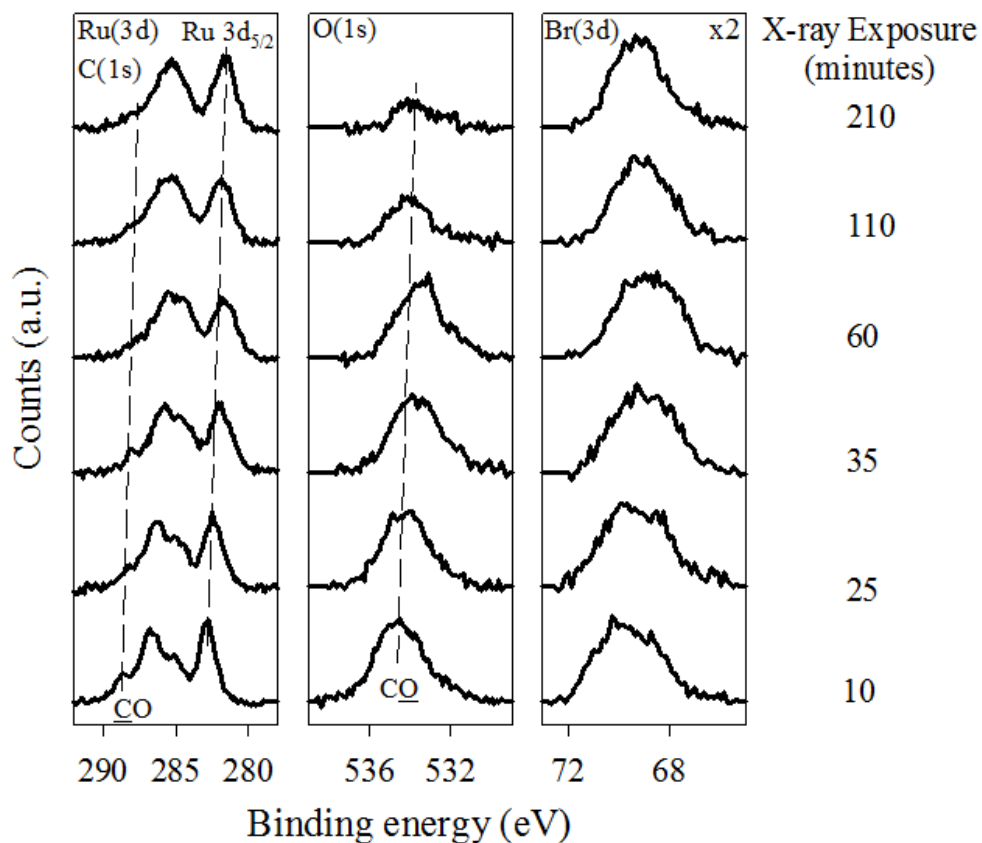
**Supporting Information, Figure 3.3**: Evolution of the Ru (3d)/C(1s), O(1s), and Br(3d) XP regions for a ~ 1.6 nm thick film of $[(\eta^3\text{-}C_3H_5)Ru(CO)_3Br]$ adsorbed on Au, irradiated with X-rays (Mg Kα 1253.6 eV); the x-ray exposure time is shown on the right hand side of each spectra.
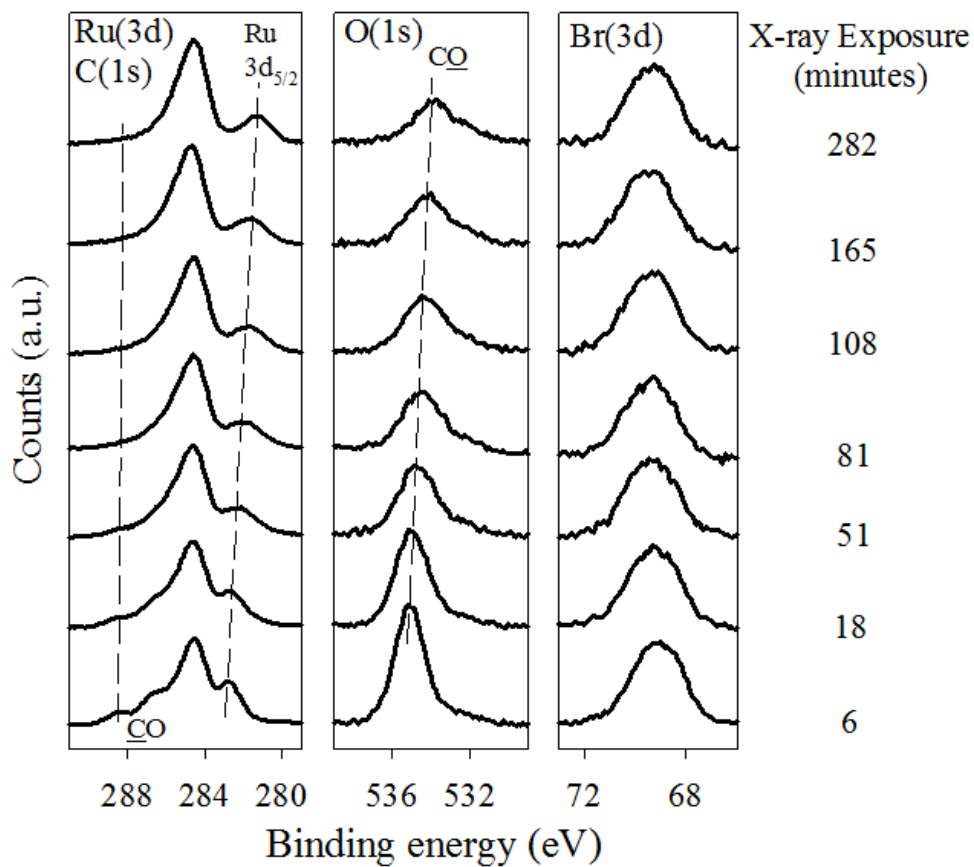
**Supporting Information, Figure 3.4**: Evolution of the Ru (3d)/C(1s), O(1s), and Br(3d) XP regions for a nanometer thick film of $[(\eta^3\text{-}C_3H_5)Ru(CO)_3Br]$ adsorbed on HOPG, irradiated with X-rays (Mg Kα 1253.6 eV); the x-ray exposure time is shown on the right hand side of each spectra.

## 3.8. References

(1)       Huth, M.; Porrati, F.; Schwalb, C.; Winhold, M.; Sachser, R.; Dukic, M.; Adams, J.; Fantner, G. *Beilstein journal of nanotechnology* **2012**, *3*, 597.

(2)       Randolph, S.; Fowlkes, J.; Rack, P. *Critical reviews in solid state and materials sciences* **2006**, *31*, 55.

(3)       Utke, I.; Hoffmann, P.; Melngailis, J. *Journal of Vacuum Science & Technology B* **2008**, *26*, 1197.

(4)       Van Dorp, W.; Hagen, C. *Journal of Applied Physics* **2008**, *104*, 081301.

(5)       van Dorp, W. *Applied Physics A* **2014**, *117*, 1615.

(6)       Van Dorp, W.; Hagen, C.; Crozier, P.; Kruit, P. *Nanotechnology* **2008**, *19*, 225305.

(7)       Edinger, K.; Becht, H.; Bihr, J.; Boegli, V.; Budach, M.; Hofmann, T.; Koops, H. W.; Kuschnerus, P.; Oster, J.; Spies, P. *Journal of Vacuum Science & Technology B* **2004**, *22*, 2902.

(8)       Heerkens, C. T. H.; Kamerbeek, M.; van Dorp, W.; Hagen, C.; Hoekstra, J. *Microelectronic Engineering* **2009**, *86*, 961.

(9)       Liang, T.; Frendberg, E.; Lieberman, B.; Stivers, A. *Journal of Vacuum Science & Technology B* **2005**, *23*, 3101.

(10)     Hübner, B.; Koops, H.; Pagnia, H.; Sotnik, N.; Urban, J.; Weber, M. *Ultramicroscopy* **1992**, *42*, 1519.

(11)     Brown, J.; Kocher, P.; Ramanujan, C. S.; Sharp, D. N.; Torimitsu, K.; Ryan, J. F. *Ultramicroscopy* **2013**, *133*, 62.

(12)     Chen, I.-C.; Chen, L.-H.; Ye, X.-R.; Daraio, C.; Jin, S.; Orme, C. A.; Quist, A.; Lal, R. *Applied physics letters* **2006**, *88*, 153102.

(13)     Mulders, J. *Nanofabrication* **2014**, *1*.

(14)     Botman, A.; Hesselberth, M.; Mulders, J. *Microelectronic Engineering* **2008**, *85*, 1139.

(15)     van Dorp, W. F.; Wu, X.; Mulders, J. J. L.; Harder, S.; Rudolf, P.; De Hosson, J. *Langmuir* **2014**, *30*, 12097.

(16)     Engmann, S.; Stano, M.; Matejc, S.; Ingolfsson, O. *Phys. Chem. Chem. Phys.* **2012**, *14*, 14611.

(17)     Engmann, S.; Stano, M.; Matejcik, S.; Ingolfsson, O. *Angew. Chem., Int. Ed.* **2011**, *50*, 9475.

(18)     Engmann, S.; Stano, M.; Papp, P.; Brunger, M. J.; Matejcik, S.; Ingolfsson, O. *J. Chem. Phys.* **2013**, *138*, 044305/1.

(19)     Wnorowski, K.; Stano, M.; Barszczewska, W.; Jówko, A.; Matejčík, Š. *Int. J. Mass Spectrom.* **2012**, *314*, 42.

(20)     Wnorowski, K.; Stano, M.; Matias, C.; Denifl, S.; Barszczewska, W.; Matejčík, Š. *Rapid Comm. Mass Spectrom.* **2012**, *26*, 1.

(21)     Bishop, J.; Lobo, C. J.; Martin, A.; Ford, M.; Phillips, M.; Toth, M. *Phys. Rev. Lett.* **2012**, *109*, 146103.

(22)     Martin, A. A.; Phillips, M. R.; Toth, M. *ACS Applied Materials & Interfaces* **2013**, *5*, 8002.

(23)     van Dorp, W. F.; Wnuk, J. D.; Gorham, J. M.; Fairbrother, D. H.; Madey, T. E.; Hagen, C. W. *Journal of Applied Physics* **2009**, *106*.

(24)     Landheer, K.; Rosenberg, S. G.; Bernau, L.; Swiderek, P.; Utke, I.; Hagen, C. W.; Fairbrother, D. H. *The Journal of Physical Chemistry C* **2011**, *115*, 17452.

(25)     Rosenberg, S. G.; Landheer, K.; Hagen, C. W.; Fairbrother, D. H. *Journal of Vacuum Science & Technology B* **2012**, *30*, 051805.

(26)     Spencer, J. A.; Rosenberg, S. G.; Barclay, M.; Wu, Y.-C.; McElwee-White, L.; Fairbrother, D. H. *Applied Physics A* **2014**, 1.

(27)     Wnuk, J.; Rosenberg, S.; Gorham, J.; Van Dorp, W.; Hagen, C.; Fairbrother, D. *Surface Science* **2011**, *605*, 257.

(28)     Wnuk, J. D.; Gorham, J. M.; Rosenberg, S. G.; van Dorp, W. F.; Madey, T. E.; Hagen, C. W.; Fairbrother, D. H. *The Journal of Physical Chemistry C* **2009**, *113*, 2487.

(29)     Hedhili, M. N.; Bredehöft, J. H.; Swiderek, P. *J. Phys. Chem. C* **2009**, *113*, 13282.

(30)     Warneke, J.; Van Dorp, W.; Rudolf, P.; Stano, M.; Papp, P.; Matejcik, S.; Borrmann, T.; Swiderek, P. *Physical Chemistry Chemical Physics* **2015**, *17*, 1204.

(31)     Rosenberg, S. G.; Barclay, M.; Fairbrother, D. H. *The Journal of Physical Chemistry C* **2013**, *117*, 16053.

(32)     Rosenberg, S. G.; Barclay, M.; Fairbrother, D. H. *Physical Chemistry Chemical Physics* **2013**, *15*, 4002.

(33)     Rosenberg, S. G.; Barclay, M.; Fairbrother, D. H. *ACS applied materials & interfaces* **2014**.

(34)     Wnuk, J. D.; Gorham, J. M.; Rosenberg, S. G.; van Dorp, W. F.; Madey, T. E.; Hagen, C. W.; Fairbrother, D. H. *Journal of Applied Physics* **2010**, *107*, 054301.

(35)     Sbrana, G.; Braca, G.; Piacenti, F.; Pino, P. *Journal of Organometallic Chemistry* **1968**, *13*, 240.

(36)     John F. Moulder, W. F. S., Peter E. Sobol, Kenneth D. Bomben *Handbook of X-ray Photoelectron Spectroscopy*; Physical Electronics USA, Inc.: Chanhassen, Minnesota, USA, 1995.

(37)     Casey, C. P.; O'Connor, J. M.; Haller, K. J. *J. Am. Chem. Soc.* **1985**, *107*, 1241.

(38)     Fuggle, J. C.; Madey, T. E.; Steinkilberg, M.; Menzel, D. *Surface Science* **1975**, *52*, 521.

(39)     Kim, K. S.; Winograd, N. *Journal of Catalysis* **1974**, *35*, 66.

(40)     Shen, J. Y.; Adnot, A.; Kaliaguine, S. *Applied Surface Science* **1991**, *51*, 47.

(41)     Tegeder, P.; Smirnov, B. M.; Illenberger, E. *International Journal of Mass Spectrometry* **2001**, *205*, 331.

(42)     Trenhaile, B. R.; Antonov, V. N.; Xu, G. J.; Agrawal, A.; Signor, A. W.; Butera, R. E.; Nakayama, K. S.; Weaver, J. H. *Physical Review B* **2006**, *73*, 125318/1.

(43)     Walter, W. K.; Jones, R. G. *Journal of Physics-Condensed Matter* **1989**, *1*, SB201.

(44)     Thorman, R.; Ómarsson, B.; Ingólfsson, O. **(in prep)**.

(45)     Boxhoorn, G.; Jesse, A. C.; Ernsting, J. M.; Oskam, A. *Thermochimica Acta* **1978**, *27*, 261.

(46)     Bestwick, T. D.; Oehrlein, G. S. *J. Vac. Sc. Technol. A* **1990**, *8*, 1698.

(47)     Reinicke, M. *Investigation of physical and chemical interactions during etching of silicon in dual frequency capacitively coupled HBr/NF3 gas discharges*; Books on Demand Gmbh, 2009.

(48)     Mulders, J.; Veerhoek, J.; Bosch, E.; Trompenaars, P. *Journal of Physics D: Applied Physics* **2012**, *45*, 475301.

Chapter 4


Electron Induced Surface Reaction of *cis*-Pt(CO)$_2$Cl$_2$: A Route to Focused Electron

Beam Induced Deposition of Pure Platinum Nanostructures

Chapter 4.      Electron Induced Surface Reactions of *cis*-Pt(CO)$_2$Cl$_2$:  A Route to Focused Electron Beam Induced Deposition of Pure Pt Nanostructures

4.1.  Introduction

Strategies capable of depositing nanoscale structures with control of location, shape, dimension, and orientation are essential for a variety of nanotechnologies, including plasmonics, semiconductor processing and catalysis.  One of the most promising techniques for depositing nanostructures with precise control is focused electron beam induced deposition (FEBID), in which nanostructures can be fabricated in a single step, without using resists or masks.

FEBID nanostructures are created in a vacuum environment (typically electron microscopes) when a high energy electron beam is focused onto a substrate in the presence of a gaseous stream of precursor molecules. Deposition takes place when electrons stimulate the decomposition of precursor molecules into volatile fragments that are pumped away and non-volatile fragments that are incorporated into the deposit.[1-4]  The size and shape of the nanoscale deposit are primarily determined by the resolution and manipulation of the electron beam.

FEBID offers a number of advantages compared to other vacuum-based nanostructure deposition strategies such as focused ion beam induced deposition (FIBID), electron beam lithography (EBL) and extreme ultraviolet lithography (EUVL). FEBID can create smaller features than FIBID, with less amorphization and no ion implantation.[5-9] FEBID resolution is comparable to EBL (although at resolutions smaller than 10 nm, FEBID has more potential)[10-13] and EUVL[14,15] but the resist layers and etching steps required for lithographic pattern transfer are unnecessary in FEBID. As a result, FEBID has already found applications, including a commercial system for repairing EUVL masks,[16-19] customized tips for local probe microscopes,[20,21] and fabrication and modification of nano-photonic and nano-plasmonic devices.[22-24]

Despite the attractive features of FEBID, several scientific and technological issues must be addressed to secure its wide applicability as a nanofabrication tool. For metal nanostructures deposited from organometallic complexes by FEBID, the biggest single issue is the low metal content.[1-4,25] Thus, FEBID structures generated from commercially available organometallic precursors are often composed of less than 50% metal. For example, structures created from $Me_2Au(acac)$ are <11% gold,[26,27] structures created from $MeCpPtMe_3$ are <22% platinum,[2,25] and structures created from $W(CO)_6$ are <39% tungsten.[28,29] The low metal content and associated impurities negatively impact the properties of FEBID nanostructures. For example, Pt wires created by FEBID from $MeCpPtMe_3$ and Au wires created by FEBID from $Me_2Au(acac)$ typically exhibit resistivity of > 1 $\Omega$ cm, compared with < 11 $\mu\Omega$ cm for pure metals, severely limiting their application as nanowires or nanoelectrodes.[26]

The presence of residual organic contamination in FEBID structures stems from the use of organometallic precursors which were developed for chemical vapor deposition (CVD) and atomic layer deposition (ALD).[2,10,25,30]  While CVD and ALD are thermal processes and often involve chemical reactions with coreactants (*e.g.*, $H_2$ or $O_2$), FEBID is driven by electron/molecule interactions.  Precursor ligands that are readily removed during the thermal reactions of CVD are often susceptible to electron stimulated decomposition in FEBID, leading to contamination in the deposit. The popular FEBID precursor MeCpPtMe$_3$ provides an example of different results obtained upon subjecting the same precursor to CVD and FEBID conditions.  Pure platinum films can be created from MeCpPtMe$_3$ using CVD,[31] while FEBID structures created from the same precursor have platinum contents of $< 22\%$.[2]

The need to improve FEBID structure purity has led to significant research in post-growth processing of Pt containing nanostructures.  Several *in situ* post-processing schemes have resulted in pure Pt nanostructures, including treatment with $O_2$ during continuous electron irradiation,[32] treatment with $H_2O$ vapor during continuous electron irradiation,[33] pulsed $O_2$ treatments at elevated temperatures,[34] and direct Pt growth by dosing MeCpPtMe$_3$ and $O_2$ in parallel, with dominant $O_2$ flux conditions.[35]  However, although techniques have been developed for contaminant removal by post-deposition processing of FEBID structures, the removal of contamination from organic ligands remains ubiquitous and challenging.[25]  The preferred approach would be to fabricate FEBID nanostructures with significantly higher metal contents (lower contaminant levels) at the time of deposition, thus removing or significantly reducing the need for post-growth processing.

Since currently available CVD precursors are typically unsuitable for FEBID, there is an urgent need to develop new organometallic precursors specifically designed to minimize ligand-derived contamination in FEBID deposits.  The preferred approach would be to fabricate FEBID nanostructures with significantly higher metal contents (lower contaminant levels) at the time of deposition.  This will require precursors that undergo electron-induced decomposition pathways to yield the desired material.

In recent years we have explored precursor decomposition in the FEBID process by means of an ultra-high vacuum (UHV) surface science approach, which allows study of chemical mechanisms that cannot be elucidated in the electron microscopes typically used to deposit FEBID nanostructures under steady state conditions.  The UHV surface science approach is a two-step process: (i) a finite amount of precursor is physisorbed to a cold, chemically inert substrate, forming nanometer thick films, and (ii) the adsorbed precursor is subjected to low energy (typically 500 eV) electron beam irradiation.[36,37]  This allows surface analytical tools, primarily X-ray Photoelectron Spectroscopy (XPS), to track changes in the bonding environment of elements contained in the precursor complex, while mass spectrometry (MS) detects the volatile species desorbed from the film as a result of electron stimulated reactions.  In particular, the UHV surface science approach allows in situ interrogation of the effects of electron irradiation on adsorbed precursors as a function of electron dose, providing information that can be used to elucidate the mechanistic steps responsible for precursor decomposition and metal deposition during FEBID.

Our prior studies on MeCpPtMe$_3$[37] and $[(\eta^3\text{-}C_3H_5)Ru(CO)_3Br]$[38] have demonstrated that polyhapto unsaturated hydrocarbon ligands result in incorporation of carbon atoms from the $\pi$-bound ligand into the deposit and should thus be avoided for applications where

carbon impurities degrade the performance of the deposited structure. The MeCpPtMe$_3$ study showed that on average, eight of the nine carbon atoms in the precursor were incorporated into the deposit,[37] consistent with gas phase studies of single electron/molecule collisions involving MeCpPtMe$_3$ that indicated loss of a single methyl group as the primary fragmentation channel in a dissociative electron attachment process.[39] Similarly, research on [($\eta^3$-C$_3$H$_5$)Ru(CO)$_3$Br] showed that all three of the carbon atoms in the $\eta^3$-allyl ($\eta^3$-C$_3$H$_5$) ligand become carbon contamination in the FEBID deposit.[38] Results obtained with hexafluoroacetylacetonate (hfac)[40] and acetylacetonate (acac)[41] complexes suggest that chelating ligands should also be avoided in the design of FEBID precursors.

Studies of W(CO)$_6$, Co(CO)$_3$NO, and [($\eta^3$-C$_3$H$_5$)Ru(CO)$_3$Br] indicated that one or more CO ligands can be ejected into the gas phase during FEBID, although not all CO ligands will necessarily be ejected from the surface.[38,42,43] One notable exception to this general trend is the bimetallic complex Co$_2$(CO)$_8$, which has been shown by some researchers to produce FEBID structures consisting of >90% Co, an effect ascribed to the catalytic properties of Co.[44-46] In studies on [($\eta^3$-C$_3$H$_5$)Ru(CO)$_3$Br] and [($\eta^3$-C$_3$H$_5$)Ru(CO)$_3$Cl], we also explored the fate of metal-halogen bonds.[38] Experimental XPS and MS data showed that although halogens of metal halides do not desorb initially as the precursor is decomposing, they can be removed as a result of post-deposition electron beam processing in a slower, electron stimulated desorption (ESD) process.[47]

The results of these studies led us to target *cis*-Pt(CO)$_2$Cl$_2$ (**1**) as a precursor for the FEBID of Pt nanostructures. We now report mechanistic study of the electron-induced decomposition of **1** under UHV conditions and the deposition of carbon free Pt

96

nanostructures under steady state conditions in an Auger spectrometer. Together these results demonstrate the electron-induced chemistry necessary to obtain pure Pt FEBID nanostructures from **1**.

### 4.2. Experimental

An ultrahigh vacuum (UHV) chamber equipped with X-ray Photoelectron Spectroscopy (XPS) and Mass Spectrometry (MS) was used to study the effects of electron irradiation on nanometer scale films of *cis*-platinum dicarbonyl dichloride (*cis*-Pt(CO)$_2$Cl$_2$). A second UHV chamber equipped with an Auger spectrometer (AES) was used to create structures using electron irradiation under steady state deposition conditions. Further details of the chambers and their analytical capabilities can be found in earlier publications.[37,41,48]

### 4.2.1 General (Synthesis)

Unless otherwise specified, all manipulations were performed under an inert atmosphere (Ar or N$_2$) using standard Schlenk line or glove box techniques. Toluene and heptane were purified by using an M. Braun solvent purification (MB-SP) system and stored over 3 Å molecular sieves prior to use. Benzene-$d_6$ (Cambridge Isotope Laboratories) was stored over 3 Å molecular sieves in a glove box prior to use. Sulfuryl chloride and PtI$_2$ were purchased from Sigma-Aldrich and used as received.

### 4.2.2 *cis*-Pt(CO)$_2$Cl$_2$ (1).

A modified literature procedure was used to synthesize *cis*-Pt(CO)$_2$Cl$_2$.[49] Platinum(II) iodide (PtI$_2$, 1.0 g, 2.2 mmol) was suspended in toluene (25 mL) in a 50 mL

Schlenk flask and stirred under CO for 30 minutes. Sulfuryl chloride (0.90 mL, 11.1 mmol) was then added and stirred for six hours to obtain a deep purple solution. The crude product from the toluene solution was recrystallized by adding *n*-heptane and chilling to -20 °C overnight to obtain the product as light yellow or off-white needle crystals. The yield was 0.52 g (73.4 %). $^{13}$C NMR ($C_6D_6$, 500 MHz): δ 151.84. ATR-IR (toluene): $\nu_{co}$ 2127, 2171 cm$^{-1}$. The compound was identified by comparison to literature data.[50] ATR data are shown in Figure S1 (Supporting Information).

### 4.2.3    Introduction of *cis*-Pt(CO)$_2$Cl$_2$ (**1**) into the UHV chamber

Precursor **1** is a solid at standard temperature and pressure.[51] Due to the precursor's sensitivity to air and moisture, it was handled inside an $N_2$ glove box. Prior to deposition, the solid precursor was added to a glass finger, which was attached to a UHV compatible leak valve coupled directly to the UHV chamber. The glass finger was evacuated at the same time as the UHV chamber was pumped down with the leak valve open into the 1.0 x 10$^{-6}$ Torr pressure regime. At this point the leak valve was closed and the main chamber was baked out and restored to the UHV pressure regime. To maintain a sufficient vapor pressure of *cis*-Pt(CO)$_2$Cl$_2$ during deposition, the precursor was heated to ~80 °C with the temperature monitored by a thermocouple.

Opening the leak valve to dose with precursor **1** caused a negligible rise in system pressure at room temperature (~20 °C). During use in the UHV XPS/MS system, when precursor **1** was heated to 60 °C the measured system pressure was ~1 x 10$^{-7}$ Torr. Depositions were typically obtained with precursor **1** heated to ~80 °C (system pressure of ~4 x 10$^{-7}$ Torr). Although the pressure of **1** decreased over time when heated to ~80 °C,

we were still able to obtain $Pt(CO)_2Cl_2$ deposition onto cooled substrates with system pressures as low as 5 x $10^{-9}$ Torr.

### 4.2.4    Substrates.

Electron irradiation of thin films of *cis*-$Pt(CO)_2Cl_2$ was conducted on an amorphous carbon (a:C) substrate and a silicon dioxide ($SiO_2$) substrate.  Both substrates allowed observation of Pt(4f) and Cl(2p) XPS transitions.  The a:C substrate allowed clean evaluation of the O(1s) transition while the $SiO_2$ substrate allowed clean evaluation of the C(1s) transition.  Substrates were regenerated in situ between experiments by ion sputtering using 4 keV $Ar^+$ ions until the substrate was verified to be clean by XPS.  After sputtering removed any adventitious carbon and residual Pt from previous experiments, the oxide layer ($SiO_2$) was restored by electron irradiation of the Si substrate in the presence of $O_2$ (P = 5.0 x $10^{-7}$ Torr) for several hours.  Depositions from $Pt(CO)_2Cl_2$ in an Auger spectrometer utilized atomically smooth Ru-capped Si/Mo multi-layer mirror substrates.[52] This substrate was chosen for depositions due to its smoothness and ease with which deposits could be imaged in the scanning electron microscope.  The cleanliness of the Ru-capped Si/Mo substrate was verified by Auger spectroscopy prior to each deposition.

### 4.2.5    Dosing the precursor on the substrate in the XPS/MS chamber.

Nanometer scale films of **1** were created by leaking the precursor into the UHV chamber through a UHV-compatible leak valve, where it was adsorbed onto a cooled substrate at 183K ($\pm$ 10K).  Average film thickness was determined for each film by measuring the attenuation of the substrate XPS photoelectrons (C(1s) or Si(2p)) after

compound adsorption,[41] using an inelastic mean free path for C(1s) and Si(2p) photoelectrons of 2.0 nm.[53-55] XPS was also used before and after the film was exposed to a known electron dose to determine changes in chemical composition and chemical bonding of the film.

### 4.2.6 Electron Source.

A commercial flood gun (Specs FG 15/40) was used as an electron source for all XPS and MS experiments. To ensure that the film was subjected to a relatively uniform electron flux, the electron source was characterized by a Faraday cup. Throughout our experiments, the incident electron energy was 500 eV; this was calculated from the sum of the electron energy from the flood gun (480 eV) and a positive bias (+20V), which was applied to prevent secondary electrons generated during irradiation from escaping. Unless otherwise noted, a target current of 5 μA was used. Electron flux is reported in terms of dose ($e^-/cm^2$). Further details of the electron source can be found in previous publications.[37,41]

### 4.2.7 X-ray Photoelectron Spectroscopy.

XPS data were acquired in a PHI 5400 XPS using Mg Kα X-rays ($h\nu = 1253.6$ eV). Spectra were deconvoluted with commercial software (CASA XPS); binding energies obtained for films deposited on the a:C substrate were aligned to the C(1s) peak at 284.6 eV,[56] while binding energies for films deposited on the $SiO_2$ substrate were aligned to the Si(2p$_{3/2}$) peak at 99.3 eV. [57]

### 4.2.8 Creating Deposits in the Auger Spectrometer (AES).

Deposits were formed by leaking $cis$-Pt(CO)$_2$Cl$_2$ into the UHV chamber of a PHI 610 Scanning Auger Microprobe system (LaB$_6$ filament) via a UHV-compatible leak valve. A directional doser was used to enhance the partial pressure of precursor at the substrate surface during deposition. The deposits were made under steady state deposition conditions with the substrate at room temperature using an incident beam energy of 3kV and varying substrate currents, precursor partial pressures and deposition times. Deposit thicknesses were not calculated but were assessed as suitably thick once the substrate peaks were no longer visible in the Auger spectrum.

### 4.2.9 Scanning Electron Microscopy (SEM) and Energy Dispersive Spectroscopy (EDS).

Deposits generated in the Auger system were imaged using a cold-cathode field emission scanning electron microscope (JEOL 6700F, LEI detector) with a 1.0 nm resolution at 15 keV equipped with an energy dispersive X-ray analyzer (EDAX Genesis 4000 X-ray analysis system, detector resolution of 129 eV).

### 4.3. Results

Figures 1 and 2 show the effect of electron irradiation on thin (~0.5 to 1 nm) films of $cis$-Pt(CO)$_2$Cl$_2$ adsorbed on SiO$_2$ at 183K ($\pm$ 10K) as measured by changes in O(1s), C(1s), Pt(4f) and Cl(2p) XPS transitions. Figure 1 shows the effect of comparatively small electron doses ($< 1.1 \times 10^{16}$ e$^-$/cm$^2$), while Figure 2 shows film evolution for larger electron doses ($1.1 \times 10^{16}$ e$^-$/cm$^2$ < electron dose < $1 \times 10^{17}$ e$^-$/cm$^2$). For reference an XPS spectrum of an "as deposited" $cis$-Pt(CO)$_2$Cl$_2$ film prior to electron irradiation is shown in Figures 1 and 2.

To account for the effect of X-ray irradiation, Figures S2 and S3 (Supporting Information) show results of control studies where a *cis*-Pt(CO)$_2$Cl$_2$ thin film adsorbed on an SiO$_2$ and an amorphous carbon (a:C) substrate was exposed to the effects of sustained X-ray irradiation alone (see Supporting Information). Results from these studies revealed that similar changes in the films occurred when they were exposed to X-rays or electrons (e.g., compare Figure S2 and Figure 1) consistent with mediation of the chemical transformations by the low energy ($< 50$ eV) secondary electrons which are produced when substrates are exposed either to X-rays or electrons. These control studies showed that the acquisition time needed to scan the O(1s), C(1s), Pt(4f) and Cl(2p) regions corresponded to an equivalent electron dose of $4.7 \times 10^{14}$ e$^-$/cm$^2$. The electron doses reported in Figures 1-7 are corrected to account for X-ray induced changes due to the time required to acquire the XPS data. In practice the electron dose from X-ray irradiation is only significant for the shortest electron exposures (electron doses $< 4 \times 10^{15}$ e$^-$/cm$^2$).

In Figure 1, prior to electron exposure the O(1s) region is characterized by a sharp peak centered at binding energy 535.5 eV, characteristic of an adsorbed CO species[58,59], as well as a peak centered at 533.5 eV with a shoulder at 532.0 eV characteristic of SiO$_2$ (SiO$_2$ [60] and a Si hydroxide species [61]). As the film is subjected to electron irradiation, the O(1s) peak corresponding to CO downshifts in binding energy and decreases in intensity with the electron dose until it has all but disappeared for electron doses $> 3.2 \times 10^{16}$ e$^-$/cm$^2$ (Figures 1 and 2). In contrast, the intensity of the SiO$_2$ substrate peaks increases as the electron dose increases, consistent with the loss of oxygen-containing species from the *cis*-Pt(CO)$_2$Cl$_2$ film.
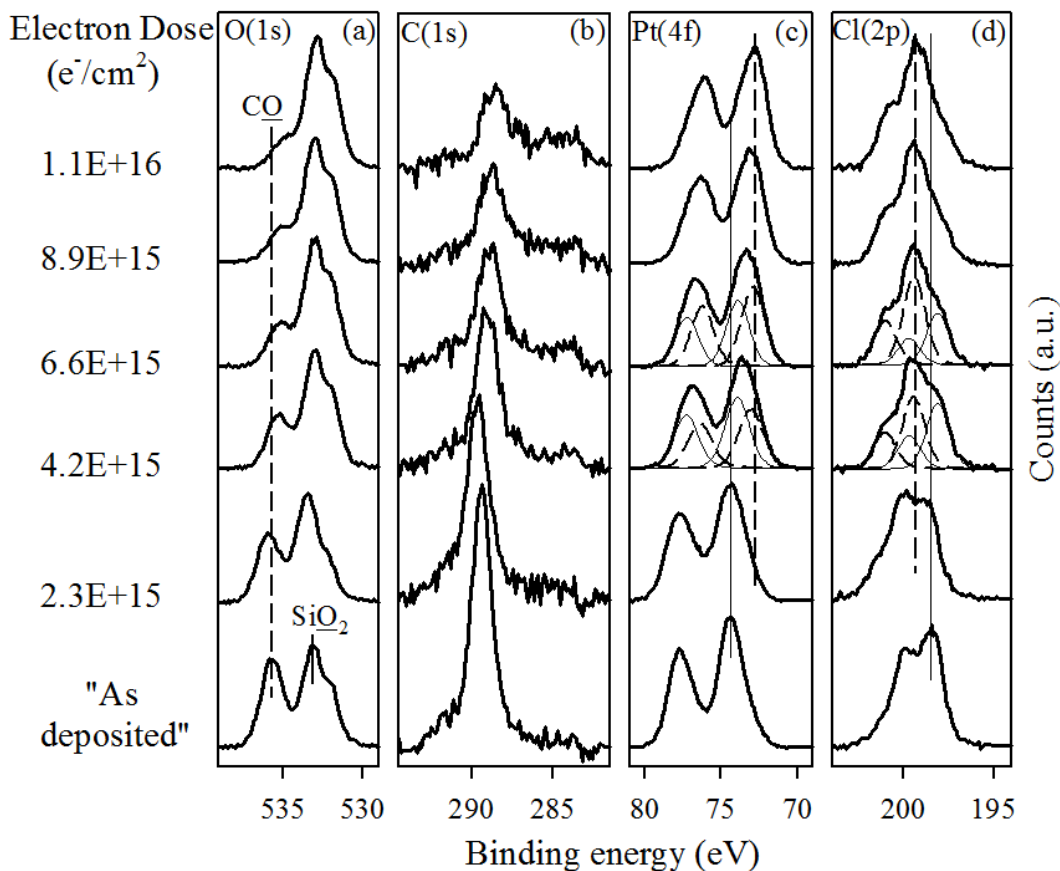
**Figure 4.1**: Evolution of the a) O(1s), b) C(1s), c) Pt(4f) and d) Cl(2p) XP regions for a 0.7 nm thick film of *cis*-Pt(CO)$_2$Cl$_2$ adsorbed on an SiO$_2$ substrate at 183K ($\pm$ 10K) and then exposed to electron doses $\leq 1.1 \times 10^{16}$ e$^-$/cm$^2$. In the Pt(4f) and Cl(2p) regions, vertical solid and dashed lines indicate the Pt(4f$_{7/2}$) and Cl(2p$_{3/2}$) positions of the initial and final species respectively. Fitting for Pt(4f) and Cl(2p) regions is shown for the 4.2 $\times 10^{15}$ and 6.6 $\times 10^{15}$ e$^-$/cm$^2$ electron doses; solid lines represent the initial species, while dashed lines represent the final species. The bottom spectrum represents the XPS data acquired on an "as deposited" film prior to electron irradiation (see text).
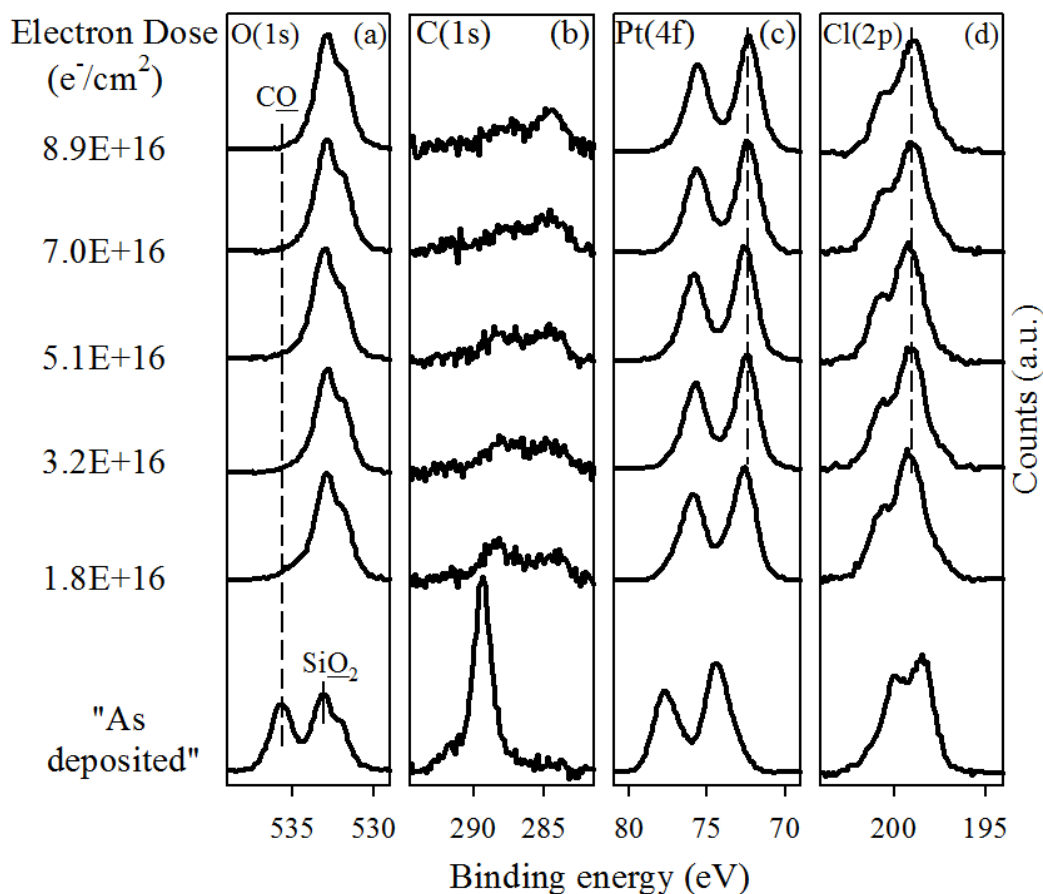
**Figure 4.2**: Evolution of the a) O(1s), b) C(1s), c) Pt(4f) and d) Cl(2p) XP regions for a ~0.7 nm thick film of *cis*-Pt(CO)$_2$Cl$_2$ adsorbed on an SiO$_2$ substrate at 183K (±10K) and exposed to electron doses $\leq$ 8.9 x 10$^{16}$ e$^-$/cm$^2$. In the Pt(4f) and Cl(2p) regions, dashed lines indicate the Pt(4f$_{7/2}$) and Cl(2p$_{3/2}$) positions of the initial and final species respectively. The bottom spectrum represents the XPS data acquired on an "as deposited" film prior to electron irradiation (see text).

The C(1s) region is initially comprised of a single sharp peak centered at 289.2 eV, consistent with the binding energy of a carbon atom in a carbonyl complex.[58,59] Figure 1 shows that during the initial stages of electron irradiation the dominant spectral change in the C(1s) region involves a significant decrease in the intensity of the carbonyl peak accompanied by a slight downshift in peak position of ≈ 1 eV. A smaller peak centered at ≈ 284.6 eV, indicative of graphitic like carbon atoms also appears.[56] As the electron dose

increases, Figure 2 shows that for electron doses $> \approx 2 \times 10^{16}$ e$^-$/cm$^2$ the rate of decrease in intensity of the carbonyl peak slows markedly with a correspondingly slow increase in intensity in the graphitic peak at $\approx 284.6$ eV. Control studies (data not shown) indicated that this graphitic peak was not caused by the adsorption of adventitious carbon atoms from the chamber or from hydrocarbon species generated by the electron gun.

In the Pt(4f) region, a Pt ($4f_{5/2}/4f_{7/2}$) doublet is observed in the "as deposited" film with peaks centered at 77.6 eV and 74.3 eV, respectively, indicative of a Pt(II) species.[62] As the electron dose increases in Figure 1 the Pt(4f) spectral envelope broadens and shifts to lower binding energies. In contrast, for larger electron doses shown in Figure 2 the Pt ($4f_{5/2}/4f_{7/2}$) peak positions remain relatively unchanged, although the peak profile narrows. After an electron dose of $> \approx 2 \times 10^{16}$ e$^-$/cm$^2$ the spectral envelope in the Pt(4f) region is in fact similar to the shape and intensity of the initial film, but downshifted in binding energy by $\approx 2.1$ eV. The fitting of the Pt(4f) envelope for electron doses of $4.2 \times 10^{16}$ and $6.6 \times 10^{16}$ e$^-$/cm$^2$ demonstrates that there are two Pt species present; one with a Pt($4f_{7/2}$) peak that closely corresponds to that of the parent compound and another Pt species with a Pt($4f_{7/2}$) peak position at $\approx 72.1$ eV which corresponds to the final position observed in Figure 2. As the electron dose increases, the contribution from the parent compound decreases while there is a corresponding increase in intensity of the low binding energy Pt species.

The Cl(2p) region is initially comprised of a Cl($2p_{3/2}/2p_{1/2}$) doublet with a Cl($2p_{3/2}$) peak position at 198.3 eV, consistent with the presence of a single bonding environment for the Cl atoms. As the film is irradiated, however, the spectral envelope in the Cl(2p) region broadens due to the appearance of a new Cl($2p_{3/2}/2p_{1/2}$) doublet with a Cl($2p_{3/2}$) peak position at 199.3 eV, which grows in as the electron dose increases at the expense of the

lower binding energy doublet. After an electron dose of $6.6 \times 10^{15}$ e$^-$/cm$^2$ peak fitting of the Cl(2p) region reveals that there is a roughly equal surface concentration of both species (see Figure 1). As the electron dose increases, the peak fitting shows that the contribution from the higher binding energy Cl species also increases. For the larger electron doses shown in Figure 2 the Cl(2p) region is composed almost exclusively of the new higher binding energy feature. Analogous to the Pt(4f) region, the Cl(2p) region after electron doses of $\approx 2 \times 10^{16}$ e$^-$/cm$^2$ is virtually unchanged in shape from the one recorded for the as deposited film, but is shifted in binding energy.

Figure 3 illustrates the evolution of the spectral intensities in the C(1s), Cl(2p) and Pt(4f) regions and the Pt $4f_{7/2}$ binding energy position as a function of the electron dose (Figures 1 and 2); for the spectral intensities, each area was normalized to the value measured prior to electron irradiation. Quantitative analysis of the O(1s) region was not performed due to overlap with the SiO$_2$ oxide peaks. Analysis of Figure 3 reveals that there is essentially no change in the Pt(4f) area, indicating that no Pt atoms desorb, while the Cl atom concentration decreases slightly to ~80% of its original value after an electron dose of $\approx 1 \times 10^{17}$ e$^-$/cm$^2$. In contrast, there is a significant reduction in C(1s) area, which decreases to $\approx 40\%$ of its original value after an electron dose of $\approx 2 \times 10^{16}$ e$^-$/cm$^2$, but remains roughly constant thereafter. The evolution in the C(1s) area correlates with the change in the Pt($4f_{7/2}$) binding energy which shifts to lower binding energies for comparatively small electron doses ($< 2 \times 10^{16}$ e$^-$/cm$^2$), but remains constant thereafter.
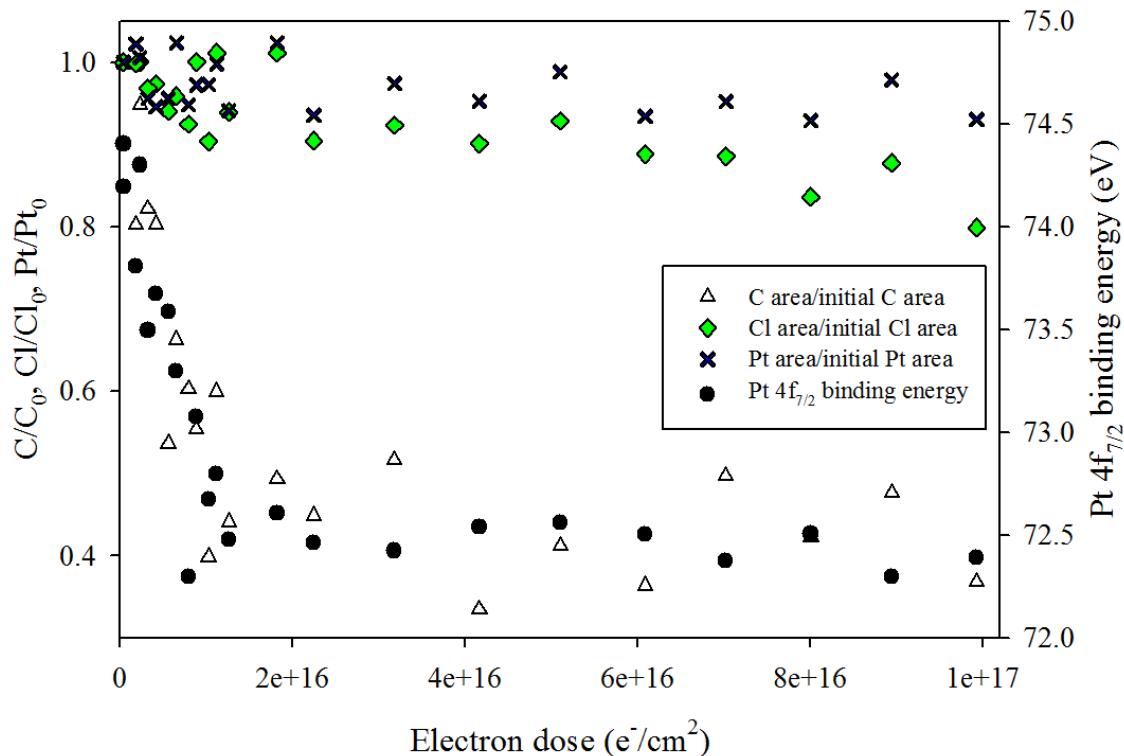
**Figure 4.3**: Electron irradiation induced changes in the (left-hand axis) fractional coverage of carbon (white triangles), chlorine (green diamonds), and platinum (blue crosses) for 0.5 - 1 nm *cis*-Pt(CO)$_2$Cl$_2$ films adsorbed on SiO$_2$ and (right-hand axis) Pt 4f$_{7/2}$ binding energy (black circles); each is plotted as a function of electron dose (electron doses < 1.0x10$^{17}$ e$^-$/cm$^2$), all determined by XPS.

Figures 4 and 5 display data for experiments analogous to the ones described in Figures 1-3 but for thin films (1 − 2 nm) of *cis*-Pt(CO)$_2$Cl$_2$ adsorbed at 183K (± 10K) onto an a:C substrate rather than SiO$_2$. In contrast to SiO$_2$, the use of a:C substrate allowed for analysis of the O(1s) region in the absence of substrate interference, but precluded a detailed analysis of the C(1s) region due to the a:C substrate. Figure 4 shows the evolution in the O(1s), C(1s), Pt(4f) and Cl(2p) regions as the electron dose increases, with an "as deposited" spectrum shown for reference. The data are seen to follow similar trends to Figures 1 and 2.
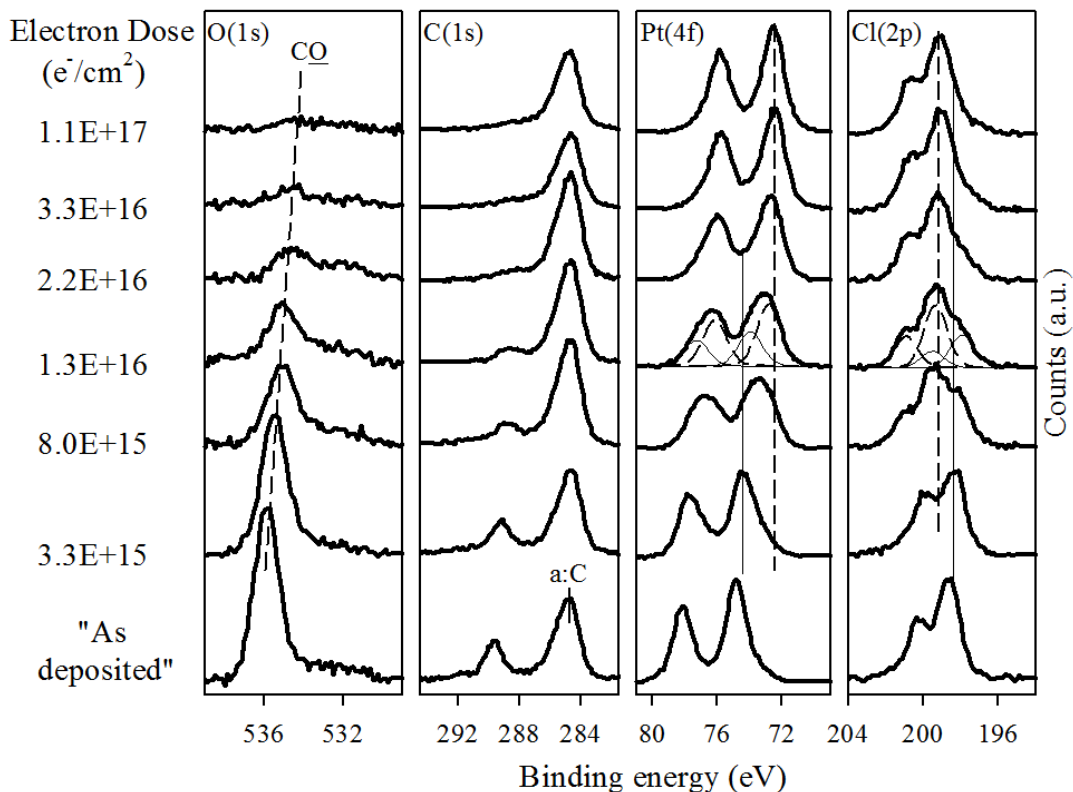
**Figure 4.4**: Evolution of the a) O(1s), b) C(1s), c) Pt(4f) and d) Cl(2p) XP regions for $1 - 2$ nm thick films of *cis*-Pt(CO)$_2$Cl$_2$ adsorbed on an a:C substrate at 183K ($\pm$10K) and then exposed to electron doses $\leq 1.1$ x $10^{17}$ e$^-$/cm$^2$. In the Pt(4f) and Cl(2p) regions, vertical solid and dashed lines indicate the Pt(4f$_{7/2}$) and Cl(2p$_{3/2}$) positions of the initial and final species respectively. Fitting for the Pt(4f) and Cl(2p) regions is shown for the $1.3$x$10^{16}$ e$^-$/cm$^2$ electron dose; solid lines represent the initial species, while dashed lines represent the final species. The bottom spectra represents the XPS data acquired on an "as deposited" film prior to electron irradiation (see text). Spectral intensities were normalized to account for slight differences in the initial film thickness.

In Figure 4 the O(1s) region is initially composed of a sharp peak centered at 535.8 eV. Under the influence of electron beam irradiation, the oxygen signal from the carbonyl group[58,59] downshifts in binding energy and decreases in intensity until only a small O(1s) signal is detected after an electron dose of 1.1 x $10^{17}$ e$^-$/cm$^2$. This behavior is analogous to the behavior observed for *cis*-Pt(CO)$_2$Cl$_2$ adsorbed on SiO$_2$. The C(1s) region is comprised of a small peak centered at 289.6 eV, corresponding to the carbon contribution from the

carbonyl group,[58,59] and a much larger peak centered at 284.6 eV, from the amorphous carbon (a:C) substrate.[56]  Under electron beam irradiation, the CO peak decreases in size until any remaining carbonyl carbon is indistinguishable from the substrate signal after an electron dose of $1.1 \times 10^{17}$ $e^-/cm^2$.  Electron irradiation causes the Pt(4f) profile to broaden and decrease in binding energy before sharpening.  For electron doses $> \approx 2 \times 10^{16}$ $e^-/cm^2$ the Pt(4f) binding energy and profile remain unchanged and resemble the Pt(4f) spectrum observed initially, prior to electron irradiation, albeit downshifted in binding energy by $\approx$ 2.3 eV.  In the Cl(2p) region, the evolution in the spectral profile also mirrors the changes seen on $SiO_2$ (compare Figures 1 and 4).  Peak fitting of the Pt(4f) and Cl(2p) regions reveals that both spectral envelopes can be well fit by two components.  In each case, one component has a principal peak ($Pt(4f_{7/2})$ or $Cl(2p_{3/2})$) which is at approximately the same value as the one measured for the "as deposited" spectra and one with a principal peak at approximately the same value as the spectra observed after an electron dose of $1.1 \times 10^{17}$ $e^-/cm^2$.

Figure 5 shows O(1s), Pt(4f) and Cl(2p) area analysis as well as change in Pt $4f_{7/2}$ binding energy obtained via XPS for cis-$Pt(CO)_2Cl_2$ thin films adsorbed on a:C and exposed to electrons.  Platinum and chlorine atoms largely remain behind on the surface for electron doses $< 1.2 \times 10^{17}$ $e^-/cm^2$, in agreement with data shown in Figure 3.  However, electron irradiation results in loss of ~80% of oxygen from the surface with a decrease which tracks with the decrease in the Pt $4f_{7/2}$ binding energy.  A comparison of Figures 3 and 5 reveals that the metrics that can be analyzed on both substrates (changes in the Pt(4f) binding energy, Pt(4f) and Cl(2p) areas) exhibit similar dependencies on the electron dose.
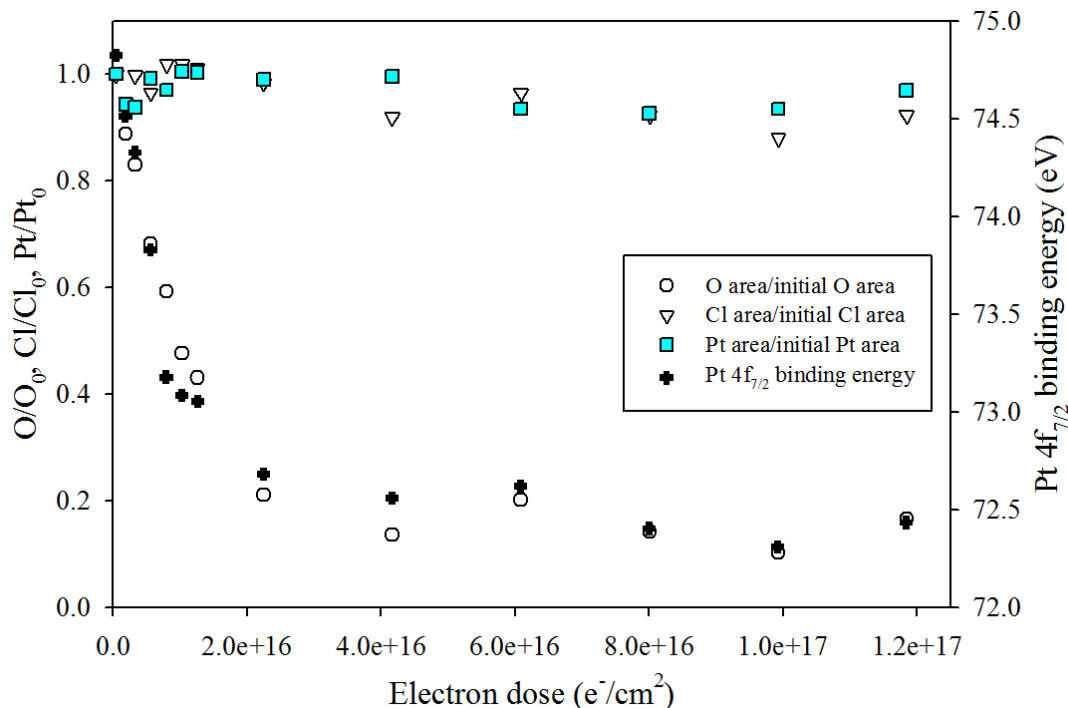
**Figure 4.5**: Electron irradiation induced changes in the (left-hand axis) fractional coverage of oxygen (open circles), chlorine (open triangles), and platinum (blue squares) and (right-hand axis) Pt $4f_{7/2}$ binding energy (black circles) all measured for 1 – 2 nm *cis*-$PtCl_2(CO)_2$ films adsorbed on a:C; each is plotted as a function of electron dose (electron doses $< 1.2 \times 10^{17}$ $e^-/cm^2$), all determined by XPS.

Figure 6a shows mass spectra of gas phase species evolved when *cis*-$Pt(CO)_2Cl_2$ adsorbed onto a $SiO_2$ substrate is electron irradiated. The spectrum is dominated by peaks at *m/z* 28, 12 and 16, indicative of CO. Smaller peaks are observed at *m/z* 36 and 38, indicative of HCl. The peak at *m/z* 18 is attributed to residual $H_2O$ in the UHV chamber. Figure 6b presents mass spectra collected for a *cis*-$Pt(CO)_2Cl_2$ film adsorbed onto a $SiO_2$ substrate at 183K ($\pm$ 10K) and then allowed to thermally desorb as the substrate slowly warmed to room temperature. The MS shows peaks at *m/z* 28, 12 and 16 consistent with CO fragments. A small *m/z* 18 peak is also observed due to residual $H_2O$. Measureable signal intensity (notably more than in Figure 6a) is also observed at *m/z* 35 and 37 consistent with $Cl^+$ produced by the electron impact dissociation of *cis*-$Pt(CO)_2Cl_2$ and HCl

(dominant peaks at $m/z$ 36 and 38) produced by secondary reactions of $Cl^+$ with the walls of the UHV chamber and/or $H_2O$ in the chamber. Figure 6c shows the variation in the $m/z$ = 12 signal as a function of electron dose for a $cis$-$Pt(CO)_2Cl_2$ film adsorbed on an a:C substrate at 183K. The $m/z$ = 12 signal was selected as a measure of CO intensity rather than the stronger signal at $m/z$ = 28 due to the lack of interference from background gases at $m/z$ = 12. Figure 6c shows that the $m/z$ = 12 signal reaches its greatest value when the $cis$-$Pt(CO)_2Cl_2$ film is first exposed to electrons and then decreases rapidly as a function of electron dose until it has reached a constant (background) signal level by $\approx$ 4 x $10^{16}$ e⁻/cm².

**Figure 4.6**: Mass spectrum (0-60 amu) of (a) the volatile species produced when a ~0.7 nm film of $cis$-$Pt(CO)_2Cl_2$, adsorbed onto a silicon dioxide ($SiO_2$) substrate at 183K was irradiated by an electron dose of 1.1 x $10^{17}$ e⁻/cm² (incident energy of 500 eV); the spectrum in (a) represents an average of MS taken every 20 s during the electron exposure and (b) gas phase $cis$-$Pt(CO)_2Cl_2$ evolved during thermal desorption of $cis$-$Pt(CO)_2Cl_2$ adsorbed on a $SiO_2$ substrate. For ease of comparison, spectra (a) and (b) were normalized to the CO peak ($m/z$ = 28) height. Panel (c) shows kinetics of gas phase CO evolution (as measured by the C peak at $m/z$ = 12 amu) from a ~0.7 nm film of $cis$-$Pt(CO)_2Cl_2$ during electron irradiation. Figure is shown on following page.
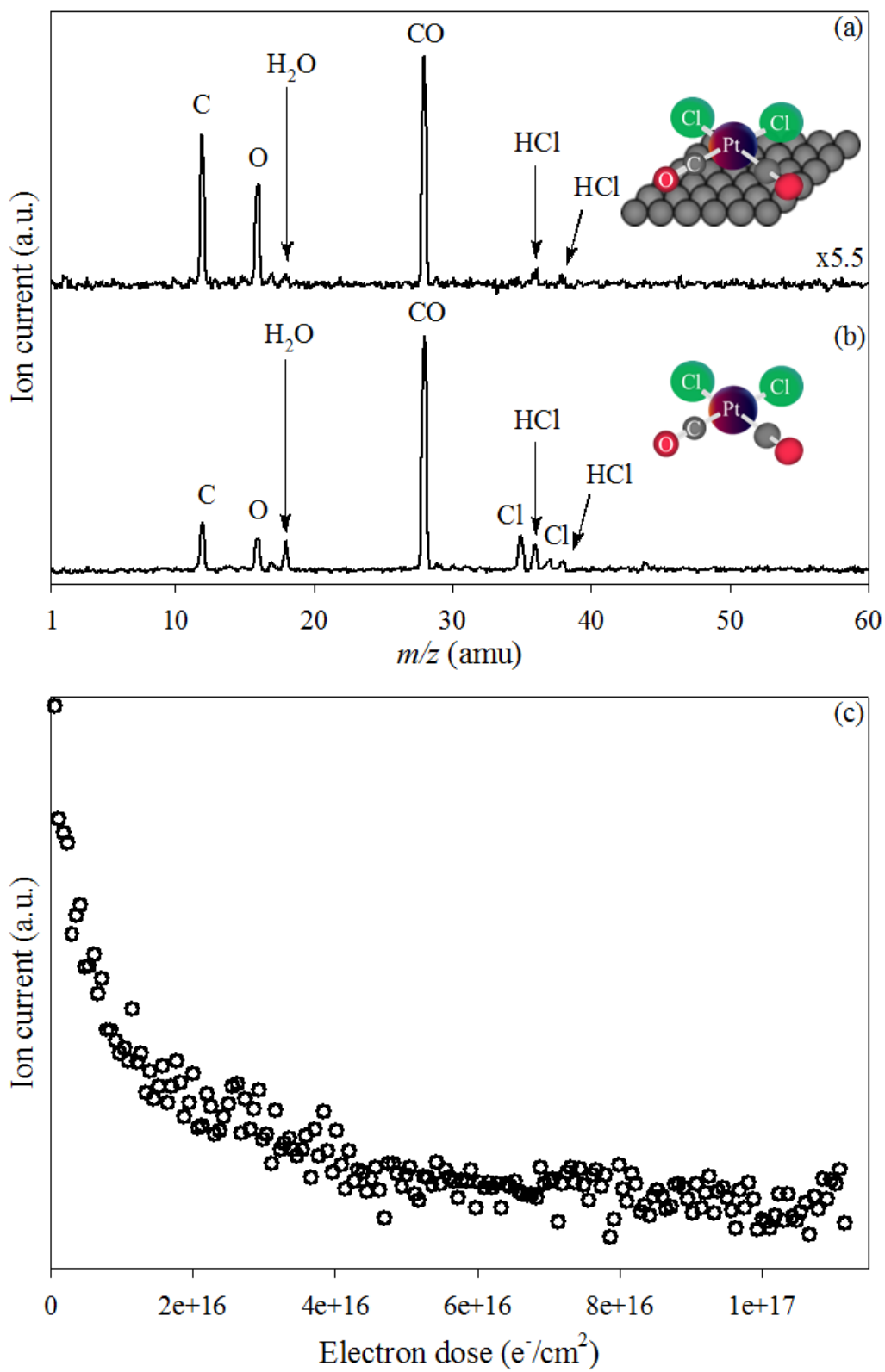
Figure 7 provides data on the effect of significantly larger electron doses up to 1.5 x $10^{19}$ e$^-$/cm$^2$ (*i.e.*, two orders of magnitude greater than those shown in Figures 1 – 6) for *cis*-Pt(CO)$_2$Cl$_2$ adsorbed onto a:C. For these much larger doses, the most significant effect was observed in the Cl(2p) XP region which decreased in intensity until essentially all chlorine had been removed from the surface after an electron dose of 1.5 x $10^{19}$ e$^-$/cm$^2$ (Figure 7a). Figure 7b and 7c show changes in the Cl(2p) peak area and the Pt(4f$_{7/2}$) peak position as a function of the electron dose (for electron doses > 1.2 x $10^{17}$ e$^-$/cm$^2$), respectively. Although there was no appreciable change in the Pt(4f) area (see Figure S4), the Pt(4f) peak positions exhibited a continuous decrease in binding energy (Figure 7(c)). A comparison of Figure 7b and 7c reveals that the decrease in Cl area and Pt 4f$_{7/2}$ peak position follow a similar exponential decay as a function of the electron dose. Data for the
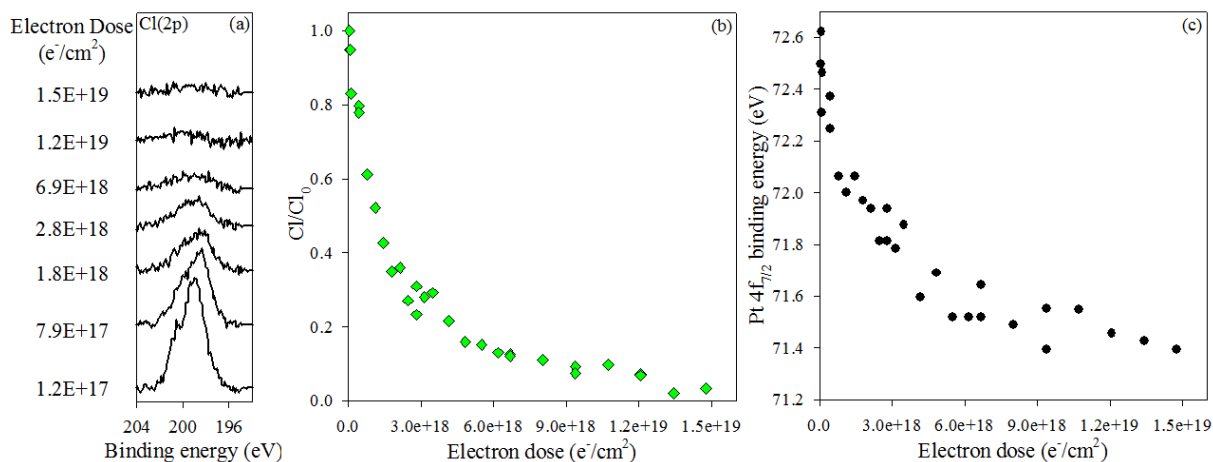


**Figure 4.7**: (a) Cl(2p) XP region for a ~1.3 nm *cis*-Pt(CO)$_2$Cl$_2$ film adsorbed on a:C, exposed to electron doses ranging from 1.2x$10^{17}$ to 1.5x$10^{19}$ e$^-$/cm$^2$ and corresponding changes in (b) the fractional coverage of adsorbed chlorine atoms normalized to the initial chlorine atom coverage (green diamonds), and (c) the Pt 4f$_{7/2}$ binding energy (black circles), each plotted as a function of electron dose.

O(1s), C(1s) and Pt(4f) XP transitions for this longer irradiation period are shown in Figure S4 (Supporting Information). The O(1s) XP transition shows little change in O content, while the C(1s) XP region shows an increase in C(1s) contribution from the a:C substrate as Cl is lost from the surface.

Figure 8 summarizes changes observed in the Pt $4f_{7/2}$ binding energy as *cis*-Pt(CO)₂Cl₂ adsorbed on $SiO_2$ is subjected to electron irradiation. Initially, the Pt $4f_{7/2}$ binding energy is at 74.8 eV. After an electron dose of ~$2.2 \times 10^{16}$ e⁻/cm², the Pt $4f_{7/2}$ binding energy has downshifted to 72.7 eV. After further electron irradiation and loss of all Cl, the Pt $4f_{7/2}$ binding energy has decreased to 71.4 eV. Reference data for pure Pt (71.1 eV) taken in the same XPS instrument are shown.[37]
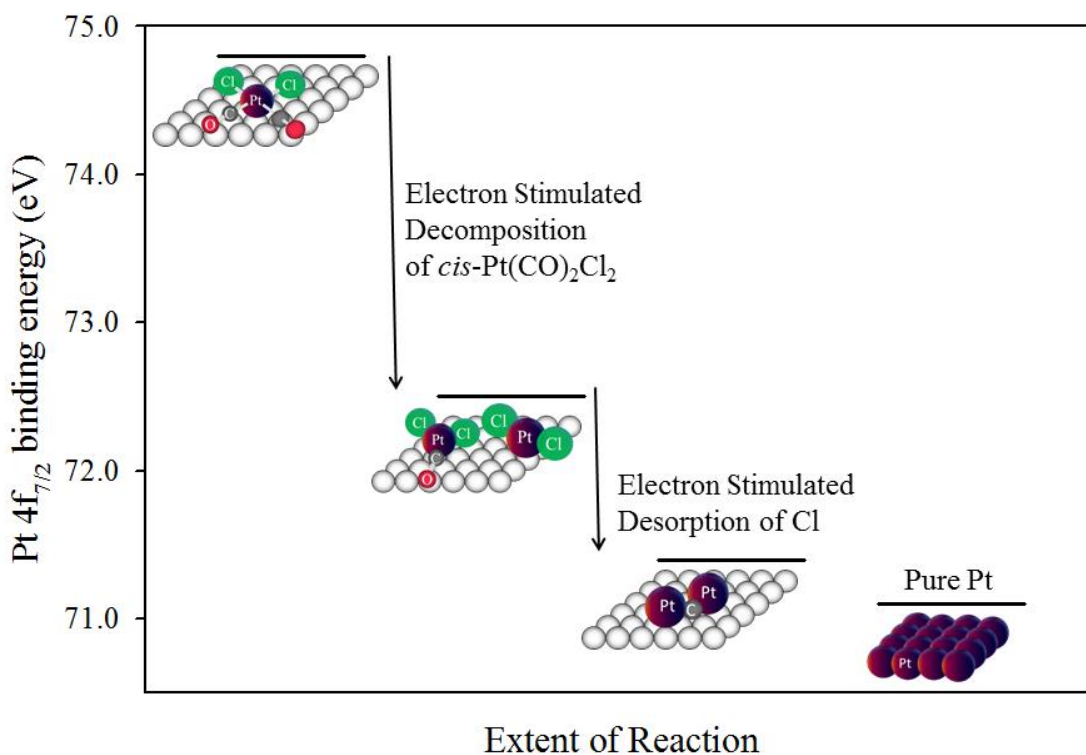


**Figure 4.8**: Evolution of Pt $4f_{7/2}$ binding energy for *cis*-Pt(CO)₂Cl₂ under the influence of electron irradiation at different stages of the reaction. The Pt $4f_{7/2}$ binding energy of a pure Pt sample is also shown for reference.

Deposits representative of those that would be created under FEBID conditions could be simulated in experiments where a substrate was exposed to a constant partial pressure of *cis*-Pt(CO)$_2$Cl$_2$ and irradiated under steady state deposition conditions in an Auger Spectrometer (Figure 9).[52] In these experiments, the precursor gas is introduced into the UHV chamber, transiently absorbed on the surface (at ambient temperature), and decomposed by the Auger electron beam (3kV). The Auger spectrum of a representative deposit (Figure 9a) indicates a composition of Pt (34.5 %) and Cl (63.8 %), with little to no C or O content (1.5% C, 0.2% O). EDS (Figure 9c) revealed that the deposit is composed exclusively of Pt (~37.6%) and Cl (~58.7%), with small contributions from the
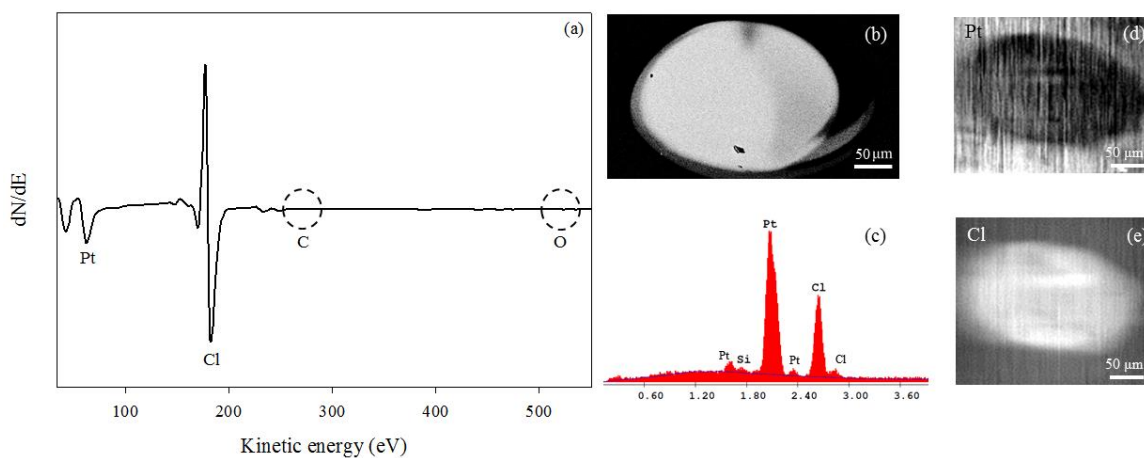


**Figure 4.9**: Auger electron and SEM data for a deposit created from *cis*-Pt(CO)$_2$Cl$_2$ in an AES instrument on a Ru coated Si/Mo multi-layer substrate under steady state deposition conditions (P$_{cis\text{-}Pt(CO)2Cl2}$ ≈ 1.5 x 10$^{-8}$ Torr for 19 h at 3kV, with average target current of 300 nA). The AES spectrum of the resulting deposit is shown in (a). The secondary electron image of the deposit acquired in a SEM (20kV, 300x) is shown in (b), along with (c) the corresponding EDS data. Auger elemental maps are shown for (d) Pt (64 eV) and (e) Cl (181 eV).

substrate (Si and Mo) also visible in the spectrum. Figures 9d and 9e show Auger elemental maps of the deposition region, in which the spatial distribution of surface Pt and Cl were obtained by measuring the difference in AES signals observed at an energy

corresponding to either a platinum (Pt MNN, (64eV)) or Cl LMM, (181eV)) Auger transition. A comparison of Auger elemental maps (Figures 9d and 9e) and the SEM image (Figure 9b) show that the deposit is spatially defined by the electron beam.

### 4.4. Discussion

#### 4.4.1 Precursor Design.

The removal of ligand-derived impurities incorporated in metal deposits, particularly carbon, is a major goal of current FEBID research and most approaches have involved post-deposition processing. In contrast, we have taken the approach of controlling the chemical composition of the deposit by designing organometallic precursors whose predicted decomposition in FEBID could lead to pure metal deposits. Given the paucity of precursors specifically developed for FEBID,[27,30,63] this study provides an opportunity to evaluate a mechanism based precursor design strategy which relies on investigation of related complexes to guide the choice of ligands in target precursors. In choosing **1** as a precursor for Pt FEBID, we have used results from our previous studies on the electron stimulated surface reactions of commercially available CVD precursors, and most recently $[(\eta^3\text{-}C_3H_5)Ru(CO)_3X]$ (X = Cl, Br) complexes, in a UHV surface science system,[38] to predict the behavior of a different late transition metal complex under FEBID conditions. Despite the common use of unsaturated polyhapto ligands such as cyclopentadienyl in FEBID, the high carbon content of Pt deposited from MeCpPtMe$_3$ and the incorporation of the allyl carbons into FEBID material from $[(\eta^3\text{-}C_3H_5)Ru(CO)_3X]$ led us to rule out anionic $\pi$-facial ligands. Instead, we have chosen *cis*-Pt(CO)$_2$Cl$_2$ (**1**), a four coordinate Pt(II) complex with a relatively simple coordination sphere of monodentate ligands. Desorption of the carbonyl groups during FEBID would

116

be consistent with our previous studies on $[(\eta^3\text{-}C_3H_5)Ru(CO)_3X]$ complexes, which also demonstrated that the halide ligands could be removed by post-deposition electron beam processing. In addition to possessing ligands that should be labile during FEBID, complex **1** possesses sufficient volatility and thermal stability for sublimation and gas phase transport to the substrate surface.

4.4.2    Adsorbate Characterization Prior to Electron Exposure.

Exposure of $SiO_2$ and a:C substrates to precursor **1** at < 200K results in molecular adsorption of *cis*-$Pt(CO)_2Cl_2$ (**1**) as evidenced by XPS (Figures 1, 2 and 4);  on both substrates the Pt(4f) and Cl(2p) spectral envelopes show the well-defined doublets expected for single species. Furthermore, the $Pt(4f_{7/2})$ binding energies observed for the adsorbed complex prior to electron irradiation are consistent with a Pt(II) species.[62] Moreover, upon adsorption of **1** onto both substrates, single peaks are observed in the C(1s) and O(1s) regions, with binding energies characteristic of carbonyl ligands.[58,59]

4.4.3    Effect of Electron Irradiation.

A comparison of the XPS results obtained on $SiO_2$ and a:C substrates reveals that the surface reactions of *cis*-$Pt(CO)_2Cl_2$ with electrons occur at similar rates to produce similar deposits (Figures 1-5). This is perhaps most clearly demonstrated by the decrease of the binding energy of Pt at similar rates on both substrates, for electron doses $< \approx 2$ x $10^{16}$ e$^-$/cm$^2$. Moreover, similar changes in the Cl(2p) region were observed during irradiation. These similarities indicate that the chemical transformations occur solely as a result of electron stimulated reactions with the adsorbed *cis*-$Pt(CO)_2Cl_2$ molecules and are not dependent on specific adsorbate-substrate interactions. Indeed, the composition of the

substrate did not affect the chemical reactions observed during the low temperature, electron induced reactions of *cis*-Pt(CO)$_2$Cl$_2$, as determined by XPS and MS.

### 4.4.4    Reactions of Adsorbed **1** at Low Electron Doses ($< \approx 2 \times 10^{16}$ e$^-$/cm$^2$).

This regime is characterized by a significant number of changes in the XPS (Figures 1-5):  (a) a decrease in the Pt(4f$_{7/2}$) binding energy, (b) a loss of more than 50% of the carbon (Figures 1 - 3) and oxygen (Figures 4 and 5) from the film with a dependence on the electron dose that tracks the decrease in the Pt(4f$_{7/2}$) binding energy, (c) no change in the concentration of adsorbed Pt atoms and little or no change in the concentration of adsorbed Cl atoms (Figures 1 – 5) and (d) the transformation of the Cl(2p) region from one well-defined Cl(2p$_{3/2}$/2p$_{1/2}$) doublet to another, the latter shifted up in binding energy (Figures 1, 2, 4).  Figure 6 shows that almost all of the gas phase CO produced during the irradiation of adsorbed *cis*-Pt(CO)$_2$Cl$_2$ molecules is evolved in this regime.  All of these experimental observations can be attributed to the electron stimulated decomposition of the parent molecule (Eq. 1):

*cis*-Pt(CO)$_2$Cl$_2$ $_{(ads)}$ + e$^-_{(g)}$ → Pt(CO)$_{2-x}$Cl$_2$ $_{(ads)}$ + xCO(g) ↑(x = 1 - 2)            (1)
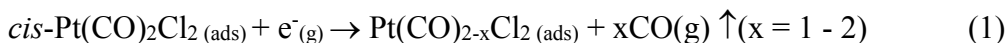
Loss of CO ligands during the initial stages of electron irradiation is clearly shown by mass spectrometry of the volatile species (Figure 6) and the loss of carbon and oxygen atoms from the surface (Figures 1, 2 and 4).  The fractional change in the concentration of adsorbed oxygen and carbon atoms indicates that at least one of the two CO ligands present in *cis*-Pt(CO)$_2$Cl$_2$ is ejected during this step.  The decrease in binding energy of the Pt(CO)$_{2-x}$Cl$_2$ species compared to precursor **1** can be ascribed to the electron induced dissociation process and an increase of electron density at the metal center due to loss of π-acid CO

ligands, as we have seen for other organometallic complexes.[38,42,43] The binding energy

shift in the Cl region reflects the changes in electronic structure of the adsorbed Pt species

upon partial decarbonylation. These changes are accompanied by broadening of the Pt(4f)

and Cl(2p) regions during the earliest stages of the reaction (see for example, the Pt(4f)

region in Figure 4 for electron doses $< 1 \times 10^{16}$ e$^-$/cm$^2$) as the ratio of starting material (*cis*-

Pt(CO)$_2$Cl$_2$) to products (Pt(CO)$_{2-x}$Cl$_2$ species) changes. The peaks then sharpen with

further electron irradiation as the product Pt(CO)$_{2-x}$Cl$_2$ species become dominant. The

conversion of the adlayer from adsorbed *cis*-Pt(CO)$_2$Cl$_2$ to adsorbed Pt(CO)$_{2-x}$Cl$_2$ also

explains the correlation between the Pt(4f$_{7/2}$) binding energy and the decrease in

concentration of adsorbed carbon and oxygen. The electron stimulated decomposition of

adsorbed *cis*-Pt(CO)$_2$Cl$_2$ in the early stage of the reaction is in accord with the results of

previous studies,[38,42,43] in which the extent of CO dissociation corresponds to a value

between one and two CO ligands per metal and reflects the statistical nature of the electron

induced dissociation process. At this stage, the vast majority of the halide ligands remain.

4.4.5    Reactions of Adsorbed **1** at Intermediate Electron Doses ($\approx 2 \times 10^{16}$ e$^-$/cm$^2$ $- \approx 1 \times 10^{17}$ e$^-$/cm$^2$).

In this regime there are a relatively small number of changes observed by XPS and MS.

The Pt(4f$_{7/2}$) and Cl(2p$_{3/2}$) binding energies and the spectral intensities in the Pt(4f), O(1s)

and Cl(2p) regions all remain relatively unchanged (Figures 2 - 5). Little if any CO is

evolved (Figure 6). The only significant changes occur in the C(1s) region of the XPS

where the intensity of the carbonyl peak decreases, along with the concomitant increase in

intensity of a new spectral feature at $\approx 284.5$ eV which can be ascribed to graphitic carbon

(see Figure 2). These changes in the appearance of the C(1s) region, in the absence of any

change in the integrated spectral intensity, are consistent with small amounts of CO decomposition in the partially decarbonylated $Pt(CO)_{2-x}Cl_2$ species (Eq. 2):

$$(CO)_{(ads)} + e^-_{(g)} \rightarrow C_{(ads)} + O_{(g)}\uparrow \qquad (2)$$
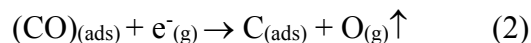
The fate of the oxygen atoms in this CO decomposition step cannot be directly determined from the experimental data, although the absence of any new spectral feature in the O(1s) region during electron irradiation (see Figures 1,2 and 4), coupled with the lower fractional concentration of residual oxygen ($\approx 0.2$) as compared to carbon ($\approx 0.4$) in this intermediate electron dose regime suggests that that the oxygen desorbs. Analysis of the C(1s) region in Figure 2 reveals that the CO decomposition described in equation (2) is, however, significantly less efficient than the CO desorption observed for electron doses $< \approx 2$ x $10^{16}$ $e^-/cm^2$; thus, after an electron dose of 5.1 x $10^{16}$ $e^-/cm^2$ the C(1s) region indicates approximately equal amounts of residual CO and graphitic carbon. A detectable population of CO exists even after an electron dose of 8.9 x $10^{16}$ $e^-/cm^2$. In contrast to previous studies on $W(CO)_6$,[42] in which ligand decomposition leads to extensive carbon contamination and tungsten oxidation due to the oxophilicity of tungsten, the electron induced decomposition of *cis*-$Pt(CO)_2Cl_2$ affords minimal carbon incorporation into the Pt deposits.

To determine the rate of precursor decomposition we performed a spectral deconvolution of the Pt 4f region into two Pt $4f_{7/2}$ and $4f_{5/2}$ doublets (data not shown), one doublet associated with the "as deposited" parent $Pt(CO)_2Cl_2$ species (observed initially) and the other associated with the final reduced Pt species observed after prolonged irradiation. Using this approach, we were able to determine that the loss of the parent $Pt(CO)_2Cl_2$ species could be reasonably well fit by an exponential decay process indicative of a one electron decomposition event typical for FEBID. Analysis of this decay profile

enabled us to determine a total reaction cross-section of $\approx 1.5 \times 10^{-16}$ cm$^2$ for the 500eV incident electrons, comparable to reaction cross-sections we have calculated for other FEBID precursors.[37,38,64,65]

4.4.6    Reactions of Adsorbed **1** at Larger Electron Doses ($> 1 \times 10^{17}$ e$^-$/cm$^2$).

For these significantly larger electron doses the changes to the adsorbate layer (Figures 7 and S4) are dominated by the loss of chlorine and the concomitant decrease in the Pt(4f$_{7/2}$) binding energy. The loss of Cl from the film is ascribed to an electron-stimulated desorption (ESD) type process[47,66-68] (Eq. 3).

$$Pt\text{-}Cl_{(ads)} + e^- \rightarrow Pt_{(ads)} + Cl^-_{(g)}\uparrow \qquad (3)$$
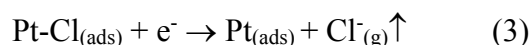
The onset of this step is evident in the earlier stages of electron irradiation (see Figure 3), in which the Cl(2p) peak area is seen to decrease by $\approx 20\%$ of its initial value as the electron dose increases from $\approx 2 \times 10^{16}$ e$^-$/cm$^2$ – $1 \times 10^{17}$ e$^-$/cm$^2$.  A comparison of Figures 3, 5 and 7 reveals that this ESD process is several orders of magnitude less efficient than the electron stimulated decomposition of **1**.  Consequently, this ESD process can be regarded as a form of electron beam processing that occurs after initial decomposition of **1**.  The loss of chlorine is a result of Pt-Cl bond cleavage and therefore correlates with the decrease in the average Pt 4f$_{7/2}$ binding energy (Figure 7).  Aside from the loss of Cl and its effect on the local electronic environment of the Pt atoms, no other significant chemical transformations occur; no CO evolution is detected by MS in this electron dose regime (Figure 6) and there are also no significant changes to the oxygen concentration as measured by XPS (Figure S4).

In summary, the XPS and MS data (Figures 1 – 7) reveal that adsorbed *cis*-Pt(CO)$_2$Cl$_2$ (**1**) decomposes through the electron stimulated desorption of at least one CO ligand. Subsequent irradiation of the partially decarbonylated Pt(CO)$_{2-x}$Cl$_2$ species leads to limited decomposition of the residual CO ligands. With additional electron dose, a less efficient electron stimulated desorption process removes almost all of the adsorbed chlorine atoms. Of note, the fate of the CO ligands and halogen atoms is analogous to what we observed for [($\eta^3$-C$_3$H$_5$)Ru(CO)$_3$Br],[38] supporting the idea that electron stimulated reactions of organometallic complexes can be predicted based on their ligands. It should be noted that the electron doses used in these UHV surface science studies are on the same order of magnitude compared to typical single loop FEBID processes (for example a 100 pA beam focused to about 10 nm$^2$, for a dwell time of 1 μs, results in an electron dose of ~6 x 10$^{15}$ e$^-$/cm$^2$).

### 4.4.7 Bonding environment of Pt atoms.

The effect of electron irradiation on the electronic environment of the adsorbed Pt atoms during the course of the reaction is best described by following the changes in the Pt(4f$_{7/2}$) binding energy (Figure 8). Prior to electron irradiation the Pt(4f$_{7/2}$) binding energy on a:C is 74.8 eV, indicative of Pt atoms in the +2 oxidation state of *cis*-Pt(CO)$_2$Cl$_2$.[62] During the initial electron induced dissociation of *cis*-Pt(CO)$_2$Cl$_2$ the Pt(4f$_{7/2}$) binding energy decreases by $\approx$ 2.3 eV. Partial decomposition of the residual CO ligands does not change the Pt(4f$_{7/2}$) binding energy, although the subsequent (and significantly slower) removal of the electronegative chlorine atoms does lead to a further decrease in the Pt(4f$_{7/2}$) binding energy to 71.4 eV. This final value is similar to the Pt(4f$_{7/2}$) binding energy of 71.1 eV we have measured previously for pure Pt in the same XPS system.[37] Thus, the Pt

present after prolonged electron irradiation of *cis*-Pt(CO)$_2$Cl$_2$ is close to metallic in character, with the small difference in binding energy of ~0.3 eV likely arising from the presence of carbon that limits the formation of a dense and continuous metallic film.

### 4.4.8    Deposition from **1** in the Auger Spectrometer.

The UHV surface science studies (Figures 1 – 7) were conducted at low temperatures ($< 200$ K), under conditions which enable us to elucidate the electron stimulated reactions in thin films of **1**.  In contrast, the deposits created in the Auger spectrometer are generated on a room temperature substrate which is being continuously irradiated by electrons while being simultaneously exposed to a constant partial pressure of *cis*-Pt(CO)$_2$Cl$_2$ molecules, representative of deposition conditions used in typical FEBID experiments.[1-4]  The Auger and EDS data shown in Figure 9 are consistent with deposits composed almost exclusively of Pt and Cl atoms, with a $\approx$ 1:2 Pt:Cl stoichiometry that matches the precursor.  The SEM image and Auger elemental maps (Figure 9) confirm that the deposits are spatially localized with a size and shape that is determined by the incident electron beam and thus do not arise from any conformal chemical vapor deposition (CVD) type deposition.  The chemical composition of the structures is consistent with CO desorption during focused electron beam induced deposition, broadly consistent with the UHV surface science data.

The presence of chloride in the deposits created in the Auger spectrometer can be ascribed to the limited electron dose that each *cis*-Pt(CO)$_2$Cl$_2$ molecule experiences during deposition.  Under the steady state deposition conditions of the AES experiments, electron irradiation/processing of the deposits, which would lead to removal of halogen atoms via the ESD process (Figure 7), competes with electron-stimulated decomposition of incoming *cis*-Pt(CO)$_2$Cl$_2$ molecules and the resulting deposition of new material.  Under the

conditions described in Figure 9, the deposition rate is greater than the rate of Cl removal by ESD, and as a result Cl is retained as the deposit grows. This preference for deposition over electron beam processing of the $PtCl_2$ deposits is not surprising given that the rate of precursor decomposition (Eq. 1, Figures 1–5) is clearly several orders of magnitude greater than the rate of Cl atom removal (Eq. 2).

The one notable difference between the films generated under UHV conditions and the deposits created under steady state AES deposition conditions is the extent of CO loss. In the UHV surface science studies, between one and two CO ligands are lost while the AES and EDS data on deposits created under steady state deposition conditions both indicate the formation of $PtCl_2$, without any significant carbon or oxygen contamination. In this respect the most significant difference in the two sets of deposition conditions is the substrate temperature. In the UHV surface science studies, the substrate temperatures are < 200K. However, in practical FEBID the substrate is at room temperature and there are often local heating effects due to the limited conductivity of the substrate and deposit (particularly likely for an ionic compound such as $PtCl_2$) and the high intensities and energies of the incident electron beams. Previous studies[69] have shown that as the substrate temperature increases during deposition, ligands can be lost by thermal desorption from intermediates produced in the initial electron stimulated decomposition of precursor. In the present case, our results suggest that residual CO groups in the partially decarbonylated intermediates thermally desorb during steady state deposition, in preference to CO decomposition, which would produce carbon and oxygen impurities in the deposit. Analogous processes have previously been observed for other metal carbonyls used in

FEBID.[69] Thus, the precursor decomposition process described in Eq. 1 is followed by thermal carbonyl loss (Eq. 4) to afford deposits of $PtCl_2$.

$$Pt(CO)_{2-x}Cl_{2\,(ads)} + \Delta \rightarrow PtCl_{2\,(ads)} + (2-x)\,CO(g)\uparrow\ (x = 1 - 2) \qquad (4)$$
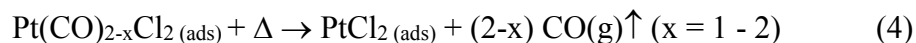
It is therefore apparent that the ultimate chemical composition of FEBID deposits is not governed exclusively by electron stimulated processes. Other processes, such as thermal reactions of intermediate species can play an important role. Moreover, comparison of the chemical compositions of the deposits created in this study is in general agreement with our previous studies on other FEBID precursors,[40,42,43,65] where data acquired under low temperature UHV conditions provide a semi-quantitative guide to the chemical composition of the deposits created under typical FEBID conditions.

### 4.4.9    *cis*-Pt(CO)$_2$Cl$_2$ as a FEBID precursor.

Our results demonstrate that *cis*-Pt(CO)$_2$Cl$_2$ (**1**) can be used to create spatially well-defined deposits free of any conformal deposition. Moreover, FEBID structures created from **1** under steady state deposition conditions in the Auger spectrometer were determined to be $PtCl_2$, free of carbon and oxygen in sharp contrast to the high levels of carbon contamination observed with other carbon-containing Pt FEBID precursors, such as MeCpPtMe$_3$ and Pt(hfac)$_2$.[2,40] The lack of carbon contamination in FEBID deposits from **1** is particularly significant because carbon impurities are notoriously difficult to remove in subsequent purification steps. Although deposits from **1** contain chlorine, we have demonstrated in the UHV studies that post-deposition processing by electron beam irradiation would result in halogen removal from the deposits. Due to the slower process of halide removal, deposits produced from **1** would be predicted to have higher metal

contents if the reaction is carried out in the precursor limited regime. In summary, our results demonstrate that the electron stimulated reactivity of organometallic precursors can be predicted from their ligands, and in the case of *cis*-Pt(CO)$_2$Cl$_2$ reveal a pathway to high metal content Pt FEBID structures through deposition from **1** followed by electron beam processing. Studies on purification strategies for FEBID structures created from *cis*-Pt(CO)$_2$Cl$_2$ are underway.

## 4.5. Conclusion

Electron irradiation of a thin layer of *cis*-Pt(CO)$_2$Cl$_2$ (**1**) during low temperature UHV surface science studies initially results in ejection of CO ligands into the gas phase. Upon continued electron irradiation, the chlorine is removed from the deposits via a less efficient electron-stimulated desorption process, which simulates post-deposition electron-beam processing in FEBID. At this stage of the surface reaction, the XPS binding energy of Pt is similar to metallic platinum. Deposits formed from **1** in an Auger spectrometer, which mimics the steady deposition conditions used in FEBID, were composed exclusively of platinum and chlorine atoms, with no contamination from carbon or oxygen. Coupled with the electron-stimulated removal of chlorine demonstrated in the UHV experiments, the Auger data establish a route to FEBID of pure Pt. In this study, we have demonstrated that mechanistic information from surface science studies of electron-induced reactions of organometallic precursors can be used to successfully identify a precursor for FEBID, supporting the idea that mechanism based precursor design could be broadly applicable to a variety of deposition techniques.

4.6. Acknowledgments.

The use of the surface analysis laboratory at Johns Hopkins University is acknowledged.

4.7. Supporting Information
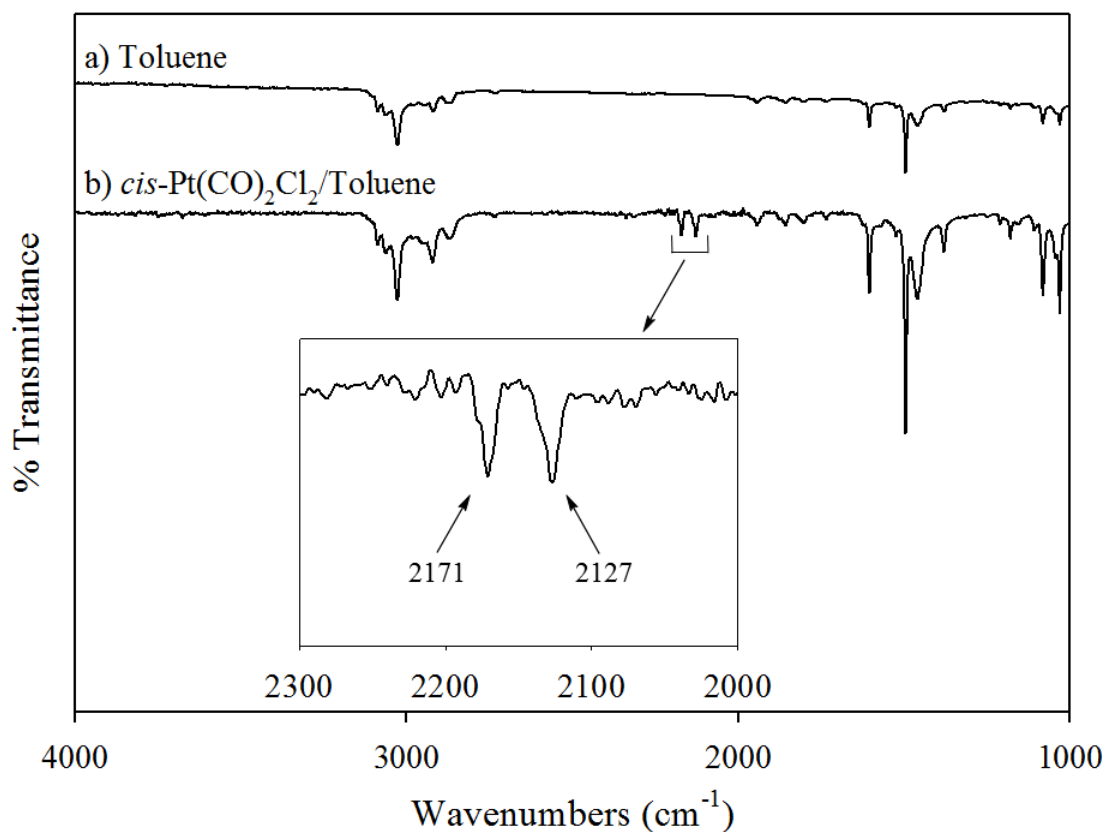


**Supporting Information, Figure 4.1:** Attenuated Total Reflectance (ATR) Infrared spectra for (a) toluene (shown as reference) and (b) *cis*-Pt(CO)$_2$Cl$_2$ in toluene. Aside from CO symmetric and asymmetric stretches shown in inset graph, all peaks in (b) are attributed to the toluene solvent.
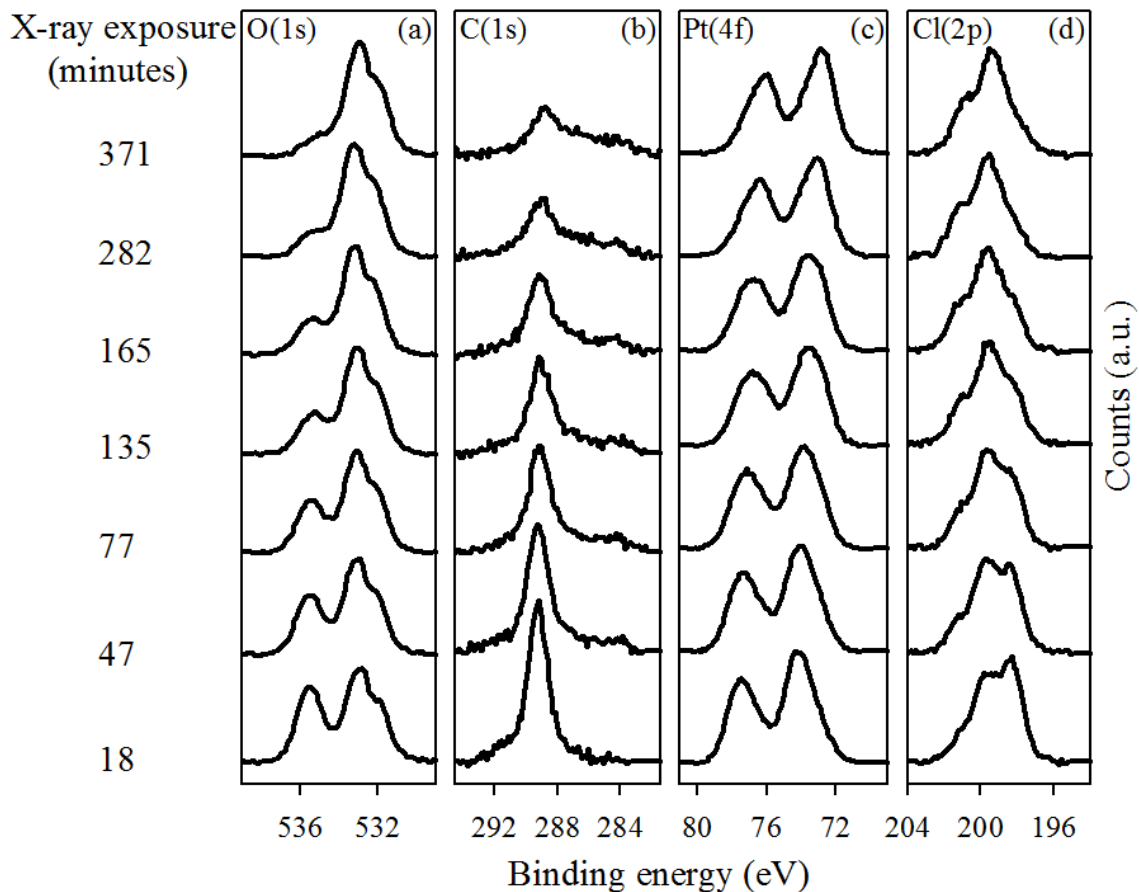
**Supporting Information, Figure 4.2:** Evolution of the a) O(1s), b) C(1s), c) Pt(4f) and d) Cl(2p) XP regions for a ~1.0 nm thick film of *cis*-Pt(CO)$_2$Cl$_2$ adsorbed on SiO$_2$, irradiated only with X-rays (Mg Kα 1253.6 eV) from the X-ray gun; the X-ray exposure time is shown on the left hand side of each spectrum.
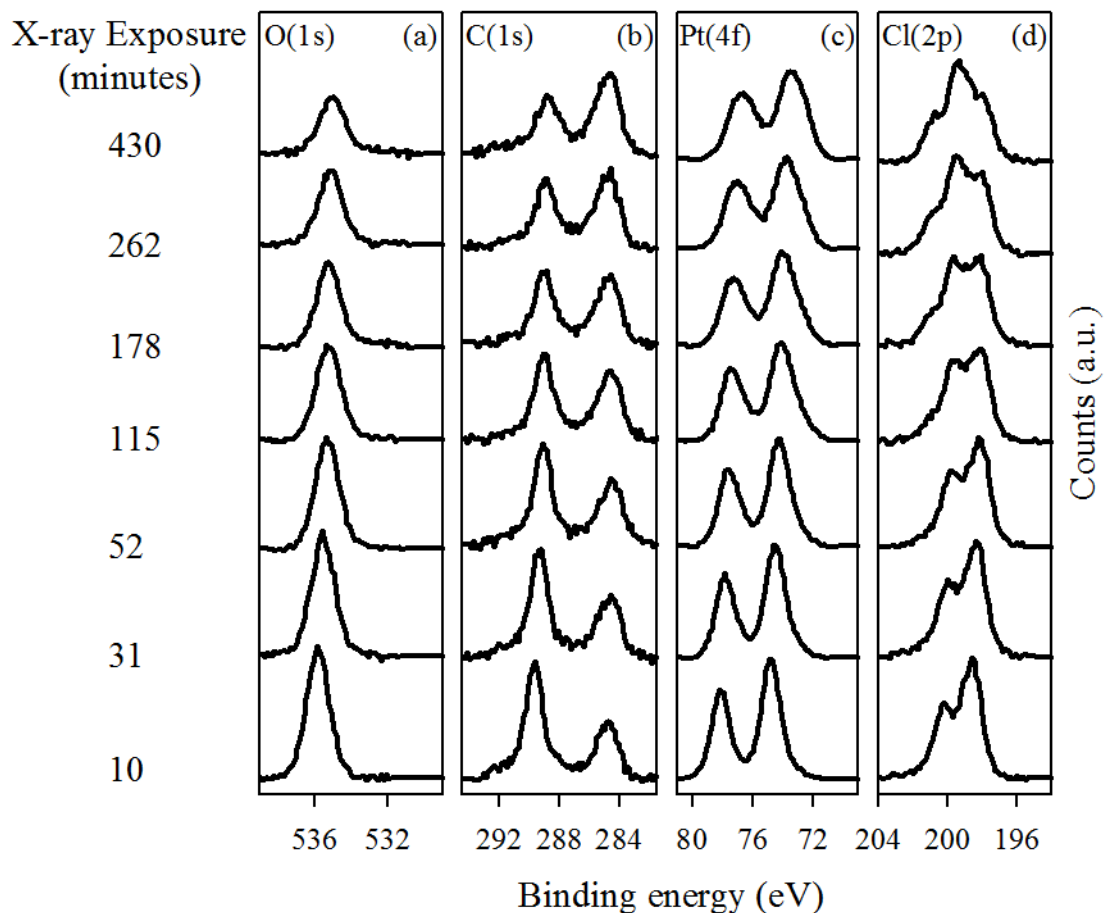
**Supporting Information, Figure 4.3:** Evolution of the a) O(1s), b) C(1s), c) Pt(4f) and d) Cl(2p) XP regions for a ~1.6 nm thick film of *cis*-Pt(CO)$_2$Cl$_2$ adsorbed on a:C, irradiated only with X-rays (Mg Kα 1253.6 eV) from the X-ray gun; the X-ray exposure time is shown on the left hand side of each spectrum.
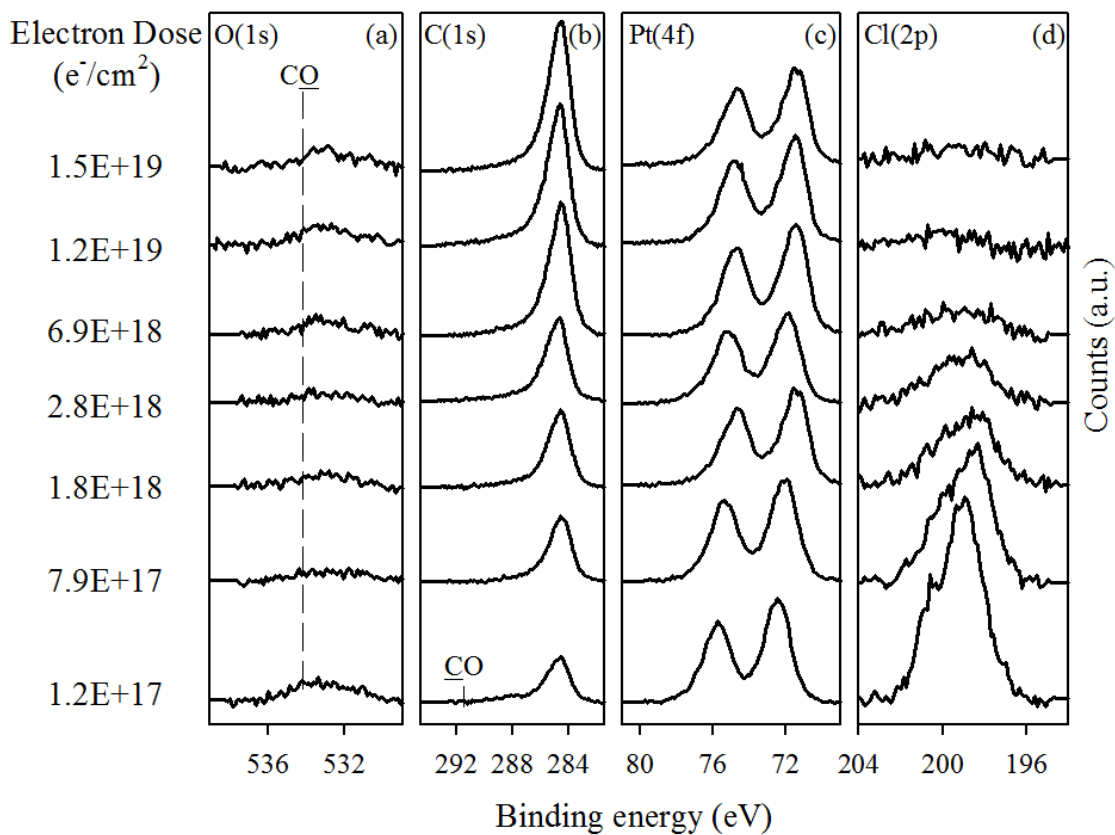
**Supporting Information, Figure 4.4**: Evolution of the a) O(1s), b) C(1s), c) Pt(4f) and d) Cl(2p) XP regions for a 1.5 nm thick film of *cis*-PtCl$_2$(CO)$_2$ adsorbed on an a:C substrate and exposed to electron doses between 1.2 x 10$^{17}$ and 1.5 x10$^{19}$ e$^-$/cm$^2$.

## 4.8. References

(1)     Randolph, S.; Fowlkes, J.; Rack, P. *Crit. Rev. Solid State Mater. Sci.* **2006**, *31*, 55.

(2)     Utke, I.; Hoffmann, P.; Melngailis, J. *J. Vac. Sci. Technol. B* **2008**, *26*, 1197.

(3)     Van Dorp, W.; Hagen, C. *J. Appl. Phys.* **2008**, *104*, 081301.

(4)     Huth, M.; Porrati, F.; Schwalb, C.; Winhold, M.; Sachser, R.; Dukic, M.; Adams, J.; Fantner, G. *Beilstein J. Nanotech.* **2012**, *3*, 597.

(5)     Frey, L.; Lehrer, C.; Ryssel, H. *Appl Phys A: Mater. Sci. Process.* **2003**, *76*, 1017.

(6)     Fujii, T.; Iwasaki, K.; Munekane, M.; Takeuchi, T.; Hasuda, M.; Asahata, T.; Kiyohara, M.; Kogure, T.; Kijima, Y.; Kaito, T. *J. Micrormechan. Microeng.* **2005**, *15*, S286.

(7)     Van Dorp, W. F. *Nano Letters* **2005**, *5*, 1303.

(8)     Volkert, C. A.; Minor, A. M. *MRS Bulletin* **2007**, *32*, 389.

(9)     Kim, C.-S.; Ahn, S.-H.; Jang, D.-Y. *Vacuum* **2012**, *86*, 1014.

(10)    Hagen, C. *Appl. Phys. A* **2014**, *117*, 1599.

(11)    Duan, H. G.; Winston, D.; Yang, J. K. W.; Cord, B. M.; Manfrinato, V. R.; Berggren, K. K. *J. Vac. Sci. Technol. B* **2010**, *28*, C6C58.

(12)    Grigorescu, A.; Hagen, C. *Nanotechnology* **2009**, *20*, 292001.

(13)    Manfrinato, V. R.; Wen, J.; Zhang, L.; Yang, Y.; Hobbs, R. G.; Baker, B.; Su, D.; Zakharov, D.; Zaluzec, N. J.; Miller, D. J. *Nano letters* **2014**, *14*, 4406.

(14)    Silverman, P. J. *J. Micro/Nanolithography, MEMS, and MOEMS* **2005**, *4*, 011006.

(15)    Wu, B.; Kumar, A. *J. Vac. Sci. Technol. B* **2007**, *25*, 1743.

(16)    Edinger, K.; Becht, H.; Bihr, J.; Boegli, V.; Budach, M.; Hofmann, T.; Koops, H. W.; Kuschnerus, P.; Oster, J.; Spies, P. *J. Vac. Sci. Technol. B* **2004**, *22*, 2902.

(17)    Heerkens, C. T. H.; Kamerbeek, M.; van Dorp, W.; Hagen, C.; Hoekstra, J. *Microelectron. Eng.* **2009**, *86*, 961.

(18)    Liang, T.; Frendberg, E.; Lieberman, B.; Stivers, A. *J. Vac. Sci. Technol. B* **2005**, *23*, 3101.

(19)    Perentes, A.; Hoffmann, P. *Chem. Vap. Deposition* **2007**, *13*, 176.

(20)    Chen, I.-C.; Chen, L.-H.; Orme, C.; Quist, A.; Lal, R.; Jin, S. *Nanotechnology* **2006**, *17*, 4322.

(21)    Hübner, B.; Koops, H.; Pagnia, H.; Sotnik, N.; Urban, J.; Weber, M. *Ultramicroscopy* **1992**, *42*, 1519.

(22)    Graells, S.; Alcubilla, R.; Badenes, G.; Quidant, R. *Appl. Phys. Lett.* **2007**, *91*, 121112.

(23)    Koops, H.; Hoinkis, O.; Honsberg, M.; Schmidt, R.; Blum, R.; Böttger, G.; Kuligk, A.; Liguda, C.; Eich, M. *Microelectron. Eng.* **2001**, *57*, 995.

(24)    Weber-Bargioni, A.; Schwartzberg, A.; Schmidt, M.; Harteneck, B.; Ogletree, D.; Schuck, P.; Cabrini, S. *Nanotechnology* **2010**, *21*, 065306.

(25)    Botman, A.; Mulders, J.; Hagen, C. *Nanotechnology* **2009**, *20*, 372001.

(26)    Botman, A.; Mulders, J. J. L.; Weemaes, R.; Mentink, S. *Nanotechnology* **2006**, *17*, 3779.

(27)    Mulders, J.; Veerhoek, J.; Bosch, E.; Trompenaars, P. *J. Phys. D: Appl. Phys.* **2012**, *45*, 475301.

(28)    Porrati, F.; Sachser, R.; Huth, M. *Nanotechnology* **2009**, *20*, 195301.

(29)    Huth, M.; Klingenberger, D.; Grimm, C.; Porrati, F.; Sachser, R. *New J. Phys.* **2009**, *11*, 033032.

(30)    van Dorp, W.; Wu, X.; Mulders, J.; Harder, S.; Rudolf, P.; De Hosson, J. *Langmuir* **2014**, *30*, 12097.

(31)    Xue, Z.; Strouse, M. J.; Shuh, D. K.; Knobler, C. B.; Kaesz, H. D.; Hicks, R. F.; Williams, R. S. *J. Am. Chem. Soc.* **1989**, *111*, 8779.

(32)    Plank, H.; Noh, J. H.; Fowlkes, J. D.; Lester, K.; Lewis, B. B.; Rack, P. D. *ACS Appl. Mater. Interfaces* **2014**, *6*, 1018.

(33)    Geier, B.; Gspan, C.; Winkler, R.; Schmied, R.; Fowlkes, J. D.; Fitzek, H.; Rauch, S.; Rattenberger, J.; Rack, P. D.; Plank, H. *J. Phys. Chem. C* **2014**, *118*, 14009.

(34)    Sachser, R.; Reith, H.; Huzel, D.; Winhold, M.; Huth, M. *ACS Appl. Mater. Interfaces* **2014**, *6*, 15868.

(35)    Villamor, E.; Casanova, F.; Trompenaars, P.; Mulders, J. *Nanotechnology* **2015**, *26*, 095303.

(36)    Wnuk, J.; Rosenberg, S.; Gorham, J.; Van Dorp, W.; Hagen, C.; Fairbrother, D. *Surf. Sci.* **2011**, *605*, 257.

(37)    Wnuk, J. D.; Gorham, J. M.; Rosenberg, S. G.; van Dorp, W. F.; Madey, T. E.; Hagen, C. W.; Fairbrother, D. H. *J. Phys. Chem. C* **2009**, *113*, 2487.

(38)    Spencer, J. A.; Brannaka, J. A.; Barclay, M.; McElwee-White, L.; Fairbrother, D. H. *J. Phys. Chem. C* **2015**, *119*, 15349−15359.

(39)    Engmann, S.; Stano, M.; Matejc, S.; Ingolfsson, O. *Phys. Chem. Chem. Phys.* **2012**, *14*, 14611.

(40)    Rosenberg, S. G.; Barclay, M.; Fairbrother, D. H. *ACS Appl. Mater. Interfaces* **2014**, *6*, 8590.

(41)    Wnuk, J. D.; Gorham, J. M.; Rosenberg, S. G.; van Dorp, W. F.; Madey, T. E.; Hagen, C. W.; Fairbrother, D. H. *J. Appl. Phys.* **2010**, *107*, 054301/1.

(42)    Rosenberg, S. G.; Barclay, M.; Fairbrother, D. H. *Phys. Chem. Chem. Phys.* **2013**, *15*, 4002.

(43)    Rosenberg, S. G.; Barclay, M.; Fairbrother, D. H. *J. Phys. Chem. C* **2013**, *117*, 16053.

(44)    Dobrovolskiy, O. V.; Kompaniiets, M.; Sachser, R.; Porrati, F.; Gspan, C.; Plank, H.; Huth, M. *Beilstein J Nanotechnol* **2015**, *6*, 1082.

(45)    Fernández-Pacheco, A.; De Teresa, J.; Córdoba, R.; Ibarra, M. R. *J. Phys. D: Appl. Phys.* **2009**, *42*, 055005.

(46)    Muthukumar, K.; Jeschke, H. O.; Valentí, R.; Begun, E.; Schwenk, J.; Porrati, F.; Huth, M. *Beilstein J. Nanotech.* **2012**, *3*, 546.

(47)    Madey, T. E.; Yates Jr, J. T. *J. Vac. Sci. Technol.* **1971**, *8*, 525.

(48)    Rosenberg, S. G.; Landheer, K.; Hagen, C. W.; Fairbrother, D. H. *J. Vac. Sci. Technol. B* **2012**, *30*, 051805/1.

(49)    Bagnoli, F.; Dell'Amico, D. B.; Calderazzo, F.; Englert, U.; Marchetti, F.; Herberich, G. E.; Pasqualetti, N.; Ramello, S. *J. Chem. Soc., Dalton Trans.* **1996**, 4317.

(50)    Calderazzo, F. *J Organomet. Chem.* **1990**, *400*, 303.

(51)    Lutton, J.; Parry, R. *J. Am. Chem. Soc.* **1954**, *76*, 4271.

(52)    Bajt, S.; Alameda, J. B.; Barbee, T. W.; Clift, W. M.; Folta, J. A.; Kaufmann, B.; Spiller, E. A. *Opt. Eng.* **2002**, *41*, 1797.

(53)    Powell, C. J.; Jablonski, A. *NIST Electron Inelastic-Mean-Free-Path Database, Version 1.2, SRD 71*; National Institute of Standards and Technology: Gaithersburg, MD, USA, 2010.

(54)    Tanuma, S.; Powell, C. J.; Penn, D. R. *Surface and Interface Analysis* **1991**, *17*, 911.

(55)    Tanuma, S.; Powell, C.; Penn, D. *Surf. Interface Anal.* **2011**, *43*, 689.

(56)    Estrade-Szwarckopf, H. *Carbon* **2004**, *42*, 1713.

(57)    Blair, D.; Rogers Jr, J.; Peden, C. *J. Appl. Phys.* **1990**, *67*, 2066.

(58)    Plummer, E.; Salaneck, W.; Miller, J. S. *Phys. Rev. B* **1978**, *18*, 1673.

(59)    Barber, M.; Connor, J.; Guest, M.; Hall, M.; Hillier, I.; Meredith, W. *Faraday Disc.* **1972**, *54*, 219.

(60)    Himpsel, F.; McFeely, F.; Taleb-Ibrahimi, A.; Yarmoff, J.; Hollinger, G. *Phys. Rev. B* **1988**, *38*, 6084.

(61)    Alam, A.; Howlader, M.; Deen, M. *ECS J. Solid State Sci. Technol.* **2013**, *2*, P515.

(62)    Riggs, W. *Anal. Chem.* **1972**, *44*, 830.

(63)    Utke, I.; Hoffmann, P.; Dwir, B.; Leifer, K.; Kapon, E.; Doppelt, P. *J. Vac. Sci. Technol. B* **2000**, *18*, 3168.

(64)    van Dorp, W. F.; Wnuk, J. D.; Gorham, J. M.; Fairbrother, D. H.; Madey, T. E.; Hagen, C. W. *J. Appl. Phys.* **2009**, *106*, 074903.

(65)    Landheer, K.; Rosenberg, S.; Bernau, L.; Swiderek, P.; Utke, I.; Hagen, C.; Fairbrother, D. H. *J. Phys. Chem. C* **2011**, *115*, 17452.

(66)    Tegeder, P.; Smirnov, B. M.; Illenberger, E. *Int. J. Mass Spectrom.* **2001**, *205*, 331.

(67)    Trenhaile, B. R.; Antonov, V. N.; Xu, G. J.; Agrawal, A.; Signor, A. W.; Butera, R. E.; Nakayama, K. S.; Weaver, J. H. *Phys. Rev. B* **2006**, *73*.

(68)    Walter, W. K.; Jones, R. G. *J. Phys.: Condens. Matter* **1989**, *1*, SB201.

(69)    Mulders, J. J. L.; Belova, L. M.; Riazanova, A. *Nanotechnology* **2011**, *22*, 055302.

Chapter 5


Purification of Platinum-Containing Nanostructures Using

Electrons and Atomic Hydrogen Radicals

Chapter 5.    Purification of Pt-containing Nanostructures with Electrons and Atomic Hydrogen Radicals

## 5.1. Introduction

As integrated circuits and technology continue to drive towards smaller features, the microchip industry is searching for the next processing innovation.  It might be an improvement in photolithography techniques, or use of extreme ultraviolet lithography (EUVL).  However, there is another developing technology that has potential in fabricating structures on the nanoscale, focused electron beam induced processing, or FEBIP.  FEBIP is comprised of focused electron beam induced etching (FEBIE) and focused electron beam induced deposition (FEBID)[1,2].  This work will focus on the emerging technique of FEBID.  FEBID is a relatively simple process that does not require any resists or masks.  In FEBID, a gaseous precursor is introduced into a vacuum chamber (typically a modified SEM) and irradiated by a focused electron beam[1-4].  The precursor decomposes under electron beam irradiation, with the central atom (often a metal) left behind while the volatile portions of the precursor desorb and are pumped away into the gas phase.  The size and shape of the nanostructure are only limited by the focusing ability and manipulation of the electron beam.  Despite the significant promise of a process that is essentially direct writing of nanostructures, FEBID has several technological drawbacks that prevent its wide application.  Two major drawbacks are processing speed and deposit purity.  Research is ongoing into schemes to increase throughput by methods such as multiple electron beams[5]. The research discussed in this chapter focuses on the methods to improve purity of platinum containing structures created by FEBID.

An ideal FEBID precursor needs to balance several somewhat conflicting

requirements[6,7]. For example, a good precursor needs to be volatile enough to sublime, and must have a long enough residence time on a surface so that it may be decomposed by the focused electron beam. It should not be extremely toxic, nor damaging to the instrument used in FEBID. To achieve an optimal precursor, these requirements must all be considered[1,2]. The goal in FEBID is that the precursor would deposit a pure metal and all the ligands would desorb, leaving behind a metallic deposit. Since FEBID has been an emerging area of research, the majority of work to date has used precursors that were optimized as chemical vapor deposition precursors[1,2], for example $Fe(CO)_5$, $W(CO)_6$ and $Pt(PF_3)_4$. Since FEBID is electron-based rather than heat-based, precursors which produce pure films in CVD often result in FEBID nanostructures with a high level of contamination, precluding their use in a wide range of applications. One such example is MeCpPtMe3, which produces pure Pt films in CVD, but results in FEBID structures containing < 20% Pt[8]. Despite the purity challenges, FEBID has already been used for a variety of applications, most notably fabrication of ultra-sharp tips[9,10] and lithographic mask repair[11-13].

Previous gas phase[14-18], surface science[6,19-22] and a wide variety of FEBID deposit research[1-4] has indicated that ligand architecture plays a large role in deposit purity for FEBID. Recently, ultrahigh vacuum (UHV) surface science studies have helped elucidate the contributions to contamination from common ligands used in FEBID precursors. The cyclopentadienyl ($\eta^5$-$C_5H_5$, Cp) ligand as well as the $\eta^3$-$C_3H_5$ ligand were found to remain behind in FEBID structures as a significant source of carbon contamination[22,23]. Small numbers of carbonyl (CO) and trifluorophosphine ($PF_3$) ligands were found to desorb readily (generally, two to three ligands), while greater numbers of ligands remain behind

on the surface and decompose, contributing to nanostructure contamination[19-21]. Halogens bonded directly to the metal center were found to act as somewhat of a "free" ligand, in that they were found to remain on the molecule initially, but are removed by a slower, electron stimulated desorption (ESD) mechanism[23,24]. By applying these design "rules," or guidelines, our previous work investigated the electron-induced surface reactions of *cis*-platinum dicarbonyl dichloride (*cis*-Pt(CO)$_2$Cl$_2$)[24]. This work indicated that electron beam irradiation of a thin film (nanometer scale) of *cis*-Pt(CO)$_2$Cl$_2$ initially resulted in loss of the carbonyl ligands, and then over a longer timeframe, loss of the chlorine, via a slower, electron stimulated desorption process, resulting in nearly pure Pt films.

In the absence of precursors that produce pure metal deposits in FEBID, significant research has been conducted into methods of purification or cleaning of FEBID structures, with varying degrees of success. Botman *et. al.*[25] detailed a variety of purification methods. Annealing nanostructures after deposition (or deposition on a heated substrate) is one method. Ervin *et. al.*[26] found that annealing of Pt(PF$_3$)$_4$ nanostructures improved resistivity and decreased P content, which was also observed in surface science studies of Pt(PF$_3$)$_4$ by Landheer *et. al.*[19] Post treatment with electrons in the presence of an oxygen flux has been used by several research groups[27-30] with the general result that metal purity was improved, but due to other variables, often there was nanostructure distortion. Geier *et. al.* reported full purification of nanostructures created from MeCpPtMe$_3$ with the use of electron post-processing in the presence of H$_2$O vapor[31], while Sachser *et. al.* demonstrated that due to the catalytic properties of Pt, an O$_2$ flux is sufficient to purify Pt containing nanostructures, when treated in a multi-step process[32]. Stanford *et. al.* reported a laser assisted electron beam induced deposition strategy in which a laser stimulates reactions to purify

136

nanostructures; they also investigated atomic layer deposition (ALD) type processes to improve nanostructure purity[33]. This listing of purification methods provides a sampling of the variety of different purification schemes being investigated to improve purity of FEBID nanostructures.

The study discussed in this chapter was conducted to more fully evaluate deposits formed from $cis$-Pt(CO)$_2$Cl$_2$, in a process closer to FEBID, and investigate purification strategies. Our deposits were created in a process analogous to FEBID, but using the 3 keV electron beam of an Auger spectrometer, rather than the typical 1 - 30 keV[1,2] electron beams used in SEMs for FEBID. This resulted in deposits that are much larger than typical FEBID deposits (on the micrometer scale rather than the nanometer scale), due the lower energy and less focused beam in the Auger spectrometer. One important difference between this work (Auger deposition experiments) as compared with previous work (adsorption of thin films on cold substrates in the XPS) is that in the Auger deposition experiments we are operating close to or in the electron limited regime (or in a combination of electron and precursor limited regimes), while the experiments conducted on thin films of adsorbed $cis$-Pt(CO)$_2$Cl$_2$ in the X-ray photoelectron spectrometer (XPS) operated in the precursor limited regime (there is a set amount of precursor[1,2] that is not continuously resupplied and is generally considered to fully react). This study investigated the effects of electron beam post-processing and atomic hydrogen purification on deposits created from $cis$-Pt(CO)$_2$Cl$_2$. Additionally, for a few experiments, other platinum containing precursors (MeCpPtMe$_3$, Pt(hfac)$_2$, and Pt(PF3)$_4$) were deposited and evaluated with atomic hydrogen purification.

## 5.2. Experimental

An ultrahigh vacuum (UHV) chamber equipped with an Auger Spectrometer (AES) was used to create structures from *cis*-platinum dicarbonyl dichloride (*cis*-Pt(CO)$_2$Cl$_2$) using electron irradiation under steady state deposition conditions. Further details of the chamber and its analytical capabilities can be found in earlier publications.[34-36]

### 5.2.1. Synthesis of *cis*-Pt(CO)$_2$Cl$_2$

#### 5.2.1.1. General (Synthesis)

All manipulations were performed under an inert atmosphere (Ar or N$_2$) using standard Schlenk line or glove box techniques, unless noted otherwise. Toluene and heptane were purified by using an M. Braun solvent purification (MB-SP) system and were stored over 3 Å molecular sieves prior to use. Benzene-$d_6$ (Cambridge Isotope Laboratories) was also stored over 3 Å molecular sieves in a glove box prior to use. Sulfuryl chloride and PtI$_2$ were purchased from Sigma-Aldrich and used as received.

#### 5.2.1.2. *cis*-Pt(CO)$_2$Cl$_2$ (**1**)

A modified literature procedure was used for synthesis of *cis*-Pt(CO)$_2$Cl$_2$.[37] Platinum(II) iodide (PtI$_2$, 1.0 g, 2.2 mmol) was suspended in toluene (25 mL) in a 50 mL Schlenk flask and stirred for 30 minutes under CO. Sulfuryl chloride (0.90 mL, 11.1 mmol) was then added and stirred for six hours to obtain a deep purple solution. The crude product from the toluene solution was recrystallized by adding *n*-heptane and overnight chilling to -20 °C to obtain the product *cis*-Pt(CO)$_2$Cl$_2$ as light-yellow or off-white needle crystals. The yield was 0.52 g (73.4 %). $^{13}$C NMR (C$_6$D$_6$, 500 MHz): δ 151.84. ATR-IR (toluene): $\nu_{co}$ 2127, 2171 cm$^{-1}$. The compound was identified by comparison to literature data.[38] ATR data are shown in the earlier investigation of this compound[24].

### 5.2.2. Introduction of *cis*-Pt(CO)$_2$Cl$_2$ (**1**) into the UHV chamber

Precursor **1** is a solid at standard temperature and pressure.[39]  The precursor was handled inside an N$_2$ glovebox due to its sensitivity to moisture and air.  Prior to deposition, the solid precursor was added to a glass finger, which was attached to a UHV compatible leak valve directly coupled to the UHV chamber.  The glass finger was evacuated at the same time as the UHV chamber was pumped down with the leak valve open into the 1.0 x 10$^{-6}$ Torr pressure regime.  At this point the leak valve was closed and the main chamber was baked out and restored to the UHV pressure regime.  To maintain a sufficient vapor pressure of *cis*-Pt(CO)$_2$Cl$_2$ during deposition, the precursor was heated to ~80 °C with the temperature monitored by a thermocouple.  Depositions were typically obtained with precursor **1** heated to ~80 °C (system pressure of ~4 x 10$^{-7}$ Torr).  Although the pressure of **1** decreased over time as it was depleted, even when heated to ~80 °C, we were still able to obtain Pt(CO)$_2$Cl$_2$ deposition in the Auger spectrometer with system pressures as low as 1 x 10$^{-9}$ Torr.

### 5.2.3. Substrates

Depositions from *cis*-Pt(CO)$_2$Cl$_2$ in the Auger spectrometer utilized atomically smooth Ru-capped Si/Mo multi-layer mirror substrates[40], and for a few experiments, SiO$_2$. The nature of the substrate did not play an apparent role in the electron stimulated reactions of the precursor.  The Ru-capped Si/Mo multi-layer mirror substrate was chosen for the majority of depositions due to its smoothness and ease with which deposits could be imaged in the scanning electron microscope.  Substrate cleanliness was verified by Auger spectroscopy prior to each deposition.

### 5.2.4. Creating Deposits in the Auger Spectrometer (AES)

Deposits were formed by leaking *cis*-$Pt(CO)_2Cl_2$ into the UHV chamber of a PHI 610 Scanning Auger Microprobe system ($LaB_6$ filament) via a UHV-compatible leak valve. A directional doser with the capability for extension and retraction and limited maneuverability was used to enhance the partial pressure of precursor at the substrate surface during deposition. The deposits were made under steady state deposition conditions with the substrate at room temperature using an incident beam energy of 3kV and varying substrate currents, precursor partial pressures and deposition times. Deposit thicknesses were not calculated but were assessed as suitably thick once the substrate peaks were no longer visible in the Auger spectrum.

### 5.2.5. Electron Source

The installed electron beam of the PHI 610 Scanning Auger Microprobe was used both to make deposits, to characterize the elemental composition of the deposits and to conduct post-electron beam processing. The beam was operated at 3kV, 80 μA emission current, and varying beam/target currents.

### 5.2.6. Scanning Electron Microscopy (SEM) and Energy Dispersive Spectroscopy (EDS)

Deposits generated in the Auger system were imaged using a cold-cathode field emission scanning electron microscope (JEOL 6700F, LEI detector) with a 1.0 nm resolution at 15 keV equipped with an energy dispersive X-ray analyzer (EDAX Genesis 4000 X-ray analysis system, detector resolution of 129 eV).

### 5.2.7. Wavelength dispersive spectroscopy (WDS)

For a few experiments, it was necessary to deconflict EDS interferences (for Pt M and P K lines), and this was done using a JEOL JXA-8600 Superprobe Scanning Electron Microscope (SEM) equipped with wavelength dispersive spectroscopy (WDS) capabilities.

### 5.2.8. Generation of Atomic Hydrogen Radicals

Atomic hydrogen radicals were produced in the Auger spectrometer *in situ*, with an installed thermal gas cracker (Oxford Applied Research). Hydrogen gas was passed through a heated iridium capillary tube to produce a consistent flux of atomic hydrogen radicals. The thermal cracker source was installed at a 45° angle to the substrate at a distance of approximately 5 cm; for atomic hydrogen purification experiments, the substrate was tilted such that it was approximately perpendicular to the thermal cracker source. The *in situ* atomic hydrogen purification was carried out with a $P_{H_2}$ pressure, measured by chamber pressure, of 5 x $10^{-7}$ Torr. The thermal cracker source is described in greater detail in an earlier publication[41].

The majority of atomic hydrogen purification was conducted *ex situ*, using a home built source, at the National Institute of Standards and Technology (NIST). This allowed use of a much higher pressure of $H_2$ gas, $P_{H_2}$ ~ 1 Torr, and thus, a significantly larger flux of atomic hydrogen radicals than generated with the *in situ* atomic hydrogen radical source.

5.3. Results

    5.3.1.   Electron Effects

Figure 1 shows general identifying characteristics for a typical deposit created in the Auger spectrometer from *cis*-Pt(CO)$_2$Cl$_2$. Figure 1a shows the Auger spectrum of a typical deposit, showing the surface composition, which is calculated to be 38.5 % Pt, 57.6 % Cl, with minimal C and O (spectral data not shown, 3.5% C, 0.5% O). Figure 1b and 1c show Auger elemental maps for a similar deposit, which were obtained by measuring the difference between a background signal and the Auger signal of interest (b) Pt MNN, 64 eV and (c) Cl LMM, 181 eV. Figure 1d and 1e show SEM data for a similar deposit. Figure 1d shows the EDS spectrum for the deposit image shown in Figure 1e. EDS elemental analysis shows that the deposit is composed of primarily Pt (34.3 %) and Cl (48.0 %), with small contributions from the substrate (0.8 % Si, 0.2 % Mo) and surface species (13.6 % C, 1.9 % O).

Figure 2 provides Auger data for a relatively thin deposit created from *cis*-Pt(CO)$_2$Cl$_2$. This deposit was subjected to electron beam irradiation for several hours. Figure 2 left pane shows progressive removal of Cl atoms until the vast majority of Cl has been removed from the deposit after ~10 hours of electron beam irradiation, producing a result similar to near complete Cl removal from thin films created in the XPS in our previous research[24]. Figure 2 right pane shows % Pt, % Cl, and Pt:Cl ratio. As the film is subjected to increasingly greater electron beam irradiation, Cl is systemically removed, until after approximately 10 hours of electron beam irradiation, less than 20 percent of the original Cl remains.

Figure 3 presents Auger data for a thicker deposit, one which is more representative

of typical deposits created in the Auger spectrometer. This deposit was created from *cis*-$Pt(CO)_2Cl_2$ with a deposition time of 22 hours (compared with 5.25 hours for the deposit shown in Figure 2). Figure 3 left pane shows Auger data as the deposit is subjected to 3kV electron beam irradiation. Initially, the deposit is composed of 35.3 % Pt and 64.7 % Cl, with minimal % C and % O (discounted in the figure as not the species of interest). Figure 3 right pane shows a graph tracking % Pt, % Cl and Pt:Cl ratio as the deposit undergoes electron beam irradiation. During electron beam irradiation, the Cl is initially removed, but Cl removal appears to reach a steady state value after ~7 hours of electron beam irradiation, as seen in both the Auger spectra and in the graph.
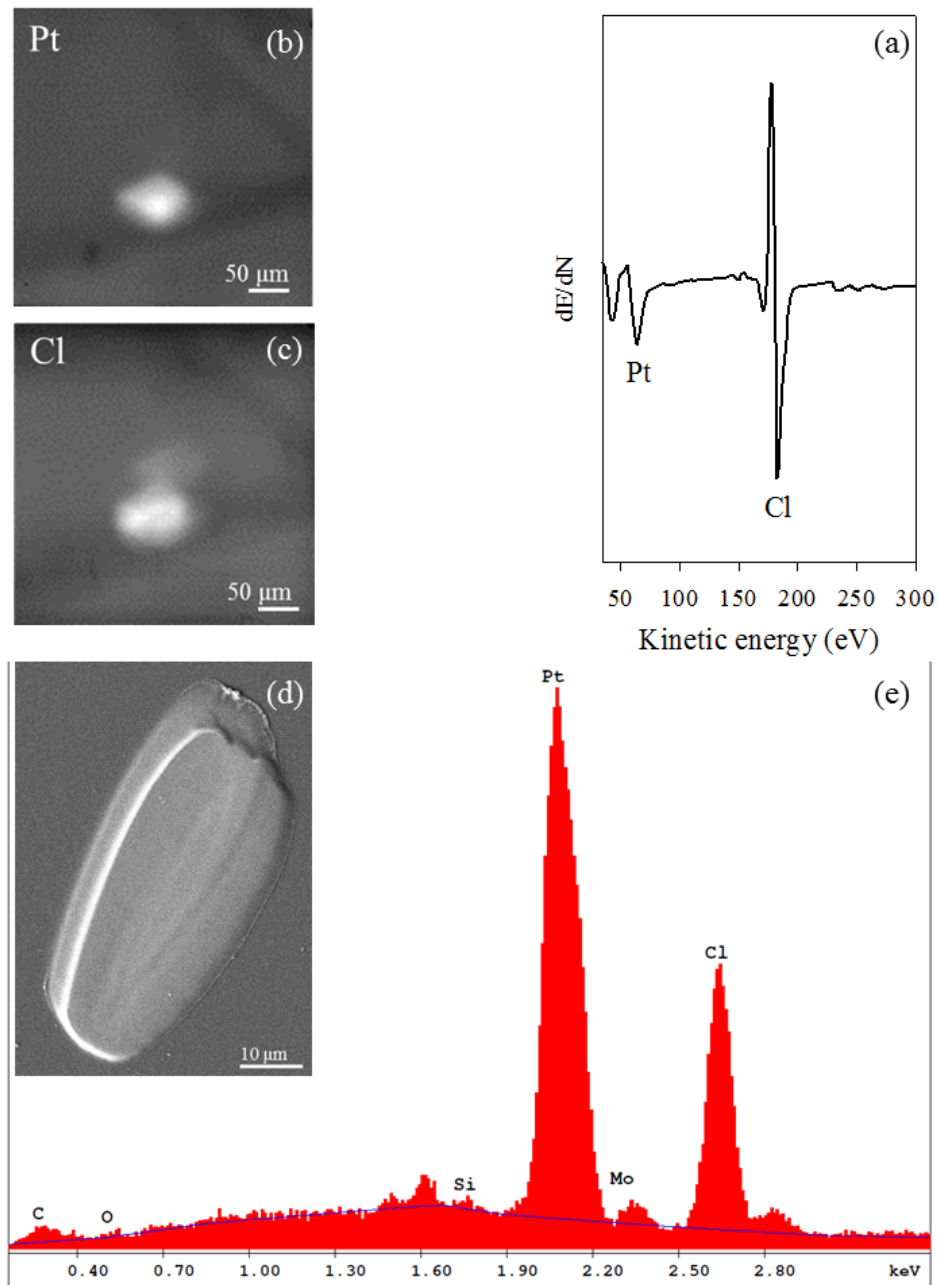
**Figure 5.1**: Auger electron and SEM data for representative deposits created from *cis*-Pt(CO)$_2$Cl$_2$ in an AES instrument on a Ru coated Si/Mo multi-layer substrate under steady state deposition conditions. The AES spectrum of a typical deposit is shown in (a). Auger elemental maps are shown for (b) Pt (64 ev) and (c) Cl 181 eV). The secondary electron image of the deposit acquired in a SEM is shown in (d), along with (e) the corresponding EDS spectrum, which provides an elemental composition of 34.3 % Pt, 48.0 % Cl, 13.6 % C, 1.9 % O, 0.8 % Si and 0.2 % Mo.
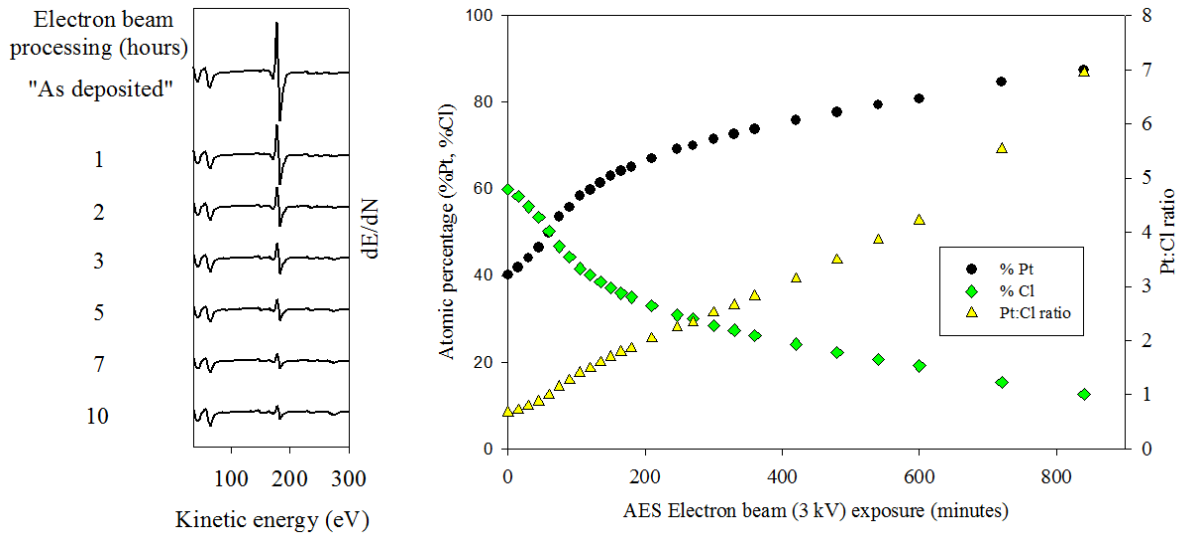
**Figure 5.2**: Auger spectra data for a deposit created from *cis*-Pt(CO)$_2$Cl$_2$ in an AES instrument on an SiO$_2$ substrate under steady state deposition conditions (P$_{cis\text{-}Pt(CO)_2Cl_2}$ ≈ 1.5 x 10$^{-8}$ Torr for 5.25 hours at 3kV, with average target current of 300 nA), and then exposed to continued electron beam processing. The left pane shows the influence of electron beam irradiation on the deposit. The right pane shows elemental analysis of the changing Pt:Cl ratio as the film is subjected to greater electron irradiation (data from AES).
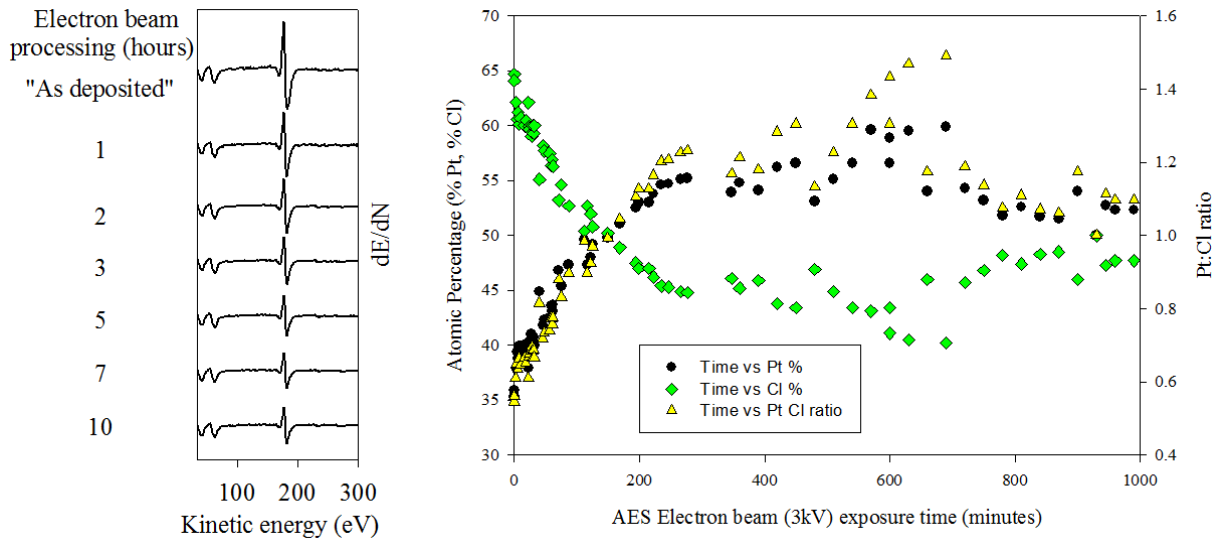
**Figure 5.3**: Auger spectra data for a deposit created from *cis*-Pt(CO)$_2$Cl$_2$ in an AES instrument on Ru-coated Si/Mo multi-layer mirror substrate under steady state deposition conditions (P$_{cis\text{-}Pt(CO)_2Cl_2}$ ≈ 1.5 x 10$^{-8}$ Torr for 22 hours at 3kV, with average target current of 300 nA), and then exposed to continued electron beam processing. The left pane shows the influence of electron beam irradiation on the deposit. The right pane shows elemental analysis of the changing Pt:Cl ratio as the film is subjected to greater electron irradiation (data from AES).

### 5.3.2. Effects of Atomic Hydrogen (General)

Figure 4 provides information regarding the fate of a deposit created from *cis*-Pt(CO)₂Cl₂ in the Auger spectrometer and subjected to *in situ* purification by atomic hydrogen radicals at P$_{H_2}$ ~ 5 x 10$^{-7}$ Torr, and then light Argon ion sputtering. This process was repeated twice. It can be observed that the initial deposit is composed primarily of Pt and Cl (35.6 % Pt, 61.9 % Cl, 2.6 % C, < 0.5 % O). As the deposit is exposed to increasingly greater doses of atomic hydrogen radicals, the Cl signal can be seen to decrease until after 10 hours of atomic hydrogen treatment, the Cl peak has significantly decreased in size and elemental composition (48.6 % Pt, 9.3 % Cl), and a small carbon

146

peak can be seen to grown in, due to adventitious carbon deposition from the atomic hydrogen source.



**Figure 5.4**: Auger spectral data for a deposit created from *cis*-Pt(CO)$_2$Cl$_2$ in an AES instrument on a Ru-coated Si/Mo multi-layer mirror substrate under steady state deposition conditions deposition conditions (P$_{cis\text{-}Pt(CO)_2Cl_2}$ ≈ 1.5 x 10$^{-8}$ Torr for 14 hours at 3kV, with average target current of 300 nA), and exposed to two cycles of atomic hydrogen cleaning, (P$_{H_2}$ ~ 5 x 10$^{-7}$ Torr, followed by 2 keV Ar$^+$ sputtering, P$_{Ar}$ ~ 5 x 10$^{-8}$ Torr. All spectra were normalized to the Pt MNN peak at 65 eV.

Next, the deposit was exposed to light Ar$^+$ sputtering, using 2 keV Ar$^+$ ions, with P$_{Ar}$ ~ 5 x 10$^{-8}$ Torr. After eight minutes of sputtering, little visible change in the Cl peak is noted, but a reduction in the C peak takes place as the adventitious carbon is removed. After 18 minutes of Ar$^+$ sputtering, the Cl peak has increased as a new surface is exposed, one which

147

still retains the majority of Cl from the original deposit, even after atomic hydrogen treatment. The cycle was continued by further atomic hydrogen treatment, and after four more hours of atomic hydrogen treatment, the surface Cl is again reduced to a minimal level, and further adventitious carbon is deposited from the atomic hydrogen source. Finally, further $Ar^+$ sputtering resulted in an increased Cl signal as a new portion of the deposit becomes the surface and thus subject to characterization by Auger electrons.

Figure 5 provides depth profile data for two deposits created from *cis*-$Pt(CO)_2Cl_2$ in the Auger spectrometer on a Ru-capped Si/Mo multi-layer mirror, and then exposed to atomic hydrogen *ex situ* at $P_{H_2} \sim 1$ Torr for two hours. The primary difference in the two deposits is the deposition time, and by extension, the thickness of the deposits. The deposit in Figure 5a had a deposition time of six hours, while the deposit in Figure 5b was deposited for 13 hours, more than twice as long. The data shown in Figure 5 contrasts with that shown in Figure 4. As sputtering occurred for the deposit in Figure 4, only a small amount of sputtering resulted in exposure of a new surface in which essentially the "as deposited" amount of Cl was retained. In contrast, for both deposits shown in Figure 5, the Pt and Cl percentages remain quite similar, with a low level of Cl, for a much longer sputtering period, indicating that the entire deposit has been cleaned of Cl. The Cl ratio only begins to rise again when the deposit has been essentially sputtered through, and the substrate becomes prevalent.

**Figure 5.5**: Graph (a) shows depth profile data for a deposit created from *cis*-Pt(CO)₂Cl₂ in the Auger Spectrometer with a deposition of time of 6 hours, and then exposed to atomic hydrogen radicals at $P_{H_2}$ ~ 1 Torr for two hours. Graph (b) shows depth profile data for a deposit created in similar conditions but a longer deposition time of 13 hours, and then treated to similar atomic hydrogen exposure.
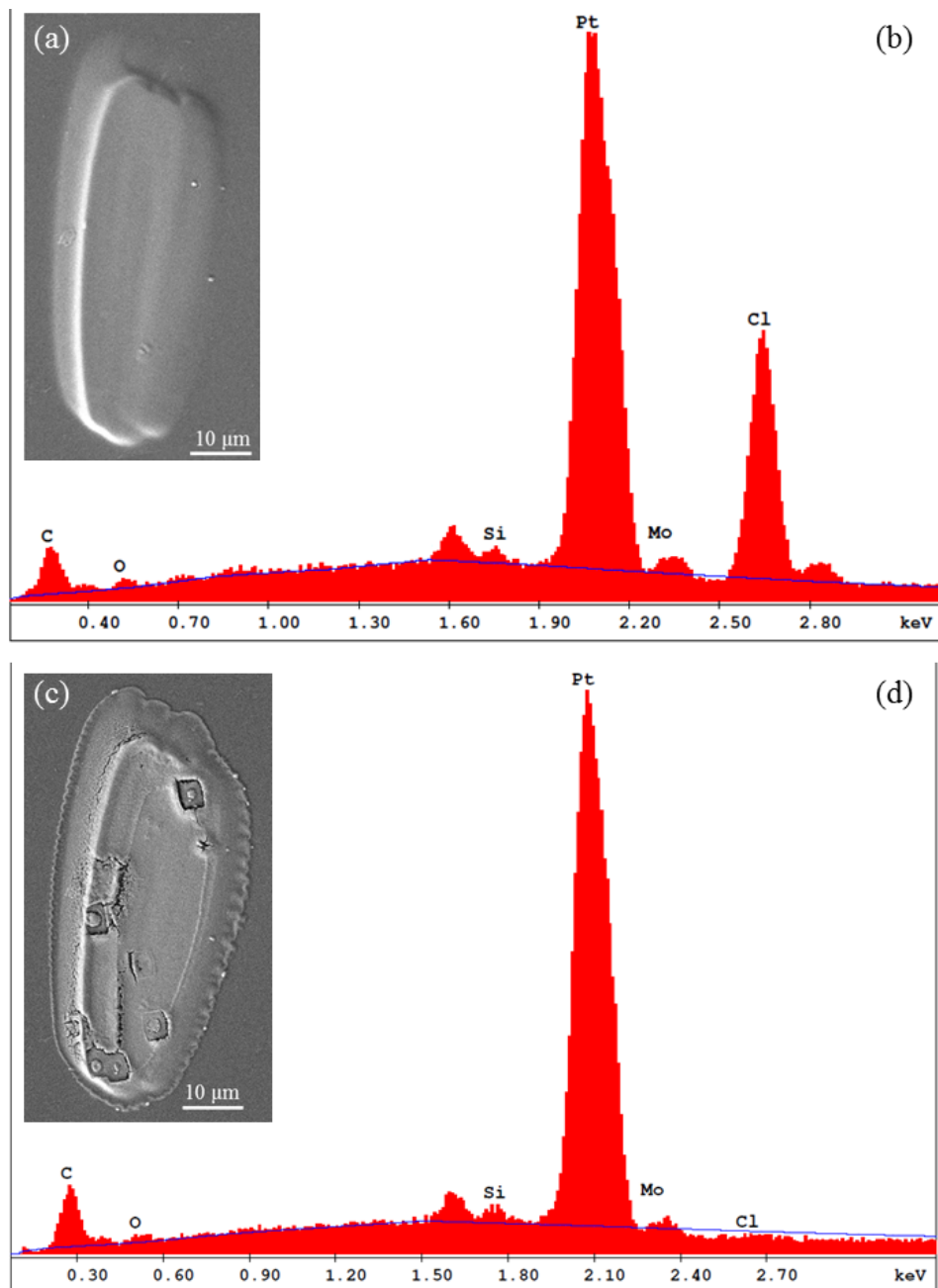
**Figure 5.6**: SEM and EDS data for a deposit created from *cis*-Pt(CO)₂Cl₂ in an AES instrument on a Ru coated Si/Mo multi-layer substrate under steady state deposition conditions and then exposed to atomic hydrogen purification. Prior to atomic hydrogen treatment, the deposit is shown in image (a) with elemental composition shown in EDS spectrum (b) as 28.6 % Pt, 36.0 % Cl, 31.2 % C, 3.0 % O, 1.3 % Si, and 0.0 % Mo. After 10 minutes of atomic hydrogen treatment at $P_{H_2} \sim 1$ Torr, the deposit is shown in image (c) with elemental composition shown in EDS spectrum (d) as 47.2 % Pt, 0.0 % Cl, 45.8 % C, 4.5 % O, 2.5 % Si, and 0.0 % Mo.

Figure 6 shows the fate of a deposit created in the Auger spectrometer from *cis*-Pt(CO)$_2$Cl$_2$ and subjected to atomic hydrogen purification *ex situ*. Figure 6a shows the initial deposit, with its EDS spectrum shown below it, indicating a composition of Pt, Cl, and minimal substrate contributions. After exposure to 10 minutes of atomic hydrogen at ~1 Torr, the deposit is shown in Figure 6b and is composed of 47.2 % Pt, with 0.0 % Cl. The most notable new features after atomic hydrogen purification are several square inclusions or sunken areas, which correspond to locations in which EDS spectra were taken.
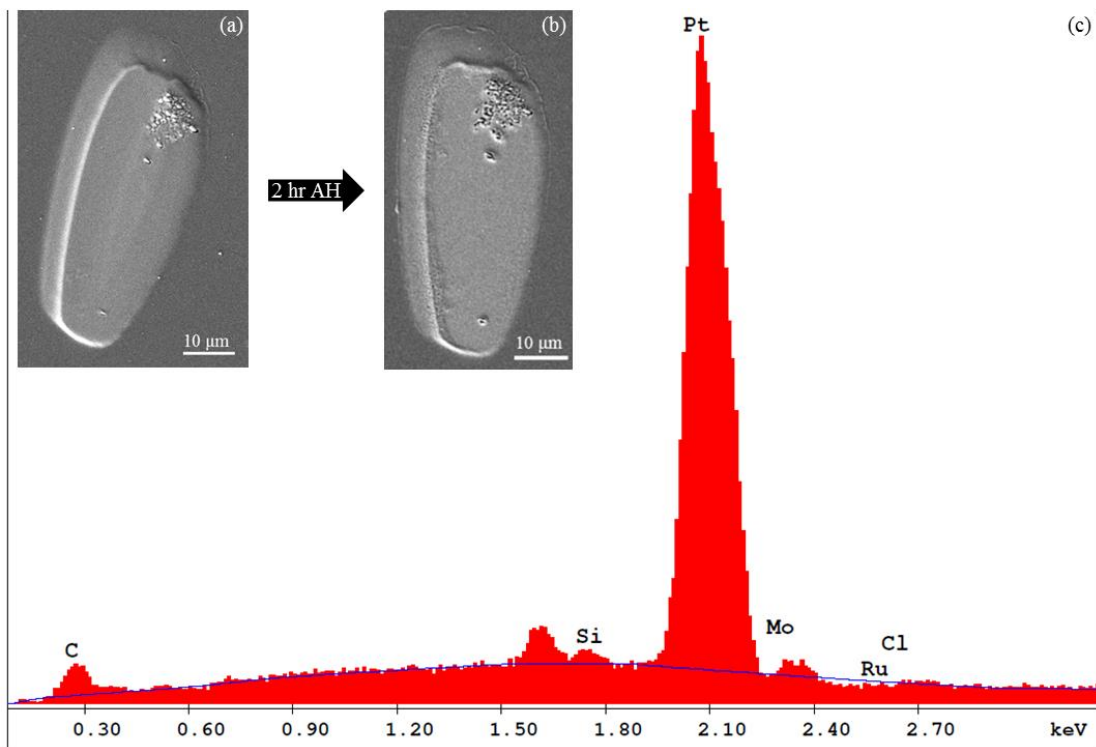


**Figure 5.7**: (a) An image of a deposit created from *cis*-Pt(CO)$_2$Cl$_2$ in an AES instrument on Ru-coated Si/Mo multi-layer mirror substrate under steady state deposition conditions (P$_{cis\text{-Pt(CO)}_2Cl_2}$ ≈ 1.5 x 10$^{-8}$ Torr for 23 hours at 3kV, with average target current of 300 nA), and (b) exposed to two hours of atomic hydrogen treatment. The EDS spectra for the deposit shown in (b), after atomic hydrogen treatment, is shown in (c), EDS elemental analysis: 67.4 % Pt, 0.0 % Cl, 29.9 % C, 2.7 % Si, 0.0 % Mo, and 0.0% O.

Figure 7 shows a deposit created from *cis*-Pt(CO)$_2$Cl$_2$ and then subjected to two hours of atomic hydrogen exposure *ex situ* at P$_{H_2}$ ~ 1 Torr. Figure 7a shows the deposit prior to atomic hydrogen purification. This deposit was only imaged prior to atomic hydrogen exposure; it did not have any EDS spectra taken prior to treatment (taking EDS spectra requires the SEM beam to stay in one location for much longer than imaging, which can affect the deposit). It appears to maintain its shape after atomic hydrogen treatment, with the notable development of the feature at the upper right of the deposit. The EDS spectrum (Figure 7b) shows that minimal Cl remains after atomic hydrogen treatment.

Figure 8 shows further treatment of the deposit originally shown in Figure 1 as a representative deposit with no treatment. Figure 8a provides EDS data for the deposit after two hours of atomic hydrogen treatment, shown in the image in Figure 8b. Arrows point to compressed or flattened areas on the deposit, which correspond to locations in which EDS data was taken, and likely correspond to deposited surface carbon. This deposit shows significant cratering into a honeycombed pattern as the Pt appears to become labile and coalesce as the atomic hydrogen removes Cl, or as the hydrogen atoms allow the Pt to become mobile and disperse/disaggregate, as observed by Horch *et. al.*[42] Figure 8c shows this deposit after two more hours of atomic hydrogen treatment. The deposit is largely unchanged, but the white box in the lower left of the image highlights an area in which the deposit is beginning to come apart. Figure 8d shows this area at a larger magnification.
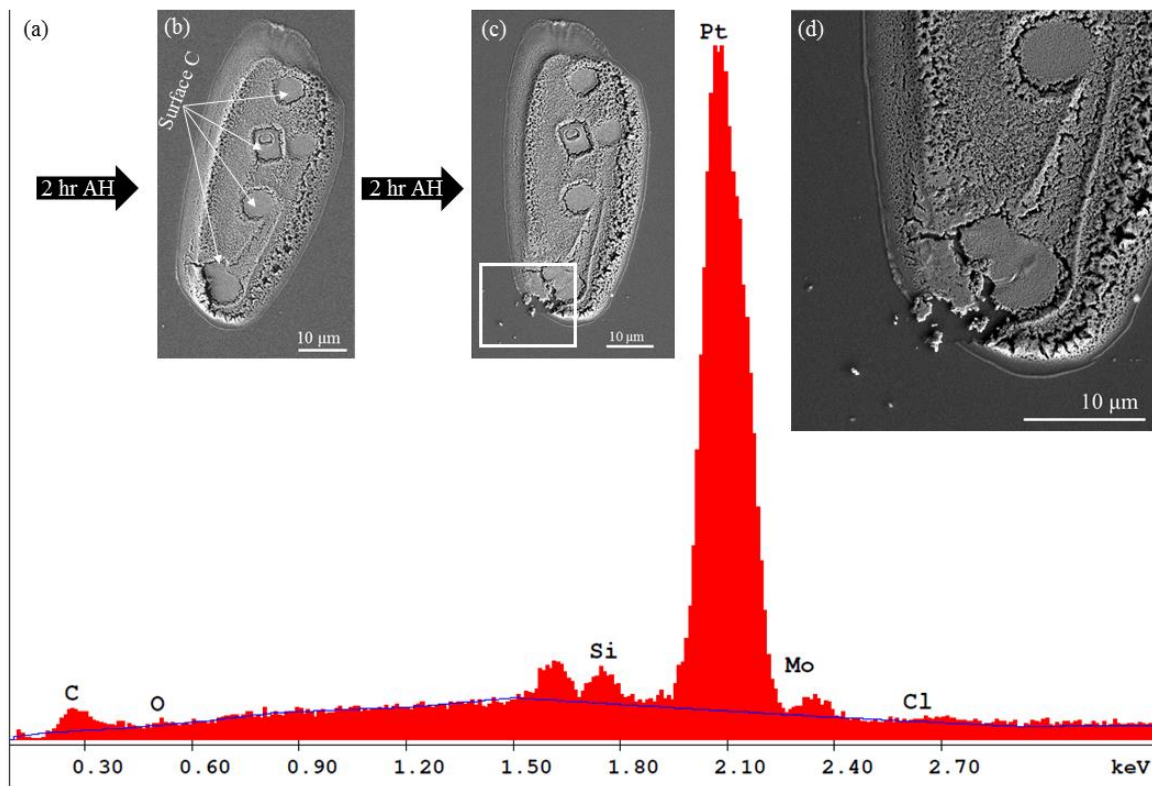
**Figure 5.8**: Figure 8 presents further processing data on the deposit displayed in Figure 1 (prior to treatment). Figure 8(a) provides EDS data (70.2 % Pt, 0.3 % Cl, 21.7 % C, 6.2 % Si, 0.0 % Mo, and 1.7 % O) for the SEM image in (b), after two hours of atomic hydrogen, with arrows labelling surface carbon. The image shown in (c) is the same deposit after two more hours of atomic hydrogen treatment; a white box highlights fragmentation; this area is shown in a larger view in (d).

Figure 9 shows a SEM image and EDS data from the deposit originally discussed in Figure 3, in which the deposit was subjected to ~20 hours of electron beam processing. Figure 9a shows the SEM image of this deposit after 20 hours of electron beam processing; it can be noted that it is still largely smooth in appearance, similar to the deposits shown prior to any treatment in Figures 1, 6, and 7. Figure 9b shows EDS data for this deposit prior to further treatment. This deposit starts with a slightly lower atomic percentage of Cl compared with other deposits prior to treatment (~42% Cl compared with ~48% Cl), as a result of electron beam processing in the Auger spectrometer. This deposit was then

153

subjected to two hours of atomic hydrogen treatment *ex situ* at $P_{H_2} \sim 1$ Torr. Figure 9c shows the deposit after atomic hydrogen treatment; the deposit begins to show some of the cratering observed in Figure 8, but to a lesser extent, possibly due to surface carbon deposition as part of the electron post-processing. The EDS data for the deposit after atomic hydrogen treatment is shown in Figure 9d; essentially all the chlorine has been removed, as seen for the previous atomic hydrogen exposures.

Figure 10 shows a deposit created from *cis*-$Pt(CO)_2Cl_2$ and subjected to two hours of atomic hydrogen treatment *ex situ* at $P_{H_2} \sim 1$ Torr. This deposit was imaged prior to atomic hydrogen purification as shown in Figure 10a, but was not subjected to EDS, to avoid surface carbon deposition or any marking of the deposit (visible or not). Figure 10b shows the fate of this deposit after two hours of atomic hydrogen treatment. The main feature evident after this deposit was exposed to atomic hydrogen is loss of structural integrity, or almost complete disintegration, as well as the honeycomb or cratering pattern also observed in Figures 8 and 9. Figure 10c shows an EDS map of the Pt region for this deposit, where it can be noted that elemental Pt is present in the remaining areas of the deposit, but not in the areas where the deposit was removed from the surface. Figure 10d shows EDS data for this deposit after two hours of atomic hydrogen (image in 10b).

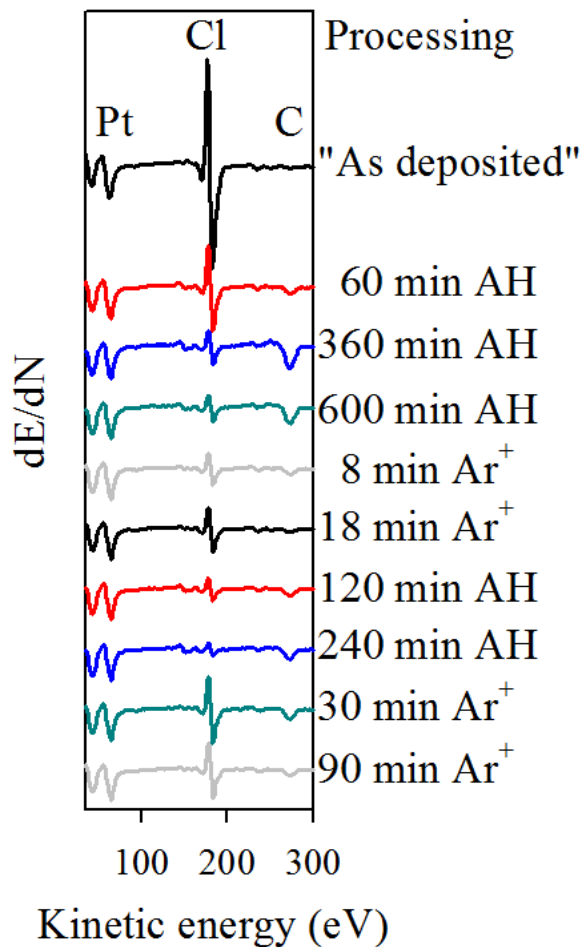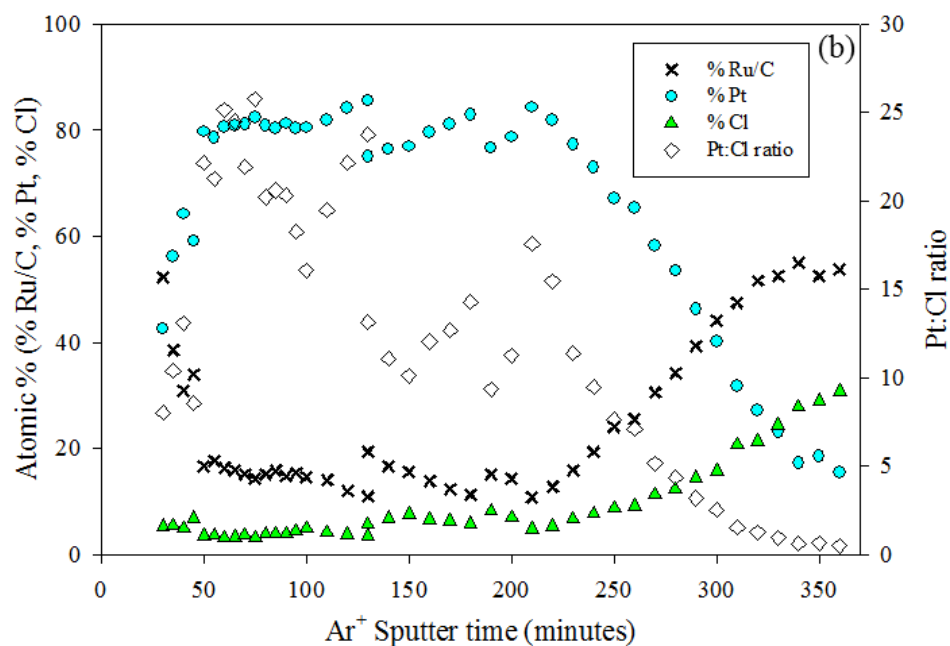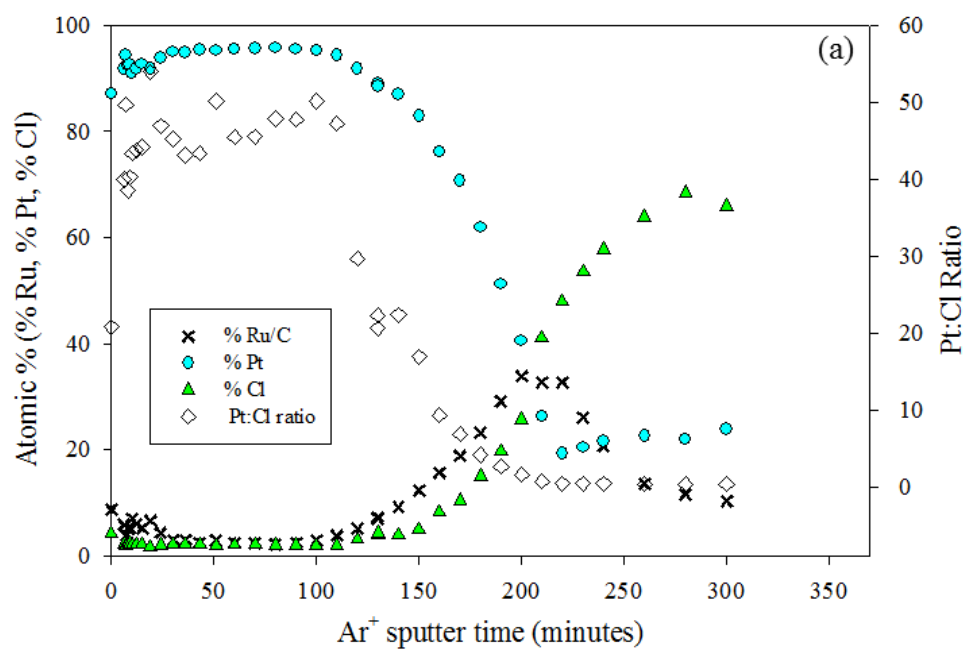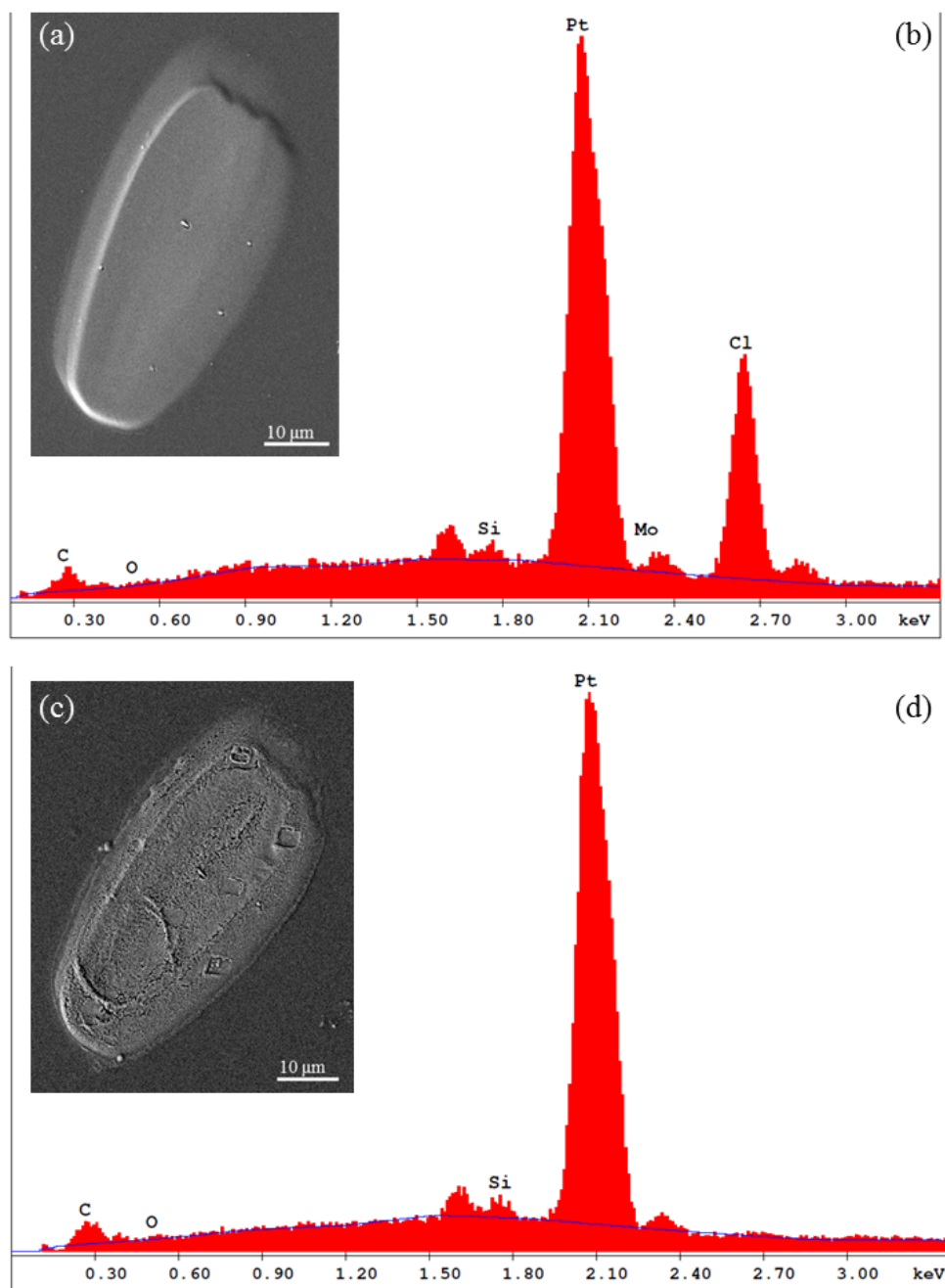**Figure 5.9**: SEM and EDS data for a deposit created from *cis*-Pt(CO)$_2$Cl$_2$ in an AES instrument on a Ru coated Si/Mo multi-layer substrate under steady state deposition conditions, and exposed to electron beam processing for 20 hours. Figure 8a shows an SEM image of this deposit, with corresponding EDS data shown in (b), elemental analysis 36.0 % Pt, 43.0 % Cl, 17.6 % C, 1.6 % O, 1.8 % Si, and 0.0 % Mo. The deposit is shown in (c) after 2 hours of atomic hydrogen treatment at P$_{H_2}$ ~ 1 Torr, and corresponding EDS data in (d) with an elemental composition of 69.0 % Pt, 0.0% Cl, 24.4 % C, 2.5 % O, 0.8 % Si, and 0.0% Mo.

155
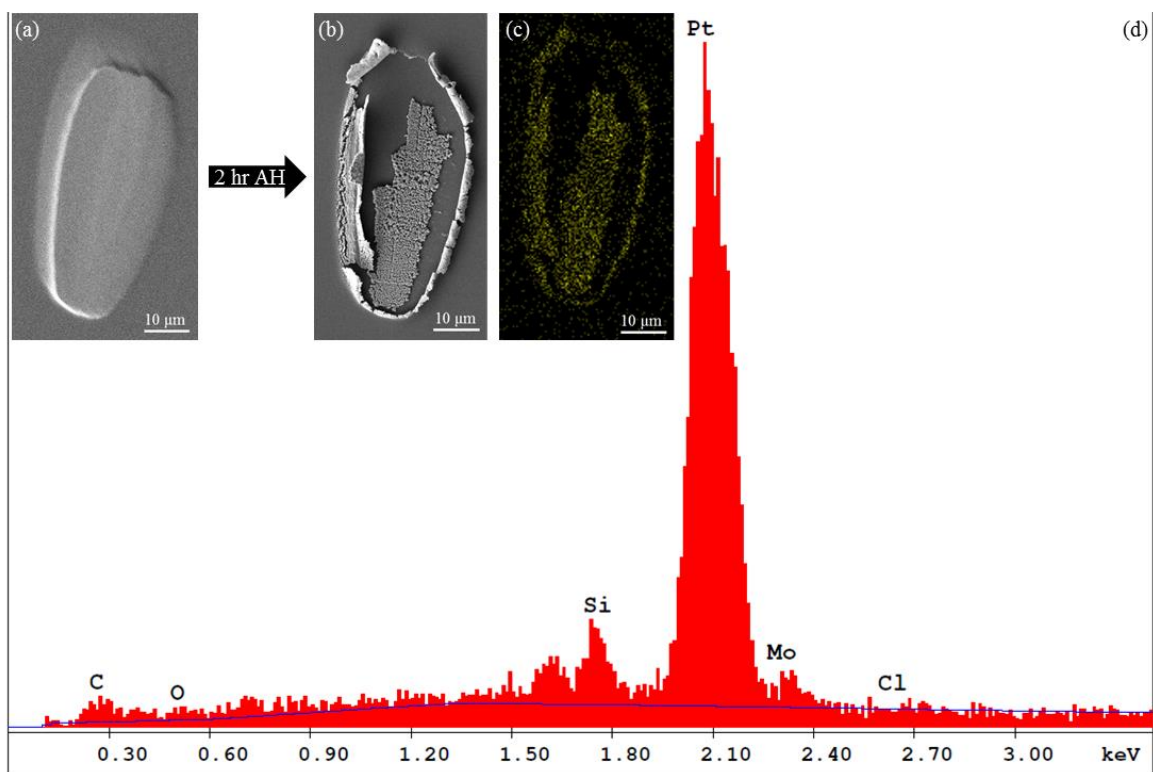
**Figure 5.10**: Figure 10(a) shows the SEM image of a deposit created from *cis*-Pt(CO)$_2$Cl$_2$ under steady state deposition conditions, without any EDS analysis and prior to any treatment. Figure 10(b) shows the deposit after two hours of atomic hydrogen treatment at P$_{H_2}$ ~ 1 Torr, with a corresponding EDS elemental map of Pt M shown in (c). EDS data for the deposit in (b), is shown as spectra (d), with an elemental analysis of 51.3 % Pt, 0.0 % Cl, 17.2 % C, 6.5 % O, 11.4 % Si, and 3.7 % Mo.

5.3.3. Effects of Atomic Hydrogen (Progressive)

Figures 11 through 15 show the fate of a deposit subjected to progressive atomic hydrogen treatment. Figure 11a shows the deposit prior to any treatment. Figure 11b shows the deposit after a control experiment was conducted, in which the deposit was subjected to two hours of exposure to the atomic radical source, in the absence of any hydrogen. No visible changes were noted. The deposit was then progressively subjected to various doses of atomic hydrogen, which are reported in cumulative exposure times. Figures 11c, 11d, and 11e show the deposit after exposure to one minute, six minutes and

18 minutes of atomic hydrogen treatment at $P_{H_2} \sim 1$ Torr. Minimal physical changes were

noted, primarily increased definition around the edges of the deposits.
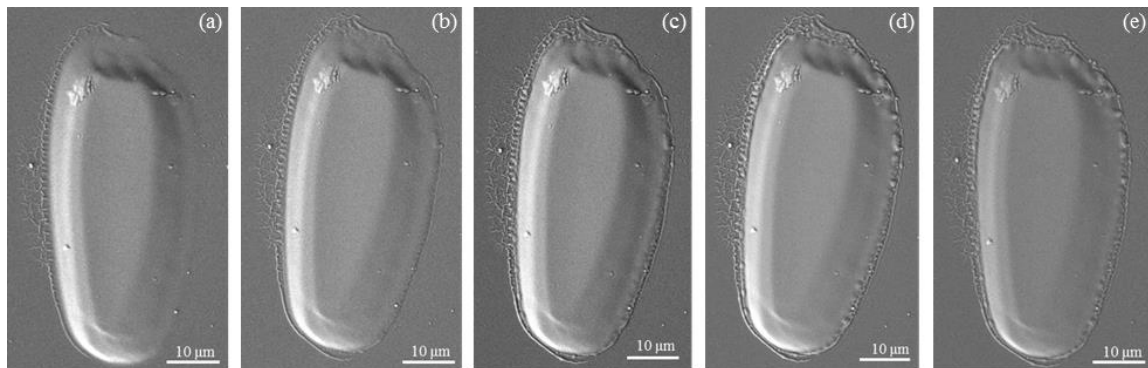


**Figure 5.11**: A deposit created from *cis*-Pt(CO)$_2$Cl$_2$ and subjected to various exposures of atomic hydrogen radicals with $P_{H_2} \sim 1$ Torr. In (a), the pristine deposit is shown before any treatment. The deposit is shown in (b) after a control experiment of exposure of 2 hours of the atomic radical source with no H$_2$ gas. The deposit is shown in (c) after 1 minute of atomic hydrogen treatment, in (d) after 6 cumulative minutes of atomic hydrogen treatment, and in (e) after 18 cumulative minutes of atomic hydrogen treatment.

Figure 12 shows this deposit after 48 and 78 minutes of cumulative atomic

hydrogen exposure time. Figure 12a shows the deposit after 48 minutes of AH, compared

with EDS maps shown in Figure 12b for Pt M, and 12c for Cl K. Figure 12d shows the

deposit after 78 minutes of AH exposure time, with EDS maps shown in Figure 12e for Pt

M and 12f for Cl K. Notable features are the start of cracks, and correlation with the EDS

maps to show that while the Pt signal remains essentially constant, the Cl species is

preferentially removed in the vicinity of the cracks. To emphasize this point, Figure 13

shows the Cl K maps for this deposit at a larger magnification for the 48 minute and 78

minute atomic hydrogen treatments. For this deposit, EDS maps are used, rather than

simple report of elemental composition from the EDS spectra, because it was noted that

elemental composition varied significantly at different points on the deposit, which had not been observed with previous deposits evaluated. For example, Cl % had decreased to < 5% in the vicinity of a cracked area, while in a bulk, smoother area, there was still > 20% Cl. In Figure 13a, it can be noted that Cl has been preferentially removed from areas at the lower left portion of the deposit, which corresponds to an area in the image where cracking has started, as well as in the upper right portion of the deposit, which corresponds to a sunken area in the image.
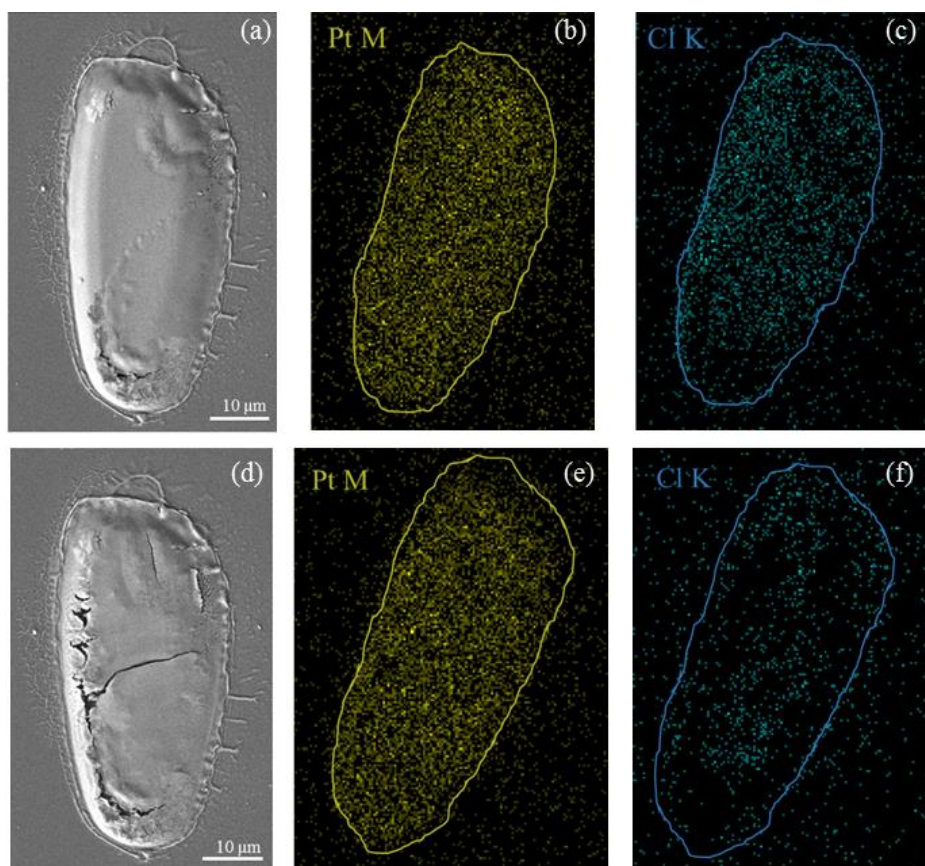


**Figure 5.12**: The deposit created from *cis*-Pt(CO)$_2$Cl$_2$ and exposed to progressive atomic hydrogen treatment is shown in (a) after 48 minutes of cumulative treatment, with EDS maps shown in (b) and (c) for Pt M and Cl K, respectively. After 78 minutes of cumulative treatment, the deposit is shown in (d), with EDS maps shown in (e) and (f) for Pt M and Cl K.

In Figure 13b, after 78 cumulative minutes of atomic hydrogen exposure, it can be seen that the Cl has been preferentially removed in an arc-like pattern around the bottom of the deposit, corresponding with development of larger cracks in that area. Interestingly, the EDS map shows structural changes (i.e. Cl removal) in areas even before the image shows changes; this highlights the ability of EDS to show composition throughout the deposit.
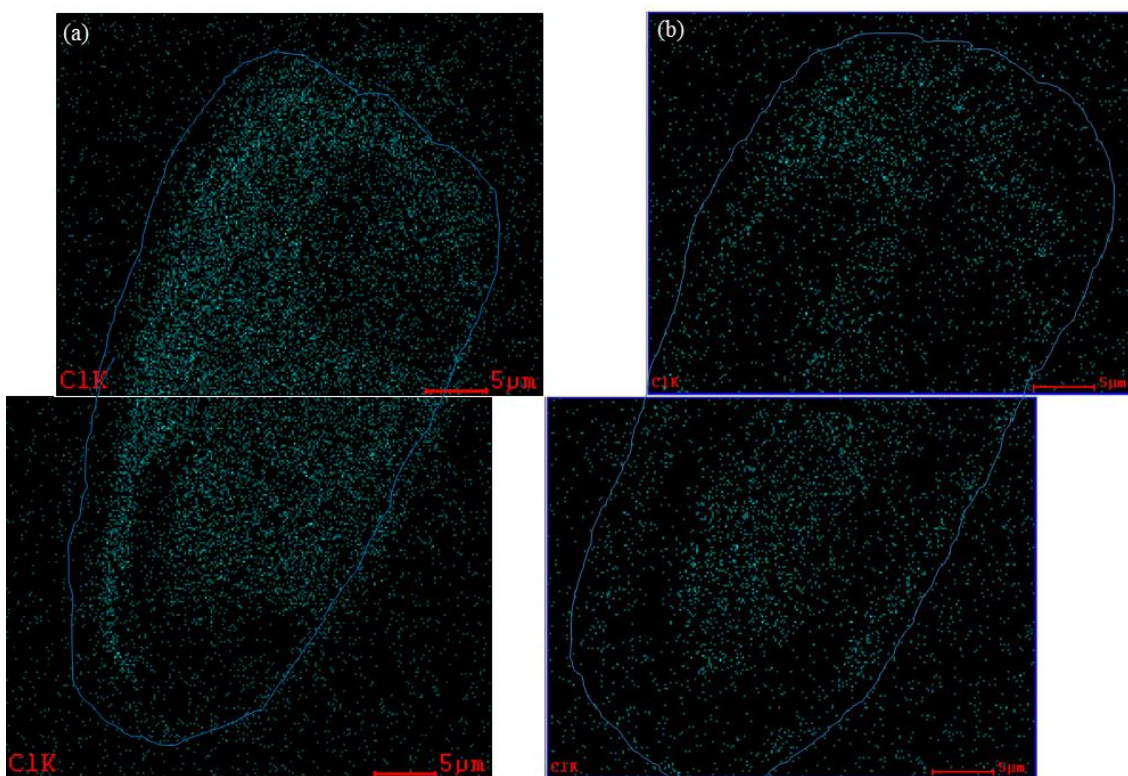


**Figure 5.13**: For the deposit created from *cis*-Pt(CO)$_2$Cl$_2$ and exposed to progressive atomic hydrogen treatment, magnified EDS Cl K maps are shown in (a) after 48 cumulative minutes of atomic hydrogen treatment, and in (b), after 78 minutes of cumulative atomic hydrogen treatment.

Figure 14 presents images and EDS maps for the deposit after continued exposure to atomic hydrogen treatment *ex situ* at $P_{H_2} \sim 1$ Torr. In Figure 14a, the deposit is shown after 108 cumulative minutes of atomic hydrogen treatment, with corresponding EDS maps shown in Figure 14b and 14c for Pt M and Cl K, respectively. The deposit is
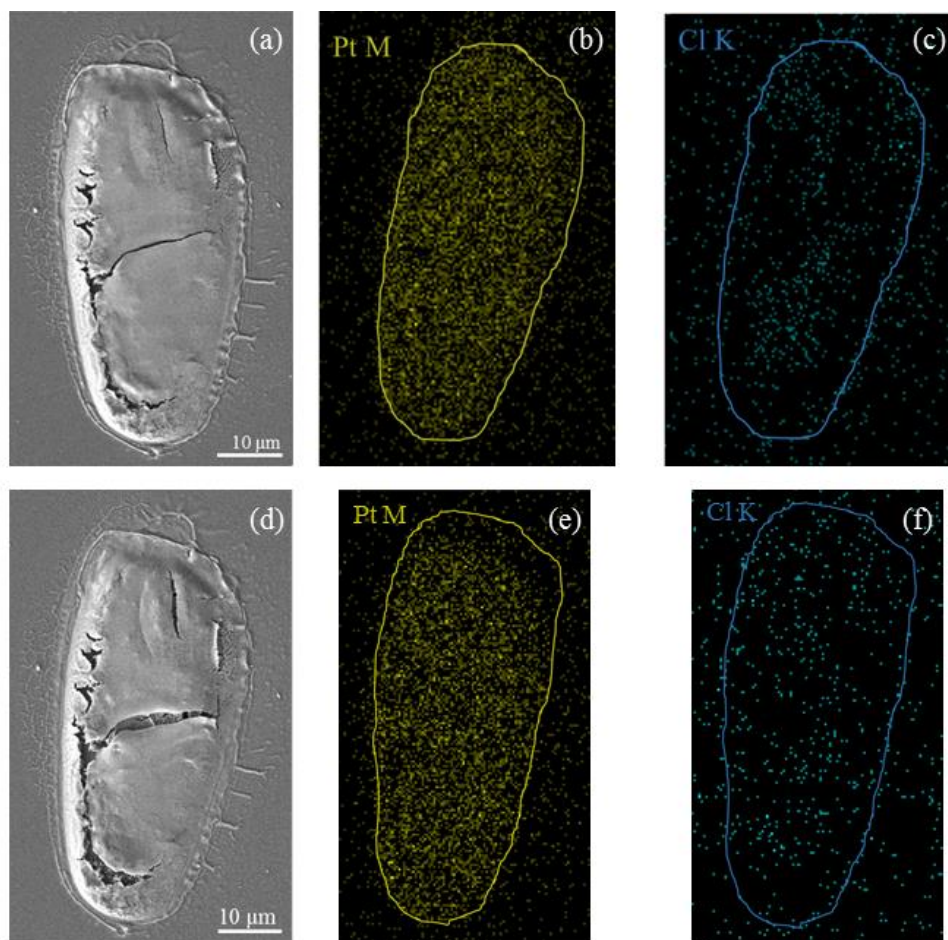


**Figure 5.14**: The deposit created from *cis*-Pt(CO)$_2$Cl$_2$ and subjected to progressive atomic hydrogen treatment at $P_{H_2} \sim 1$ Torr is shown in Figure 14. After 108 minutes of cumulative atomic hydrogen exposure, the SEM image of the deposit is shown in (a), with the EDS Pt M and Cl K maps shown in (b) and (c), respectively. After 138 minutes of cumulative atomic hydrogen exposure, the SEM image of the deposit is shown in (d), with the EDS Pt M and Cl K maps shown in (e) and (f), respectively.

shown after 138 minutes of cumulative atomic hydrogen exposure with the image in Figure 14d, and the EDS maps shown in Figure 14e and 14f.  An increased amount of cracking and changes in structural integrity can be observed as the deposit is exposed to continued atomic hydrogen treatment.  The Pt M maps retain a similar Pt signal, while the Cl K signal is observed to continue to lessen, and it becomes difficult to see the image of the deposit in the Cl map after 138 minutes of atomic hydrogen exposure.
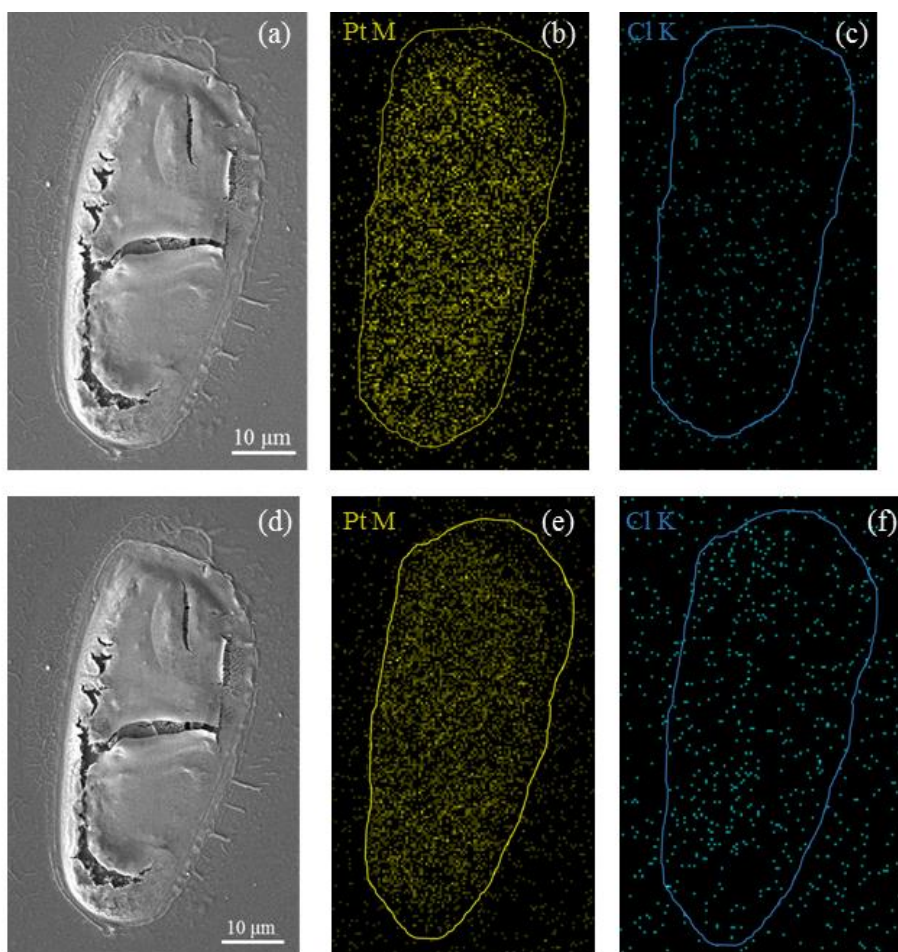


**Figure 5.15**:    The deposit created from *cis*-Pt(CO)$_2$Cl$_2$ and subjected to progressive atomic hydrogen treatment at P$_{H_2}$ ~1 Torr is shown in Figure 15.  After 168 minutes of cumulative atomic hydrogen exposure, the SEM image of the deposit is shown in (a), with the EDS Pt M and Cl K maps shown in (b) and (c), respectively.  After 198 minutes of cumulative atomic hydrogen exposure, the SEM image of the deposit is shown in (d), with the EDS Pt M and Cl K maps shown in (e) and (f), respectively.

Figure 15 provides data regarding the fate of the deposit created from *cis*-Pt(CO)$_2$Cl$_2$ and subjected to progressive atomic hydrogen treatment. Figures 15a, 15b, and 15c show the SEM image of the deposit and the Pt M and Cl K EDS maps after 168 minutes of atomic hydrogen treatment. Figures 15d, 15e, and 15f shown the SEM image of the deposit and the Pt M and Cl K EDS maps after 198 minutes of atomic hydrogen treatment. At this point, the deposit is not changing significantly in appearance, and the majority of Cl has been removed. There is still Cl present, as shown in the EDS maps, but it is mostly dispersed. EDS spectra (data not shown) indicate that there is still varying amounts of Cl in different locations on the deposit, but the amount is small. Further treatment and evaluation of this deposit may continue to see if all Cl may be removed or if this is the limit of Cl removal. This deposit shows differences from the others discussed in that the Cl removal was slower, and if no more Cl can be removed (to be determined), that all Cl was not removed with atomic hydrogen cleaning. It is possible that the differences in observations are due to the longer timeframe of exposure and the significant amount of SEM and EDS exposure experienced by this deposit.

### 5.3.4. Other Platinum Containing Compounds

Several other Pt-containing precursors were evaluated with atomic hydrogen purification, but it was found to have little effect. Particularly of interest were MeCpPtMe$_3$, Pt(hfac)$_2$, and Pt(PF$_3$)$_4$. Figure 16 summarizes data for a deposit created on a Ru-capped multi-layer mirror substrate from MeCpPtMe$_3$, a widely used FEBID precursor despite relatively low purity (<20% Pt)[8]. There is little change observed in either the images or EDS spectra for MeCpPtMe$_3$ after two hours of atomic hydrogen exposure *ex situ* at P$_{H_2}$ ~ 1 Torr.
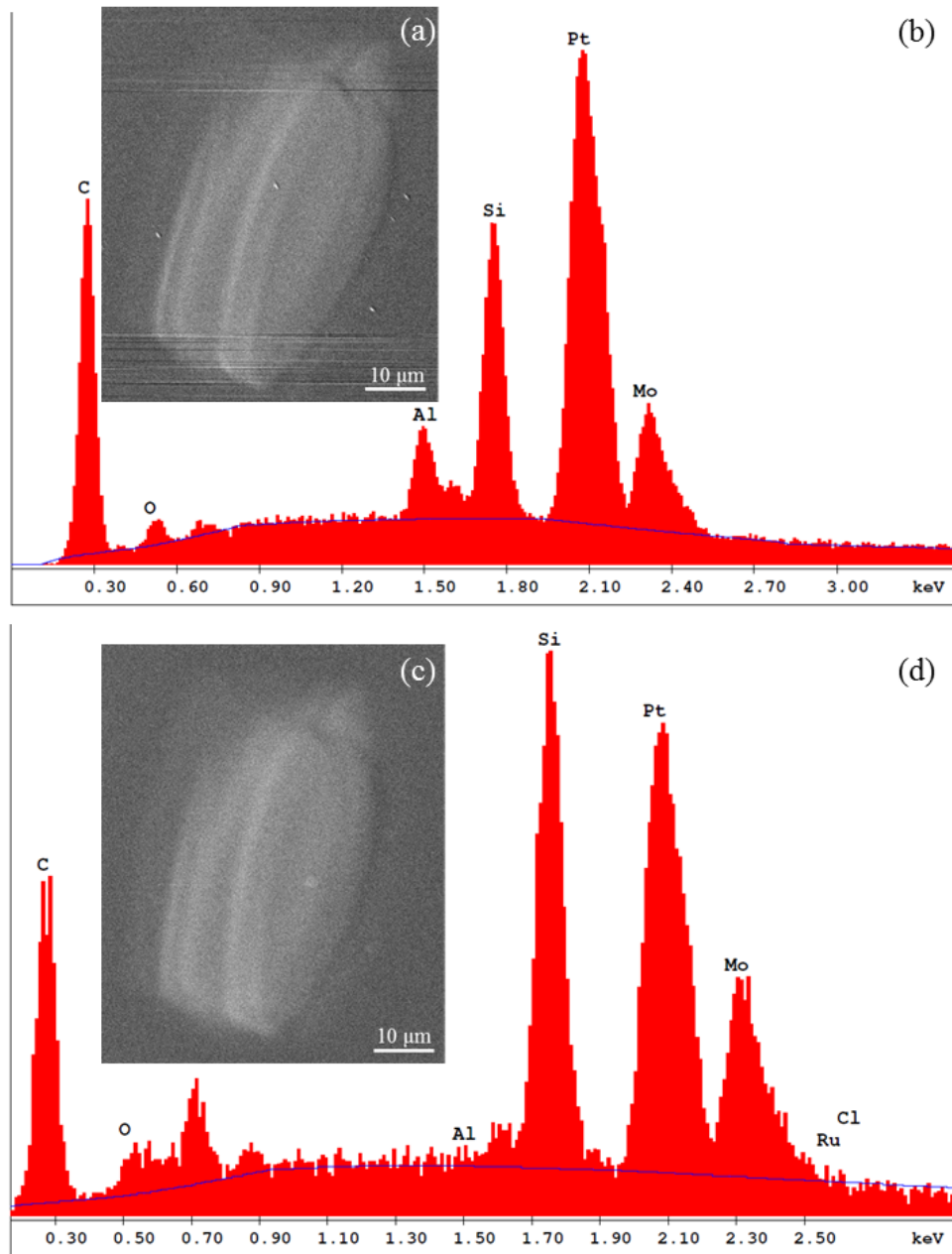
**Figure 5.16**: SEM and EDS data for a deposit created from MeCpPtMe$_3$ in an AES instrument on a Ru coated Si/Mo multi-layer substrate under steady state deposition conditions. A SEM image of this deposit prior to atomic hydrogen treatment is shown in (a), with the corresponding EDS spectra shown in (b), elemental analysis 66.6 % C, 10.5 % Pt, 11.1 % Si, 3.6 % O, 5.0 % Mo, and 3.2 % Al. The deposit is shown in (c) after 2 hours of atomic hydrogen treatment at P$_{H_2}$ ~ 1 Torr, and corresponding EDS data is shown in (d) with an elemental composition of 59.8 % C, 8.8 % Pt, 17.0 % Si, 7.6 % Mo, 0.3 % Ru, 6.1 % O, and 0.4 % Al.

Figure 17 summarizes data for deposits created from $Pt(hfac)_2$ on a $SiO_2$ substrate. The $Pt(hfac)_2$ deposit was exposed to 2.5 hours of atomic hydrogen treatment at $P_{H_2} \sim 1$ Torr. As with $MeCpPtMe_3$, there is little change observed in the EDS data before and after atomic hydrogen exposure. There is some appearance change in the deposit, as it appears that the platinum may be coalescing, or the deposit edge is broadening, but there is no observed change in the microstructure of the deposit (SEM images not shown), nor the appearance of cracks, as seen for deposits created from $cis$-$Pt(CO)_2Cl_2$. Further investigation would be required to determine if the Pt is actually mobile in the deposit formed from $Pt(hfac)_2$ or if the changes observed around the deposit edge are due to another factor.
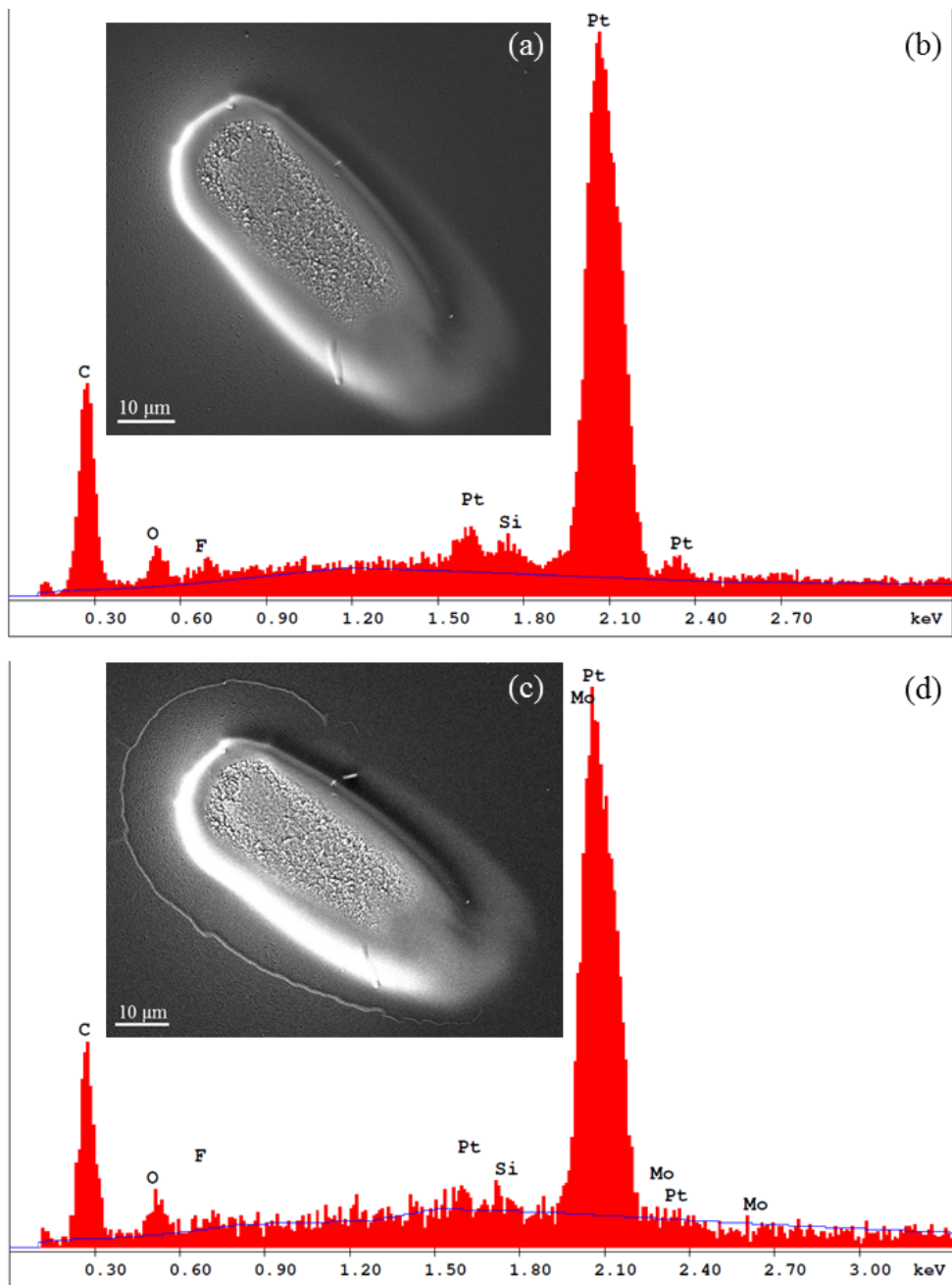
**Figure 5.17**: SEM and EDS data for a deposit created from Pt(hfac)$_2$ in an AES instrument on a SiO$_2$ substrate under steady state deposition conditions. A SEM image of this deposit prior to atomic hydrogen treatment is shown in (a), with (b) the corresponding EDS spectra, elemental analysis 61.6 % C, 23.1 % Pt, 2.4 % Si, 9.0 % O, and 3.9 % F. The deposit is shown in (c) after 2.5 hours of atomic hydrogen treatment at P$_{H_2}$ ~ 1 Torr, and corresponding EDS data is shown in (d) with elemental analysis of 62.2 % C, 24.4 % Pt, 1.2 % Si, 9.7 % O, and 2.5 % F.

Figure 18 summarizes data for deposits created from Pt(PF$_3$)$_4$ on a Ru-coated Si/Mo mirror substrate and then exposed to two hours of atomic hydrogen treatment at $P_{H_2}$ ~ 1 Torr. These deposits were conducted for a much longer deposition time in the Auger spectrometer (~61 hours) and a "double" deposit effect can be seen, where the Auger beam shifted slightly during the deposition. However, this has no effect on the elemental composition or analysis. After exposure to atomic hydrogen treatment, the main differences noted are in appearance. There is a slight peeling up around the edges of the deposit, but otherwise, no major changes are observed. The line of dots that can be observed traversing the deposit after atomic hydrogen treatment are due to wavelength dispersive spectroscopy (WDS) processing.

In order to resolve EDS signal overlap between the Pt M and P K x-ray signals, WDS was used to evaluate the Pt(PF$_3$)$_4$ deposits. The EDS peak composed of Pt M and P K X-ray signals can be resolved by WDS as shown in Figure 19, to the P K$\alpha$ and P satellite peaks, and the Pt M$\alpha$ and Pt M$\beta$ peaks. In Figure 19, the lower spectra shows the Pt and P signals prior to atomic hydrogen treatment. The upper spectra shows the Pt and P signals after two hours of atomic hydrogen treatment at $P_{H_2}$ ~ 1 Torr. The upper spectra has been normalized to the P K$\alpha$ peak, and once this difference in signal strength is accounted for, the two spectra are virtually identical. Atomic composition ratios (data not shown) show little change between Pt/P ratios measured before and after atomic hydrogen treatment; thus, atomic hydrogen had minimal effect on deposits created from Pt(PF$_3$)$_4$ in the Auger spectrometer.
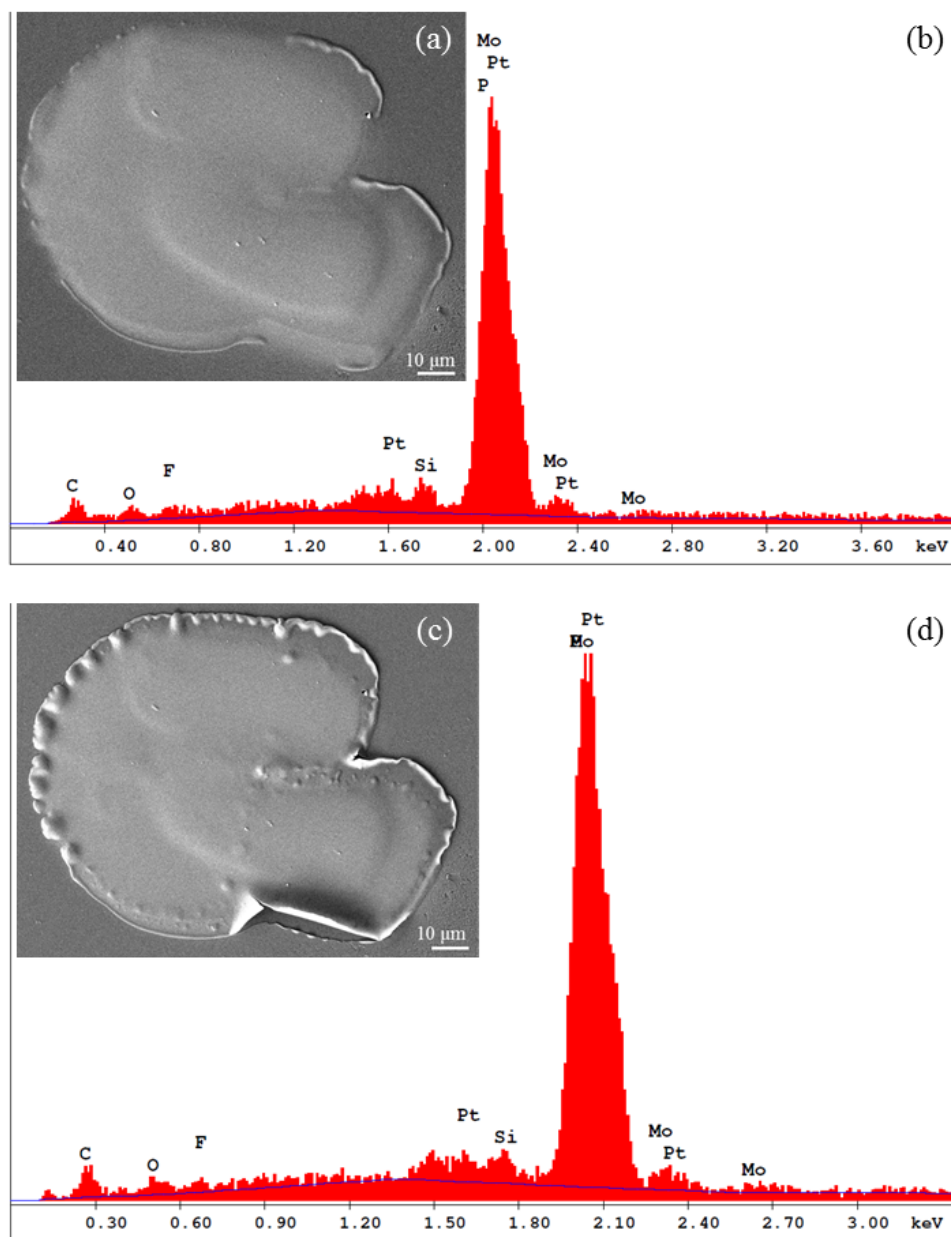
**Figure 5.18**: SEM and EDS data for a deposit created from $Pt(PF_3)_4$ in an AES instrument on a $SiO_2$ substrate under steady state deposition conditions. A SEM image of this deposit prior to atomic hydrogen treatment is shown in (a), with (b) the corresponding EDS spectra, elemental analysis 19.5 % C, 23.4 % Pt, 37.9 % P, 4.7 % Si, 7.1 % O, 2.6 % Mo and 4.9 % F. The deposit is shown in (c) after 2 hours of atomic hydrogen treatment at $P_{H_2}$ ~ 1 Torr, and corresponding EDS data is shown in (d) with elemental analysis of 21.1 % C, 22.3 % Pt, 40.3 % P, 3.7 % Si, 7.1 % O, 2.1 % Mo and 3.3 % F.
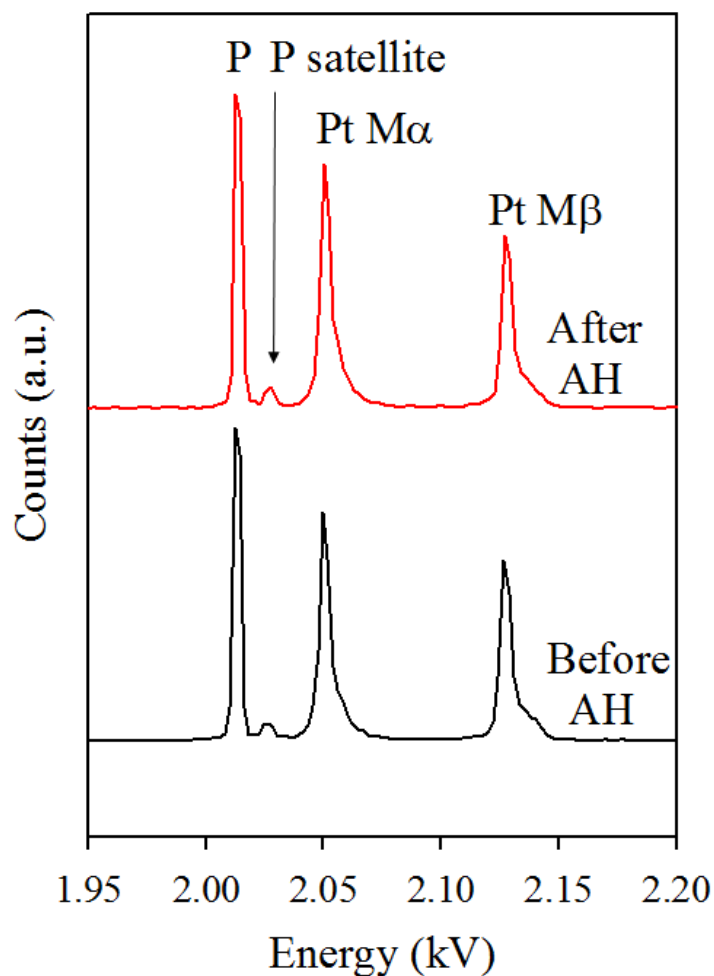
**Figure 5.19**: Wavelength dispersive spectroscopy (WDS) data is shown for the deposit created from Pt(PF$_3$)$_4$ and then exposed to two hours of atomic hydrogen treatment at P$_{H_2}$ ~ 1 Torr. In the lower spectra (black line), the Pt and P signals are shown prior to atomic hydrogen (AH) treatment. The upper spectra (red line) shows the Pt and P signals after atomic hydrogen treatment. For ease of comparison, the upper spectra was normalized to the P signal (P Kα).

## 5.4. Discussion

Focused electron beam induced deposition (FEBID) has great promise to produce nanostructures with useful capabilities, but frequently there is a significant amount of contamination in the nanostructures, limiting their usefulness. The main precursor evaluated in this paper, *cis*-Pt(CO)$_2$Cl$_2$, showed promise to produce pure Pt films, based on

research conducted on thin films, in an UHV environment, as discussed in our previous work[24]. Due to this promise, it was interesting to further evaluate deposits produced from this precursor for structural characteristics, as well as purification potential. This research investigated two means of post-processing or purification, electrons and atomic hydrogen radicals. Deposits created in the Auger spectrometer using the 3kV electron beam were spatially defined by the beam and were composed exclusively of Pt and Cl, as shown in Figures 1, 6, 7, and 9. This agrees with results seen in a deposit evaluated in our previous work. Electron beam post-processing removed virtually all of the Cl from the adsorbed $cis$-Pt(CO)$_2$Cl$_2$ in our previous work[24]. However, the deposits evaluated in the present study were generally much thicker than the $1-2$ nm films evaluated previously, and thus, it can be seen that there is a limit to the penetration depth where electrons can effectively scrub halogens. In the XPS studies, a finite amount of precursor was used in a thin film; electrons were able to penetrate the entire structure and remove Cl by a slower, electron-stimulated desorption process, which is orders of magnitude slower than the desorption of CO[24]. In contrast, in these steady state deposition studies, analogous to the FEBID process, each $cis$-Pt(CO)$_2$Cl$_2$ molecule is exposed to electrons and has minimal further electron processing before another precursor molecule is decomposed, thus trapping the Cl in the deposits. The CO actually may be assisted in desorption by local heating[43] in addition to electron stimulated desorption; regardless of the dominant force for CO removal, the deposits created in the Auger spectrometer are largely C and O free, in contrast to the films evaluated in the XPS study, in which the precursor molecularly adsorbed to a cold substrate, and then was removed by electron stimulated desorption. This may also be due to the substrate temperature, as local heating in the experiments in which depositions were

made at ambient temperature likely assisted in thermal CO removal.

Figures 2 and 3 highlight these differences in the ability of electrons to remove Cl atoms from the $PtCl_2$ deposit. Figure 2 provides data regarding a relatively thin deposit (thickness not measured), in which the continued electron beam processing slowly removed the majority of Cl atoms, resulting a film with 8.3% Cl, producing a similar result to that observed in our previous work[24]. In contrast, Figure 3 shows data regarding a thicker deposit, which was thick enough to be imaged in the SEM, and was created by deposition for approximately four times as long as the thinner deposit. Thickness still isn't measured, but the important point is that electron processing is able to remove surface Cl; after a certain point, Cl removal is complete from the surface, but not from the deposit bulk, due to the significant Cl inventory in the larger deposit, which is not removed by electron beam processing. Separate control experiments were conducted in the SEM on thick deposits created from $cis$-$Pt(CO)_2Cl_2$ in the Auger spectrometer, in which the deposit was continually exposed to the SEM electron beam (at both 10kV and 20kV) for several hours, conditions more analogous (indeed, harsher due to longer exposure times) to those in FEBID experiments, and minimal Cl loss was observed. This is perhaps due to two factors: (1), the electrons have a limited penetration depth (thus, electrons only remove surface Cl) and the majority of deposits evaluated in the SEM were by necessity, of a suitable thickness to be imaged in the SEM and to show minimal substrate contribution at 10kV in EDS, and/or (2), the $PtCl_2$ deposits are more susceptible to lower energy secondary electrons which are produced in greater numbers by the lower energy primary beams used in the XPS experiments (500 eV), and the Auger experiments (3 kV), than in the SEM (10kV, 20kV). Our experiments show that electron post-processing has the ability to remove

halogen atoms from FEBID deposits, but its overall utility is very specific to the size and shape of deposits created. It will be interesting to observe the elemental composition and structural integrity of FEBID deposits created from *cis*-Pt(CO)$_2$Cl$_2$ in a typical FEBID set-up, investigations which are expected to take place in the future by other research groups.

Next, we evaluated the deposits formed from *cis*-Pt(CO)$_2$Cl$_2$ with atomic hydrogen radicals as a potential method to remove Cl. Atomic hydrogen radical purification was observed both *in situ* in the Auger spectrometer, and *ex situ*, at a much higher atomic radical flux. Figure 4 shows the effects of the *in situ* atomic hydrogen processing. Initially, the atomic hydrogen is effective at removing Cl atoms, and the Auger spectra show Cl removal to the point where surface Cl is removed, but the remainder of the deposit retains its Cl and the continual supply of Cl from within the deposit maintains the level of measured surface Cl at approximately a constant level. This is analogous to the result seen for electrons above and also in agreement with data reported by Plank *et. al.* (unpublished work) for atomic oxygen radicals. Light Ar$^+$ sputtering shows that the deposit composition is still mainly PtCl, and as the surface is removed, the Cl appears to return as a new portion of the deposit is exposed. Further atomic hydrogen treatment is observed to again remove the surface Cl. Thus, *in situ* atomic hydrogen purification at a relatively low $P_{H_2}$ ($\sim$ 5 x 10$^{-7}$ Torr) was able to remove surface Cl but could only penetrate a limited distance into the deposit.

The next portion of the discussion will focus on the fate of several deposits subjected to atomic hydrogen treatment *ex situ* at a higher $P_{H_2}$ ($\sim$ 1 Torr). Interestingly, a variety of structural results were observed from deposits subjected to atomic hydrogen treatment, suggesting that several factors may be at play; the overall effect on elemental

composition was removal of all Cl on varying timescales. Figure 6 shows that 10 minutes of atomic hydrogen was sufficient to remove all Cl from the deposit, and the deposit largely retains its shape. Some aggregation and small cracks are observed. It appears that the longer SEM beam dwell time required to obtain the EDS spectra caused surface carbon deposition or changed the surface composition sufficiently that cracks were preferentially generated in these locations (not visible in the SEM prior to atomic hydrogen treatment) during atomic hydrogen treatment, possibly providing a favorable location for Cl to exit the deposit without causing significant loss of deposit structural integrity.

Figure 7 shows another deposit before and after atomic hydrogen treatment. This deposit was not subjected to EDS prior to atomic hydrogen treatment, as the longer SEM electron beam dwell time required to collect an EDS spectra (especially longer spectra) impacted the deposit, and thus influenced the end result, as observed in Figures 6 and 8. This deposit largely retains its shape, and doesn't appear to have significant cracking. It appears likely that the features created in the Auger spectrometer and visible on top left of the deposit, provided a nucleation site for the atomic hydrogen and Cl to desorb, without significant structural changes.

Figure 8 shows the fate of a third deposit after atomic hydrogen treatment. This deposit shows four flat, dense regions which appear to be due to deposition of surface carbon during EDS spectra, and presents a notably different appearance than the relatively uniform honeycomb appearance of the broader deposit. This honeycomb appearance is similar to what would be expected based on observations by Horch *et. al.*, that H atoms allow Pt to become mobile[42]. Figure 9 shows a combination of effects on a deposit which was first exposed to electron beam post-processing, and then to atomic hydrogen

purification. The cracking observed in Figure 8 still takes place, but to a lesser extent, perhaps due to deposition of surface carbon or other structural changes caused by electron beam irradiation prior to atomic hydrogen treatment.

Figure 10 shows the fate of a fourth deposit after two hours of atomic hydrogen. Similarly to the deposit shown in Figure 7, this deposit was not exposed to longer SEM beam dwell times for EDS prior to atomic hydrogen exposure. In this particular case, two hours of atomic hydrogen exposure resulted in a complete loss of structural integrity, as the atomic hydrogen removed the Cl. EDS maps show that the Pt atoms do aggregate, but overall structural integrity is lost. Interestingly, Figures 8 and 10 both indicate that once the Cl has been cleaned from the structure, there is minimal change in appearance, aside from minor changes (probably physical) as observed in Figure 7d. This suggests that the mobility of the Pt and the removal of the Cl cause the structural changes observed in these deposits, rather than the treatment with atomic hydrogen alone; i.e., if all species present are inert to atomic hydrogen, then atomic hydrogen treatment will not cause significant changes to deposit structural integrity.

Figures 11 through 15 provided the opportunity to observe the slow removal of Cl from the deposit due to atomic hydrogen exposure. It isn't possible to make an accurate determination of removal (i.e. first order decay) based on the uncertainties involved in the introduction and removal of the deposit into several different systems. It is apparent that the Cl was removed much more slowly from this deposit than all the other deposits. It is possible that this is due to a significant amount of surface carbon deposition, as the first treatment for the deposit was a control experiment in which the deposit was exposed to the atom source without any hydrogen. It is possible that the atomic hydrogen pressure

decreased significantly (although this was not observed). No significant changes in deposit appearance (or EDS elemental composition) were observed until after 18 minutes of atomic hydrogen exposure. After 18 minutes of exposure, Cl removal starts to noticeably occur and the deposit was progressively exposed to 30 minutes of atomic hydrogen and then reevaluated. However, Cl removal is not uniform across the deposit and it occurs preferentially in the areas of cracks or fissures, as the deposit slowly loses structural integrity with increasing exposure to atomic hydrogen. This supports the premise that as the structure loses integrity, the Cl able to desorb more efficiently, and indeed, that the Cl removal promotes loss of structural integrity as the Pt becomes mobile. It would be interesting to evaluate the effects of a lower flux of atomic hydrogen on FEBID deposits created from $cis$-Pt(CO)$_2$Cl$_2$, as there could be an optimal pressure to remove Cl entirely without loss of structural integrity, which we could not observe due to operation at the lower pressure ($\sim$5 x $10^{-7}$ Torr) and higher pressure ($\sim$ 1 Torr) extremes of atomic hydrogen radical production. Lastly, three other Pt containing precursors were evaluated with atomic hydrogen radicals, but nothing significant was observed, either in terms of structural changes or elemental composition changes. Thus, atomic hydrogen appears to have an impact on certain chemical compositions and structures, but not on every type of structure. The structural changes observed in this chapter appear to be due to the aggregation of Pt and rapid loss of Cl, causing structural changes to the deposit due to the chemical changes. Previous work by Wnuk $et.$ $al.$[41] has shown successful purification treatment of deposits formed from Me$_2$Au(acac), in which treatment by atomic oxygen, followed by treatment with atomic hydrogen, can result in pure Au deposits. It is apparent that atomic hydrogen treatment has a similar effect on Pt deposits containing halogen atoms. Larger implications

for FEBID are that again, many competing processes are taking place for FEBID deposits and different conditions play a large role, both in deposit formation and purification.

## 5.5. Conclusion

Deposits were created from *cis*-Pt(CO)$_2$Cl$_2$ in a FEBID-like process, and then subjected to electron beam or atomic hydrogen radical processing. Electron beam treatment and atomic hydrogen treatment at lower $P_{H_2}$ ($\sim 5 \times 10^{-7}$ Torr) resulted in removal of primarily surface Cl. More aggressive atomic hydrogen cleaning, at a much higher $P_{H_2}$ ($\sim 1$ Torr) resulted in removal of all Cl from structures, but also modified the structures to a honeycombed or open structure, or caused loss of structural integrity. Under certain conditions, atomic hydrogen atoms can cause deposited Pt atoms to mobilize and disperse/disaggregate, which limits the applicability of atomic hydrogen cleaning for FEBID, but may have interesting possibilities for use of Pt in catalysis. Evaluation of other Pt containing precursors (MeCpPtMe$_3$, Pt(hfac)$_2$, and Pt(PF$_3$)$_4$) showed minimal impact from atomic hydrogen treatment.

## 5.6. Acknowledgements

## 5.7. References

(1)     Utke, I.; Hoffmann, P.; Melngailis, J. *Journal of Vacuum Science & Technology B* **2008**, *26*, 1197.

(2)     Van Dorp, W.; Hagen, C. *Journal of Applied Physics* **2008**, *104*, 081301.

(3)     Huth, M.; Porrati, F.; Schwalb, C.; Winhold, M.; Sachser, R.; Dukic, M.; Adams, J.; Fantner, G. *Beilstein journal of nanotechnology* **2012**, *3*, 597.

(4)     Randolph, S.; Fowlkes, J.; Rack, P. *Critical reviews in solid state and materials sciences* **2006**, *31*, 55.

(5)     Post, P.; Mohammadi-Gheidari, A.; Hagen, C.; Kruit, P. *Journal of Vacuum Science & Technology B* **2011**, *29*, 06F310.

(6)     Spencer, J. A.; Rosenberg, S. G.; Barclay, M.; Wu, Y.-C.; McElwee-White, L.; Fairbrother, D. H. *Applied Physics A* **2014**, *117*, 1631.

(7)     Mulders, J. *Nanofabrication* **2014**, *1*, 74.

(8)     Xue, Z.; Strouse, M. J.; Shuh, D. K.; Knobler, C. B.; Kaesz, H. D.; Hicks, R. F.; Williams, R. S. *Journal of the American Chemical Society* **1989**, *111*, 8779.

(9)     Chen, I.-C.; Chen, L.-H.; Orme, C.; Quist, A.; Lal, R.; Jin, S. *Nanotechnology* **2006**, *17*, 4322.

(10)    Hübner, B.; Koops, H.; Pagnia, H.; Sotnik, N.; Urban, J.; Weber, M. *Ultramicroscopy* **1992**, *42*, 1519.

(11)    Edinger, K.; Becht, H.; Bihr, J.; Boegli, V.; Budach, M.; Hofmann, T.; Koops, H. W.; Kuschnerus, P.; Oster, J.; Spies, P. *Journal of Vacuum Science & Technology B* **2004**, *22*, 2902.

(12)    Heerkens, C. T. H.; Kamerbeek, M.; van Dorp, W.; Hagen, C.; Hoekstra, J. *Microelectronic Engineering* **2009**, *86*, 961.

(13)    Liang, T.; Frendberg, E.; Lieberman, B.; Stivers, A. *Journal of Vacuum Science & Technology B* **2005**, *23*, 3101.

(14)    Engmann, S.; Stano, M.; Matejčík, Š.; Ingólfsson, O. *Physical Chemistry Chemical Physics* **2012**, *14*, 14611.

(15)    Engmann, S.; Stano, M.; Papp, P.; Brunger, M. J.; Matejčík, Š.; Ingólfsson, O. *The Journal of chemical physics* **2013**, *138*, 044305.

(16)    May, O.; Kubala, D.; Allan, M. *Physical Chemistry Chemical Physics* **2012**, *14*, 2979.

(17)    Wnorowski, K.; Stano, M.; Matias, C.; Denifl, S.; Barszczewska, W.; Matejčík, Š. *Rapid Communications in Mass Spectrometry* **2012**, *26*, 2093.

(18)    Thorman, R. M.; Ragesh Kumar, T.; Fairbrother, D. H.; Ingólfsson, O. *Beilstein journal of nanotechnology* **2015**, *6*, 1904.

(19)    Landheer, K.; Rosenberg, S. G.; Bernau, L.; Swiderek, P.; Utke, I.; Hagen, C. W.; Fairbrother, D. H. *The Journal of Physical Chemistry C* **2011**, *115*, 17452.

(20)    Rosenberg, S. G.; Barclay, M.; Fairbrother, D. H. *Physical Chemistry Chemical Physics* **2013**, *15*, 4002.

(21)    Rosenberg, S. G.; Barclay, M.; Fairbrother, D. H. *The Journal of Physical Chemistry C* **2013**, *117*, 16053.

(22)    Wnuk, J. D.; Gorham, J. M.; Rosenberg, S. G.; van Dorp, W. F.; Madey, T. E.; Hagen, C. W.; Fairbrother, D. H. *The Journal of Physical Chemistry C* **2009**, *113*, 2487.

(23)    Spencer, J. A.; Brannaka, J. A.; Barclay, M.; McElwee-White, L.; Fairbrother, D. H. *The Journal of Physical Chemistry C* **2015**, *119*, 15349.

(24)    Spencer, J. A.; Wu, Y.-C.; McElwee-White, L.; Fairbrother, D. H. *Journal of the American Chemical Society* **2016**.

(25)    Botman, A.; Mulders, J.; Hagen, C. *Nanotechnology* **2009**, *20*, 372001.

(26)    Ervin, M. H.; Chang, D.; Nichols, B.; Wickenden, A.; Barry, J.; Melngailis, J. *Journal of Vacuum Science & Technology B* **2007**, *25*, 2250.

(27)    Lewis, B. B.; Stanford, M. G.; Fowlkes, J. D.; Lester, K.; Plank, H.; Rack, P. D. *Beilstein journal of nanotechnology* **2015**, *6*, 907.

(28)    Mehendale, S.; Mulders, J.; Trompenaars, P. *Microelectronic Engineering* **2015**, *141*, 207.

(29)    Villamor, E.; Casanova, F.; Trompenaars, P.; Mulders, J. *Nanotechnology* **2015**, *26*, 095303.

(30)     Botman, A.; Mulders, J.; Weemaes, R.; Mentink, S. *Nanotechnology* **2006**, *17*, 3779.

(31)     Geier, B.; Gspan, C.; Winkler, R.; Schmied, R.; Fowlkes, J. D.; Fitzek, H.; Rauch, S.; Rattenberger, J.; Rack, P. D.; Plank, H. *The Journal of Physical Chemistry C* **2014**, *118*, 14009.

(32)     Sachser, R.; Reith, H.; Huzel, D.; Winhold, M.; Huth, M. *ACS applied materials & interfaces* **2014**, *6*, 15868.

(33)     Stanford, M. G.; Lewis, B. B.; Noh, J. H.; Fowlkes, J. D.; Rack, P. D. *ACS applied materials & interfaces* **2015**, *7*, 19579.

(34)     Rosenberg, S. G.; Landheer, K.; Hagen, C. W.; Fairbrother, D. H. *J. Vac. Sci. Technol. B* **2012**, *30*, 051805/1.

(35)     Wnuk, J. D.; Gorham, J. M.; Rosenberg, S. G.; van Dorp, W. F.; Madey, T. E.; Hagen, C. W.; Fairbrother, D. H. *J. Phys. Chem. C* **2009**, *113*, 2487.

(36)     Wnuk, J. D.; Gorham, J. M.; Rosenberg, S. G.; van Dorp, W. F.; Madey, T. E.; Hagen, C. W.; Fairbrother, D. H. *J. Appl. Phys.* **2010**, *107*, 054301/1.

(37)     Bagnoli, F.; Dell'Amico, D. B.; Calderazzo, F.; Englert, U.; Marchetti, F.; Herberich, G. E.; Pasqualetti, N.; Ramello, S. *J. Chem. Soc., Dalton Trans.* **1996**, 4317.

(38)     Calderazzo, F. *J Organomet. Chem.* **1990**, *400*, 303.

(39)     Lutton, J.; Parry, R. *J. Am. Chem. Soc.* **1954**, *76*, 4271.

(40)     Bajt, S.; Alameda, J. B.; Barbee, T. W.; Clift, W. M.; Folta, J. A.; Kaufmann, B.; Spiller, E. A. *Opt. Eng.* **2002**, *41*, 1797.

(41)     Wnuk, J. D.; Gorham, J. M.; Rosenberg, S. G.; Madey, T. E.; Hagen, C. W.; Fairbrother, D. H. *Journal of Vacuum Science & Technology B* **2010**, *28*, 527.

(42)     Horch, S.; Lorensen, H.; Helveg, S.; Lægsgaard, E.; Stensgaard, I.; Jacobsen, K. W.; Nørskov, J. K.; Besenbacher, F. *Nature* **1999**, *398*, 134.

(43)     Mulders, J.; Belova, L.; Riazanova, A. *Nanotechnology* **2010**, *22*, 055302.

Chapter 6

Electron Induced Surface Reactions of CpFe(CO)$_2$Mn(CO)$_5$ and Co$_2$(CO)$_8$

Chapter 6.    Electron induced surface reactions of CpFe(CO)$_2$Mn(CO)$_5$ and Co$_2$(CO)$_8$

## 6.1.  Introduction

As technological advances require integrated circuits with smaller and smaller feature sizes, both industry and academia continue to search for methods to fabricate increasingly smaller nanostructures.  There are a variety of methods that can produce nanoscale features; each technique has benefits and drawbacks that can govern the best method for a particular application.  One promising area of research is a process called focused electron beam induced deposition (FEBID).  FEBID involves a gaseous precursor introduced into a vacuum chamber (typically a modified SEM), and transiently adsorbed on a substrate[1-4].  The precursor is irradiated by a focused electron beam, which causes decomposition of the precursor into volatile and non-volatile fragments.  The volatile fragments are pumped into the vacuum, while the non-volatile fragments remain behind, forming a deposit.  FEBID deposits are size and shape specific and are only limited by the manipulation of the electron beam; they do not require any resist layers or masks[2,3].  To date, FEBID nanostructures (dots) have been made with a diameter of 0.72 nm; FEBID shows significant promise in writing features in the sub-10 nm regime[5,6].

Despite many advantages, there are several challenges that prevent wide-spread application of FEBID to nanostructure fabrication.  The largest challenge is the purity of nanostructures created by FEBID, which is directly related to choice of precursor[2,7,8].  Many precursors used in FEBID were designed as chemical vapor deposition (CVD) precursors, which produce largely pure metallic films under heat.  However, FEBID is an electron based rather than heat based process, and due to the different mechanisms,

precursors that produce pure films in CVD often have significant amounts of contamination in FEBID nanostructures, which severely limits their use. A classic example is the precursor MeCpPtMe3, which produces pure Pt films in CVD, but results in deposits containing ~20% Pt and ~80% C in FEBID[9]. Even in the face of contamination issues, FEBID nanostructures have found a variety of applications, most notably in lithographic mask repair[10,11] and fabrication of ultrasharp probe tips[12,13].

Recently, we have applied a surface science approach to evaluate potential FEBID precursors and enable us to determine mechanistic details of precursor decomposition under electron beam irradiation[14-17]. The surface science approach relies on use of an ultrahigh vacuum (UHV) environment, which allows detailed evaluation of species that cannot be evaluated in the SEMs typically used for FEBID. The surface science experiments are conducted in two steps: the first step involves dosing of the precursor and adsorption on a cooled substrate (usually < 200K) as a thin film (nanometer scale thickness). X-ray photoelectron spectroscopy (XPS) is used to verify adsorption of the precursor on the substrate. An electron gun is used to irradiate the adsorbed precursor; XPS is used to evaluate changes on the surface, while mass spectrometry (MS) is used to characterize the species ejected into the gas phase during electron beam irradiation. Further details of this approach may be found in several previous publications[15,16].

There are a wide variety of compounds that have been used in the FEBID process or evaluated for use in the FEBID process to deposit a variety of metals, $SiO_2$, and other substances[2]. However, the vast majority of these compounds contain only one metal center. The few compounds evaluated for FEBID that contain more than one metal center are generally cluster compounds, which contain multiples of the same metal center, for

example $Co_2(CO)_8$, $Fe_3(CO)_{12}$, and $Rh_2Cl_2(PF_3)_4$[2]. Little work has been reported to date about the performance of precursors with dissimilar metal centers, with the exception of recent work on FEBID deposits created from $HFeCo_3(CO)_{12}$ by Porrati *et. al.*, which resulted in CoFe alloy magnetic nanostructures composed of approximately 80% metal content and 10% carbon and oxygen content[18]. Given the difficulty in controlling deposition of different species by processes such as injection of more than one gas feed[19], it is interesting to explore the performance of a bimetallic compound under electron beam irradiation, as it has potential to deposit both metals as noted above, potentially retaining the metal stoichiometry of the molecule. Due to design requirements, there are a dearth of bimetallic precursors that could be useful in FEBID[2,7]; for example, the precursor must have a long enough residence time on the substrate surface to be decomposed by electrons, but must also be volatile enough that non-desirable ligands desorb, which can be challenging with heavier molecular weight compounds. Our collaboration with synthetic organometallic chemists has led to investigation of the current compound, $CpFe(CO)_2Mn(CO)_5$. Previous research has indicated that some proportion of carbonyl (CO) ligands are likely to desorb under electron beam irradiation[14,20,21], while the cyclopentadienyl (Cp) ligand is expected to remain behind on the surface[16,21], contributing to carbon contamination in resulting structures; thus $CpFe(CO)_2Mn(CO)_5$ is not expected to be a viable FEBID compound to produce pure bimetallic structures. However, as a model compound to evaluate mixed metals under electron beam irradiation, it will provide valuable data. Additionally, a few experiments were conducted with the binuclear homometallic compound $Co_2(CO)_8$, which is currently used for FEBID of relatively pure magnetic nanostructures, and has produced magnetic nanostructures of > 90% purity[22].

6.2.Experimental

An ultrahigh vacuum (UHV) chamber equipped with X-ray Photoelectron Spectroscopy (XPS) and Mass Spectrometry (MS) was used to study the effects of electron irradiation on nanometer scale films of $CpFe(CO)_2Mn(CO)_5$ and dicobalt octacarbonyl $(Co_2(CO)_8)$. Another UHV chamber equipped with an Auger Spectrometer (AES) was used to create deposits under steady state deposition conditions, using electron irradiation. Further details of the chambers' analytical capabilities can be found in earlier publications[15,16,23].

### 6.2.1.   Synthesis of $CpFe(CO)_2Mn(CO)_5$

#### 6.2.1.1.    General (Synthesis)

Unless otherwise stated, all reactions were carried out under an inert atmosphere using Schlenk line and glovebox techniques.  $CpFe(CO)_2I$ and $Mn_2(CO)_{10}$ were purchased from Sigma-Aldrich and used as received.  Tetrahydrofuran (THF) was distilled from sodium benzophenone ketyl and was stored over 3 Å molecular sieves prior to use. IR spectroscopy was performed on a Bruker Alpha spectrometer using a sealed KBr liquid cell from Sigma-Aldrich.

#### 6.2.1.2.    $CpFe(CO)_2Mn(CO)_5$

Modified literature procedures were used to synthesize $CpFe(CO)_2Mn(CO)_5$[24-26]. A 1% Na/Hg amalgam was made by dissolving Na (0.1237 g, 5.381 mmol) in Hg (12.4140

g). $Mn_2(CO)_{10}$ (0.7690 g, 1.978 mmol) was dissolved in THF (15 mL) and added to the Na/Hg amalgam. The solution was stirred for one hour. The organic layer was transferred to a Schlenk flask containing $CpFe(CO)_2I$ (1.2056 g, 3.9767 mmol) and stirred for two days, under the exclusion of light. MeOH (2.0 mL) was added to the deep red solution. The solvent was removed *in vacuo* and column chromatography was performed on a silica column with pentane as the eluant. Three bands were seen: yellow due to $Mn_2(CO)_{10}$, red which was product, and brown due to remaining $CpFe(CO)_2I$, which stays on the baseline. The product was obtained as a dark red solid (sublimation: 46 °C, 100 mTorr). Crude yield: 0.5418 g, 37%. Sublimed yield: 0.2840 g, 19%. The compound was characterized by comparison to literature data[24]. $^1H$ NMR (300 MHz, $C_6D_6$) δ 3.97 (s, 5H). IR (hexanes): 2082, 2014, 1991, 1976, 1945 $cm^{-1}$.

### 6.2.2. $Co_2(CO)_8$

$Co_2(CO)_8$ was purchased from Sigma-Aldrich and used as received. It was stored in a freezer and handled inside an $N_2$ glovebox due to its sensitivity to air and moisture, as well as its pyrophoric nature.

### 6.2.3. Precursor handling and coupling to UHV systems

Both $CpFe(CO)_2Mn(CO)_5$ and $Co_2(CO)_8$ are solids at standard temperature and pressure. Due to the sensitivity of $CpFe(CO)_2Mn(CO)_5$ to air and moisture, it was stored in the freezer of and handled inside an $N_2$ glove box. To prepare the precursor for deposition, it was added to a glass finger, which was attached to a UHV compatible leak valve coupled directly to the UHV chamber. To minimize chamber pump down time, the

glass finger was evacuated at the same time as the UHV chamber was pumped down with the leak valve open into the 1.0 x $10^{-6}$ Torr pressure regime, at which point the leak valve was closed and the main chamber baked out and restored to the UHV pressure regime. To maintain a sufficient vapor pressure of $CpFe(CO)_2Mn(CO)_5$, the precursor was heated to ~35 °C during deposition with the temperature monitored by a thermocouple. Conditions were similar for $Co_2(CO)_8$, with the difference that some experiments were conducted with the precursor at room temperature (~21 °C), while other experiments were conducted with the precursor heated to ~30 - 40 °C. It is also important to note other dosing conditions for $Co_2(CO)_8$. In an effort to minimize the large CO pressure in preparation for dosing, each day the test tube containing $Co_2(CO)_8$ was evacuated to the vacuum chamber for about 30 minutes while the precursor was cooled with liquid nitrogen. Then the liquid nitrogen was removed and the compound warmed and pumped off to remove residual hexanes. Due to challenges with this compound, the UHV system was baked briefly each night for approximately four hours.

### 6.2.4.  Substrates

Electron irradiation of thin films of $CpFe(CO)_2Mn(CO)_5$ and $Co_2(CO)_8$ was conducted on a gold (Au) substrate in the XPS. The Au substrate allowed a clean evaluation of the C(1s), O(1s), and Fe(2p) XPS transitions, for $CpFe(CO)_2Mn(CO)_5$, and for all transitions for $Co_2(CO)_8$. Unfortunately, due to a conflict between the Mn $2p_{3/2}$ (642 eV) and Au $4p_{1/2}$ (647eV) transitions, the Mn(2p) transition could not be fully elucidated. Further work will address this issue by conducting experiments on an amorphous carbon (a:C) substrate, which will allow evaluation of all transitions except C(1s). Ion sputtering using 4 keV Ar$^+$ ions was conducted in between experiments to regenerate the substrate *in*

*situ* until the substrate was verified clean by XPS. Depositions from $CpFe(CO)_2Mn(CO)_5$ in an Auger spectrometer utilized an atomically smooth Ru-capped Si/Mo multi-layer mirror substrate[27], which was chosen for depositions due to ease with which deposits could be imaged in the scanning electron microscope. Prior to deposition, the cleanliness of the Ru-capped Si/Mo substrate was verified by Auger spectroscopy.

### 6.2.5. Dosing the precursor on the substrate in the XPS/MS chamber

Nanometer scale films of $CpFe(CO)_2Mn(CO)_5$ or $Co_2(CO)_8$ were created by leaking the precursor into the UHV chamber through a UHV-compatible leak valve, where it was adsorbed onto a cooled substrate at 113K ($\pm$ 10K), except for one experiment with $Co_2(CO)_8$ in which the precursor was adsorbed onto a cooled substrate at 168 K($\pm$ 10 K). Average film thickness was determined for each film by measuring the attenuation of the substrate XPS photoelectrons (Au(4f)) after compound adsorption,[28] using an inelastic mean free path for Au(4f) photoelectrons of 2.0 nm[29-31].

### 6.2.6. Electron Source

A commercial flood gun (Specs FG 15/40) was used as an electron source for all XPS and MS experiments. In order to ensure that the film was subjected to a relatively uniform electron flux, the electron source was characterized by a Faraday cup. Throughout our experiments, the incident electron energy was 500 eV; this was calculated from the sum of the electron energy from the flood gun (480 eV) and a positive bias (+20V), which was applied to prevent secondary electrons generated during irradiation from escaping.

Various electron currents were used. Electron flux is reported in terms of dose ($e^-$/cm$^2$). Further details of the electron source can be found in previous publications.[28,32]

### 6.2.7. X-ray Photoelectron Spectroscopy

XPS data were acquired in a PHI 5400 XPS using Mg Kα X-rays (hν = 1253.6 eV). Spectra were deconvoluted with commercial software (CASA XPS); binding energies obtained for films deposited on the Au substrate were aligned to the Au(4f$_{7/2}$) peak at 84.0 eV.

### 6.2.8. Creating Deposits in the Auger Spectrometer (AES)

Deposits were formed by leaking CpFe(CO)$_2$Mn(CO)$_5$ into the UHV chamber of a PHI 610 Scanning Auger Microprobe system (LaB$_6$ filament) using a UHV-compatible leak valve. The partial pressure of precursor at the substrate surface was enhanced by the use of a directional doser, similar in concept to the nozzles used in FEBID. The deposits were made under steady state deposition conditions with the substrate at room temperature, using an incident electron beam energy of 3kV and varying deposition times, substrate currents, and precursor partial pressures. Deposit thicknesses were assessed as suitably thick (but were not calculated) once the substrate peaks were no longer visible in the Auger spectrum.

### 6.2.9. Scanning Electron Microscopy (SEM) and Energy Dispersive Spectroscopy (EDS)

After deposits were generated in the Auger spectrometer, a cold-cathode field emission scanning electron microscope (JEOL 6700F, LEI detector) with a 1.0 nm

resolution at 15 keV equipped with an energy dispersive X-ray analyzer (EDAX Genesis 4000 X-ray analysis system, detector resolution of 129 eV) was used for deposit imaging and EDS analysis.

6.3. Results

6.3.1. $CpFe(CO)_2Mn(CO)_5$

Figure 1 shows the effect of electrons on the evolution of the C(1s), O(1s), Fe(2p), and Mn(2p) XPS transitions at the beginning of the reaction, on thin films ($\sim 0.5$ - $1.2$ nm) of "as deposited" $CpFe(CO)_2Mn(CO)_5$ adsorbed on Au at 113K ($\pm$ 10K) which is considered as largely the adsorbed but unreacted parent compound, and as similar films were exposed to increasingly larger electron doses up to $3.7 \times 10^{16}$ e$^-$/cm$^2$. Since both X-ray and electron beam irradiation generate electrons when they impinge on the substrate, separate control studies (data not shown) were conducted in which adsorbed $CpFe(CO)_2Mn(CO)_5$ was exposed to X-ray irradiation. These studies revealed that similar changes occur to adsorbed films of $CpFe(CO)_2Mn(CO)_5$ when exposed to either X-rays or electrons, and that $CpFe(CO)_2Mn(CO)_5$ is reactive to electrons from either X-ray or electron irradiation; thus, the data shown in Figure 1 was collected by taking a limited number of sweeps to characterize each XP region. This resulted in slightly noisier but more accurate data, since X-rays caused a minimal amount of the precursor to react. The effect of X-ray irradiation was found to be significant and a factor for all but the larger electron doses. Thus, for all data points, each film was exposed to electron beam irradiation, then to a short x-ray irradiation period to characterize the changes resulting from the electron beam irradiation. For doses greater than $1.9 \times 10^{16}$ e$^-$/cm$^2$, the film was
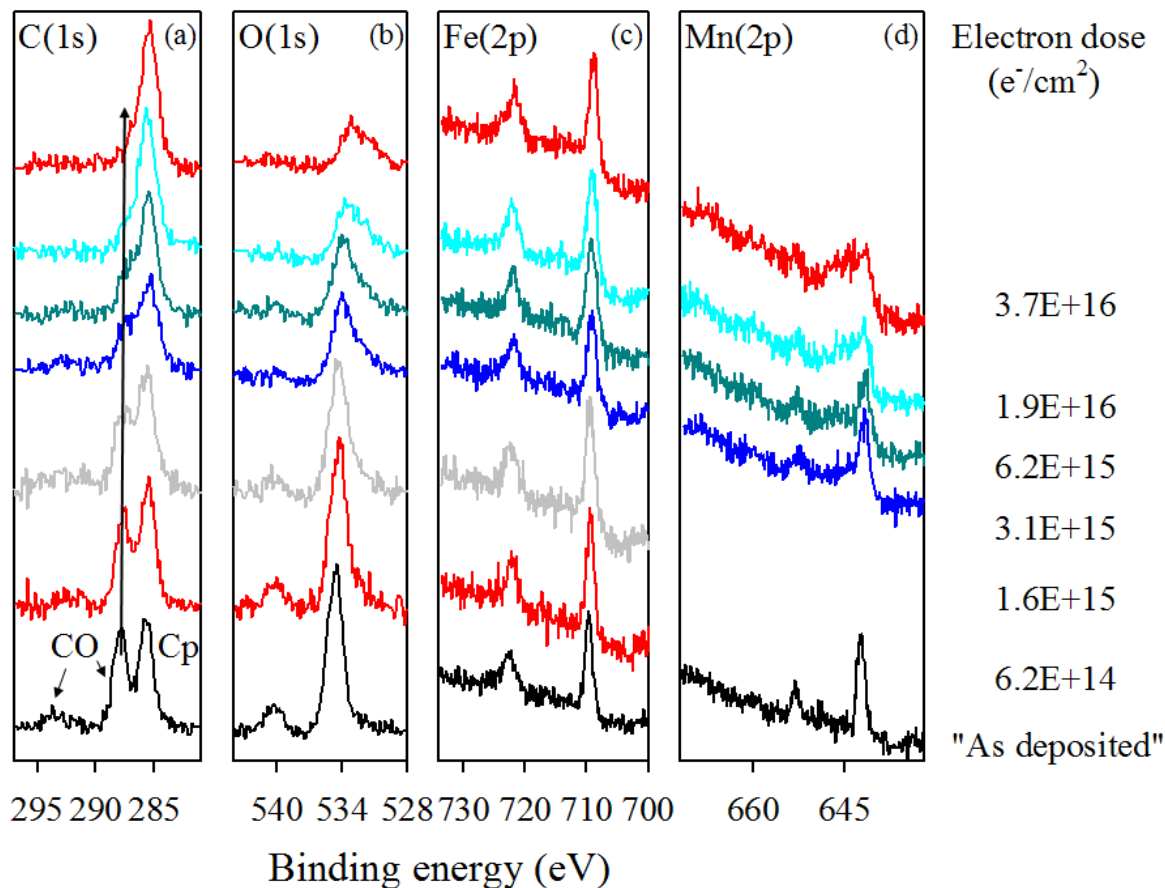
**Figure 6.1**: Evolution of the (a) C(1s), (b) O(1s), (c) Fe(2p) and (d) Mn(2p) XP regions for thin films (~0.5 – 1.2 nm) of $CpFe(CO)_2Mn(CO)_5$ adsorbed on an Au substrate at 113K (± 10K) and exposed to electron irradiation at 5 µA. In each panel, the lower spectrum is an "as deposited" dose, after only brief x-ray exposure. The arrow in the C(1s) region is shown as a guide to the eye.

exposed twice to the cycle of electron beam then x-ray characterization, as the effects of X-rays were assessed as minimal at this point.

In Figure 1, after precursor adsorption, the C(1s) region is characterized by two strong peaks, one at 287.9 eV, corresponding to contribution from a carbonyl (CO) ligand, and the second at 285.7 eV, corresponding to contribution from the cyclopentadienyl (Cp, $\eta^5$-$C_5H_5$) ligand. A smaller feature is also apparent at 293.7 eV, which is ascribed to a $\pi$-$\pi^*$ CO shake-up transition[33]. The stoichiometry of the two C(1s) species roughly

corresponds to that of the precursor; the peak at 287.9 eV and the shake-up feature are the result of the seven CO ligands, while the peak at 285.7 eV is consistent with the five carbon cyclopentadienyl ligand. Rough calculation of peak area from XPS data provides a qualitative molecular ratio of 7.6 C: 5 O: 1.2 Fe: 1 Mn, which roughly correlates with the expected molecular ratio of 12 C: 7 O: 1 Fe: 1 Mn. As the films are exposed to increasingly greater electron beam irradiation, the C(1s) region markedly changes, as the higher binding energy peak and shake-up feature gradually decrease in size and largely disappear, while the lower binding energy feature remains relatively unchanged, aside from a slight decrease in binding energy. After exposure to an electron dose of $3.7 \times 10^{16}$ e$^-$/cm$^2$, which is assessed as completion of the reaction (or nearly so), the C(1s) region is composed primarily of a large peak at 285.5 eV, consistent with the Cp ligand.

The O(1s) region is initially characterized by a single peak at 534.6 eV, characteristic of carbonyl ligands, and a $\pi$-$\pi$* CO shake-up transition centered at 540.3 eV[33]. After the film was subjected to electron irradiation, the O(1s) peak corresponding to CO has downshifted in binding energy to 532.9 eV, broadened (characteristic of oxide formation), and decreased in intensity; after electron irradiation of approximately $1.9 \times 10^{16}$ e$^-$/cm$^2$, the shake-up feature is no longer apparent in either the C(1s) or O(1s) regions.

In the Fe(2p) region, a sharp Fe ($2p_{1/2}$/$2p_{3/2}$) doublet is observed in the "as deposited" film with peaks centered at 722.6 eV and 709.7 eV, indicative of Fe in a single bonding environment. As the film is exposed to electron irradiation, small changes are noted. The Fe doublet peaks have broadened slightly and downshifted in binding energy to 721.8 eV and 708.9 eV, respectively. The decrease in binding energy is consistent with reduction in formal oxidation state typically observed as ligands desorb from a metal, while

189

the small amount of peak broadening (best observed on the left side of the Fe2p$_{3/2}$ peak) is consistent with changes in Fe bonding. The shape of the Fe peaks indicates that the Fe largely retains its metallic nature, and is not indicative of a formation of a significant amount of oxide.

Similarly, the Mn(2p) region is initially comprised of a Mn(2p$_{1/2}$/2p$_{3/2}$) doublet with peak positions at 653.2 and 642.2 eV. Unfortunately, the Mn peaks are partially obscured by interference of the Au(4p$_{1/2}$) peak at 647 eV. As the film is exposed to increasingly greater electron irradiation, it becomes difficult to distinguish either Mn(2p) peak; as
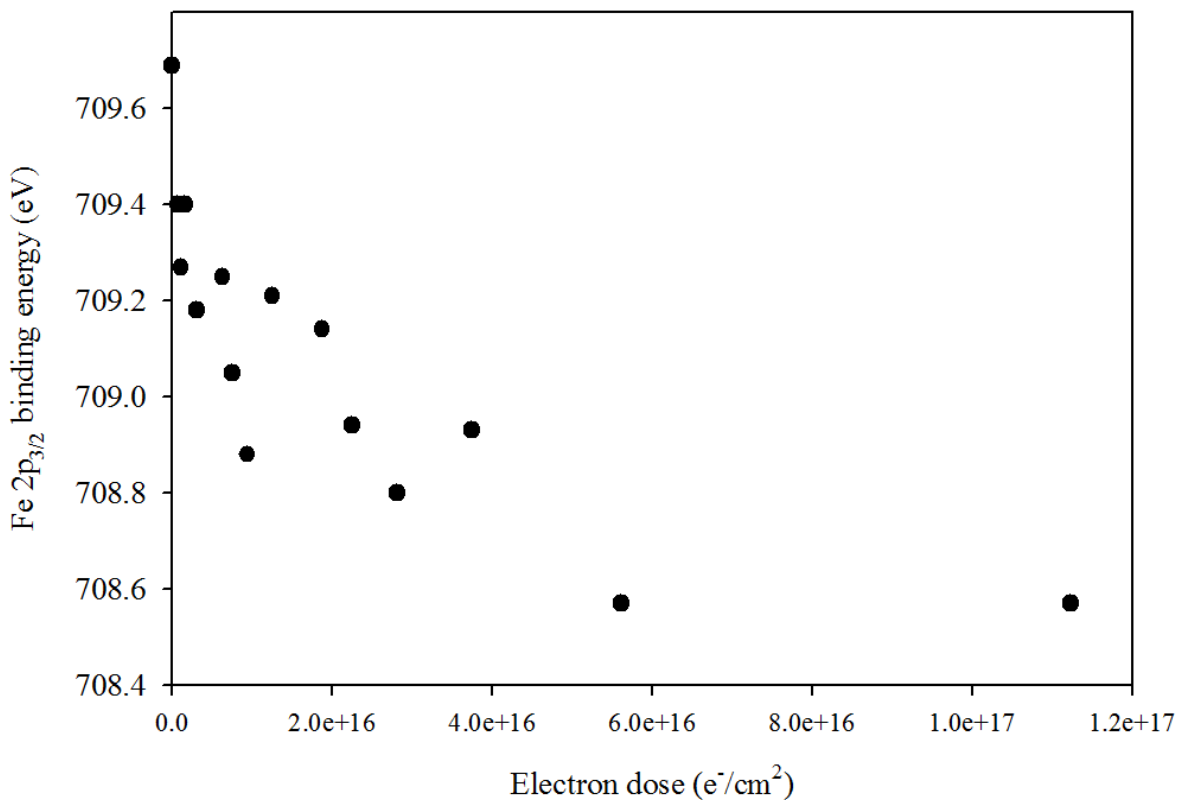


**Figure 6.2**: Electron irradiation induced changes in the Fe 2p$_{3/2}$ binding energy for 0.5 -1.2 nm CpFe(CO)$_2$Mn(CO)$_5$ films adsorbed on an Au substrate; each is plotted as a function of electron dose, as determined by XPS.

material is removed from the film (primarily due to CO loss), the substrate signal becomes stronger. Although it is expected that Mn would experience similar electron irradiation effects as Fe, this interesting point will be elucidated further on a different substrate without interference.

Figure 2 shows changes in the Fe $2p_{3/2}$ binding energy as the films are exposed to increasingly greater electron doses. The initial Fe $2p_{3/2}$ binding energy is 709.7 eV, which is consistent with Fe in a formal Fe(I) oxidation state[34]. Under electron beam irradiation, the Fe $2p_{3/2}$ binding energy decreases to approximately 708.6 eV after an electron dose of $1.1 \times 10^{17}$ $e^-/cm^2$ (for metallic iron, Fe$2p_{3/2}$ binding energy is 707.0 eV[34]). This is consistent with the metal center undergoing reduction towards a more metallic state, which has been observed for other precursors studied for FEBID[14,16,21,35].

Figure 3 displays mass spectrometry (MS) data obtained during electron beam irradiation at an electron current of 30 μA of $Cp(CO)_2FeMn(CO)_5$ adsorbed on an Au substrate. In Figure 3a, during electron beam irradiation, the primary species desorbed are CO, C, and O, at $m/z$ 28, 12, and 16, which are characteristic of carbonyl ligand desorption. A small $m/z = 18$ peak is also observed, which is attributed to residual $H_2O$ in the UHV chamber. Figure 3b presents data obtained during slow thermal compound desorption, conducted to capture the signature of the compound. Figure 3b shows MS peaks at $m/z$ 28, 12, and 16, ascribed to the CO ligand, as well as residual $H_2O$. Several characteristic features of Cp ligands are also observed in Figure 3b, most notably fragments at $m/z$ 40 and $m/z$ 62 - 65 amu. This MS data closely mirrors fragmentation patterns observed in previous research on precursors containing Cp ligands[16].

Figure 4 shows a kinetic analysis of species desorbed during electron beam

irradiation. The carbonyl species (*m/z* 28) was evaluated as it is the strongest signal during desorption. For reference, a similar analysis for another recently evaluated compound, *cis*-$Pt(CO)_2Cl_2$[35], is provided. Both precursors are observed to follow a roughly first order exponential decay profile. Interestingly, the CO species evolution for $CpFe(CO)_2Mn(CO)_5$ has decreased to background after an electron dose of $2 \times 10^{16}$ $e^-/cm^2$, while the CO species evolved from the *cis*-$Pt(CO)_2Cl_2$ film required an electron dose of $4 \times 10^{16}$ $e^-/cm^2$ to reach background levels (data not shown)[35].
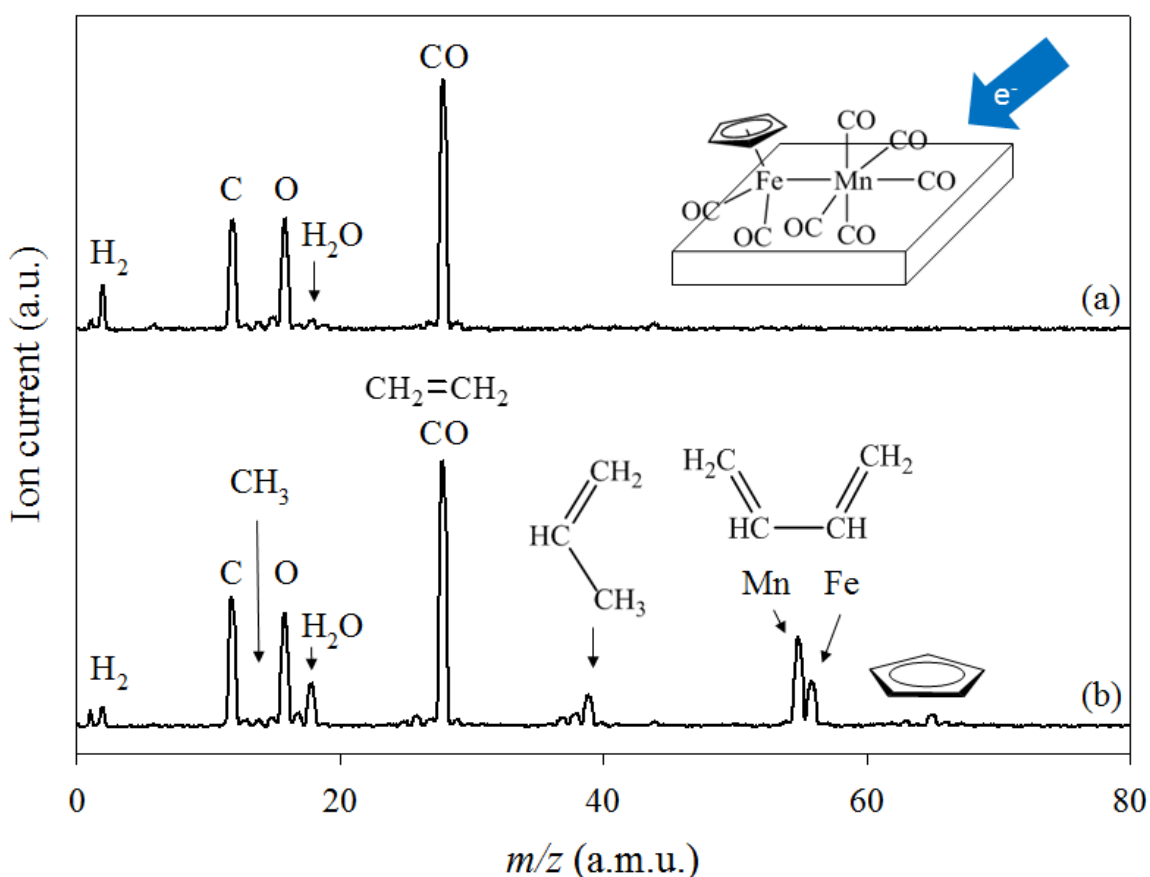


**Figure 6.3**: Mass spectrum (0-80 amu) for (a) the volatile species produced when a ~1.4 nm film of $CpFe(CO)_2Mn(CO)_5$ adsorbed on an Au substrate at 113K was irradiated by an electron dose of $1.7 \times 10^{17}$ $e^-/cm^2$ (incident electron energy of 500 eV, 30 µA); the spectrum represents an average of MS taken every 20 s during the electron exposure and (b) gas phase $CpFe(CO)_2Mn(CO)_5$ evolved when the adsorbed precursor was allowed to thermally desorb. For ease of comparison, spectra (a) and (b) were normalized to the CO peak height (*m/z* = 28).
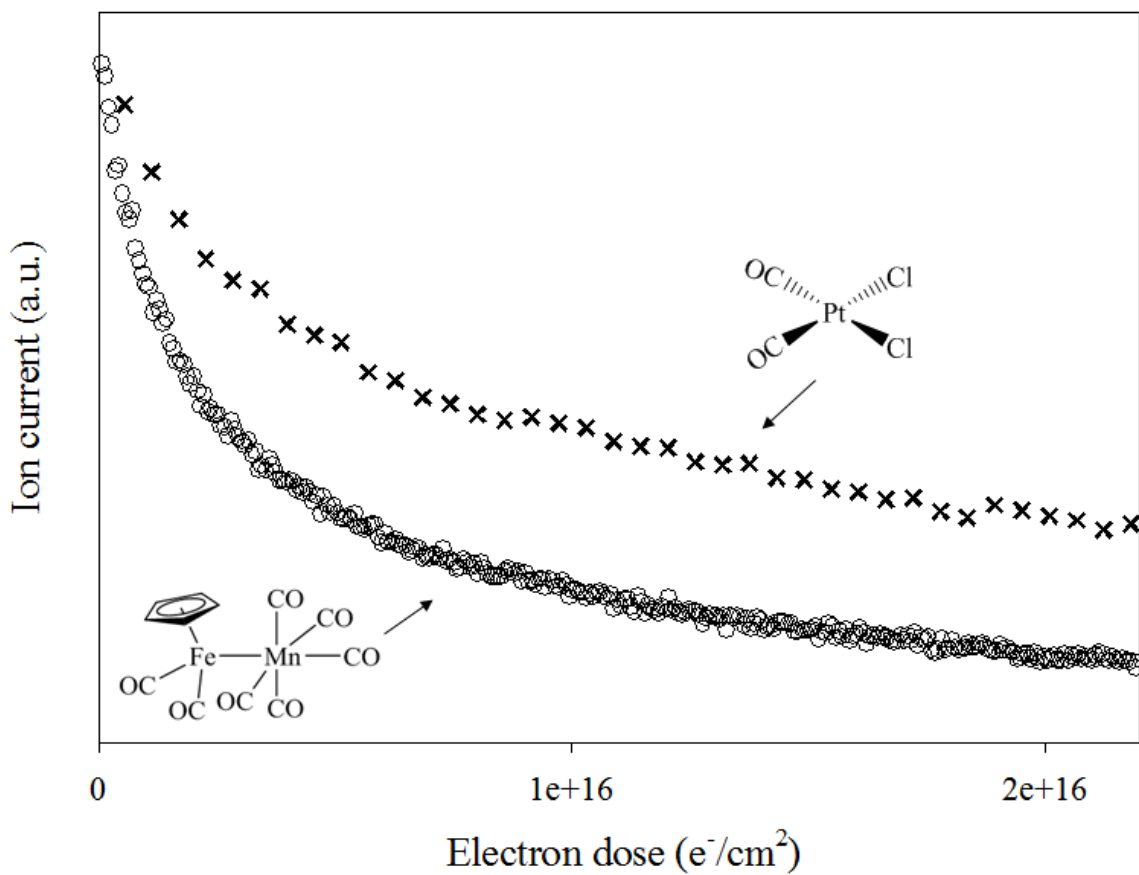
**Figure 6.4**: Kinetics of gas phase CO evolution during electron irradiation from a ~0.8 nm film of $CpFe(CO)_2Mn(CO)_5$ (open circles) compared with a ~0.7 nm film of *cis*-$Pt(CO)_2Cl2$ (x's), as measured by the CO peak at $m/z = 28$.

An electron target current of 1 μA was used for irradiation of CpFe(CO)$_2$Mn(CO)$_5$, while a current of 5 μA was used for irradiation of *cis*-Pt(CO)$_2$Cl$_2$.

The majority of experiments were conducted in a XPS on a cooled substrate. However, a few experiments were conducted at steady state deposition conditions, with the substrate at ambient temperature, using the 3kV electron beam in an Auger spectrometer. These deposits are representative of those that would be created under FEBID conditions. A Ru-coated Si/Mo multi-layer substrate was exposed to a continuous partial pressure of gas phase CpFe(CO)$_2$Mn(CO)$_5$, and irradiated by the Auger electron beam. Figure 5 shows a) an Auger spectrum of a deposit created from CpFe(CO)$_2$Mn(CO)$_5$, which is composed of C, O, Mn, and Fe; no contributions from the Ru/Si/Mo substrate are observed. Auger maps in which spatial distribution of surface Mn and Fe are determined by measuring the difference between the Auger transition of interest and a reference signal are shown for the b) Mn LMM (589 eV) and the c) Fe LMM (703 eV) transitions. Figure 5d shows the EDS spectrum for this deposit, which has an elemental composition of 18.2% Fe Lα, 18.2 % Mn Kα, 50.4% C Kα, and 12.6% O Kα, and Figure 5e shows the SEM image of this deposit. Both the Auger maps and the SEM image indicate that the deposit is defined by the electron beam; no conformal CVD-type deposition is observed.
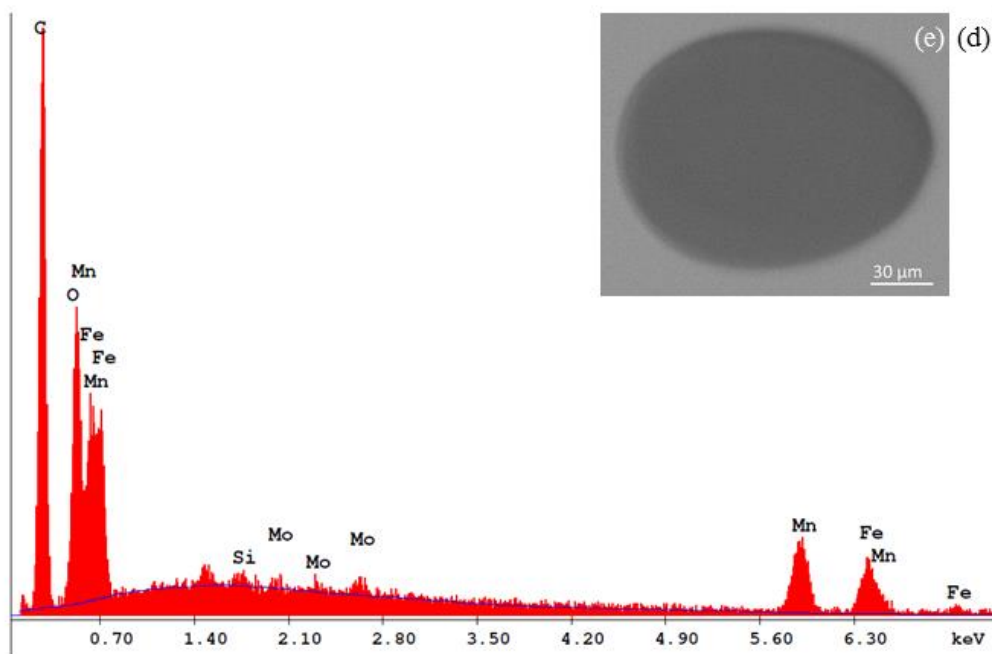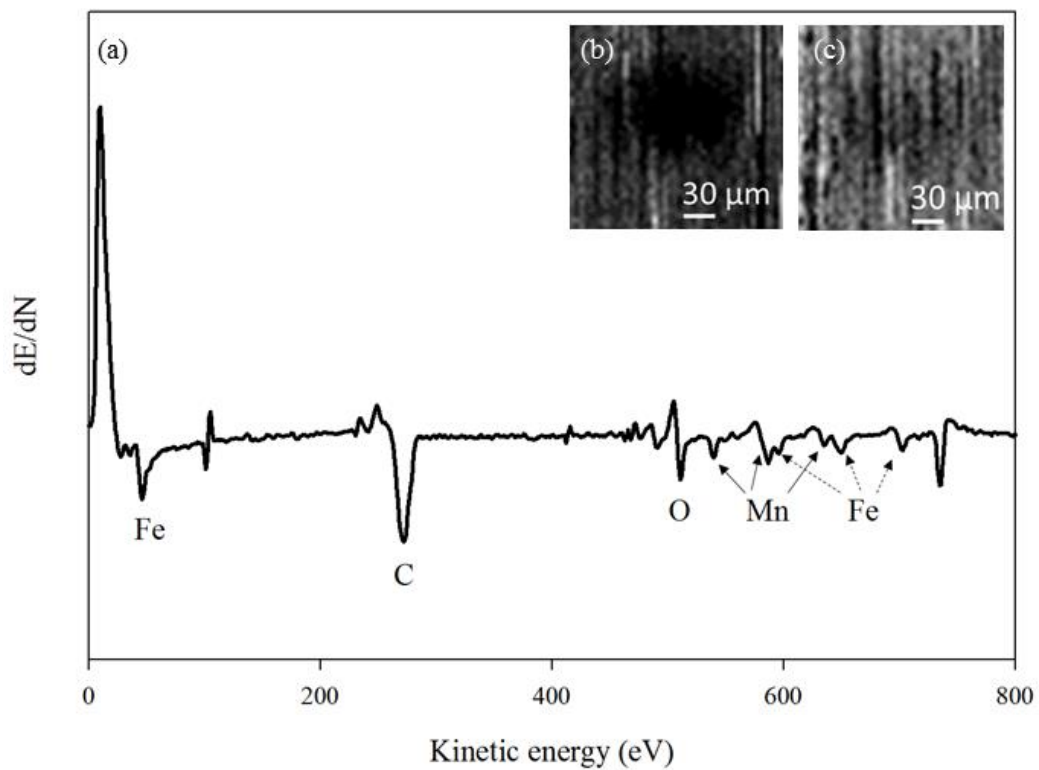
**Figure 6.5**: Auger electron and SEM data for a FEBID deposit created from CpFe(CO)$_2$Mn(CO)$_5$. The AES spectrum for a deposit on a Ru coated Si Mo multi-layer substrate is shown in (a) and Auger elemental maps for this deposit are shown for (b) Mn (589 eV) and (c) Fe (703 eV). Scanning electron microscope data for this deposit includes (d) EDS data, with elemental composition of 18.2 % Fe Lα, 18.2 % Mn Kα, 50.4 % C Kα, and 12.6 % O Kα, and (e) an SEM image taken at 10kV, 600x.

### 6.3.2. $Co_2(CO)_8$

Due to the wide usage of $Co_2(CO)_8$ as a FEBID precursor to produce magnetic nanostructures of relatively high purity and potentially interesting applications due to the catalytic properties of cobalt[22,36,37], a few experiments were conducted to evaluate the effects of electron beam irradiation on $Co_2(CO)_8$. Previous work (unpublished, data not shown) had indicated that $Co_2(CO)_8$ molecularly adsorbed on both $SiO_2$ and Au substrates, and that under electron beam irradiation, the majority of CO desorbed, while Co was reduced towards a more metallic state. Recently, investigations were conducted that somewhat corroborated earlier data but presented some new challenges that warrant further investigation. These more recent experiments showed an interesting result that it was quite difficult to adsorb the precursor and characterize it, due to its extremely quick reaction to either x-rays or the photoelectrons generated by X-ray irradiation. This resulted in the rapid desorption of the vast majority of CO ligands, leaving some amount of Co on the surface. The only known experimental differences between the two series of experiments are (1) the earlier experiments were conducted with $Co_2(CO)_8$ heated to 30-40 °C, while the more recent experiments discussed in Figures 6, 7, and 8 were conducted with $Co_2(CO)_8$ held at room temperature (~21 °C) and (2) some of the earlier experiments adsorbed $Co_2(CO)_8$ onto a substrate cooled to 168 K (± 10 K), while other earlier and the more recent experiments adsorbed $Co_2(CO)_8$ onto a substrate cooled to 113 K (± 10 K).

Figure 6 shows survey XPS spectra for the clean Au substrate in the bottom spectra. The middle spectra shows adsorbed $Co_2(CO)_8$; it can be noted that the Au substrate peaks are essentially absent, due to the thickness of the $Co_2(CO)_8$ adlayer. The top spectra shows the system after a pressure excursion caused by the brief X-ray exposure, in which it can

be see that the majority of CO ligands have desorbed, and the Au substrate peaks have largely returned, although Co is still present on the substrate.
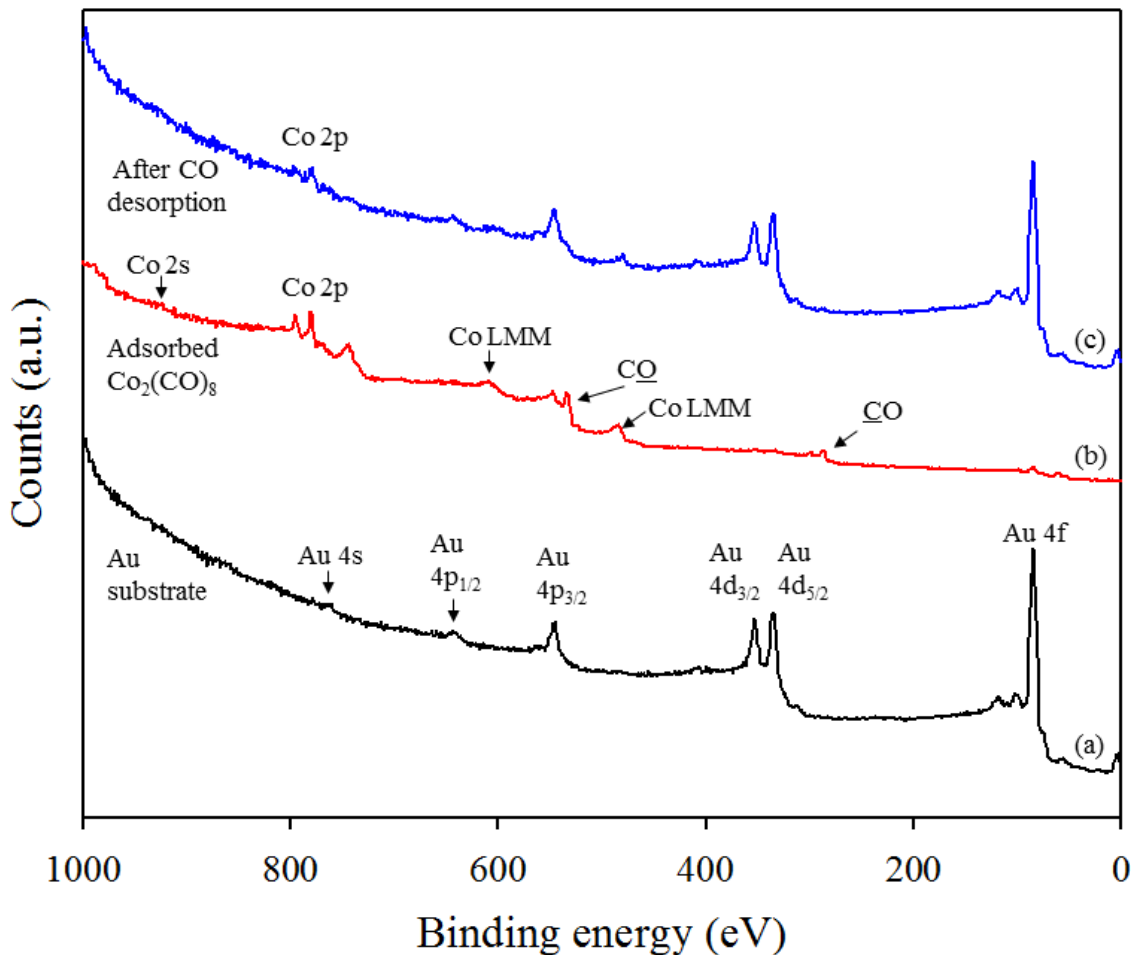


**Figure 6.6**: Wide-scan survey spectra shown for (a) a clean Au substrate cooled to 113 K, (b) adsorbed $Co_2(CO)_8$, and (c) the Au substrate immediately after X-ray exposure.

Figure 7 presents XPS data for $Co_2(CO)_8$ for the C(1s), O(1s), and Co(2p) XP regions for one experiment conducted with $Co_2(CO)_8$ heated to 30 °C during dosing to the UHV chamber, adsorbed onto a $SiO_2$ substrate at 168 K ($\pm$ 10 K), and then exposed to an electron dose of 5.6 x $10^{16}$ e⁻/cm². In the C(1s) region, the "as deposited" film shows a large peak centered at 287.7 eV, characteristic of C contribution from a CO ligand[33], a

smaller peak at 293.1 eV, attributed to a $\pi$-$\pi^*$ shake-up feature typically seen for carbonyls[33] and a small peak at 284.3 eV, attributed to graphitic carbon, ascribed to hexanes used to stabilize the $Co_2(CO)_8$, or hydrocarbons adsorbed from the UHV chamber. After electron beam irradiation, the peak has shifted lower in binding energy to 285.5 eV, and the two CO features are no longer visible, indicating decomposition of some of the CO ligands and deposition of graphitic carbon from the electron gun.

In the O(1s) region, the dominating factor is the large contribution from the $SiO_2$ substrate, with the substrate peak centered at 532.9 eV; however, a small $\pi$-$\pi^*$ CO shake-up feature is observed, centered at 540.1 eV. The larger CO peak expected from CO species is obscured by the substrate but the presence of the CO (or another species, since it is obscured by the $SiO_2$ peak) can be extrapolated by the widening of the $SiO_2$ peak, and the appearance of a shoulder centered at 534.2 eV. After electron beam irradiation, the shake-up feature has disappeared, and the $SiO_2$ oxide peak has returned to the appearance of a clean $SiO_2$ substrate, without the broadening effect of another species.

In the Co(2p) region, the "as deposited" spectra shows a well-defined Co $(2p_{1/2}/2p_{3/2})$ doublet with peaks centered at 795.7 eV and 780.9 eV. The sharp appearance of the peaks and minimal broadening indicates Co in a close to metallic state. After electron beam irradiation, the peaks have decreased in binding energy to 794.8 eV and 779.8 eV, and the peaks have broadened, most noticeably the Co $2p_{3/2}$ peak. This is indicative of a change in the bonding of the Co, and possibly of an oxide formation, although this figure does not provide enough information to make that determination.
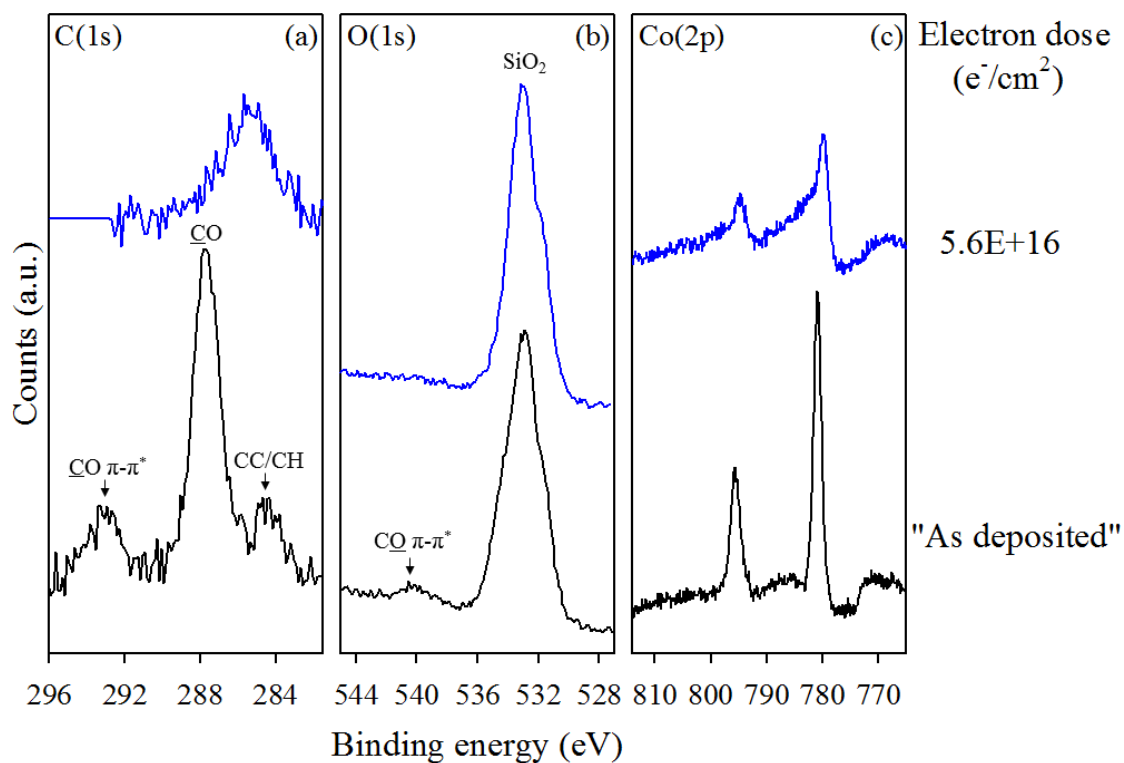
**Figure 6.7**: Evolution of the (a) C(1s), (b) O(1s) and (c) Co(2p) XP regions for a thin film (~0.5 − 1 nm) of $Co_2(CO)_8$ adsorbed on an $SiO_2$ substrate at 163 K (± 10 K) and exposed to electron irradiation at 5 μA. In each panel, the lower spectrum is an "as deposited" dose, after only brief x-ray exposure. For this experiment, $Co_2(CO)_8$ was dosed to the UHV chamber at 30 °C (± 5 °C).
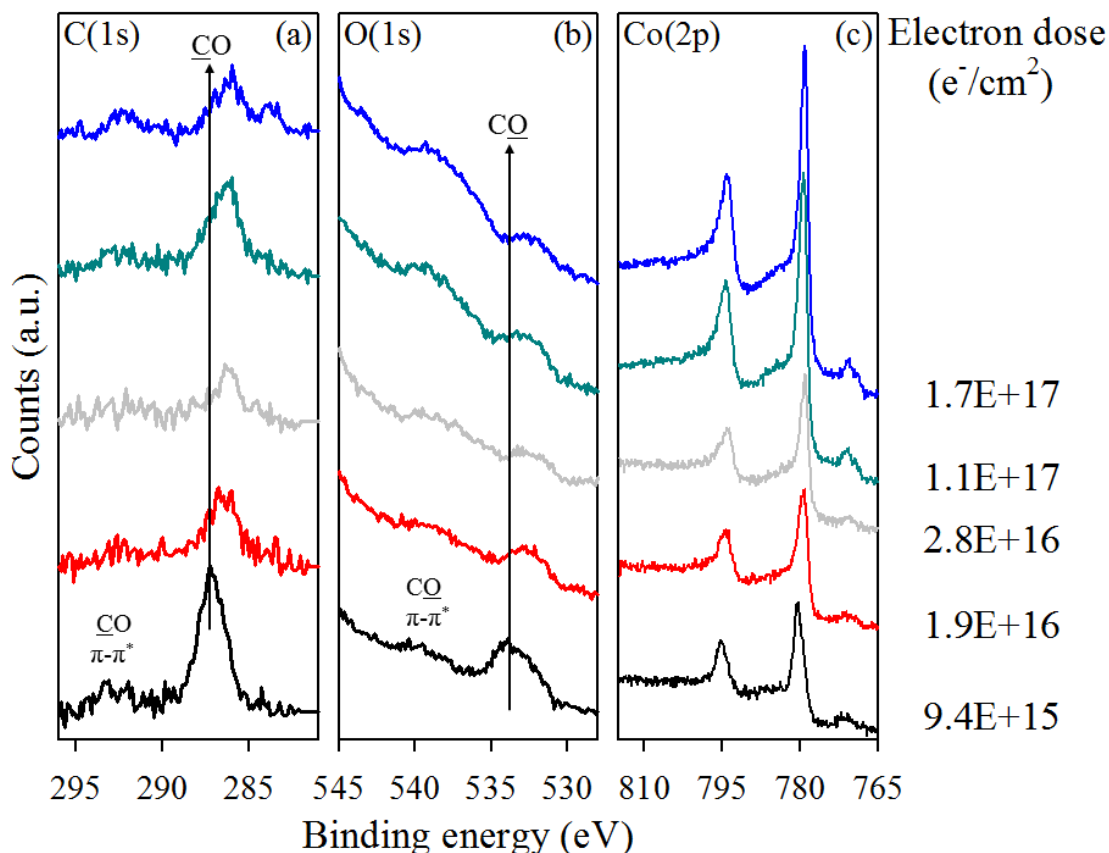
**Figure 6.8**: Evolution of the (a) C(1s), (b) O(1s) and (c) Co(2p) XP regions for thin films (~0.5 – 1 nm) of $Co_2(CO)_8$ adsorbed on an Au substrate at 113 K (± 10 K) and exposed to electron irradiation at 5 μA. In each panel, the lower spectrum is an "as deposited" dose, after only brief x-ray exposure. For these experiments, $Co_2(CO)_8$ was dosed to the UHV chamber at ~21 °C.

Figure 8 presents XPS data for $Co_2(CO)_8$ for the C(1s), O(1s), and Co(2p) XP regions for experiments conducted with $Co_2(CO)_8$ held at room temperature (~21 °C) during dosing to the UHV chamber, adsorbed on an Au substrate at 113 K (± 10 K) and then exposed to increasingly greater electron beam irradiation. This figure does not have an "as deposited" spectra, as it was not possible to adsorb it without rapid desorption from the surface. Thus, the data in this figure was obtained by adsorbing the compound, then exposing it to a specified electron dose, and then characterizing with X-rays. The data is

consistent with what would be expected for an "as deposited" dose as shown in Figure 7. This challenge also affected the ability to calculate film thickness accurately; thus, film thicknesses for films shown in Figure 8 are only estimations.

In the C(1s) region, the spectra for an electron dose of 9.4 x $10^{15}$ $e^-/cm^2$ shows a large peak centered at 287.2 eV and a smaller peak at 293.1 eV attributed to a $\pi$-$\pi^*$ shake-up feature, both typical of carbonyl ligands. As the film is exposed to increasingly greater electron doses, the large CO peak downshifts in binding energy to 286.1 eV, and broadens, indicative of both CO desorption and decomposition of CO ligands on the surface. A small peak grows in at 283.8 eV, ascribed to graphitic carbon from the electron gun, hydrocarbons from the UHV chamber, or decomposition of CO on the surface. The CO $\pi$-$\pi^*$ shake-up feature does not show expected behavior as it is still visible after an electron dose of 1.7 x $10^{17}$ $e^-/cm^2$, although it is also apparent that there is still carbonyl carbon from the larger peak on the surface in this experiment as well. In Figure 8, the bottom three spectra are from one film, and the top two spectra are from a $2^{nd}$ film; thus, a direct comparison can be made between the bottom three and top two spectra. It is apparent that there are differences in film thickness between the two films (i.e. the film used in the top two spectra appears to be thicker than the film characterized by the bottom three spectra), which may be the source of the differing results observed. The shake-up feature is seen to disappear in the bottom three spectra. The top two spectra tell a different story, and in fact, it appears that the shake-up feature grows stronger between the 1.1 x $10^{17}$ and 1.7 x $10^{17}$ $e^-/cm^2$ doses, when it would be expected to decrease, or disappear. This is especially odd since the larger CO peak decreases in intensity and broadens, while the shake-up feature seems to grow stronger. The reaction is assessed as not completed at this point due to the

presence of a significant CO species on the surface. The unusual shake-up manifestation may be due to an experimental issue but it warrants further investigation.

In the O(1s) region, the initial spectra, after an electron dose of $9.4 \times 10^{15}$ e$^-$/cm$^2$, is composed of a broad peak centered at 533.4 eV, characteristic of oxygen in a CO ligand and a smaller peak at 539.5 eV, ascribed to the CO shake-up feature. The large peak just to the left of the CO features is the beginning of the substrate Au $4p_{3/2}$ peak. It can be implied from the broadness of the primary CO peak that a portion of CO has already desorbed and the peak is starting to downshift in binding energy, as compared to the "as deposited" film shown in Figure 7. In fact, the peak was originally centered at 534.0 eV (from XPS data) before beginning to downshift due to ligand desorption/decomposition. As the film is exposed to increasingly greater electron doses, the major CO peak is observed to decrease in binding energy and size, indicative of CO desorption, CO ligand decomposition, and likely some oxide formation. A similar trend with the shake-up feature in the O(1s) region is observed as seen and discussed in the C(1s) region.

In the Co(2p) region, after an electron dose of $9.4 \times 10^{15}$ e$^-$/cm$^2$, the region is initially composed of a Co $2p_{1/2}$/$2p_{3/2}$ doublet with sharp peaks at 795.2 eV and 780.4 eV. In contrast to the "as deposited" film shown in Figure 7, this region already has some peak broadening, indicative of changes in the Co bonding environment. After exposure to increasingly greater electron doses, the Co $2p_{3/2}$ peak has decreased in binding energy to 778.0 eV after an electron dose of $2.8 \times 10^{16}$ e$^-$/cm$^2$, or 779.0 eV after an electron dose of $1.7 \times 10^{17}$ e$^-$/cm$^2$. This discrepancy is due to the differences in film thickness between the films used for first three and second two spectra, or possibly other factors, but the trend is the same, showing Co reduction towards a more metallic state.

202

6.4.  Discussion


6.4.1.  CpFe(CO)$_2$Mn(CO)$_5$


Evaluation of CpFe(CO)$_2$Mn(CO)$_5$ under electron beam irradiation is ongoing research, and thus, there is still further information to be gained.  However, it is possible to draw some preliminary conclusions about its performance under electron beam irradiation.  Figure 1 shows XPS data for the beginning, or "as dosed" compound, compared with data at the end of the first, or deposition/decomposition stage of the reaction.  The reaction was assessed as being complete when the vast majority of carbonyl carbon and oxygen had desorbed.  Previous studies have indicated that identity of the metal center does not impact the behavior of the ligands during focused electron beam induced deposition, as was observed in studies on M(hfac)$_2$[38].  This study provided the opportunity to evaluate the carbonyl ligand (CO) bonded independently to Fe and Mn and thus, might be expected to show two distinct carbonyl species in the C(1s) or O(1s) regions.  This wasn't observed, supporting the fact that the metal center does not substantially change the electronic environment of the ligand.  In this particular case, despite the fact that Mn is surrounded by five CO ligands while Fe has two CO ligands and a Cp ring, no difference in carbonyl binding energy was apparent (if present, it is below the resolution of the XPS). A strong CO $\pi$-$\pi$* shake-up feature is also observed, due to the large number of carbonyl ligands.  After electron irradiation, the C(1s) region is composed of primarily Cp carbon, and the O(1s) region is composed of a small amount of oxygen at a lower binding energy, characteristic of a small amount of decomposition and oxide formation, and consistent with previous observations that multiple CO ligands can desorb under electron beam

203

irradiation[14,20,21,35].

Under electron irradiation, Fe decreases in binding energy, reducing towards a more metallic state as CO ligands desorb. There is a small amount of bonding change visible in the Fe(2p) XP region, as well possibly oxide formation, based on the O(1s) region. It is an open question as to which metal experiences the most oxidation; it appears that it is manganese as iron shows minimal oxidation. The oxide formation may also be due to decomposition of CO ligands or due to oxidation from residual $H_2O$ vapor in the UHV chamber.

The mass spectrometry data shown in Figure 2a indicates that the primary species ejected during electron beam irradiation is CO, which correlates with previous experimental observations[14,20,21,35]. Figure 3 shows that the majority of the CO ligands have desorbed after an electron dose of ~2 x $10^{16}$ e⁻/cm². Interestingly, this is a faster reaction than observed for many other compounds with single metal centers; initial results indicate that it is approximately five times as fast, but this is still being investigated. One possible reason for the faster kinetics could be instability in the $CpFe(CO)_2Mn(CO)_5$ molecule, which may be more susceptible to electron irradiation than a molecule with a single metal center. Lastly, the SEM and EDS data show that $CpFe(CO)_2Mn(CO)_5$ does deposit under steady state conditions similar to those used in FEBID, with no conformal CVD deposition observed.
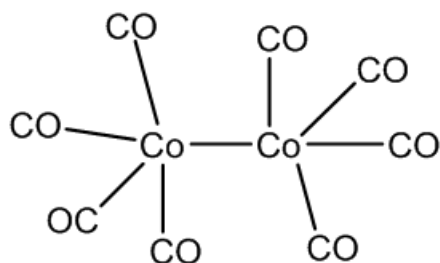
### 6.4.2. $Co_2(CO)_8$

$Co_2(CO)_8$ presented interesting challenges in the more recent experiments discussed briefly in this chapter. $Co_2(CO)_8$ was successfully adsorbed on the cooled Au
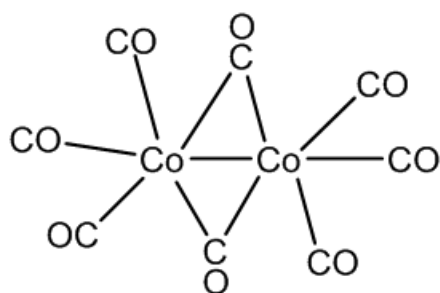
substrate, but after brief exposure to X-ray irradiation (and thus, the stimulated photoelectrons), the adsorbed precursor reacted very quickly and the vast majority of CO desorbed from the substrate, leaving Co behind.  This was not observed in previous experiments, but it was consistently observed with the current experimental protocol and it is possible that this behavior will provide some interesting insights into the catalytic capabilities of the $Co_2(CO)_8$, which are considered as a primary reason why $Co_2(CO)8$ is able to deposit nanostructures of relatively high purity in FEBID[22].  The only known differences between the two series of experiments are (1) the earlier set of experiments used $Co_2(CO)_8$ heated to 30-40 °C while dosing to the UHV chamber, while the more recent set of experiments primarily used $Co_2(CO)_8$ at room temperature (~21 °C), and (2) the substrate temperature was lower (colder) for the more recent experiments (113 K vs. 168 K) which may have caused some differences in the results.  Another possible difference is that earlier experiments may have only pumped $Co_2(CO)_8$ to the UHV chamber with the precursor held at liquid nitrogen temperatures, and may not have allowed further pumping to the UHV chamber as the precursor was allowed to warm up.

Our experimental protocol began with evacuation to the UHV chamber of the glass finger containing $Co_2(CO)_8$, while maintaining the precursor at ~77 K (~ -195 °C) using liquid nitrogen.  Next, the liquid nitrogen was removed and the precursor was allowed to warm while still being evacuated to the UHV chamber, with the intent to remove residual

hexanes used to stabilize the compound. This has the effect of removing CO from the test tube, but keeping the majority of the precursor intact. It is likely that removal of the excess CO, coupled with the warming, caused two effects. Figure 9 shows two isomers of $Co_2(CO)_8$. Based on IR studies, Noack noted that at room temperature, $Co_2(CO)_8$ is present mainly in the isomer in which each Co is bonded to the other Co and four CO ligands[39]. Removal of the CO by pumping it to the UHV chamber has the effect of quantitatively converting $Co_2(CO)_8$ to $Co_4(CO)_{12}$ on a relatively short timescale (~ 9 hours) as noted by Bor and Deitler[40]. Tannenbaum *et. al.* noted that under a relatively rough vacuum (10-20 mTorr), $Co_2(CO)_8$ decomposes to $Co_4(CO)_{12}$ with a first order decay process that is dependent on the mole fraction of $Co_4(CO)_{12}/Co_2(CO)_8$; this would be expected to be accelerated with the use of the UHV environment[41]. $Co_2(CO)_8$ and its conversion to $Co_4(CO)_{12}$ has a series of complex equilibria at different temperatures and pressures[40,42], which almost certainly contributes to the myriad of results obtained when using $Co_2(CO)_8$ for FEBID[43]. Sweany and Brown noted that under ultraviolet light, $Co_2(CO)_8$ decomposes to $Co_2(CO)_7$ ($h\nu$ = 254 nm) and $Co(CO)_4$ radicals ($h\nu$ = 350 nm)[44], and Palyi *et. al.* noted that $Co(CO)_4$ radicals play a role as intermediates in the elementary steps of reactions of $Co_2(CO)_8$[45]. In FEBID experiments, Muthukumar *et. al.* reported



non-CO-bridged isomer



CO-bridged isomer

**Figure 6.9**: Isomers of $Co_2(CO)_8$

spontaneous decomposition of $Co_2(CO)_8$ on pretreated $SiO_2$ surfaces, but did not observe spontaneous decomposition on untreated $SiO_2$ surfaces except for longer exposure times[22]. Their results also suggest that $Co_2(CO)_8$ has the ability to auto-catalytically decompose to $Co_4(CO)_{12}$ under FEBID conditions. It is apparent that the complex equilibria for $Co_2(CO)_8$, coupled with the catalytic properties of cobalt, can provide a variety of results for FEBID nanostructures, and minor variations in experimental conditions can cause large differences in the resulting nanostructures. It is possible that the change in our experimental conditions resulted in a higher proportion of $Co(CO)_4$ radicals adsorbed on the surface, which are very reactive to any amount of irradiation, or that autocatalytic behavior is taking place under X-ray irradiation. Further investigation is required into the cause of the rapid desorption of the majority of the CO ligands from the substrate under x-ray irradiation, which may illuminate other interesting details for FEBID.

Figures 7 and 8 show XPS spectra of $Co_2(CO)_8$ under electron beam irradiation. Once this compound was adsorbed, its reactions with electrons are similar to those observed for several other compounds, in which the vast majority of CO ligands desorb, while the remainder decompose on the surface. FEBID experiments conducted with the substrate at room temperature would likely see less CO ligand decomposition, as local heating can assist in the electron stimulated desorption of CO ligands. The degree of oxide formation is difficult to gage, but the net reduction in Co binding energy, coupled with the retention of sharp peak shapes, suggests that minimal oxide is formed. The broadening seen at the base of the Co peaks is likely due to changes in Co bonding, but more broadening would be expected for oxide formation. Thus, the lower binding energy feature in the O(1s) region is likely due to CO ligand decomposition rather than oxide formation.

## 6.5. Conclusion

The dissimilar bimetallic compound $CpFe(CO)_2Mn(CO)_5$ was adsorbed onto an Au substrate and exhibited expected desorption characteristics under electron beam irradiation. The compound showed much quicker reaction rates than observed for other precursors studied to date, possibly due to greater instability of the complex overall, and more opportunities for desorption to occur. Continuing work on this ongoing project is anticipated to include evaluation on an amorphous carbon (a:C)/highly ordered pyrolytic graphite substrate, which will allow analysis of the Mn(2p) XP transitions, which are masked by the Au $4p_{1/2}$ XP transition on the Au substrate.

$Co_2(CO)_8$ manifested an unusual reactivity either due to X-ray irradiation or a much quicker reaction to electrons than observed for $CpFe(CO)_2Mn(CO)_5$. Ongoing gas phase investigation of $Co_2(CO)_8$ will provide interesting information that may help elucidate the open questions about $Co_2(CO)_8$ behavior under x-ray irradiation; further evaluation is required. Further work will involve evaluation of another interesting bimetallic compound, $Cp(CO)_3W-Co(CO)_4$, as well as comparison with gas phase mass spectrometry data from both $CpFe(CO)_2Mn(CO)_5$ and $Cp(CO)_3W-Co(CO)_4$.

## 6.6. Acknowledgements

## 6.7. References

(1)     Huth, M.; Porrati, F.; Schwalb, C.; Winhold, M.; Sachser, R.; Dukic, M.; Adams, J.; Fantner, G. *Beilstein journal of nanotechnology* **2012**, *3*, 597.

(2)     Utke, I.; Hoffmann, P.; Melngailis, J. *Journal of Vacuum Science & Technology B* **2008**, *26*, 1197.

(3)     Van Dorp, W.; Hagen, C. *Journal of Applied Physics* **2008**, *104*, 081301.

(4)     Randolph, S.; Fowlkes, J.; Rack, P. *Critical reviews in solid state and materials sciences* **2006**, *31*, 55.

(5)     van Dorp, W. *Applied Physics A* **2014**, *117*, 1615.

(6)     Van Dorp, W.; Hagen, C.; Crozier, P.; Kruit, P. *Nanotechnology* **2008**, *19*, 225305.

(7)     Mulders, J. *Nanofabrication* **2014**, *1*, 74.

(8)     Hagen, C. *Applied Physics A* **2014**, *117*, 1599.

(9)     Xue, Z.; Strouse, M. J.; Shuh, D. K.; Knobler, C. B.; Kaesz, H. D.; Hicks, R. F.; Williams, R. S. *Journal of the American Chemical Society* **1989**, *111*, 8779.

(10)    Edinger, K.; Becht, H.; Bihr, J.; Boegli, V.; Budach, M.; Hofmann, T.; Koops, H. W.; Kuschnerus, P.; Oster, J.; Spies, P. *Journal of Vacuum Science & Technology B* **2004**, *22*, 2902.

(11)    Liang, T.; Frendberg, E.; Lieberman, B.; Stivers, A. *Journal of Vacuum Science & Technology B* **2005**, *23*, 3101.

(12)    Chen, I.-C.; Chen, L.-H.; Orme, C.; Quist, A.; Lal, R.; Jin, S. *Nanotechnology* **2006**, *17*, 4322.

(13)    Hübner, B.; Koops, H.; Pagnia, H.; Sotnik, N.; Urban, J.; Weber, M. *Ultramicroscopy* **1992**, *42*, 1519.

(14)    Rosenberg, S. G.; Barclay, M.; Fairbrother, D. H. *Physical Chemistry Chemical Physics* **2013**, *15*, 4002.

(15)    Rosenberg, S. G.; Landheer, K.; Hagen, C. W.; Fairbrother, D. H. *Journal of Vacuum Science & Technology B* **2012**, *30*, 051805.

(16)    Wnuk, J. D.; Gorham, J. M.; Rosenberg, S. G.; van Dorp, W. F.; Madey, T. E.; Hagen, C. W.; Fairbrother, D. H. *The Journal of Physical Chemistry C* **2009**, *113*, 2487.

(17)    Spencer, J. A.; Rosenberg, S. G.; Barclay, M.; Wu, Y.-C.; McElwee-White, L.; Fairbrother, D. H. *Applied Physics A* **2014**, *117*, 1631.

(18)    Porrati, F.; Pohlit, M.; Müller, J.; Barth, S.; Biegger, F.; Gspan, C.; Plank, H.; Huth, M. *Nanotechnology* **2015**, *26*, 475701.

(19)    Porrati, F.; Kämpken, B.; Terfort, A.; Huth, M. *Journal of Applied Physics* **2013**, *113*, 053707.

(20)    Rosenberg, S. G.; Barclay, M.; Fairbrother, D. H. *The Journal of Physical Chemistry C* **2013**, *117*, 16053.

(21)    Spencer, J. A.; Brannaka, J. A.; Barclay, M.; McElwee-White, L.; Fairbrother, D. H. *The Journal of Physical Chemistry C* **2015**, *119*, 15349.

(22)    Muthukumar, K.; Jeschke, H. O.; Valentí, R.; Begun, E.; Schwenk, J.; Porrati, F.; Huth, M. *Beilstein journal of nanotechnology* **2012**, *3*, 546.

(23)    Wnuk, J. D.; Gorham, J. M.; Rosenberg, S. G.; van Dorp, W. F.; Madey, T. E.; Hagen, C. W.; Fairbrother, D. H. *Journal of Applied Physics* **2010**, *107*, 054301.

(24)    Johnston, P.; Hutchings, G. J.; Denner, L.; Boeyens, J. C.; Coville, N. J. *Organometallics* **1987**, *6*, 1292.

(25)    King, R.; Stone, F. *Inorganic Syntheses, Volume 7* **1963**, 196.

(26)    King, R., Treichel, P.M., Stone, F.G.A. *Chemistry and Industry* **1961**, 747.

(27)    Bajt, S.; Alameda, J. B.; Barbee, T. W.; Clift, W. M.; Folta, J. A.; Kaufmann, B.; Spiller, E. A. *Optical engineering* **2002**, *41*, 1797.

(28)    Wnuk, J. D.; Gorham, J. M.; Rosenberg, S. G.; van Dorp, W. F.; Madey, T. E.; Hagen, C. W.; Fairbrother, D. H. *J. Appl. Phys.* **2010**, *107*, 054301/1.

(29)    Powell, C. J.; Jablonski, A. *NIST Electron Inelastic-Mean-Free-Path Database, Version 1.2, SRD 71*; National Institute of Standards and Technology: Gaithersburg, MD, USA, 2010.

(30)    Tanuma, S.; Powell, C. J.; Penn, D. R. *Surface and Interface Analysis* **1991**, *17*, 911.

(31)     Tanuma, S.; Powell, C.; Penn, D. *Surf. Interface Anal.* **2011**, *43*, 689.

(32)     Wnuk, J. D.; Gorham, J. M.; Rosenberg, S. G.; van Dorp, W. F.; Madey, T. E.; Hagen, C. W.; Fairbrother, D. H. *J. Phys. Chem. C* **2009**, *113*, 2487.

(33)     Plummer, E.; Salaneck, W.; Miller, J. S. *Physical Review B* **1978**, *18*, 1673.

(34)     Moulder, J. F., Stickle, William F., Sobol, Peter E., Bomben, Kenneth D. *Handbook of X-ray Photoelectron Spectroscopy*; Physical Electronics USA, Inc.: Chanhassen, Minnesota, USA, 1995.

(35)     Spencer, J. A.; Wu, Y.-C.; McElwee-White, L.; Fairbrother, D. H. *Journal of the American Chemical Society* **2016**.

(36)     Dobrovolskiy, O. V.; Kompaniiets, M.; Sachser, R.; Porrati, F.; Gspan, C.; Plank, H.; Huth, M. *Beilstein journal of nanotechnology* **2015**, *6*, 1082.

(37)     Fernández-Pacheco, A.; De Teresa, J.; Córdoba, R.; Ibarra, M. R. *Journal of Physics D: Applied Physics* **2009**, *42*, 055005.

(38)     Rosenberg, S. G.; Barclay, M.; Fairbrother, D. H. *ACS applied materials & interfaces* **2014**.

(39)     Noack, K. *Spectrochimica Acta* **1963**, *19*, 1925.

(40)     Bor, G.; Dietler, U. K. *Journal of Organometallic Chemistry* **1980**, *191*, 295.

(41)     Tannenbaum, R.; Bor, G. *Journal of organometallic chemistry* **1999**, *586*, 18.

(42)     Mirbach, M. F.; Saus, A.; Krings, A.-M.; Mirbach, M. J. *Journal of Organometallic Chemistry* **1981**, *205*, 229.

(43)     Utke, I.; Michler, J.; Gasser, P.; Santschi, C.; Laub, D.; Cantoni, M.; Buffat, P. A.; Jiao, C.; Hoffmann, P. *Advanced Engineering Materials* **2005**, *7*, 323.

(44)     Sweany, R. L.; Brown, T. L. *Inorganic Chemistry* **1977**, *16*, 421.

(45)     Pályi, G.; Ungváry, F.; Galamb, V.; Markó, L. *Coordination chemistry reviews* **1984**, *53*, 37.

**Curriculum Vitae**

Julie A. Spencer was born on November 14, 1971, in Fort Leavenworth, Kansas. She graduated from Kadena High School, located on Kadena Air Force Base, Okinawa, Japan, in June 1990. She entered the U.S. Naval Academy in Annapolis, Maryland, in July 1990. She graduated from the U.S. Naval Academy in May, 1994 with a Bachelor of Science degree in Chemistry and a minor in Japanese, and was commissioned as an Ensign in the United States Navy.

She served in the United States Navy as a Surface Warfare Officer for 18 years and made several shipboard deployments around the world. She served in various shipboard positions, culminating in her assignment as Executive Officer, USS RODNEY M DAVIS (FFG 60) from July, 2008 through October, 2010. She earned a Master of Arts Degree in Education (Curriculum and Instruction) from Chapman University in August, 2000. She earned a Master of Arts Degree in National Security Studies from the U.S. Naval War College in 2010.

She was selected by the U.S. Navy for the Permanent Military Professor program in Chemistry in September, 2011. She entered the graduate studies program at Johns Hopkins University in the Department of Chemistry in August 2012. Later that year, she joined the laboratory of Dr. D. Howard Fairbrother with whom she completed her doctoral studies in surface and interface chemistry studying the effects of electron beam irradiation on organometallic precursors for focused electron beam induced deposition (FEBID). In August, 2016, she assumed duties as an Assistant Professor of Chemistry at the U.S. Naval Academy.